



**Andreia Filipa Cardoso Ruivo**

Mestre em Química

## **Synthesis and characterization of innovative luminescent glasses for artistic applications**

Dissertação para obtenção do Grau de Doutor em  
Química Sustentável

Orientador: Professor Doutor Fernando Pina, Professor  
Catedrático, FCT/UNL

Co-orientador: Doutor César A. T. Laia, Investigador Auxiliar,  
FCT/UNL

Co-orientador: Professor Doutor António Pires de Matos, Professor  
Catedrático Jubilado, FCT/UNL

Júri:

Presidente: Prof. Doutora Maria Rosa Santos de Paiva

Arguentes: Prof. Doutor Carlo George Pantano  
Prof. Doutora Sílvia Marília de Brito Costa

Vogais: Prof. Doutor Rui Manuel Amaral de Almeida  
Prof. Doutor José Martinho Marques de Oliveira



**Dezembro 2013**



Copyright © Andreia Filipa Cardoso Ruivo, Faculdade de Ciências e Tecnologia, Universidade Nova de Lisboa

A Faculdade de Ciências e Tecnologia e a Universidade Nova de Lisboa têm o direito, perpétuo e sem limites geográficos, de arquivar e publicar esta dissertação através de exemplares impressos reproduzidos em papel ou de forma digital, ou por qualquer outro meio conhecido ou que venha a ser inventado, e de a divulgar através de repositórios científicos e de admitir a sua cópia e distribuição com objectivos educacionais ou de investigação, não comerciais, desde que seja dado crédito ao autor e editor.





## **Agradecimentos**

Se estou a escrever os agradecimentos é bom sinal, é sinal que depois de muito trabalho, muitas horas sem dormir, muitas colaborações, muita entreaajuda e principalmente depois de muita paciência das pessoas que me rodeiam, estou a chegar ao fim. Gostaria de começar por agradecer ao meu orientador professor Fernando Pina pelo entusiasmo com que faz ciência, pela força que me deu para continuar e ir sempre mais além, e também pelo facto de embora estar sempre ocupado ter sempre a porta aberta para longas conversas como se tivesse todo o tempo do mundo. Gostaria também de agradecer ao professor António Pires de Matos com quem já trabalho há 7 anos (sim professor, já me atura há muito tempo) pelas inúmeras ideias que me deu e por se ter tornado um grande amigo. Um grande obrigada para o meu incansável “chefinho” Doutor César Laia, sem o qual este trabalho não seria possível (depois de muitas discordâncias, alguma teimosia da tua doutoranda, horas ao computador, cálculos loucos chegámos ao fim desta etapa e sinceramente nem tenho palavras para te agradecer).

Gostaria também de agradecer ao Professor Marco Gomes da Silva, ao Professor Hugo Águas, à Doutora Suzana Andrade, à Professora Sílvia Costa, ao Professor Luís Carlos, à Professora Maria Rute André e ao Professor João Rocha pela forte colaboração, sem a qual não seria possível apresentar grande parte dos resultados.

Gostaria de agradecer também a todos os membros da Vicarte e do DCR. Apesar de serem colegas de trabalho, ao longo do tempo tornaram-se grandes amigos. Obrigada às minhas colegas de gabinete, Augusta Lima, Teresa Almeida, Solange Muralha, Mathilda Larson e Márcia Vilarigues (sei que não és do gabinete mas é como se fosses) com quem posso sempre contar. Nem imaginam o quanto lhes estou grata pelo companheirismo ao longo destes anos e por estarem sempre presentes tanto para discussões de trabalho como para aquelas horas que apetece falar de tudo excepto de composições, análises e cálculos. Muito obrigada ao grupo de artistas da Vicarte em especial ao Robert Wiley, Fernando Quintas e Teresa Almeida que foram realmente fundamentais para a escrita da tese, não tivesse esta no título materiais de vidro para a arte. Gostaria de agradecer também à Magda Troeira pela disponibilidade e companheirismo principalmente nesta ultima fase. Ao Carlos Queiroz pelas análises de dilatométrica, principalmente nos últimos meses, mesmo quando tinha inúmeras análises para fazer dava prioridade às minhas. À Vanessa Otero pelas ajuda no FTIR e claro pela sua amizade, à Catarina Miguel e à Ana Isabel Pereira que de diferentes maneiras também me ajudaram ao longo destes anos.

Muito obrigada à Ana Maria, à Cremilde e à Isabel por estarem sempre dispostas a resolverem os problemas burocráticos, que estão sempre a surgir nem se sabe de onde, e por fazerem-no prontamente e sempre com um sorriso.

Muito obrigada a todo o grupo da fotoquímica, pelos momentos bem passados dentro do laboratório (descobri coisas fascinantes sobre flavílios) e também fora do laboratório. Tenho a dizer que é um prazer trabalhar com vocês. Gostaria de agradecer em particular ao professor Jorge Parola e ao professor João Carlos Lima pelo apoio tanto na parte experimental como teórica mas também por me terem aturado tantas vezes no vosso gabinete. Ao João Avó e ao Artur Moura gostaria de agradecer por serem os meus companheiros de montagem e desmontagem do spex. Muito obrigada à Ana Marta Diniz e à Raquel Gavara por toda a ajuda no laboratório, pela companhia quando o trabalho acabava mais tarde e pelas conversas na varanda ótimas para descarregar más energias. Um obrigada especial à Márcia Ventura com quem aprendi muito e que foi um forte apoio para o “pesadelo sol-gel”. À aluna Carla Almeida gostaria de agradecer pela ajuda no trabalho do sol-gel.

Gostaria de agradecer a toda a minha família e amigos, pessoas que parece que já não vejo à uma eternidade mas sempre me incentivaram e apoiaram. Muito obrigado às “mininas” e ao Zé pela amizade e principalmente por nesta última fase me terem dado força para nunca desistir (sendo que nem sequer me deixavam abrandar). Também gostava de agradecer aos ex-fculianos com quem até posso não estar, mas ao mesmo tempo estão sempre presentes.

Um obrigada especial para o Pedro por ter estado sempre envolvido nas diferentes etapas da minha vida e por me ter aturado nesta fase, que ambos sabemos que não foi nada fácil. Obrigada principalmente por conseguir sempre, mesmo nos piores momentos, que eu respire fundo e volte a ver tudo de outra perspectiva. Muito muito obrigada.

Estou a chegar ao fim e espero não me ter esquecido de ninguém. Foram vários anos de trabalho, várias colaborações e muitas pessoas que tornaram possível o desenvolvimento deste trabalho e portanto muito obrigada a todos os que estiveram envolvidos neste projecto.

Como não podia deixar de ser um super obrigada para os meus papás que me tornaram a pessoa que sou. Muito obrigada por estarem sempre presentes em todos os momentos da minha vida, pelo apoio incondicional em todas as minhas decisões, pelas longas conversas e até mesmo pelo silêncio quando este era necessário. Esta tese também é vossa.

## Resumo

Nesta tese será apresentada a síntese e caracterização de novos materiais de vidro para aplicações artísticas. O principal objectivo deste trabalho consistiu na produção de vidros luminescentes, o qual foi atingido utilizando duas estratégias: dopando os vidros com diferentes lantanídeos (capítulos 2 e 3) e utilizando outros elementos tais como halogenetos de chumbo e cobre (capítulo 4). Foram estudados vidros silicatados sodo-cálcicos com diferentes concentrações de  $\text{Eu}_2\text{O}_3$  e de  $\text{CaO}$ . Observou-se uma menor tendência de agregação do európio quando a concentração de  $\text{Eu}_2\text{O}_3$  diminui e quando a de  $\text{CaO}$  aumenta. A síntese de vidros dopados com diferentes óxidos de lantanídeos ( $\text{Tb}_4\text{O}_7$ ,  $\text{Eu}_2\text{O}_3$  e  $\text{CeO}_2$ ) deu origem a várias cores de luminescência. Também foram realizados estudos de cromaticidade que permitiram estimar qual a cor de luminescência obtida para uma determinada composição e/ou compreender o impacto de processos de estado excitado na cor.

Vidros aluminoborosilicatos dopados com chumbo e halogenetos deram origem a um material com luminescência azul. Diferentes técnicas revelaram a existência de nanopartículas cristalinas, que foram atribuídas a nanopartículas de halogenetos de chumbo. Adicionou-se à mesma composição óxido de cobre que gerou luminescência amarela devido à formação de  $\text{Cu}^+$ .

A síntese de vidros rubi de ouro também foi explorada neste trabalho. No capítulo 5 é apresentado um método inovador para a produção de vidros com nanopartículas de ouro, através do método de sol-gel, após adição de um líquido iónico,  $[\text{bmim}][\text{BF}_4]$ , que actua como formador de poros no gel e como agente redutor.

Os vidros produzidos são materiais que os artistas podem utilizar para melhorar ou complementar as suas obras de arte. No capítulo 6 vários artistas da Vicarte deram a sua opinião sobre os materiais desenvolvidos, dando várias ideias para a sua aplicação na arte e na indústria e também para o desenvolvimento de novos materiais em trabalho futuro.

Palavras chave: Vidros luminescentes, espectroscopia, nanopartículas de halogenetos de chumbo, ião cuproso, lantanídeos, vidros rubi de ouro.



## Abstract

This thesis reports the synthesis and characterization of new glass materials for artistic applications. The production of innovative luminescent glasses was the main objective and it was accomplished through two strategies: using lanthanide oxides (chapters 2 and 3) and using other elements such as lead halides and copper (chapter 4).  $\text{Eu}_2\text{O}_3$  doped soda-lime silicate glasses were investigated as dependent of  $\text{Eu}_2\text{O}_3$  and  $\text{CaO}$  concentrations in order to obtain a better structural understanding of this glass system. Spectroscopic measurements provided evidence of a less clustering tendency when  $\text{Eu}_2\text{O}_3$  concentration decreases and when  $\text{CaO}$  increases. Doping the same glass with a mixture of lanthanides oxides ( $\text{Tb}_4\text{O}_7$ ,  $\text{Eu}_2\text{O}_3$  and  $\text{CeO}_2$ ), a large range of luminescence colours was obtained. Chromaticity studies were applied, which can allow the estimation of the luminescent colour produced for a given composition and/or understand the impact of excited-state processes in the final luminescence colour.

When an aluminoborosilicate glass was doped with lead and halides a blue luminescence was produced. Using different techniques, crystalline nanoparticles were identified and attributed to lead halide nanoparticles. The same glass composition was doped with copper, which gave rise to a yellow luminescence due to formation of  $\text{Cu}^+$ .

Finally, the synthesis of ruby gold glass was also studied. In chapter 5 is shown an innovative way to produce gold nanoparticles on glass materials using sol-gel synthesis with an ionic liquid,  $[\text{bmim}][\text{BF}_4]$ , that acts in this system not only as porogen but also as reductive agent, since the reduction is achieved by the  $[\text{bmim}][\text{BF}_4]$  decomposition products.

The glasses produced are materials that artists can use to improve or to complement their artworks. In chapter 6, the artists from Vicarte were confronted with the materials developed in this thesis, giving important insights about the use of luminescent glass by artists and industry and future developments worth pursuing.

**Keywords:** Luminescent glass, spectroscopy, lead halide nanoparticles, cuprous ion, lanthanides, gold ruby glass.



**Abbreviations List**

A	Absorbance
$a$	pre-exponential
a.u.	Arbitrary units
BG	Base glass
$c$	Speed of light
CIE	Commission Internationale de l' Eclairage
CTE	Coefficient of Thermal Expansion
$d$	Density
DSC	Differential scanning calorimetry
ED	Electric dipole
$e$	Electron charge
E	Energy
EDS	Energy dispersive X-ray spectroscopy
FT-IR	Fourier transform infrared spectroscopy
FWHM	Full width at half maximum
GC/qMS	Gas chromatography/mass spectrometry (quadrupole)
$T_g$	Glass transition temperature
HS-SPME	Headspace-solid phase microextraction
IL	Ionic liquid
$\tau$	Lifetime
MD	Magnetic dipole
$\mu$ -EDXRF	Micro-energy dispersive X-ray fluorescence
$\varepsilon$	Molar absorption coefficient
$f$	Oscillator strength
$h$	Planck's constant
$k_B$	Boltzmann constant
NIR	Near infrared
$n$	Refractive indices
PL	Photoluminescence
SAED	Selected area diffraction
SPC	Single photon counting
$T_{\text{sint}}$	Sintering temperature
$t_{\text{sint}}$	Sintering time
$T_s$	Softening temperature point
$T$	Transmission
TEOS	Tetraethoxysilane
TMOS	Tetramethyl orthosilicate

## Synthesis and characterization of innovative luminescent glasses for artistic applications

TGA	Thermogravimetry
TEM	Transmission electron microscopy
UV/Vis	Ultraviolet/visible
$\lambda$	Wavelength
$\lambda_{\text{em}}$	Emission wavelength
$\lambda_{\text{exc}}$	Excitation wavelength
wt	Weight
W-LED	White light emitting diodes
XRD	X-ray Diffraction



**Index of Contents**

<b>1. Introduction</b>	<b>1</b>
1.1. Coloured and Luminescent glass in art	1
1.2. Glass	6
1.3. Colour in glass	10
1.3.1. Colour due to metallic ions	12
1.3.2. Colour due to chromophores in a colloidal state	12
1.4. Luminescence in glass	13
1.4.1. Lanthanide doped glasses	14
1.4.2. Other element doped glasses	20
1.5. Focus of the present thesis	21
 <b>2. Synthesis and characterization of luminescent <math>\text{Eu}_2\text{O}_3</math> doped glasses</b>	
2.1. Europium oxide doped glasses	23
2.2. Experimental Part	24
2.2.1 Synthesis and samples preparation	24
2.2.2. Measurements	25
2.3. Synthesis and characterization of $\text{Eu}_2\text{O}_3$ doped $\text{Na}_2\text{O-CaO-SiO}_2$ glass	26
2.3.1. Physical properties	26
2.3.2. UV/Vis/NIR Absorption Spectroscopy	28
2.3.3. Luminescence Spectroscopy	34
2.3.4. Spectroscopic measurements analysis and discussion	41
2.4. Conclusions	45
 <b>3. Synthesis of luminescent glasses using different lanthanides</b>	<b>47</b>
3.1. Lanthanide oxides in glass	47
3.2. Experimental Part	49
3.2.1 Synthesis and samples preparation	49
3.2.2. Measurements	50
3.3. Different lanthanides in a $\text{Na}_2\text{O-CaO-SiO}_2$ glass matrix: single, binary and ternary systems	50
3.3.1. Glasses doped with one lanthanide – Single system	51
3.3.2. Glasses doped with two lanthanides – Binary system	54
3.3.3. Glasses doped with three lanthanides – Ternary system	63
3.3.4. Luminescence Colour Coordinates	66
3.4. Conclusions	73

<b>4. Luminescent aluminoborosilicate glass with lead halide nanoparticles and cuprous ion</b>	<b>75</b>
4.1. Luminescent glasses without lanthanide oxides	75
4.2. Experimental Part	77
4.2.1. Synthesis and samples preparation	77
4.2.2. Measurements	79
4.3. Synthesis and characterization of luminescent glasses in aluminoborosilicate glass using different metals: lead halides and CuO	80
4.3.1. Luminescent aluminoborosilicate glasses doped with different lead halides	82
4.3.2 Aluminoborosilicate glass doped with different copper concentrations	95
4.4. Conclusions	106
<b>5. Sol-gel glass materials with gold nanoparticles</b>	<b>107</b>
5.1. Synthesis of gold nanoparticles in different materials	107
5.2. Experimental Part	109
5.2.1. Sol-gel preparation and densification	109
5.2.2. Measurements	110
5.3. Synthesis of sol-gel glass with gold nanoparticles using an ionic liquid as a reduction agent	112
5.3.1. Monoliths characterization by UV-VIS absorption spectroscopy	115
5.3.2. TEM and EDS Measurements	117
5.3.3 Ionic liquid decomposition	120
5.3.4 Formation of gold nanoparticles	124
5.4. Conclusions	125
<b>6. Impact of the produced materials in art</b>	<b>127</b>
6.1. Developed materials	127
6.2. Vicarte glass artists' interview	128
6.2.1. Teresa Almeida	128
6.2.2. Robert Wiley	129
6.2.3. Fernando Quintas	129
6.3. Insights given by Vicarte artists and directions for future work	131
<b>7. References</b>	<b>135</b>
<b>8. Publications</b>	<b>145</b>

<b>9. Supplementary Material</b>	<b>147</b>
9.1. Synthesis and characterization of luminescent $\text{Eu}_2\text{O}_3$ doped glasses	147
9.1.1. $\text{Eu}_2\text{O}_3$ doped glass compositions and quantity of oxides used in the glass synthesis.	147
9.1.2. Linear thermal expansion of the base glass - glass sample E0 (74% $\text{SiO}_2$ , 16% $\text{Na}_2\text{O}$ and 10% $\text{CaO}$ )	147
9.1.3. Modelling used to determine the refractive index using ellipsometry technique	148
9.1.4. Linear dependence between absorbance and $\text{Eu}_2\text{O}_3$ concentration	148
9.2. Synthesis of luminescent glasses using different lanthanides	149
9.2.1. Quantity of oxides used to prepare 30 g of each glass with different lanthanides	149
9.2.2. Linear thermal expansion of the base glass (74% $\text{SiO}_2$ , 16% $\text{Na}_2\text{O}$ and 10% $\text{CaO}$ ) doped with different lanthanide oxides ( $\text{Eu}_2\text{O}_3$ , $\text{Tb}_4\text{O}_7$ , $\text{CeO}_2$ , $\text{Dy}_2\text{O}_3$ , $\text{Tm}_2\text{O}_3$ and $\text{Sm}_2\text{O}_3$ )	150
9.2.3. Normalized emission spectra of soda-lime silicate glass doped with 1% $\text{Tb}_4\text{O}_7$ and 2% $\text{Tb}_4\text{O}_7$ (wt%)	153
9.2.4. Lanthanides fraction in the synthesized glasses	154
9.3. Luminescent aluminoborosilicate glass with lead halide nanoparticles and cuprous ion	155
9.3.1. Quantity of oxides used to prepare 30 g of each aluminoborosilicate glass	155
9.3.2. Raman spectra of aluminoborosilicate glass samples	156
9.3.3. $\mu$ - EDXRF analysis of the aluminoborosilicate glass doped with $\text{PbBr}_2$	156
9.3.4. Emission spectra of $\text{PbBr}_2$ doped glass at different temperatures	157
9.4. Sol-gel glass materials with gold nanoparticles	
9.4.1 TEM images of the glass samples with gold nanoparticles	158
9.4.2. FT-IR spectra of the glasses prepared with $\text{Eu}^{3+}$ and with the ionic liquid [bmim][ $\text{BF}_4$ ]	159
9.5. Impact of the produced materials in art	160
9.5.1 Photochromic glass – preliminary studies	160



## Index of Figures

<b>Figure 1.1.</b> Glass art works of several artists members of the research unit Vicarte.....	2
<b>Figure 1.2.</b> Stained glass of Almada Negreiros at Nossa Senhora de Fátima Church, Lisbon, 1938.....	3
<b>Figure 1.3.</b> <i>Teardrops</i> , “Pâte de verre” sculpture, Teresa Almeida, 2008.....	3
<b>Figure 1.4.</b> Sports and Leisure Center in Saint-Cloud France, Koz Architects, 2007-2009.....	3
<b>Figure 1.5.</b> <i>Stained Glass Art House</i> in Copenhagen, Denmark, Tom Fruin, 2010.....	4
<b>Figure 1.6.</b> Teresa Almeida glass sculptures using cerium and europium doped glass under UV-light (ca. 370 nm) .....	5
<b>Figure 1.7.</b> <i>Subtle movements of the corals in the Blue Ocean II</i> , Teresa Almeida, 2008. Art work under UV-light (ca. 370 nm) using europium, terbium and cerium doped glasses and “pâte-de-verre” technique. ....	5
<b>Figure 1.8.</b> Detail of a float glass panel with europium, terbium and cerium doped luminescent thin rods and small pieces, using also commercial black enamels, Fernando Quintas, 2011. Left: under daylight; right: under UV-light (ca. 370 nm). ....	5
<b>Figure 1.9.</b> Sol-gel process with different possible steps. ....	8
<b>Figure 1.10.</b> Hydrolysis mechanisms of a silicon alkoxide obtained by acid and base catalysis. ....	9
<b>Figure 1.11.</b> Condensation mechanisms obtained by acid and base catalyse. ....	9
<b>Figure 1.12.</b> Light interaction with a transparent material. ....	10
<b>Figure 1.13.</b> Electromagnetic spectrum with a zooming of the visible region. ....	11
<b>Figure 1.14.</b> (Top) Electromagnetic radiation interaction with a spherical metal nanoparticle. A dipole is induced and oscillates in phase with an electric field of the received light. (Bottom) Transversal and longitudinal oscillation of the electrons in a rod form metal nanoparticle. (Source: Luis M. Liz-Marzán, <i>Materials Today</i> , p. 26, February 2004).....	13
<b>Figure 1.15.</b> Perrin–Jablonski diagram. IC – internal conversion, ISC – intersystem crossing (Source: B. Valeur, <i>Molecular Fluorescence: Principles and Applications</i> , p.35, 2001). ....	13
<b>Figure 1.16.</b> Rare Earth ion atomic structure. (Source: B.M. Walsh, in <i>Advances in spectroscopy for lasers and sensing</i> , p. 406, 2006).....	15
<b>Figure 1.17.</b> Energetic levels of various luminescent lanthanides. (Source: I. Hemmil and V. Laitala, <i>Journal of Fluorescence</i> , Vol. 15, p.530, July 2005). ....	16
 <b>Figure 2.1.</b> Glasses synthesized with 7% of $\text{Eu}_2\text{O}_3$ and with different CaO concentrations: 0 (C1), 5 (C2), 10 (C3) and 15 (C4) wt%, under UV-light (ca. 370 nm). ....	26
<b>Figure 2.2.</b> Glasses synthesized with different $\text{Eu}_2\text{O}_3$ concentrations: 0.1 (E1), 0.5 (E2), 1.0 (E3), 1.5 (E4), 2.0 (E5), 2.5 (E6) and 7.0 (C3) wt%, under UV-light (ca. 370 nm). ....	26
<b>Figure 2.3.</b> (Top) UV/VIS absorption spectra of $\text{Eu}_2\text{O}_3$ (7 wt%) doped glasses with different CaO concentrations 0 (C1), 5 (C2), 10 (C3) and 15 (C4) wt%. (Bottom) UV/VIS absorption spectra of glasses doped with different $\text{Eu}_2\text{O}_3$ concentrations 0.5 (E2), 1.0 (E3), 2.0 (E5) and 7%(C3) wt%, with the correspondent electronic transition. ....	29

<b>Figure 2.4.</b> (Left side) NIR absorption spectrum of 7% wt $\text{Eu}_2\text{O}_3$ doped glass (C3) and decomposition with four pseudo-Voigt bandshapes. The bands decomposition was made in energy. (Right side) NIR absorption spectra of 7% wt $\text{Eu}_2\text{O}_3$ doped glass (C3) at different temperatures. * represents the transitions that decrease with temperature and $\Delta$ the one that increase with temperature. ....	31
<b>Figure 2.5.</b> (A) Luminescence spectra of glasses with different $\text{Eu}_2\text{O}_3$ concentrations (0.5, 1.0, 1.5, 2.0, 2.5 and 7.0%) and (B) luminescence spectra of 7% $\text{Eu}_2\text{O}_3$ doped glasses with different CaO concentrations (0, 5, 10 and 15%), $\lambda_{\text{exc}}=532$ nm . The spectra were normalised based on the total MD band area ( $^5\text{D}_0 \rightarrow ^7\text{F}_1$ ). ....	35
<b>Figure 2.6.</b> Luminescence decays at single wavelengths of glass C4, with 7% of $\text{Eu}_2\text{O}_3$ and 15% CaO (wt %), $\lambda_{\text{exc}}=532$ nm. ....	38
<b>Figure 2.7.</b> Schematic energy-level of $\text{Eu}^{3+}$ .....	38
<b>Figure 2.8.</b> (Up) Luminescence decays of glasses with $\text{Eu}^{3+}$ (7 wt%) and CaO (0 to 15% wt) at 609 nm. (Bottom) Luminescence decays of glasses with different $\text{Eu}^{3+}$ concentrations (0.5, 1, 2 and 7%, wt%) at 609 nm. ....	39
<b>Figure 2.9.</b> Luminescence pre-exponential factors spectrum using different conditions, according to bi-exponential analysis for the $^5\text{D}_0 \rightarrow ^7\text{F}_n$ decay, for glass samples with different $\text{Eu}_2\text{O}_3$ concentrations and with different CaO concentrations. White squares – Long component; Black squares – Short component. ....	41
<b>Figure 2.10.</b> Fitting of the energy transfer efficiency calculated with the shortest component of the $^5\text{D}_0 \rightarrow ^7\text{F}_n$ decay (see Table 2.9), using eq. 2.18 and eq. 2.19 for glasses changing $\text{Eu}^{3+}$ concentration. ....	44
 <b>Figure 3.1.</b> Electromagnetic spectrum in the visible region and emission spectra of $\text{Ce}^{3+}$ , $\text{Tb}^{3+}$ and $\text{Eu}^{3+}$ doped soda-lime silicate glasses ( $\lambda_{\text{exc}} = 377\text{nm}$ ). ....	48
<b>Figure 3.2.</b> Glasses doped with 2% of different lanthanide oxides (wt %) under a UV light (365 nm). ....	51
<b>Figure 3.3.</b> Absorption spectra of glass samples with different lanthanide oxides ( $\text{Tb}_4\text{O}_7$ , $\text{Eu}_2\text{O}_3$ , $\text{Sm}_2\text{O}_3$ , $\text{CeO}_2$ , $\text{Dy}_2\text{O}_3$ and $\text{Tm}_2\text{O}_3$ ) and the correspondent electronic transitions.....	52
<b>Figure 3.4.</b> Luminescence spectra of glass samples with different lanthanide oxides, $\text{Tb}_4\text{O}_7$ , $\text{Eu}_2\text{O}_3$ , $\text{Sm}_2\text{O}_3$ , $\text{CeO}_2$ , $\text{Dy}_2\text{O}_3$ and $\text{Tm}_2\text{O}_3$ , and the correspondent electronic transitions, $\lambda_{\text{exc}}=377$ nm except in $\text{Tm}_2\text{O}_3$ doped glass case where $\lambda_{\text{exc}}=340$ nm was used. ....	53
<b>Figure 3.5.</b> Glasses doped with 2% (wt) of different lanthanides, $\text{Eu}_2\text{O}_3$ , $\text{Tb}_4\text{O}_7$ and $\text{CeO}_2$ , under UV light (365 nm). ....	55
<b>Figure 3.6.</b> Glasses doped with different concentrations of $\text{Eu}_2\text{O}_3$ and $\text{Tb}_4\text{O}_7$ (wt%), under UV light (370 nm).....	55
<b>Figure 3.7.</b> Luminescence spectra of glass samples with 2% $\text{Tb}_4\text{O}_7$ (green), 2% $\text{Eu}_2\text{O}_3$ (red) and 2% $\text{Tb}_4\text{O}_7$ + 2% $\text{Eu}_2\text{O}_3$ (purple), $\lambda_{\text{exc}}=377$ nm. ....	56
<b>Figure 3.8.</b> (A) Excitation spectra at 700 nm of glasses with 2% $\text{Eu}_2\text{O}_3$ (red line), 2% $\text{Tb}_4\text{O}_7$ (green line) and 2% $\text{Eu}_2\text{O}_3$ + 2% $\text{Tb}_4\text{O}_7$ (purple line). (B) Excitation spectrum of glass with 2%	

Eu <sub>2</sub> O <sub>3</sub> , $\lambda_{em}$ =700 nm (red line) and luminescence spectrum of the glass sample with 2% Tb <sub>4</sub> O <sub>7</sub> , $\lambda_{exc}$ =377 nm (green line). .....	56
<b>Figure 3.9.</b> Luminescence spectra of different glass samples: (A) with 1% of Tb <sub>4</sub> O <sub>7</sub> and different Eu <sub>2</sub> O <sub>3</sub> concentrations, 3.76% (BET1), 1.85% (BET2) and 1.0% (BET3); (B) with 2% of Tb <sub>4</sub> O <sub>7</sub> and different Eu <sub>2</sub> O <sub>3</sub> concentrations, 2.0% (BET 4), 0.94% (BET 5) and 0.62% (BET 6), $\lambda_{exc}$ =377 nm.....	57
<b>Figure 3.10.</b> Luminescence intensity of Tb <sup>3+</sup> emission at 549 nm (green lines) and Eu <sup>3+</sup> emission at 700 nm (red lines) as function of Eu <sub>2</sub> O <sub>3</sub> concentration, for the glass samples doped with 1% (lighter lines) and 2 % of Tb <sub>4</sub> O <sub>7</sub> (darker lines). The black line corresponds to the intensities of Eu <sup>3+</sup> at 700 nm without the presence of Tb <sub>4</sub> O <sub>7</sub> . .....	57
<b>Figure 3.11.</b> Glasses doped with different concentrations of Eu <sub>2</sub> O <sub>3</sub> and CeO <sub>2</sub> (wt%), under UV light (370 nm).....	58
<b>Figure 3.12.</b> Luminescence spectra of glass samples with 2% CeO <sub>2</sub> (blue), 2% Eu <sub>2</sub> O <sub>3</sub> (red) and 2%CeO <sub>2</sub> + 2% Eu <sub>2</sub> O <sub>3</sub> (violet), $\lambda_{exc}$ =377 nm.....	58
<b>Figure 3.13.</b> (A) Excitation spectra at 700 nm of glasses with 2% Eu <sub>2</sub> O <sub>3</sub> (red line), 2% CeO <sub>2</sub> (dark blue line) and 2% Eu <sub>2</sub> O <sub>3</sub> + 2% CeO <sub>2</sub> (light blue line). (B) Excitation spectra of glass with 2% Eu <sub>2</sub> O <sub>3</sub> , $\lambda_{em}$ =700 nm (red line) and luminescence spectrum of the glass sample with 2% CeO <sub>2</sub> , $\lambda_{exc}$ =377 nm (blue line). .....	59
<b>Figure 3.14.</b> Luminescence spectra of different glass samples: (A) with 1% of CeO <sub>2</sub> and different Eu <sub>2</sub> O <sub>3</sub> concentrations, 4.0% (BEC1), 2.0% (BEC2) and 1.0% (BEC3); (B) with 2% of CeO <sub>2</sub> and different Eu <sub>2</sub> O <sub>3</sub> concentrations, 2.0% (BEC 4), 1.0% (BEC 5) and 0.68% (BEC 6), $\lambda_{exc}$ =377 nm.....	60
<b>Figure 3.15.</b> Luminescence intensity of Ce <sup>3+</sup> emission at 450 nm (blue lines) and Eu <sup>3+</sup> emission at 700 nm (red and orange line) as function of Eu <sub>2</sub> O <sub>3</sub> concentration, for the glass samples doped with 1% (lighter lines) and 2 % of CeO <sub>2</sub> (darker lines). The black line represents the Eu <sup>3+</sup> intensity at 700 nm without CeO <sub>2</sub> . .....	60
<b>Figure 3.16.</b> Glasses doped with different concentrations of CeO <sub>2</sub> and Tb <sub>4</sub> O <sub>7</sub> (wt%), under UV light (370 nm).....	60
<b>Figure 3.17.</b> Luminescence spectra of glass samples with 2% Tb <sub>4</sub> O <sub>7</sub> (green), 2% CeO <sub>2</sub> (blue), 2%Tb <sub>4</sub> O <sub>7</sub> + 2% CeO <sub>2</sub> (light blue) and sum of 2% CeO <sub>2</sub> and Tb <sub>4</sub> O <sub>7</sub> luminescence spectra (grey dashed line), $\lambda_{exc}$ =377nm. ....	61
<b>Figure 3. 18.</b> (A) Excitation spectra at 620 nm of glasses with 2% Tb <sub>4</sub> O <sub>7</sub> (green line), 2% CeO <sub>2</sub> (blue line) and 2% Eu <sub>2</sub> O <sub>3</sub> + 2% CeO <sub>2</sub> (orange line). (B) Excitation spectra of glass with 2% Tb <sub>4</sub> O <sub>7</sub> , $\lambda_{em}$ =700 nm (green line) and luminescence spectrum of the glass sample with 2% CeO <sub>2</sub> , $\lambda_{exc}$ =377 nm (blue line). .....	62
<b>Figure 3.19.</b> Luminescence spectra of different glass samples: (A) with 1% of CeO <sub>2</sub> and different Tb <sub>4</sub> O <sub>7</sub> concentrations, 3.3% (BTC1), 2.2% (BTC2) and 1.0% (BTC3); (B) with 2% of CeO <sub>2</sub> and different Tb <sub>4</sub> O <sub>7</sub> concentrations, 2.0% (BTC4), 1.0% (BTC5) and 0.55% (BTC6), $\lambda_{exc}$ =377 nm.....	62

<b>Figure 3.20.</b> Luminescence intensity of $\text{Ce}^{3+}$ emission at 450 nm and $\text{Tb}^{3+}$ emission at 619 nm as function of $\text{Tb}_4\text{O}_7$ concentration, for the glass samples doped with 1% and 2% of $\text{CeO}_2$ . The black line corresponds to the intensity of $\text{Tb}^{3+}$ at 617 nm without the presence of $\text{CeO}_2$ . .....	63
<b>Figure 3.21.</b> Glasses doped with $\text{Eu}_2\text{O}_3$ , $\text{CeO}_2$ and $\text{Tb}_4\text{O}_7$ , changing $\text{Eu}_2\text{O}_3$ concentration ( $x\text{Eu}_2\text{O}_3 + 1\%\text{Tb}_4\text{O}_7 + 1\%\text{CeO}_2$ and $4.5\%\text{Eu}_2\text{O}_3 + 0.5\%\text{Tb}_4\text{O}_7 + 0.5\%\text{CeO}_2$ ), $\text{Tb}_4\text{O}_7$ concentration ( $1\%\text{Eu}_2\text{O}_3 + x\text{Tb}_4\text{O}_7 + 1\%\text{CeO}_2$ and $0.5\%\text{Eu}_2\text{O}_3 + 4.5\%\text{Tb}_4\text{O}_7 + 0.5\%\text{CeO}_2$ ) and $\text{CeO}_2$ concentration ( $1\%\text{Eu}_2\text{O}_3 + x\text{Tb}_4\text{O}_7 + 1\%\text{CeO}_2$ and $0.5\%\text{Eu}_2\text{O}_3 + 0.5\%\text{Tb}_4\text{O}_7 + 4.5\%\text{CeO}_2$ ), wt%, under a UV-light (370 nm). .....	64
<b>Figure 3.22.</b> Luminescence spectra of several glass samples doped with different concentrations of $\text{Eu}_2\text{O}_3$ , $\text{CeO}_2$ and $\text{Tb}_4\text{O}_7$ as indicated in figure 3.21. Luminescence intensity of $\text{Ce}^{3+}$ emission at 450 nm (blue triangles), of $\text{Tb}^{3+}$ emission at 549 nm (green squares) and of $\text{Eu}^{3+}$ emission at 700 nm (red circles) as function of $\text{Eu}_2\text{O}_3$ concentration (A1), $\text{Tb}_4\text{O}_7$ concentration (B1) and $\text{CeO}_2$ concentration (C1). Dashed lines represent the intensity of $\text{Eu}^{3+}$ (red) and of $\text{Tb}^{3+}$ (green) in the absence of the other two lanthanides. ....	65
<b>Figure 3.23.</b> Colour matching functions, $x_{10}(\lambda)$ , $y_{10}(\lambda)$ and $z_{10}(\lambda)$ of the 1964 CIE standard observer.....	67
<b>Figure 3.24.</b> CIE diagram with the colour coordinates of glass samples doped with 2 % (wt) of different lanthanides: $\text{Eu}_2\text{O}_3$ , $\text{Sm}_2\text{O}_3$ , $\text{Dy}_2\text{O}_3$ , $\text{Tb}_4\text{O}_7$ and $\text{CeO}_2$ ( $\lambda_{\text{exc}} = 377$ nm).....	67
<b>Figure 3.25.</b> (Left side) Luminescence spectra of glass samples doped with 2% (wt %) of $\text{CeO}_2$ (blue line), $\text{Tb}_4\text{O}_7$ (green line) and $\text{Eu}_2\text{O}_3$ (red line). (Right side) CIE diagram with the colour coordinates of the glass samples with 1 and 2% of $\text{Tb}_4\text{O}_7$ , 1 and 2% of $\text{CeO}_2$ and 1 and 2% of $\text{Eu}_2\text{O}_3$ . .....	68
<b>Figure 3.26.</b> CIE diagram with the colour coordinates of the binary system glass samples (table 3.1): Black squares – doped with one lanthanide; white rhombus – $\text{Eu}^{3+}/\text{Ce}^{3+}$ system; white triangles - $\text{Tb}^{3+}/\text{Ce}^{3+}$ system; white circles - $\text{Eu}^{3+}/\text{Tb}^{3+}$ system ( $\lambda_{\text{exc}} = 377$ nm). ....	68
<b>Figure 3.27.</b> (A) $f_{\text{Eu}}$ calculated from the colour coordinates vs $f_{\text{Eu}}$ used in the glass synthesis, for the binary system $\text{Eu}^{3+}/\text{Tb}^{3+}$ , with two different $\text{Tb}_4\text{O}_7$ concentrations: 1% (red circles) and 2% (orange squares). (B) $f_{\text{Eu}}$ calculated from the colour coordinates vs $f_{\text{Eu}}$ used in the glass synthesis, for the binary system $\text{Eu}^{3+}/\text{Ce}^{3+}$ , with two different $\text{CeO}_2$ concentrations 1% (purple circles) and 2% (pink squares). (C) $f_{\text{Tb}}$ calculated from the colour coordinates vs $f_{\text{Tb}}$ used in the glass synthesis, for the binary system $\text{Tb}^{3+}/\text{Ce}^{3+}$ , with two different $\text{CeO}_2$ concentrations 1% (green triangles) and 2% (blue rhombus). .....	70
<b>Figure 3.28.</b> CIE diagram with the colour coordinates of the ternary system glass samples (table 3.1): Black squares – doped with one lanthanide; green rhombus – changing $\text{Tb}_4\text{O}_7$ concentration; red triangles – changing $\text{Eu}_2\text{O}_3$ concentration; blue circles – changing $\text{CeO}_2$ concentration ( $\lambda_{\text{exc}} = 377$ nm). .....	71
<b>Figure 3.29.</b> CIE diagram with the colour coordinates of the ternary system glass samples (table 3.1): Black squares – doped with one lanthanide; green rhombus – changing $\text{Tb}_4\text{O}_7$ concentration; red triangles – changing $\text{Eu}_2\text{O}_3$ concentration; blue circles – changing $\text{CeO}_2$ concentration ( $\lambda_{\text{exc}} = 373$ nm). .....	71



**Figure 3.30.** (A)  $f_{Eu}$  calculated from the colour coordinates vs  $f_{Eu}$  used in the glass synthesis, for the ternary system changing Eu (red triangles), Tb (orange circles) and Ce concentration (pink squares) (B)  $f_{Tb}$  calculated from the colour coordinates vs  $f_{Tb}$  used in the glass synthesis, for the ternary system changing Eu (light green triangles), Tb (dark green circles) and Ce concentration (yellow squares) (C)  $f_{Ce}$  calculated from the colour coordinates vs  $f_{Ce}$  used in the glass synthesis, for the ternary system changing Eu (grey triangles), Tb (light blue circles) and Ce concentration (dark blue squares)..... 72

**Figure 4.1.** Schematic model of the  $Pb^{3+}$  STEL center in  $PbCl_2$  and the orientation of the coordinate axes. This scheme was taken from Nistor, Phys. Rev. B, 48 (1993) 9575-9580..... 76

**Figure 4.2.** Synthesis conditions of the different aluminoborosilicate glasses studied. .... 79

**Figure 4.3.** Glass sample 1, under a UV light (365 nm). .... 81

**Figure 4.4.** Essential components to obtain blue luminescence in an aluminoborosilicate glass and glass sample 4, under UV light (365 nm). .... 82

**Figure 4.5.** Absorption spectra (dashed lines) and emission spectra (full lines) of glass the BG (base glass) +BaO (pink), BG + BaO + PbO (green line), BG + BaO + Halogens (red line), BG + BaO + PbO+ Halogens (strong blue line) and of BG + PbO + Halogens (light blue line)..... 83

**Figure 4.6.** TEM image of glass sample 1 after the glass thermal treatment at 650°C..... 84

**Figure 4.7.** Aluminoborosilicate glasses doped with lead oxide and with different sodium halides (molar ration X/Pb=1.33) under a UV-light (364 nm) ..... 85

**Figure 4.8.** TEM image of the glass sample doped with no halide and with different halides (Cl, Br and I) in X/Pb molar ratio of 1.33. An image of the SAED pattern of  $PbI_2$  doped glass is shown in the inset..... 85

**Figure 4.9.** XRD of the base glass, without halogens (black line), with  $PbCl_2$  (violet line), with  $PbBr_2$  (blue line) and with  $PbI_2$  from 0 to 70°. .... 86

**Figure 4.10.** Emission spectra of aluminoborosilicate glasses doped with different lead halides,  $PbF_2$ ,  $PbCl_2$ ,  $PbBr_2$  and  $PbI_2$  ( $\lambda_{exc}$ =350 nm). CIE diagram with colour coordinates of the luminescent samples doped with  $PbBr_2$  and  $PbI_2$ . .... 86

**Figure 4.11.** Absorption spectra of glasses without halides and of glasses containing different lead halides, ( $PbF_2$ ,  $PbCl_2$ ,  $PbBr_2$  and  $PbI_2$ ). Extrapolation of the linear part of the represented spectra to obtain the  $E_{gap}$ . .... 87

**Figure 4.12.** Energy diagram between valence and conduction bands. (Source: B. G. Yacobi, Semiconductor Materials: An Introduction to Basic Principles, Kluwer p.83, 2003). .... 88

**Figure 4.13.** Electron affinity values of the different halogens used to dope the aluminoborosilicate glass and correspondent  $E_{gap}$  of absorption and  $E_{emission}$  (energy at the maximum of emission). .... 88

**Figure 4.14.** Luminescence decays of aluminoborosilicate glasses doped with different lead halides synthesized with molar ratio X/Pb=1.33 ( $\lambda_{exc}$ =355 nm). .... 89

**Figure 4.15.** TEM image of the glass sample doped with bromide (A) and TEM image of the glass sample without halides..... 90

<b>Figure 4.16.</b> XRD of glasses with PbBr <sub>2</sub> (blue line) and without any halogen (red line), from 0 to 70° and expansion of the areas where the small peaks exists. ....	90
<b>Figure 4.17.</b> Raman spectra of glass without halogen (grey line) and with Br (black line). ....	91
<b>Figure 4.18.</b> Absorption coefficient of glass without halide (black line, PbO) and glass with bromide (blue line, PbBr <sub>2</sub> ) and emission spectra of glass with PbBr <sub>2</sub> at 293 and 77 K ( $\lambda_{exc}$ =370 nm). ....	92
<b>Figure 4.19.</b> Normalized time-resolved emission spectra of Br doped glass, with the area of the emission peak between 2.2 and 3.2 eV ( $\lambda_{exc}$ =355 nm). ....	93
<b>Figure 4.20.</b> Luminescence decays at 298 K (red points) and 77 K (blue points) at 440 nm fitted with equation 4.4 ( $\lambda_{ex}$ = 372 nm). Anisotropy decay at 298 K, at 440 nm with $\lambda_{ex}$ = 372 nm. ....	94
<b>Figure 4.21.</b> Glass sample 13 (BG+PbO+CuO), left: under daylight; right: under a UV-light (370 nm) .....	96
<b>Figure 4.22.</b> Left side: Glass samples 12, BG + CuO. Right side: Base glass + PbO+CuO, under a UV-light (370 nm). ....	96
<b>Figure 4.23.</b> (A) Optical Absorption spectra of the base glass – BG (black line), of BG + CuO (pink line) and of BG + CuO +PbO (orange line). (B) Luminescence spectra of the base glass – BG (black line), of BG + CuO (pink line) and of BG + CuO +PbO (orange line), $\lambda_{ext}$ =370 nm . .	97
<b>Figure 4.24.</b> Luminescence spectrum of glass 13 - BG + CuO + PbO (full orange line) and decomposition with three Gaussian curves (blue, green and purple dashed lines), $\lambda_{ext}$ =370 nm. The fitted curve is represented with a dashed black line. ....	98
<b>Figure 4.25.</b> Schematic energy level diagram for Cu <sup>+</sup> monomer and dimer. ....	98
<b>Figure 4.26.</b> Aluminoborosilicate glass 3 (base glass+PbO+ZrO <sub>2</sub> +BaO) doped with different CuO concentrations, (up) under daylight, (down) under a UV-light (365 nm). ....	99
<b>Figure 4.27.</b> Left side: Optical absorption spectra of glass samples 3 with different CuO concentrations 0.0% (3a), 0.00375% (3b), 0.0075% (3c), 0.015% (3d), 0.03% (3e), 0.045% (3f) and 0.06% (3g), wt %. Right side: Dependence of the absorbance at the maximum of the absorption spectra (1.63 eV) with the CuO concentration (mol). ....	99
<b>Figure 4.28.</b> Luminescence spectra of glass sample 3 with different CuO concentrations 0.0% (3a), 0.00375% (3b), 0.0075% (3c), 0.015% (3d), 0.03% (3e), 0.045% (3f) and 0.06% (3g), wt%, exciting at 355 nm. ....	100
<b>Figure 4.29.</b> Relation between the normalized pre-exponential factors of the different Gaussian bands used to decompose the luminescence spectra and CuO concentration. ....	101
<b>Figure 4.30.</b> Luminescence decays of the glass sample 3g doped with 0.06% CuO at 490, 600 and 650 nm. ....	101
<b>Figure 4.31.</b> Relation between the relative pre-exponential factors obtained by three-exponential decay fittings for $\tau$ = 1.4 (blue squares) 5.3 (green triangles) and 23.5 $\mu$ s (purple rhombus) at different wavelengths for the glass sample 3 doped with 0.06% CuO. ....	102
<b>Figure 4.32.</b> Absorption spectra of glass sample 3e, in the region with yellow luminescence (yellow line) and in the hole without luminescence (black line). Inset - Glass sample 3e after irradiation with the flash photolysis laser (355 nm). ....	103

<b>Figure 4.33.</b> Aluminoborosilicate glass 1 (base glass+PbO+ZrO <sub>2</sub> +BaO+H+CuO) doped with different CuO concentrations, (up) under daylight, (down) under a UV-light (365 nm).....	104
<b>Figure 4.34.</b> Optical absorption spectra of glass sample 1 with different CuO concentrations 0.0% (1a), 0.00375% (1b), 0.0075% (1c), 0.015% (1c), 0.03% (1e), 0.045% (1f) and 0.06% (1g), %wt. Right side: Dependence of the absorbance at the maximum of the absorption spectra (1.63 eV) with the CuO concentration (M).....	104
<b>Figure 4.35.</b> Luminescence spectra of glass sample 1 with different CuO concentrations 0.0% (1a), 0.00375% (1b), 0.0075% (1c), 0.015% (1d), 0.03% (1e), 0.045% (1f) and 0.06% (1g), wt% ( $\lambda_{exc}=355$ nm). ....	105
<b>Figure 4.36.</b> CIE (x, y) chromaticity diagram with the colour coordinates of luminescence of glass 1 with different CuO concentrations.....	105
 <b>Figure 5.1.</b> Schematic diagram of the sol-gel synthesis containing chloroauric acid (A) and containing chloroauric acid and the ionic liquid [bmim][BF <sub>4</sub> ] (B). ....	110
<b>Figure 5.2.</b> Different steps of the sol-gel process used in synthesis B, with the ionic liquid. ...	113
<b>Figure 5.3.</b> Glass monoliths obtained from synthesis A, without ionic liquid, sintered at 400°C. ....	114
<b>Figure 5.4.</b> Glass monoliths obtained from synthesis B, with ionic liquid, sintered at 350°C, 400°C and 450°C.....	114
<b>Figure 5.5.</b> Sol-gel obtained from synthesis B, with ionic liquid, sintered at 365°C and 375°C. ....	115
<b>Figure 5.6.</b> Experimental UV–Vis absorption spectrum of glass monolith samples with Au nanoparticles (after subtracting the background from the sol-gel), produced after the thermal treatment of the ionogel at 365, 375, 400 and 425°C (arrow indicates the increase of the sintering temperature) during 60 min. An image of the glass monoliths obtained at 400°C is shown in the inset.....	116
<b>Figure 5.7.</b> Experimental UV–Vis absorption spectrum of glass monolith samples with Au nanoparticles (after subtracting the background from the sol-gel), produced after the thermal treatment of the ionogel at 400°C during different times (15, 30, 60 and 120 min). ....	116
<b>Figure 5.8.</b> Plot of the wavelength corresponding to the maximum absorbance of the SPR band for samples sintered at different temperatures ( $T_{sint}$ ) for 60 minutes (A) and sintered at 400°C for different times ( $t_{sint}$ ) (B). Error bars corresponds to one standard deviation, see section 5.2.2. for details. ....	117
<b>Figure 5.9.</b> TEM image and size distribution analysis of Au nanoparticles in glass produced after the thermal treatment of the ionogel at 375 and 425°C during 60 minutes. The size distribution was determined with a log normal distribution using the statistic data obtained from the histograms here shown as well. ....	118
<b>Figure 5.10.</b> EDS analysis of the nanoparticles (np, red and blue line) with two different $T_{sint}$ (375 and 425°C) and in an area without nanoparticles (out, green line).....	118

<b>Figure 5.11.</b> Number of gold nanoparticles per $\mu\text{m}^2$ found by TEM for samples sintered at different temperatures ( $T_{\text{sint}}$ ) for 60 minutes (A) and sintered at 400°C for different times ( $t_{\text{sint}}$ ) (B).	119
<b>Figure 5.12.</b> Histograms of TEM images and size distribution analysis of Au nanoparticles in glass produced after the thermal treatment of the ionogel at 400°C with different sintering times. The size distribution was determined with a log normal distribution using the statistic data obtained from the histograms here shown as well.	119
<b>Figure 5.13.</b> TGA (grey line) and DSC (black line) measurements of the material synthesized according to synthesis A, without the ionic liquid [bmim][BF <sub>4</sub> ].	121
<b>Figure 5.14.</b> TGA (red line) and DSC (pink line) measurements of the material synthesized according to synthesis B, with ionic liquid. Graphic A shows the full results of both experiments, while graphic B focus on the region where two mass losses steps are seen. In graphic B the TGA result is renormalized at $T=230^\circ\text{C}$	122
<b>Figure 5.15.</b> (A) $\mu$ -EDXRF analysis of the glass samples sintered at different temperatures: 50°C, 150°C and 365°C, normalized in the Si peak. (B) Chlorine intensity taken from the XRF spectra (normalized in the Si peak) of the samples with different $T_{\text{sint}}$ .	123
<b>Figure 5.16.</b> Mechanism proposed for the thermal degradation of [bmim][Cl]	124
 <b>Figure 6.1.</b> “Pâte de verre” artwork, using Tb <sup>3+</sup> , Eu <sup>3+</sup> and Dy <sup>3+</sup> doped glasses; Teresa Almeida, 2009. Left: shown under daylight; right: shown under UV-light (ca. 370 nm).	130
<b>Figure 6.2.</b> Result of an experiment made with europium doped borosilicate glass (lampwork) under UV-light (ca. 370 nm); Robert Wiley, 2012.	130
<b>Figure 6.3.</b> Tests for float glass luminescence, using Sm <sup>3+</sup> , Tb <sup>3+</sup> and Ce <sup>3+</sup> doped glasses, under a UV-light (ca. 370 nm); F. Quintas, 2011.	131
<b>Figure 6.4.</b> Glass sample before (a) and after (b) being exposed to daylight and TEM image and EDS measurement of the same glass. EDS analysis of the nanoparticle region (red spectra) and in regions without nanoparticles (blue spectra) show the existence of silver mainly within nanoparticles.	131
 <b>Figure 9.1.</b> Linear thermal expansion of glass sample E0, without Eu <sub>2</sub> O <sub>3</sub> .	147
<b>Figure 9.2.</b> Dependence between absorbance and Eu <sub>2</sub> O <sub>3</sub> concentration (wt %) in soda-lime-silicate glasses	148
<b>Figure 9.3.</b> Linear thermal expansion of glass sample doped with 2% Eu <sub>2</sub> O <sub>3</sub> (wt %).	150
<b>Figure 9.4.</b> Linear thermal expansion of glass sample doped with 2% Tb <sub>4</sub> O <sub>7</sub> (wt %).	151
<b>Figure 9.5.</b> Linear thermal expansion of glass sample doped with 2% CeO <sub>2</sub> (wt %).	151
<b>Figure 9.6.</b> Linear thermal expansion of glass sample doped with 2% Dy <sub>2</sub> O <sub>3</sub> (wt %).	152
<b>Figure 9.7.</b> Linear thermal expansion of glass sample doped with 2% Tm <sub>2</sub> O <sub>3</sub> (wt %).	152
<b>Figure 9.8.</b> Linear thermal expansion of glass sample doped with 2% Sm <sub>2</sub> O <sub>3</sub> (wt %).	153
<b>Figure 9.9.</b> Normalized emission spectra of the glass samples doped with 1% (violet line) and 2% (green dashed line) of Tb <sub>4</sub> O <sub>7</sub> .	153

<b>Figure 9.10.</b> Normalized Raman spectra of the BG (base glass-purple line), BG+BaO (yellow line), BG+BaO+PbO (pink line), BG+BaO+Halogens (green line) and BG+BaO+PbO+Halogens.	156
<b>Figure 9.11.</b> $\mu$ -EDXRF analysis of the glass sample doped with $\text{PbBr}_2$ .	156
<b>Figure 9.12.</b> Emission spectra of glass sample with $\text{PbBr}_2$ nanoparticles at 77 K and at 293 K.	157
<b>Figure 9.13.</b> TEM image of the glass samples heat-treated at 400°C during different times: 15, 30 and 120 min.	158
<b>Figure 9.14.</b> TEM image of the glass samples heat-treated at different temperatures: 375, 400 and 425°C during 60 min.	159
<b>Figure 9.15.</b> FT-IR spectra of the glasses prepared with $\text{Eu}^{3+}$ and with the ionic liquid [bmim][BF <sub>4</sub> ] treated at different temperatures: 350°C; 500°C; 750°C; 800°C; and without the ionic liquid treated at 550°C.	159
<b>Figure 9.16.</b> Glass sample before (a) and after (b) being exposed to day light.	160
<b>Figure 9.17.</b> Optical absorption spectra (A) and absorbance at 520 nm after increasing the irradiation time, measured at different times.	160
<b>Figure 9.18.</b> UV-Vis absorption spectra of the photocromic glass after being irradiated 5 min in a medium pressure mercury lamp using a 366 nm band pass filter.	161
<b>Figure 9.19.</b> Absorbance at 520 nm, after irradiate glass A for 5 min and after waiting one hour. This procedure was repeated five times.	161



## Index of Tables

<b>Table 1.1.</b> Principle reactions of a $\text{SiO}_2\text{-CaO-Na}_2\text{O}$ glass melting, being the raw materials $\text{SiO}_2$ , $\text{CaCO}_3$ and $\text{Na}_2\text{CO}_3$ .	7
<b>Table 1.2.</b> Chromophores classification depending on their size in the coloured glasses	11
<b>Table 2.1.</b> Composition of the europium doped soda-lime-silicate glasses studied (in wt %).	25
<b>Table 2.2.</b> Densities values ( $d$ ) of all the synthesized glasses.	27
<b>Table 2.3.</b> Physical properties of glasses with different CaO concentrations. Refractive index ( $n_d$ ), density ( $d$ ), molar refractivity ( $R_M$ ), $\text{Eu}^{3+}$ ion concentration ( $N$ ), interionic distance ( $r_i$ ) and contribution of oxygen to the molar refractivity ( $R_M(\text{O}^{2-})$ ).	27
<b>Table 2.4.</b> Analysis of $\text{Eu}_2\text{O}_3$ absorption spectroscopy in glasses with different CaO concentrations. Attribution of the energy levels to each absorption peak and the correspondent value found in the literature, in nm. These peaks were obtained with the bands decomposition in energy. ED – transition allowed by electric dipole mechanism, MD - transition allowed by magnetic dipole mechanism.	30
<b>Table 2.5.</b> Absorption band positions (in nm) and experimental ( $f_{\text{exp}}$ ) and calculated ( $f_{\text{cal}}$ ) oscillator strengths ( $\times 10^6$ ) for 7% $\text{Eu}_2\text{O}_3$ doped glasses with different CaO concentrations (C1, C2, C3 and C4).	33
<b>Table 2.6.</b> Judd-Ofelt parameters (in $10^{-20} \text{ cm}^2$ ) calculated for glasses with different wt% of CaO by fitting the experimental absorption.	34
<b>Table 2.7.</b> Data analysis of the emission spectra of Figure 2.5 (B). Probability of ${}^5D_0 \rightarrow {}^7F_1$ MD transition ( $A_{\text{MD } J=1}$ ), probability of different ED transitions ( $A_{\text{ED}}$ ) and experimental and calculated branching ratio ( $\beta_j$ ) for glass samples with different CaO concentrations.	36
<b>Table 2.8.</b> Judd-Ofelt parameters (in $10^{-20} \text{ cm}^2$ ) calculated for glasses with different wt% of CaO by fitting the experimental steady state emission.	37
<b>Table 2.9.</b> Lifetimes, $\tau_i$ , obtained by tetra-exponential decay fittings of the glasses 7% of $\text{Eu}_2\text{O}_3$ and with different CaO concentrations and by bi-exponential decay fittings of glasses with 10% of CaO and different $\text{Eu}_2\text{O}_3$ concentrations.	40
<b>Table 2.10.</b> Judd-Ofelt parameters (in $10^{-20} \text{ cm}^2$ ) calculated for glasses with different wt% of CaO by fitting the time-resolved emission spectra.	41
<b>Table 2.11.</b> Number of energy J-sublevels in a given point symmetry vs. the quantum number J	42
<b>Table 3.1.</b> Composition of the soda-lime-silicate glasses doped with different lanthanide oxides (wt%). Glasses doped with only one (Mono system), with a mixture of two (Binary system) and with a mixture of three (Ternary system) lanthanides oxides- $\text{Tb}_4\text{O}_7$ , $\text{Eu}_2\text{O}_3$ and $\text{CeO}$ .	49

**Table 3.2.**  $T_g$  and CTE values obtain for the glass samples doped with different lanthanides. CTE values were taken from the 25-300°C temperature range. .... 54

**Table 4.1.** Synthesized glasses and the different components used in each glass. .... 78

**Table 4.2.** Glasses 1 and 3 (without halides) with different CuO concentrations (wt %). .... 78

**Table 4.3.** Different components used in the synthesized glasses, besides the base glass ( $\text{SiO}_2 + \text{B}_2\text{O}_3 + \text{Al}_2\text{O}_3 + \text{Alkaline oxides}$ ), ✓ when the components are added to the base glass, X when they are not. The correspondent colour at day light and the colour obtained exciting the glasses with a 370 nm UV-light. .... 81

**Table 4.4.**  $T_g$  and COE values obtained for the glass samples without and with bromide. CTE was taken from the 30-400°C temperature range. .... 91

**Table 4.5.** Fitting results of the luminescence decays (Figure. 4.20) with equation 4.4..... 95

**Table 4.6.** Lifetimes obtained by three-exponential decay fittings ( $\lambda_{\text{ext}}=355$  nm) for glass sample 3 ( $\text{BG}+\text{CuO}+\text{PbO}+\text{BaO}+\text{ZrO}_2$ ) with different CuO concentrations, 0.00375% (3b), 0.0075% (3c), 0.03% (3e), 0.045% (3f) and 0.06% (3g), wt %..... 102

**Table 5.1.** Different ionic liquids used in the sol-gel synthesis, their chemical formula, structure and solubility in water. Sol-gel characteristics before the heat treatment and after the heat treatment at 300°C ..... 112

**Table 5.2.** Band position at the maximum of intensity ( $\lambda_{\text{max}}$ ) of the gold nanoparticles taken from the absorption spectra, number of particles seen in TEM images (N), average diameter and the size standard deviation (log normal distribution,  $\sigma$ ) for different sintering temperatures ( $T_{\text{sint}}$ ) and times ( $t_{\text{sint}}$ ). .... 117

**Table 5.3.** Thermal decomposition of different [bmim] based ionic liquids and comparison with the thermal processes observed in sol-gel with ionic liquid.  $T_{\text{starts}}$  is when the decompositions starts and  $T_{\text{middle}}$  is the middle temperature value of the decomposition temperatures range. These values were taken from the TGA analysis..... 120

**Table 9.1.** Composition of the europium doped soda-lime-silicate glasses studied (in wt %) and the quantity of oxides used to prepare 25 g of each glass..... 147

**Table 9.2.** Quantity of oxides used to prepare 30 g of the glasses synthesized in chapter 3 with different lanthanides. .... 149

**Table 9.3.** Lanthanides fraction (europium-  $f_{\text{Eu}}$ , terbium-  $f_{\text{Tb}}$  and cerium-  $f_{\text{Ce}}$ ) and calculated lanthanides fraction in the binary glasses ..... 154

**Table 9.4.** Lanthanides fraction (europium-  $f_{\text{Eu}}$ , terbium-  $f_{\text{Tb}}$  and cerium-  $f_{\text{Ce}}$ ) and calculated lanthanides fraction in the ternary glasses..... 154

**Table 9.5.** Quantity of oxides used to prepare 30 g of the glasses synthesized in chapter 4. . 155

**Table 9.6.** Quantity of oxides used to prepare 30 g of the glasses synthesized in chapter 4 with different halides ..... 155



## Chapter 1 - Introduction

### 1.1. Coloured and Luminescent glass in art

Glass is a fascinating material. It is easy to manufacture and can be found all over the world throughout all times, but at the same time is a very complex material.

The discovery of glassforming was discussed by several historians. Pliny the Elder, a historian from 1<sup>st</sup> century B.C., stated that the glass invention was made by Phoenician traders (around 2000 b.C.). He narrates a legend that says that the merchants were preparing their meal near the Belus River and not having stones to support their pots, they used lumps of natron from the ship. The natron fused and mixed with the sands of the shore gave rise to a new translucent liquid, and thus was the origin of glass.<sup>1</sup> Natron is an alkaline material composed essentially of sodium carbonate that exists in the lakes site of the Wadi Natroun region, Egypt.<sup>2</sup>

However this episode is considered only a legend. Some researchers believe that glass resulted from the evolution of Egypt faience manufacture (ground quartz or quartz sand body coated with a glaze).<sup>3,4</sup> This faience is produced at an inferior temperature than glass, but using the same components in different proportions and at higher temperatures it is possible to produce glass. These vitreous materials started to be made in the Near East and Egypt to produce small objects such as beads, scarabs, seals and amulets.<sup>2</sup> The most antique glass to the best of our knowledge was created in the 7000 B.C. in Asia Minor, but a significant glass production only occurred in 2500 B.C. in Mesopotamia (modern Iraq) and in Egypt.<sup>5</sup>

Glass unique characteristics such as transparency, translucency, brightness and versatility, make it not only essential in our daily lives but also a very interesting material to be used in the art field. Besides these qualities glass is a sustainable material that can be easily recycled and therefore it can be used repeatedly.

Over the centuries, many artists used glass to produce art works and even now it is commonly used in contemporary art. Some examples of glass art works made by different artists from our research unit Vicarte "Glass and Ceramic for the Arts" are shown in figure 1.1.



*Teresa Almeida, 2008*



*Richard Meitner, 2007<sup>(1)</sup>*



*Michael Taylor, 2011*



*Fernando Quintas, 2007/2008*



*Robert Wiley, 2010*

**Figure 1.1.** Glass art works of several artists members of the research unit Vicarte.

The use of different colours was always important for artists, not only to seduce the observers but also to illustrate the reality that surrounds the artists. One of the major examples are stained glasses, where several colours are used in the same panel, see figure 1.2.

---

<sup>(1)</sup> Image taken from <http://www.vicarte.org/cont/artwrks.html> on 02.09.2013



**Figure 1.2.** Stained glass of Almada Negreiros at Nossa Senhora de Fátima Church, Lisbon, 1938.<sup>(2)</sup>

Glasses with different colours are often explored for example in glass sculptures, installations and also in architecture. Some examples are shown in figures 1.3, 1.4 and 1.5:



**Figure 1.3.** *Teardrops*, “Pâte de verre” sculpture, Teresa Almeida, 2008.



**Figure 1.4.** Sports and Leisure Center in Saint-Cloud France, Koz Architects, 2007-2009.<sup>(3)</sup>

---

<sup>(2)</sup> Image taken from [http://www.citi.pt/cultura/artes\\_plasticas/pintura/almada/igreja.html](http://www.citi.pt/cultura/artes_plasticas/pintura/almada/igreja.html) on 02.09.2013

<sup>(3)</sup> Image taken from <http://www.archdaily.com/36552/sports-and-leisure-center-in-saint-cloud-koz-architectes/koz-15/> on 02.09.2013



**Figure 1.5.** *Stained Glass Art House* in Copenhagen, Denmark, Tom Fruin, 2010.<sup>(4)</sup>

Colour, as it was exemplified, has an exceptional effect in the art field. Special optical properties are constantly being explored by contemporary artists. For example several artists have made neon installations in museums, cloisters and other public places<sup>6</sup> and artistic installations using fluorescent light tubes<sup>7</sup> and fluorescent materials.<sup>8</sup> Photoluminescent (PL) glass also has a very interesting effect for artists to explore, since luminescent colour only appears under UV-light.<sup>9,10</sup> Luminescent glasses can be understood as “smart materials”, a relatively new term for materials which have changeable properties and that are able to reversibly change their shape or colour in response to physical and/or chemical influences.<sup>8</sup> PL glasses can be obtained by the addition of lanthanide elements. These glasses display interesting luminescent colours which can be tuned by changing the lanthanide and the composition of the glass matrix.<sup>11</sup> The light effects thus obtained improve the visual value of the artworks and seem to have extraordinary potential. Some artworks made with luminescent lanthanide doped glasses are shown in figures 1.6, 1.7 and 1.8.

---

<sup>(4)</sup> Image taken from <http://www.juxtapoz.com/current/the-stained-glass-art-house-by-tom-fruin> on 02.09.2013





**Figure 1.6.** Teresa Almeida glass sculptures using cerium and europium doped glass under UV-light (ca. 370 nm)



**Figure 1.7.** *Subtle movements of the corals in the Blue Ocean II*, Teresa Almeida, 2008. Art work under UV-light (ca. 370 nm) using europium, terbium and cerium doped glasses and "pâte-de-verre" technique.

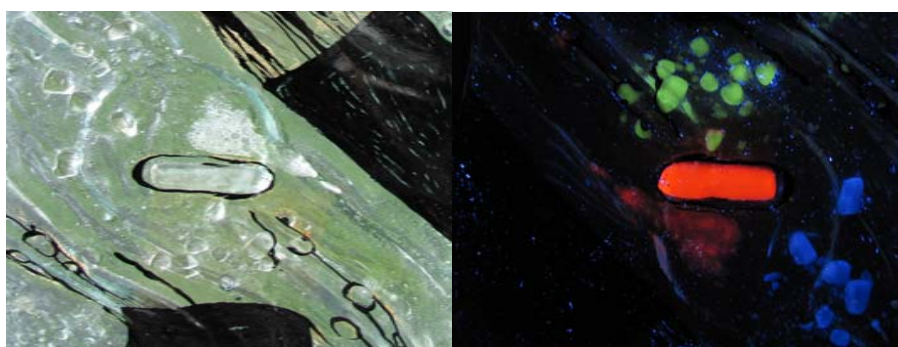


**Figure 1.8** Detail of a float glass panel with europium, terbium and cerium doped luminescent thin rods and small pieces, using also commercial black enamels, Fernando Quintas, 2011. Left: under daylight; right: under UV-light (ca. 370 nm).

The development of new glass materials, including of luminescent glass, is being explored in order to access new and interesting aesthetic possibilities in architecture, art and design. In this thesis the development of new materials for art is a result of an ongoing collaboration between the research unit Vicarte and the photochemistry group of the associated laboratory Requimte.

## 1.2. Glass

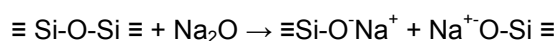
What is glass? This question was asked by different scientists all over the years. The American Society for Testing and Materials (ASTM) defined glass as “*an inorganic product of fusion which has cooled to a rigid condition without crystallizing*”.<sup>12,13</sup> However this definition was not well accepted because many organic glasses were already known and glasses can also be prepared without being cooled from the liquid state.

In 1990, another definition was stated by A. Paul according to which a glass is a state of matter that maintains the energy, volume and atomic arrangement of a liquid but whose changes in energy and volume with temperature and pressure are similar in magnitude to those of a crystalline solid.<sup>14</sup> Further, J. E. Shelby defined glass as “an amorphous solid completely lacking in long range, periodic atomic structure, and exhibiting a region of glass transformation behaviour”. Any material (inorganic, organic, or metallic, formed by any technique) which exhibits glass transformation behaviour is a glass.<sup>15</sup> More recently, A. K. Varshneya stated that the term non-crystalline solid includes two subclasses: *glass* and *amorphous solid* and attributed the word *glass* to a solid having a liquid-like structure and which continuously converts to a liquid upon heating.<sup>16</sup>

Glass can be produced using different methods such as sol-gel process, melt-quenching and chemical vapour deposition. However the latter is not used so commonly. It is an example of glass making directly from the gaseous state, where for example a mixture of  $\text{SiCl}_4$  and  $\text{H}_2\text{O}$  vapour can be introduced into a reaction vessel at high temperatures giving rise to  $\text{SiO}_2$  amorphous particles.<sup>16</sup>

The melt-quenching method, which consists in fusion followed by cooling of inorganic raw materials at high temperatures, is the most common technique to produce inorganic glasses. The raw materials are sources of several oxides, and these oxides can be divided in four categories:<sup>15</sup>

- a) *Glass former or network former* - The primary glass formers in commercial oxide glasses are  $\text{SiO}_2$ ,  $\text{B}_2\text{O}_3$ ,  $\text{PbO}$  and  $\text{P}_2\text{O}_5$ , which all readily form single component glasses. Other compounds may act as glass formers under certain circumstances, for example  $\text{GeO}_2$ ,  $\text{Bi}_2\text{O}_3$ ,  $\text{As}_2\text{O}_3$ ,  $\text{Sb}_2\text{O}_3$ ,  $\text{TeO}_2$ ,  $\text{Al}_2\text{O}_3$ ,  $\text{Ga}_2\text{O}_3$ , and  $\text{V}_2\text{O}_5$ . The principal glass former component is silica,  $\text{SiO}_2$ , but silica glass can only be synthesized at very high temperatures (1700 °C), making it a very expensive process.
- b) *Flux or modifier network* - To decrease the fusion temperature fluxes are added to the glass composition, ex.  $\text{Na}_2\text{O}$ ,  $\text{K}_2\text{O}$ ,  $\text{Li}_2\text{O}$  and also  $\text{PbO}$  that is especially useful in dissolving any refractory or other impurity particles ( $\text{PbO}$  can act as glass former and as glass modifier). But those oxides besides decreasing the fusion temperatures also cause partial net ruptures that decrease the glass stability (corrosion):



- c) *Stabilizer* – Stabilizes certain glass properties and act with an intermediate character between the network former and the network modifier, ex.: CaO, Al<sub>2</sub>O<sub>3</sub>, PbO, ZnO.
- d) *Secondary components* – have very specific functions, such as colourants, (Fe, Co, Cu, Au), decolourants (As<sub>2</sub>O<sub>3</sub>), opacifiers (F<sup>-</sup>) and fining agents that promote the bubbles removing (arsenic and antimony oxides, potassium and sodium nitrates, NaCl, a number of fluorides and sulphates).

The melt-quenching process involves a series of chemical physical transformations. In table 1.1 it is possible to observe an example of the chemical and physical reactions that occur in a SiO<sub>2</sub>-CaO-Na<sub>2</sub>O glass melting.

**Table 1.1.** Principle reactions of a SiO<sub>2</sub>-CaO-Na<sub>2</sub>O glass melting, being the raw materials SiO<sub>2</sub>, CaCO<sub>3</sub> and Na<sub>2</sub>CO<sub>3</sub>.<sup>17</sup>

Temperature (°C)	Tranformation
≈ 600	$\text{Na}_2\text{CO}_3 + \text{CaCO}_3 \rightarrow \text{Na}_2\text{Ca}(\text{CO}_3)_2$
< 760	$3[\text{Na}_2\text{Ca}(\text{CO}_3)_2] + 10[\text{SiO}_2] \rightarrow 2[\text{Na}_2\text{O}.2\text{SiO}_2] + [\text{Na}_2\text{O}.3\text{CaO}.6\text{SiO}_2] + 6(\text{CO}_2)$
≈ 760	Peritetic fusion $[\text{Na}_2\text{O}.3\text{CaO}.6\text{SiO}_2] + [\text{Na}_2\text{O}.2\text{SiO}_2] \rightarrow [\text{Na}_2\text{O}.2\text{CaO}.3\text{SiO}_2] + \text{liquidus}$
785	Eutetic fusion $2\text{CaCO}_3.3\text{Na}_2\text{CO}_3$
790	Eutetic fusion $\text{Na}_2\text{O}.2\text{SiO}_2.\text{SiO}_2$
827-834	Peritetic fusion $2\text{Na}_2\text{O}. \text{CaO}.3\text{SiO}_2 + \text{Na}_2\text{O}.2\text{SiO}_2 \rightarrow \text{Na}_2\text{O}.2\text{CaO}.3\text{SiO}_2 + \text{liquidus}$
1045	Incongruent Melting of $\text{Na}_2\text{O}.3\text{CaO}.6\text{SiO}_2$
1125	Incongruent Melting of $4\text{Na}_2\text{O}.3\text{CaO}.5\text{SiO}_2$
1141	Incongruent Melting of $2\text{Na}_2\text{O}. \text{CaO}.3\text{SiO}_2$
1284	Congruent Melting of $\text{Na}_2\text{O}.2\text{CaO}.3\text{SiO}_2$
≈ 1450	Congruent Melting of $\text{Na}_2\text{O}.2\text{CaO}.3\text{SiO}_2$

As previously stated, the melt-quenching technique is the most common technique used to synthesize glass, although the use of the sol-gel technique has also become very frequent, mainly in scientific studies. In this process metals or metalloid colloids are prepared using several compounds, designated precursors, which consist of metals or metalloid elements surrounded by various ligands. The class of precursors most commonly used in sol-gel synthesis are the metals or metalloid alkoxides, such as Si(OC<sub>2</sub>H<sub>5</sub>)<sub>4</sub> (tetraethoxysilane, TEOS), Si(OCH<sub>3</sub>)<sub>4</sub> (tetramethyl orthosilicate, TMOS) and Al(OC<sub>4</sub>H<sub>9</sub>)<sub>3</sub> (aluminium tri-sec-butoxide). The alkoxide is commonly represented by •OR where R is an alkyl. Other types of ligands can also be used as for example an alkyl or even ligands without carbons as in the case of Al(NO<sub>3</sub>)<sub>3</sub> (aluminium nitrate).<sup>21</sup> This method has several advantages compared with the melt-quenching process. For example the mixture of all the components in solution leads to a higher

homogeneity.<sup>18, 19, 20</sup> The lower temperature needed to obtain glass samples, the ability to produce new glass materials, since it is relatively easily to introduce new reagents in the glass synthesis, the possibility to obtain a high-purity products and the capability to use this method in net-shape casting, fiber pulling and film coatings are other advantages of the sol-gel process.<sup>20, 21, 22</sup> But sol-gel synthesis also has limitations, as the precursors are usually expensive and in order to get good results all the steps have to be very well controlled, limiting the large scale production and are generally time-consuming.<sup>22</sup> As mentioned above, different routes can be followed in the sol-gel process (Figure 1.9.).<sup>21</sup>

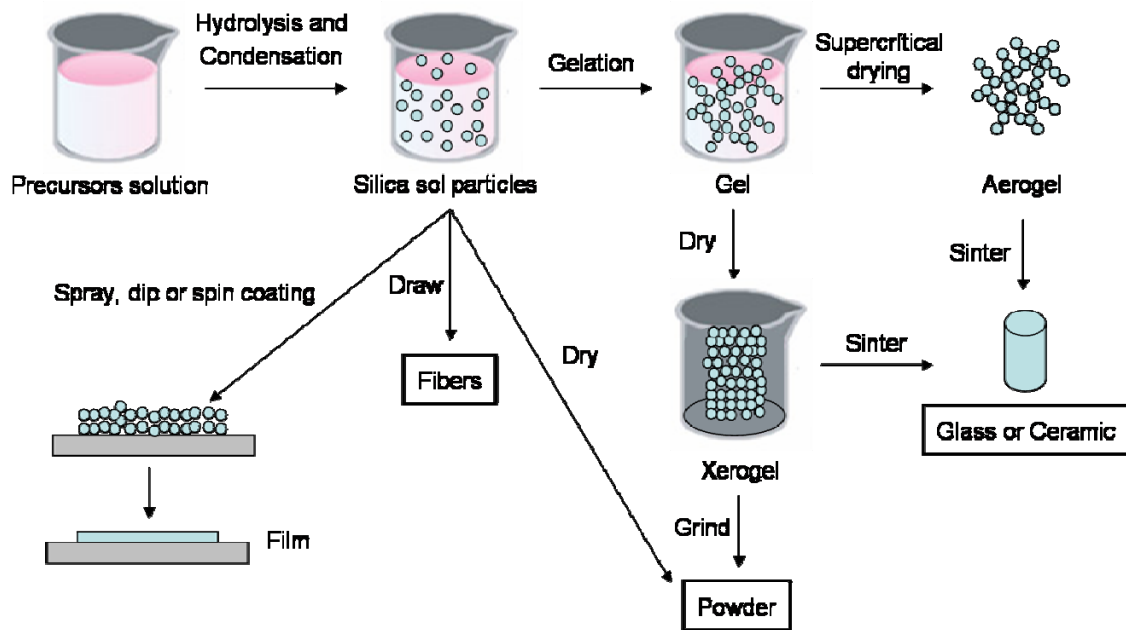
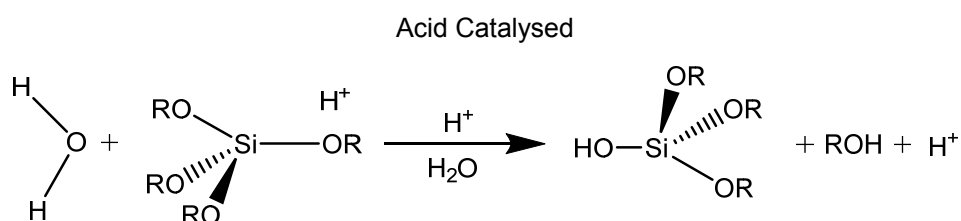


Figure 1.9. Sol-gel process with different possible steps.

Silicates are the most familiar structural units used to produce glass, so a brief description of the steps needed to obtain a silicate gel and afterwards to obtain powder or monoliths is described as follows:<sup>21,22</sup>

- a) *Hydrolysis* – Is the first reaction that occurs. A hydroxyl ion becomes attached to the metal atom, as shown in figure 1.10. Depending on the water and catalyst quantity all the OR groups can be replaced by OH. This reaction takes place with a nucleophilic substitution  $S_N2$ .





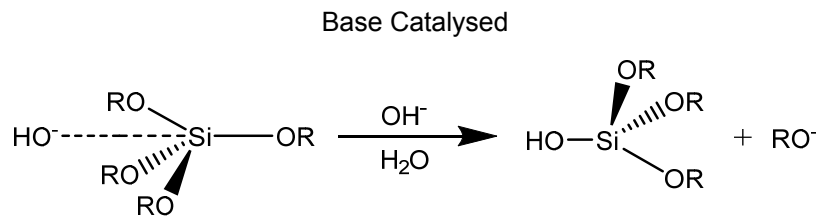


**Figure 1.10.** Hydrolysis mechanisms of a silicon alkoxide obtained by acid and base catalysis.

b) *Condensation* – It happens when the hydrolyzed molecules link together. The condensation reactions, as in the case of hydrolysis reactions may be acid or base catalysed (figure 1.11). This reaction takes place with an  $S_N2$  reaction mechanism.

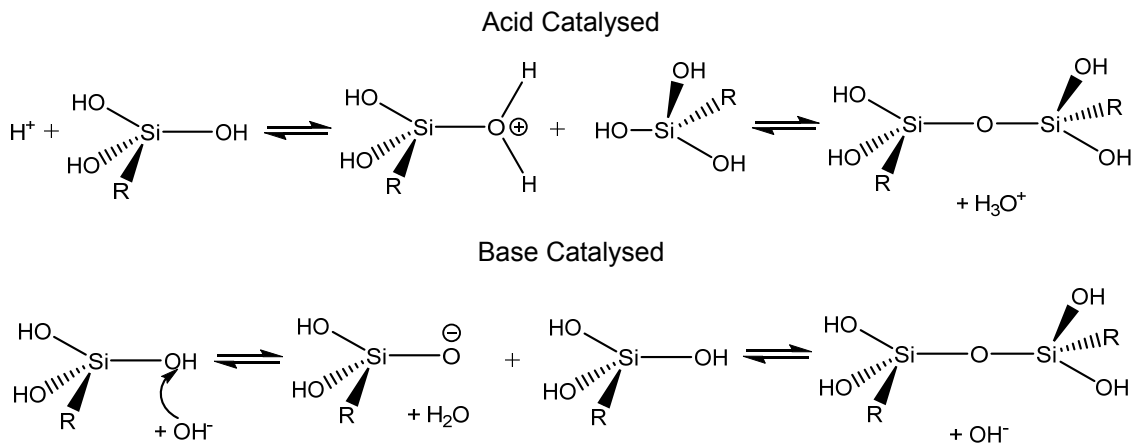


**Figure 1.11.** Condensation mechanisms obtained by acid and base catalyse.

Hydrolysis and condensation as described in figures 1.11 and 1.12 lead to the growth of clusters that afterwards link together into a gel. On the gel synthesis from silicon alkoxides an acid catalyst is generally used to accelerate the hydrolysis of alkoxide to hydroxyl groups, along with a Lewis or Brönsted base that catalyzes the condensation in order to obtain the siloxane link.

c) *Gelation* – In this stage of the sol-gel process the clusters formed before keep growing by condensation of polymers or aggregation of particles until they collide, afterwards links are formed between the clusters giving rise to a big cluster that is called gel (network which entraps the remain solution, with high viscosity)

d) *Ageing* - The chemical reactions that cause gelation continue after the gel point. In this step the formation of further crosslinks takes place.

e) *Drying* - Involves the loss of water, alcohol and other volatile solvents. In this step it is possible to use a supercritical drying agent, such as supercritical  $\text{CO}_2$ .

f) *Sintering* - Process of densification that is obtained with a thermal treatment.

Sol-gel route synthesis, since it offers a flexible way to obtain new glass materials, due to the low processing temperatures and facility to introduce new reagents, is a hot subject nowadays, not only of importance in the materials science<sup>22, 23, 24, 25, 26, 27</sup> but also in biological and pharmaceutical fields, in the synthesis of bioactive glasses.<sup>28,29,30</sup>

Glass materials are ubiquitous in everyday life and used in a wide range of technological applications such as optical and electronic devices. The advantages of glass as a host material are its transparency, easy shape-forming, economic mass production, high chemical durability and thermal stability. Being easy to modify the glass composition it is possible to bring out the abovementioned functionalities required for each application.<sup>31</sup>

#### 1.4. Colour in glass

To observe colour it is needed a light source, an object where light interact and a receptor to observe colour, therefore colour depends of several factors.

Light when interacts with a transparent material can be transmitted, reflected, absorbed or scattered. Some of the absorbed energy can emit light in a process named luminescence (Figure 1.12).<sup>32</sup> These phenomena can give rise to colour.

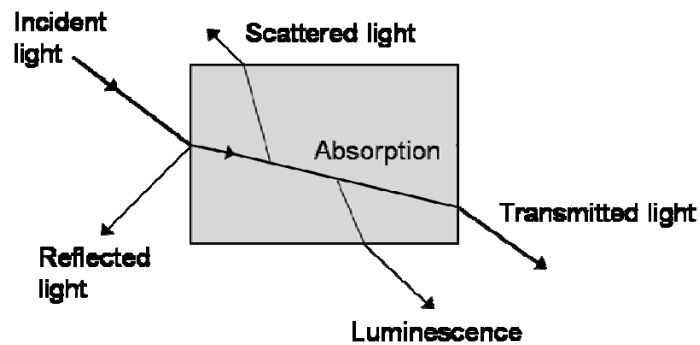


Figure 1.12. Light interaction with a transparent material.

The colour observed in transparent materials frequently has its origin in the transmitted light,  $T$ , that depends on the chromophore concentration  $c$ , the absorption coefficient of the chromophore,  $\epsilon$ , and the distance that light travels through the material,  $l$ . This dependence is known as the Lambert-Beer law (equation 1.1) and it can also be expressed in terms of absorbance  $A$  at a particular wavelength (equation 1.2).<sup>32,33</sup>

$$T = \frac{I}{I_0} = 10^{-\varepsilon \ell c} \quad (1.1)$$

$$A = -\log \frac{I}{I_0} = \varepsilon \ell c \quad (1.2)$$

where  $I_0$  and  $I$  are light intensities of the beams entering and leaving the object that is absorbing light.

The human eye is only sensitive to colour in a certain region of the electromagnetic spectrum, the visible region, which corresponds to the wavelength range between 380 and 720 nm, see figure 1.13.<sup>33</sup>

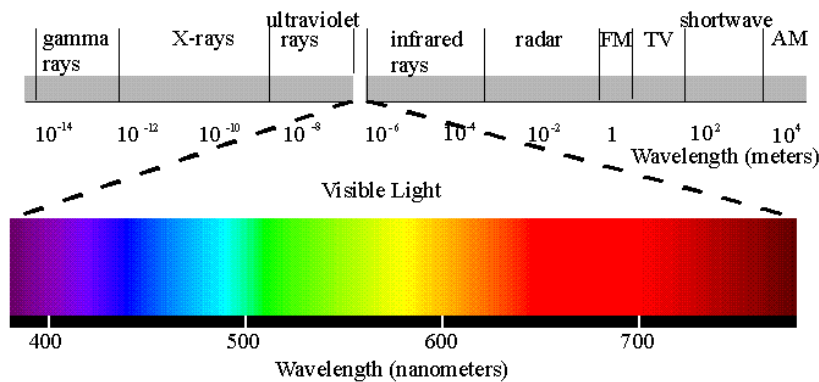


**Figure 1.13.** Electromagnetic spectrum with a zooming of the visible region.<sup>5</sup>

The colour in glass results from the glass interaction with the electromagnetic radiation and depends on their spectral characteristics, the chromophore that was used and of the glass composition.<sup>17</sup> Different types of chromophores can be used to colour glass (Table 1.2):

**Table 1.2.** Chromophores classification depending on their size in the coloured glasses.<sup>17</sup>

Chromophores	State	Magnitude order of the chromophore	Examples
Ionic or molecular	Dissolved	1 nm	$\text{Fe}^{2+}$ , $\text{Fe}^{3+}$ , $\text{Cr}^{3+}$ , $\text{Cr}^{6+}$ , $\text{Cu}^{2+}$ , $\text{V}^{5+}$ , $\text{Ce}^{4+}$ , $\text{Co}^{3+}$
Colloidal e microcrystalline	Colloidal dispersion and microcrystalline	1 nm – 100 nm	$\text{Cu}_2\text{O}$ , $\text{Ag}^0$ , $\text{Au}^0$ , $\text{Cd}_{(x+y)}\text{S}_x\text{Se}_y$
Crystalline	Crystalline Dispersion	> 100 nm	$\text{Cr}_2\text{O}_3$

<sup>5</sup> Image taken from <http://www.yorku.ca/eye/spectru.htm> on 02.09.2013

### 1.3.1. Colour due to metallic ions

Colour in glass can be obtained through the introduction of metallic ions in the glass matrix. This colour is due to transitions between electronic energy levels. An electronic transition is due to an electron excitation from a ground state energy state to an excited-state by absorption of a photon (photoexcitation). Ions have characteristic electronic states; therefore different ions give rise to different colours.<sup>34</sup>

Normally colour in glass is associated to the addition of transition d metals or lanthanides, f elements. The more commonly elements used in industry are Fe, Cu, Cr, V, Mn, Ti, Co e Ni.<sup>17</sup> The same element can have different oxidation states giving different colours to glass. Iron, for example, can be in the oxidation state 3+, giving yellow glasses or in the reduced state 2+, originating blue glasses. Normally both oxidation states are present in iron doped glasses. This explains the colour of glass windows (float glass), which are usually green, due to the iron present as an impurity.

The glass colour can also depend on the composition.  $\text{Co}^{2+}$ , for example, can originate pink or blue glasses if cobalt is exhibiting an octahedral or tetrahedral coordination, respectively. The lanthanide doped glasses are not so sensitive to the composition, since the 4f shell is efficiently shielded by the closed 5s and 5p shells and the ligand environment has only a weak influence on the electronic cloud of the lanthanide ion.<sup>11,17,35,36</sup>

### 1.3.2. Colour due to chromophores in a colloidal state

Chromophores can be aggregates of colloidal nature, where one or more components have dimensions between 1 nm and 1  $\mu\text{m}$ . In this group are included cadmium sulfoselenide, copper and gold nanoparticles which give colour to ruby glasses and also silver nanoparticles usually on the yellow glasses. The glasses containing cadmium sulfoselenide, which is a semiconductor, were commonly used to produce red glass, but due to the cadmium toxicity, red glasses are being produced using copper and also gold in certain applications.<sup>37</sup> Cadmium sulfoselenide glasses are called semiconductors because their source of absorption is electron transitions across the band gap.<sup>16</sup>

Over the years ruby glasses were the object of several scientific studies,<sup>38,39,40,41,42,43</sup> not only due to their attractive colour, but also due to the complexity of synthesis and the coloration process of ruby glass. Colour in these gold and copper glasses is caused by the interaction of electromagnetic radiation with metallic nanoparticles, giving rise to an absorption band, generally with a maximum around 530 nm for gold nanoparticles and 560 nm in the case of copper nanoparticles. However the wavelength and shape of this absorption band, mainly depends on the size, shape and dielectric properties of the metal nanoparticles and the surrounding matrix.<sup>17,37</sup> This band can be considered as a surface plasmon resonance (SPR) band where the free electrons in the metal particles behave as a connected plasmon (Figure

1.14).<sup>44,45</sup> The unique optical properties of the metal nanoparticles, with origin on the surface plasmon resonance, result from the absorption and scattering of light as a consequence of the match between the incident light frequency and the intrinsic electron oscillation frequency.<sup>46</sup>

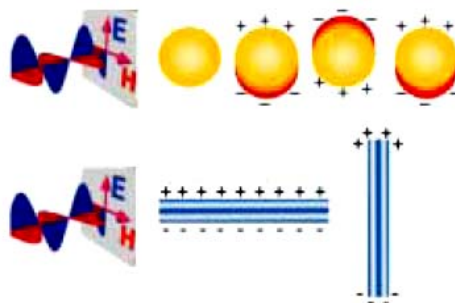


**Figure 1.14** (Top) Electromagnetic radiation interaction with a spherical metal nanoparticle. A dipole is induced and oscillates in phase with an electric field of the received light. (Bottom) Transversal and longitudinal oscillation of the electrons in a rod form metal nanoparticle. (Source: Luis M. Liz-Marzán, *Materials Today*, p. 26, February 2004)<sup>45</sup>

Sometimes glass colour can also be due to the presence of crystals (chromophores in crystalline state) that are formed after a slow temperature decreasing of the vitreous mass. Some examples are the aventurine and haematium glass.

#### 1.4. Luminescence in glass

The excitation energy obtained by a molecule when a photon is absorbed may be dissipated by different processes, such as fluorescence and phosphorescence (figure 1.15).<sup>34,47,48</sup>

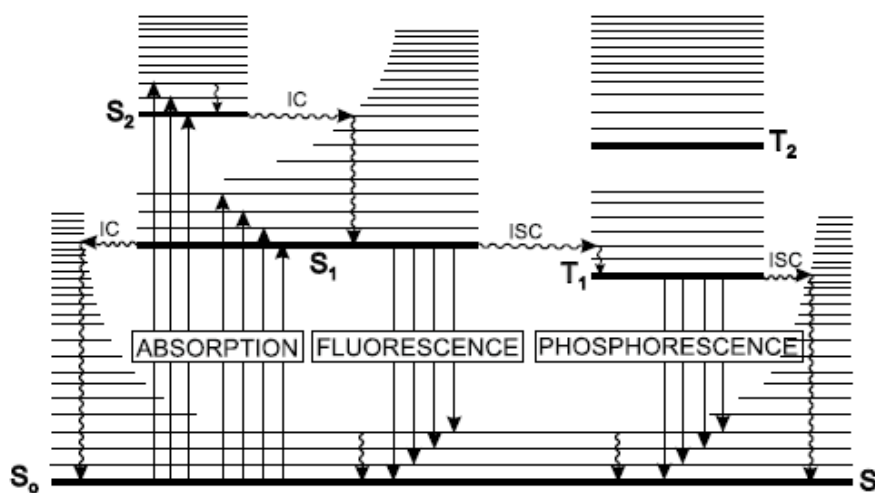


**Figure 1.15.** Perrin-Jablonski diagram. IC – internal conversion, ISC – intersystem crossing (Source: B. Valeur, *Molecular Fluorescence: Principles and Applications*, p.35, 2001).

After the photon absorption, non-radiative transitions can occur. The non-radiative transition between two excited states of the same spin multiplicity is called internal conversion and of different spin multiplicity is called intersystem crossing.

Fluorescence is the emitted radiation originated from an excited state that has the same spin multiplicity, normally from  $S_1$ , to the ground state ( $S_1 \rightarrow S_0$  relaxation in figure 1.15). On the other hand phosphorescence is originated from a de-excitation of an excited state with a different spin multiplicity from the ground state one ( $T_1 \rightarrow S_0$  in figure 1.15).<sup>48</sup>

A luminescent material can be fluorescent or phosphorescent, since luminescence is defined as an emission of ultraviolet, visible or infrared photons from an electronically excited species.<sup>34</sup> A major difference between this two luminescence types is the characteristic decay times since in fluorescence if the source of excitation is turned off the emission decays very fast ( $10^{-9}$ - $10^{-6}$  s), is immediate for the human eye. In phosphorescent materials the emission decays much more slowly, existing numerous examples in which the emission can be observed by the naked eyes during several hours.<sup>49,50,51</sup>

Luminescent glasses are commonly synthesized using lanthanide oxides, but due to the lanthanides high cost other possibilities are also being explored.

### 1.4.1. Lanthanide doped glasses

Rare earths, according to IUPAC (*International Union of Pure and Applied Chemistry*), correspond to the elements 21 (Sc), 39 (Y) and from 57 (La) to 71 (Lu). Lanthanide term (Ln) is used to designate the elements from 57 (La) to 71 (Lu). Contrarily to what the name indicates some of these elements exist in relatively large quantities and are commonly used for several applications such as electroluminescent devices, biomedical applications, chemical sensors, as a catalyst, in the study of biomolecules by spectroscopic imaging and used in many other fields.<sup>52,53,54</sup> In particular lanthanide doped glass are used in a wide range of technological applications such as optical and electronic devices. For example different studies have shown that  $\text{CaSiO}_3$  has excellent bioactivity and doped with europium is a potential candidate for new biomaterials<sup>55</sup> and also that lanthanide silicate glasses can be used to develop efficient photonic devices.<sup>56</sup>

Photoluminescent (PL) glass is easily obtained by addition of lanthanide elements. PL glasses can give rise to materials displaying interesting luminescent colours, which can be tuned by changing the rare earth dopant and the composition of the glass matrix.<sup>11</sup> Besides their importance in technological applications, these glass materials are finding their way and becoming very interesting in truly interdisciplinary studies such as artistic applications and in glass craft.<sup>9,10</sup> To use PL glasses for the different aforementioned applications is essential to have a detailed structural understanding of the influence of the lanthanide concentration, the lanthanide ion environment (glass composition), their distribution and clustering behaviour in order to develop efficient materials.

The many applications are due to special magnetic and spectroscopic properties of those elements. The lanthanides chemical properties are very similar, in consequence of their electronic configuration and to their existence mainly in the trivalent state; they differ in the

electronic configuration of the inner f orbitals. Ce, Gd, e Lu electron configuration in their fundamental state is  $[\text{Xe}] 4f^{n-1} 5d^1 6s^2$  and the electron configuration of the remaining lanthanide elements is  $[\text{Xe}] 4f^n 6s^2$ , n representing the number of electrons present in the f orbitals. For the trivalent lanthanides a regular increase of the electron configuration with the elements of the periodic table is observed:  $[\text{Xe}] 4f^0$  (La),  $[\text{Xe}] 4f^1$  (Ce),  $[\text{Xe}] 4f^2$  (Pr) to  $[\text{Xe}] 4f^{13}$  (Yb) and  $[\text{Xe}] 4f^{14}$  (Lu).<sup>53</sup> Lanthanides are strongly electropositive and their bonds can be considered merely ionic. As it was already said, the most common oxidation state for lanthanides is the trivalent state. For  $\text{Ln}^{2+}$  and  $\text{Ln}^{4+}$  the more stable oxidation states found are  $\text{Eu}^{2+}$  ( $[\text{Xe}] 4f^7$ ),  $\text{Yb}^{2+}$  ( $[\text{Xe}] 4f^{14}$ ),  $\text{Ce}^{4+}$  ( $[\text{Xe}] 4f^0$ ) and  $\text{Tb}^{4+}$  ( $[\text{Xe}] 4f^7$ ), having empty f orbitals or semi or totally full orbitals. But  $\text{Eu}^{2+}$  is very difficult to obtain as oxidises easily to  $\text{Eu}^{3+}$ , normally is only obtained in strong reducing atmospheres.<sup>57,58</sup>

The trivalent lanthanide ions have unique spectroscopic properties, with sharp absorption and emission lines, since the 4f shell is efficiently shielded by the closed 5s and 5p shells (Figure 1.16). Consequently, the materials hosting lanthanide ions such as  $\text{Eu}^{3+}$  have a weak influence on the electronic cloud of the lanthanide ion.<sup>11,36,59,60</sup>

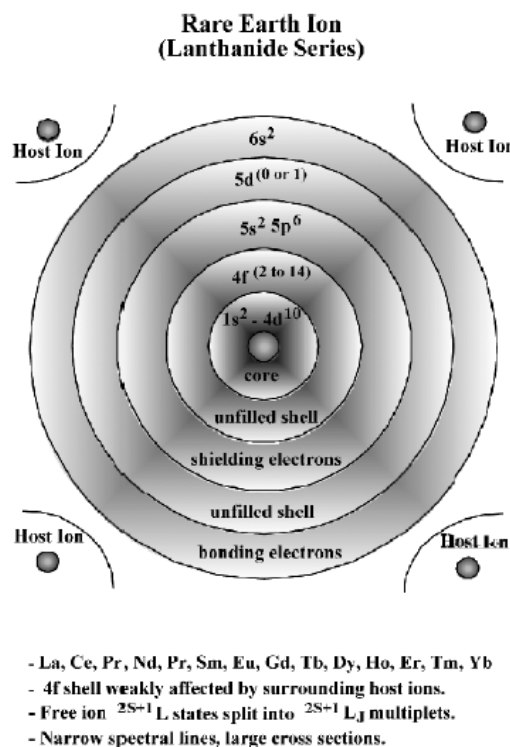


**Figure 1.16.** Rare Earth ion atomic structure. (Source: B.M. Walsh, in *Advances in spectroscopy for lasers and sensing*, p. 406, 2006).<sup>60</sup>

It is known, according to Laporte selection rule, that all the f-f transitions are forbidden, since they are caused by electronic transitions within the 4f subshell.<sup>11,36,60</sup> However the aforementioned transitions can be allowed for magnetic dipole (MD) or electric quadrupole radiation and also forbidden f-f electric dipole (ED) transitions appear from the admixture into the  $4f^n$  configuration of configurations of opposite parity. For this reason those transitions are generally characterized by long lifetimes, from microseconds to milliseconds.<sup>61</sup> In some cases

4f-5d transitions can occur originating more intense and broader bands in opposition to the sharp lines obtained from f-f transitions. 4f-5d transitions are parity allowed and since they are not protected like the f-f transitions, the band position of lower energy is strongly dependent on the ion local environment and the nature of their ligands.<sup>62, 63</sup>  $\text{Eu}^{2+}$  ( $4f^7$ ) and  $\text{Ce}^{3+}$  ( $4f^1$ ) luminescence are examples of 4f-5d transitions.<sup>11, 58</sup>

Luminescence from direct excitation of the lanthanide ion is not very efficient due to its low molar absorbance. However luminescence intensity may be enhanced by introducing the so-called antenna effect. In the antenna effect a ligand absorbs light and transfers energy to the lanthanide ion. Intramolecular energy transfer takes place from the ligand to the central metallic ion. This energy transfer efficiency depends on the chemical nature of the coordinated ligand.<sup>64, 65</sup>

Is shown in figure 1.17 a diagram of relevant energy levels of different luminescent lanthanides:

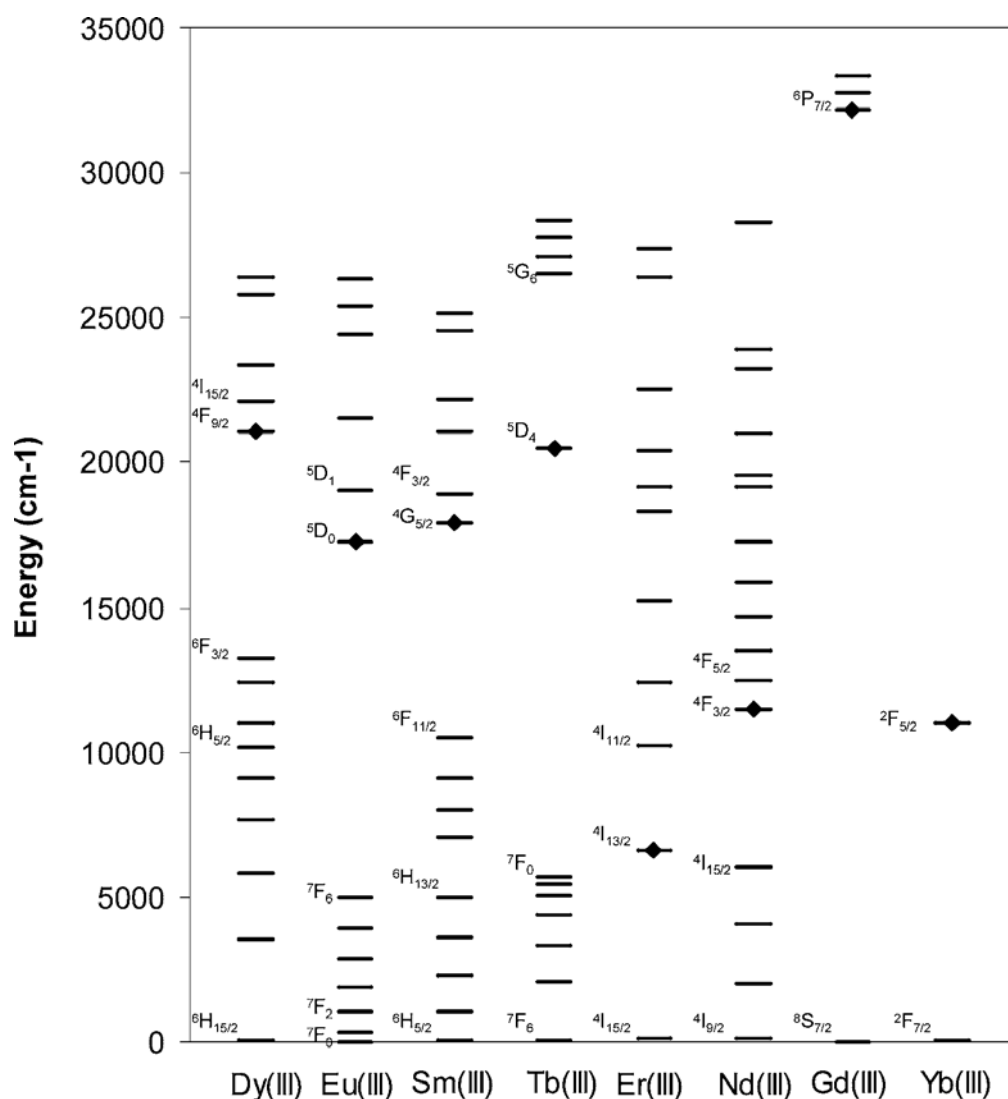


**Figure 1.17.** Energetic levels of various luminescent lanthanides. (Source: I. Hemmil and V. Laitala, *Journal of Fluorescence*, Vol. 15, p.530, July 2005).<sup>66</sup>



To obtain different luminescent colours, or even white luminescence, three primary luminescent colours can be mixed, using europium (red), terbium (green) and cerium (blue).

$\text{Eu}^{3+}$  displays an intense red luminescence, with several emissions lines for wavelengths above 570 nm. Each emission line corresponds to a radiative deactivation from a  $^5\text{D}_0$  excited state to  $^7\text{F}_n$  ( $n=0$  to 6) “ground” states. The most important emission lines are the  $^5\text{D}_0 \rightarrow ^7\text{F}_1$ , with a peak around 590 nm, that is a magnetic dipole transition<sup>67</sup> which intensity is rather insensitive to the environment (it only changes with the medium refractivity index) and the hypersensitive  $^5\text{D}_0 \rightarrow ^7\text{F}_2$  electronic transition that depends critically on the environment, with a peak around 610 nm. The photoluminescence colour, therefore, depends on how intense the  $^5\text{D}_0 \rightarrow ^7\text{F}_2$  electronic transition is, giving orange or red luminescence.<sup>11</sup>

Terbium ions,  $\text{Tb}^{3+}$ , can illustrate a strong luminescence in the green spectral region due to the  $^5\text{D}_4 \rightarrow ^7\text{F}_6$  and  $^5\text{D}_4 \rightarrow ^7\text{F}_5$  transitions.<sup>11</sup> The  $\text{Tb}^{3+}$  emission spectra consist in several peaks located at 487 nm, 542 nm, 547 nm, 582 nm, and 620 nm, which are attributed to transitions from the  $^5\text{D}_4$  excited state to  $^7\text{F}_n$ , being  $n=6, 5, 4, 3$  and 2 states respectively.<sup>68,69</sup>

$\text{Ce}^{3+}$  can show a broad band luminescence from the lowest crystal-field level  $5d^1$  to  $^2\text{F}_{5/2}$  and  $^2\text{F}_{7/2}$  of the ground configuration  $4f^1$ , originating an emission in the ultraviolet or in the blue spectral region.<sup>11</sup>

Theoretically, the existing framework to rationalize the lanthanide ions optical properties in different hosts is the Judd-Ofelt theory.<sup>11,36,60,70,71,72,73</sup>

### **Judd-Ofelt theory**

Judd-Ofelt theory was constructed using several approximations where the central ion is affected by the surrounding host ions by a static electric field, the host environment is treated as a perturbation of the free ion Hamiltonian and the interaction of electrons between configurations can be ignored.

This theory rationalizes the intensities of the lanthanides transitions between 4f electronic states. It is based in a model where the intensity of the forbidden f-f ED transitions derives from the admixture into the  $4f^N$  configuration of configurations of opposite parity.<sup>11,36,60,70,71,74</sup> In the Judd-Ofelt theory, it is also considered that Stark levels at ground state are equally populated (an assumption reasonable for experiments at room temperature), and the host matrix is optically isotropic. Therefore only ED transitions between different manifolds are considered, which simplifies the problem. Under this formalism, a set of parameters  $\Omega_\lambda$  ( $\lambda=2, 4, 6$ ) are determined from oscillator strengths of electric dipole transitions in the UV/VIS/NIR absorption spectroscopy, or from relative intensities in the photoluminescence spectra.

This theory relates the dipole strength  $D$  of the electronic transitions with the Judd-Ofelt parameters using the following equation:

$$D = \frac{1}{(2J+1)} \frac{(n^2 + 2)^2}{9n} e^2 \sum_{\lambda=2,4,6} \Omega_{\lambda} \left\langle f^N \Psi J \left\| U^{(\lambda)} \right\| f^N \Psi' J' \right\rangle^2 \quad (1.3)$$

where  $D$  is the dipole strength of the electronic transition,  $\left\langle f^N \Psi J \left\| U^{(\lambda)} \right\| f^N \Psi' J' \right\rangle$  are the reduced matrix elements,  $e$  is the elementary charge and  $n$  is the medium refraction index which should be taken into account since the lanthanide ion is a dielectric medium and therefore, affected by polarizability interactions with the host glass. Because the electric dipole transitions arise from a small crystal field perturbation, the matrix elements are not highly dependent on the host material. These matrix elements are integrals of the dipole operator between the upper and lower wave functions of the transition.<sup>60</sup>

The experimental oscillator strength ( $f_{\text{exp}}$ ) of an f-f transition in the absorption spectrum can be obtained using the following equation:

$$f_{\text{exp}} = 4.318 \times 10^{-9} \int \varepsilon(\nu) d\nu \quad (1.4)$$

where  $\varepsilon(\nu)$  is the frequency dependent molar extinction coefficient and  $\nu$  is the energy (or wavenumber) in  $\text{cm}^{-1}$ .

The oscillator can also be calculated using Judd-Ofelt theory for an electric dipole transition, since  $D$  and  $f$  are interrelated by:

$$f = \frac{8\pi mc}{3h} \overline{D} \quad (1.5)$$

where  $D$  is the dipole strength of the electronic transition.

Since  ${}^7F_0$ ,  ${}^7F_1$  and  ${}^7F_2$  manifolds are populated in the ground state at room temperature, Boltzmann distribution should also be taken into account. The expression to calculate the molar fractions of each state is:

$$X_{{}^7F_j}(T) = \frac{(2J+1) \exp\left(-\frac{\Delta E_{{}^7F_j / {}^7F_0}}{k_B T}\right)}{\sum_{j=0}^m (2j+1) \exp\left(-\frac{\Delta E_{{}^7F_j / {}^7F_0}}{k_B T}\right)} \quad (1.6)$$

Usually for low crystal field symmetry, as is the case of various sorts of glass systems,  ${}^7F_1$  splits into 3 different Stark levels and  ${}^7F_2$  into 5 different Stark levels. Usually the number of Stark

levels is derived from the luminescence spectrum of the lanthanide ion. The parameter  $\Delta E_{\gamma_{F_J} / \gamma_{F_0}}$  is an average for the energy difference between the manifolds. The equation that describes the calculated oscillator strength,  $f_{\text{cal}}$ , is now:

$$f_{\gamma_{F_J} \rightarrow \gamma_{L_J}} = \frac{8\pi n c}{3h X_{\gamma_{F_J}}(T)} \bar{\nu} D \quad (1.7)$$

The  $f_{\text{exp}}$  is calculated using equation 1.4 and can be used in equation 1.7 to determine the  $\Omega_\lambda$  parameters. A least squares fitting approximation is used for equation 1.7 which give the best fit between experimental and calculated oscillator strengths. The theoretical oscillator strengths ( $f_{\text{cal}}$ ) are then determined using  $\Omega_\lambda$  parameters.

The Judd-Ofelt parameters can also be calculated from the emission spectra. The radiative transition probability (A) for a determine transition can be calculated using equation 1.8.<sup>75</sup>

$$A = A_{ED} + A_{MD} \quad (1.8)$$

where  $A_{ED}$  is the probability of an ED transition (equation 1.9) and  $A_{MD}$  is the probability of a MD transition (equation 1.10).

$$A_{ED} = \frac{64\pi^4 e^2 \bar{\nu}^3}{3h(2J+1)} \frac{n(n^2+2)^2}{9} \sum_{\lambda=2,4,6} \Omega_\lambda \left\langle f^N \Psi J \left\| U^{(\lambda)} \right\| f^N \Psi' J' \right\rangle^2 \quad (1.9)$$

$$A_{MD} = \frac{64\pi^4 e^2 \bar{\nu}^3}{3h(2J+1)} n^3 D_{MD} \quad (1.10)$$

$\beta_j$  is a branching ratio, giving the intensity of a  $j$  transition compared to other peaks of the luminescence spectra. It is, therefore, a value that can be accessed experimentally. The branching ratio can be theoretically calculated, since  $A_{MD}$  value is independent of the medium.<sup>67</sup> Assuming  $D_{MD, j=1}$ ,  $\Omega_\lambda$  can be calculated, considering that MD mechanism is negligible for other transitions.

$$\beta_j = \frac{A_{ED}^j}{\sum_{i=1}^6 A_{ED}^i + A_{MD}^i} \quad (1.11)$$

$$\Omega_\lambda = \frac{A_{J=\lambda}}{A_{J=1}} \frac{9n^2}{(n^2+2)^2} \left( \frac{\bar{\nu}_\lambda}{\bar{\nu}_{j=1}} \right)^3 \frac{D_{J=1}^{MD}}{\left\langle f^N \Psi J \left\| U^{(\lambda)} \right\| f^N \Psi J' \right\rangle} \quad (1.12)$$

These parameters are important to describe the absorption and emission properties. In the case of europium, for example, the  $\Omega_2$  parameter plays an important role, since it defines the  $^5D_0 \rightarrow ^7F_2$  electronic transition intensity and also gives important indication of how covalently are the ligands bonded to  $\text{Eu}^{3+}$ . All the transitions whose probability is dominated by  $\Omega_2$  are very sensitive to the environment. Normally, high  $\Omega_2$  values confer more photoluminescence around 610 nm, lower luminescence lifetimes and higher intensity on the absorption spectra. However the degree of covalency of the Eu-O bond reflected on higher  $\Omega_2$  values, is not the only parameter affecting the  $\text{Eu}^{3+}$  luminescence in glasses. The non-symmetric part of the field has a major influence on these parameters, for example different modifier ions are responsible for the distortion of the oxygen, lowering the site symmetry and increasing the f-f transitions probability.<sup>60</sup>

#### 1.4.2. Other element doped glasses

Luminescence in glasses can also be due to other elements besides lanthanides. For example different d transition metals were already used in several studies. Contrarily to what happen in lanthanide doped glasses, using the transition metals where the unfilled 3d shell is strongly affected by host ions, the emission spectrum usually consists of a broad band.<sup>17,60</sup> This can be very interesting for the reason that with the same element different luminescent colours can be achieved.

Some examples of d transition metals that can give rise to luminescent glasses are given bellow. Copper is one element that can confer luminescence to glasses.  $\text{Cu}^+$  exhibits a characteristic luminescence normally assigned to the electronic transition  $3d^9 4s^1 \rightarrow 3d^{10}$ . Several studies of luminescence of  $\text{Cu}^+$  doped materials can be found in the literature and the colours obtained can range from blue to near infrared.<sup>76,77,78,79</sup> Different applications, such as tunable lasers and optical switches are being studied.<sup>80,81</sup> Another example of a d transition metal that can create luminescent glasses is manganese, where the luminescence is produce by  $\text{Mn}^{2+}$  due to the electronic transition  $^4T_{1g} \rightarrow ^6A_{1g}$ .<sup>17,82</sup> Like in  $\text{Cu}^+$  doped materials,  $\text{Mn}^{2+}$  also displays several colours of luminescence in different host compositions.<sup>82,83,84</sup>

Besides the d transition metals, also nanoparticles can confer luminescence to glasses. There are several examples of luminescent nanoparticles that can be introduced in the glass matrix such as copper nanoparticles,<sup>85</sup> nanoparticles of semiconductors ( $\text{ZnSe}$ ,  $\text{ZnS}$  and  $\text{Cd}_{1-x}\text{Mn}_x\text{S}$ ),<sup>86,87</sup>  $\text{Al}_2\text{O}_3$  and  $\text{PbS}$  nanoparticles.<sup>88,89</sup>

### 1.5. Focus of the present thesis

This thesis aimed to develop new glass materials to be used in artworks with focus on their optical properties. A collaboration between artists and scientists is a benefit since it is important to understand the artists necessities and also to understand the materials properties before proceeding to create the artwork.

In the following chapters experiments developed in order to obtain luminescent glasses were described. Several lanthanide doped soda-lime silicate glasses were synthesized in order to increase the colour palette of luminescence and also to obtain white luminescence (chapters 1 and 2). Aluminoborosilicate luminescent glasses without lanthanides, containing lead halides and copper were studied to explore the possibility of producing different colours without using lanthanides (chapter 4).

On a different context, one chapter of this thesis was dedicated to the ruby colour on glass. Due to its complexity, the synthesis of ruby glass has been investigated for many years. A new approach to obtain this glass using the sol-gel technique and an ionic liquid as a reductive agent was discussed.



## Chapter 2 – Synthesis and characterization of luminescent $\text{Eu}_2\text{O}_3$ doped glasses

Materials with singular properties were explored by many artists in contemporary glass art, therefore the development of new luminescent glass materials have promising applications in art-works. In this chapter, structural and optical properties of  $\text{Eu}_2\text{O}_3$  doped soda-lime silicate glasses (type of glass normally used for utilitarian and decorative applications) were investigated as function of  $\text{Eu}_2\text{O}_3$  and CaO concentrations in order to obtain a better structural understanding of this glass system.

### 2.1. Europium oxide doped glasses

As it was mentioned in chapter 1, to optimize the efficiency of photoluminescent glasses in the art field and/or for other applications, such as electroluminescent devices, biomedical applications, chemical sensors and as a catalyst, it is essential to have a detailed structural understanding of the influence of the lanthanide concentration, its environment (which depends of the glass composition), distribution and clustering behaviour in order to enhance the performance of those glass materials according to the desired applications. Intense investigations were made using several lanthanides in diverse glass compositions for a long period of time and still very recent studies can be found.<sup>55,56, 90, 91, 92, 93, 94, 95, 96, 97, 98</sup> Photoluminescent glass is easily obtained by addition of rare earth elements and can give rise to materials displaying interesting luminescent colours which can be tuned by changing the rare earth dopant and the composition of the glass matrix.<sup>11</sup> Concerning the art field, these luminescent glasses have high potentialities, not only because several colours can be obtained but also because the UV-lights required to obtain luminescence are in the near-UV region (wavelengths higher than 350 nm), being those commonly used in public places.

In chapter 1 it was referred that trivalent lanthanide ions have unique spectroscopic properties with sharp emission lines, since the 4f shell is efficiently shielded by the closed 5s and 5p shells. In this chapter the luminescence of  $\text{Eu}^{3+}$  doped glasses are studied in more detail.  $\text{Eu}^{3+}$  displays an intense red luminescence, with several emissions lines for wavelengths above 570 nm. Each emission line corresponds to a radiative deactivation from a  $^5\text{D}_0$  excited state to  $^7\text{F}_n$  ( $n=0$  to 6) “ground” states. The most important emission lines are the  $^5\text{D}_0 \rightarrow ^7\text{F}_1$ , with a peak around 590 nm, that is a magnetic dipole transition,<sup>11,67</sup> and the hypersensitive  $^5\text{D}_0 \rightarrow ^7\text{F}_2$  electronic transition that depends critically on the environment, with a peak around 610 nm. The photoluminescence colour, therefore, depends on how intense the  $^5\text{D}_0 \rightarrow ^7\text{F}_2$  electronic

transition is, giving orange or red luminescence.<sup>11</sup> Theoretically, the existing framework to rationalize the lanthanide ions optical properties in different hosts is the Judd-Ofelt theory (explained in more detail in chapter 1): from this theory a set of parameters  $\Omega_\lambda$  ( $\lambda=2,4,6$ ) can be determined.<sup>11,36,60,70,71,72,73</sup> In europium case the  $\Omega_2$  parameter plays an important role, since it defines the  $^5D_0 \rightarrow ^7F_2$  electronic transition intensity and also gives important indication of how covalently are the ligands bonded to Eu<sup>3+</sup>.<sup>72,73</sup> Normally, high  $\Omega_2$  values confer more photoluminescence around 610 nm, lower luminescence lifetimes and higher intensity on the absorption spectra. However the degree of covalency of the Eu-O bond reflected on higher  $\Omega_2$  values is not the only parameter affecting the Eu<sup>3+</sup> luminescence in glasses. The non-symmetric part of the field has a major influence on these parameters, for example different modifier ions are responsible for the distortion of the oxygen, lowering the site symmetry and increasing the f-f transitions probability.<sup>96,99</sup> Moreover, aggregation of Eu<sub>2</sub>O<sub>3</sub> in the glass (e.g., as clusters or nanoparticles) has an important effect on the glass photoluminescence,<sup>92,100</sup> but usually it is not a desired effect since it can quench the luminescence through cross relaxation and energy-transfer processes. Usually the presence of Eu<sub>2</sub>O<sub>3</sub> aggregates is studied by Fluorescence Line Narrowing technique.<sup>31,101,102,103</sup> However, if large differences exist between  $\Omega_2$  values for isolated Eu<sup>3+</sup> and for Eu<sub>2</sub>O<sub>3</sub> aggregates, significant differences between luminescence lifetimes would be expected. In such case, time-resolved luminescence techniques, such as Flash Photolysis technique can be used to distinguish both species.<sup>100</sup>

Europium-doped silica and sodium silicate glasses, with different sodium concentrations were already investigated.<sup>92,104</sup> As the addition of fluxes to the glass decreases the chemical durability of silicate glasses, a stabilizer, such as calcium oxide, have an important role in glass production,<sup>15</sup> therefore in this work a more stable glass system with a glass former (SiO<sub>2</sub>), a flux (Na<sub>2</sub>O) and a stabilizer (CaO) was chosen. A spectroscopic and time-resolved luminescence study of soda-lime silicate glasses (Na<sub>2</sub>O-CaO-SiO<sub>2</sub>) doped with different Eu<sub>2</sub>O<sub>3</sub> and CaO concentrations was performed. Comparisons of results between different techniques are made using Judd-Ofelt theory and group symmetry analysis.

## 2.2. Experimental Part

### 2.2.1 Synthesis and samples preparation

Europium doped soda-lime-silicate glasses synthesized with different CaO contents (Group A) and doped with different Eu<sub>2</sub>O<sub>3</sub> concentrations (Group B) were studied. Table 2.1 summarizes the chemical composition of the several synthesized glasses. Approximately 25 g batches were mixed and melted in platinum crucibles in an electric furnace at 1500 °C for 3 hours in air. The quantity of oxides used to prepare the different glass compositions can be found in section 9.1.1, Supplementary Material. Reagent grade SiO<sub>2</sub> (p.a., Fluka), CaCO<sub>3</sub> (p.a.,



Panreac), Na<sub>2</sub>CO<sub>3</sub> (p.a., Riedel de Haen) and Eu<sub>2</sub>O<sub>3</sub> (99.9%, Metall Rare Earth Limited) were used as starting materials in all the synthesized glasses.

The melted glasses were quenched pouring them into a metal sheet at room temperature and further annealed at ca. 550°C for one hour. The glass samples were cut and carefully polished, for optical measurements, with 0.7 cm thickness and 0.8 cm width.

**Table 2.1.** Composition of the europium doped soda-lime-silicate glasses studied (in wt %).

	Glass sample	Composition (wt %)			
		SiO <sub>2</sub>	Na <sub>2</sub> O	CaO	Eu <sub>2</sub> O <sub>3</sub>
<b>Group A</b>	<b>C1</b>	76.5	16.5	<b>0.0</b>	7.0
	<b>C2</b>	72.4	15.6	<b>5.0</b>	7.0
	<b>C3</b>	68.2	14.8	<b>10.0</b>	7.0
	<b>C4</b>	64.2	13.8	<b>15.0</b>	7.0
<b>Group B</b>	<b>E0</b>	74.0	16.0	10.0	<b>0.0</b>
	<b>E1</b>	73.9	16.0	10.0	<b>0.1</b>
	<b>E2</b>	73.6	15.9	10.0	<b>0.5</b>
	<b>E3</b>	73.3	15.8	9.9	<b>1.0</b>
	<b>E4</b>	72.9	15.8	9.9	<b>1.5</b>
	<b>E5</b>	72.5	15.7	9.8	<b>2.0</b>
	<b>E6</b>	72.2	15.6	9.8	<b>2.5</b>

### 2.2.2. Measurements

Absorption spectra were recorded using a Varian Cary-5000 UV/VIS/NIR spectrophotometer over the 300-2300 nm wavelength range with a 0.02 nm resolution. Luminescence spectra were measured using a SPEX Fluorolog-3 Model FL3-22 spectrofluorimeter, with 0.5 nm spectral resolution. Experiments were performed at room temperature (22°C). Lifetime measurements were run on a LKS.60 nanosecond laser photolysis spectrometer from Applied Photophysics, with a Brilliant Q-Switch Nd-YAG laser from Quantel, using the second harmonics ( $\lambda_{\text{exc}} = 532$  nm, laser pulse half width equal to 6 ns). Emission decays were obtained with spectral resolution of 2 nm, with a perpendicular geometry in relation with the laser excitation, by averaging between two to ten measurements at each emission wavelength depending on the sample intensity. For time-resolved spectra acquisition an optical cut-off filter (570 nm) for the emitted light was used in order to avoid scattering light contamination. Laser flash photolysis traces at each wavelength were analyzed using least squares fittings of the experimental data.

Ellipsometry spectra were measured using a Horiba Jobin Yvon UVISSEL ellipsometer, with a fixed 70° incidence angle, in the range of 1.5–6.5 eV to determine the refractive index,  $n$ , of the glasses. The glass transition temperature ( $T_g$ ) and the Coefficient of Thermal Expansion (CTE) were measured using a Netvcshe Dil402PC dilatometer in a temperature range of 20-750°C,

with a heating rate of  $5 \text{ K}\cdot\text{min}^{-1}$ . To do these  $T_g$  analyses the samples were cut with 0.5 cm thickness, 0.5 cm width and 2.5 cm length.

### 2.3. Synthesis and characterization of $\text{Eu}_2\text{O}_3$ doped $\text{Na}_2\text{O}$ - $\text{CaO}$ - $\text{SiO}_2$ glass

In order to better understand how the europium concentration and the glass composition influence the europium distribution and its clustering behaviour, and how it influences the photoluminescence colour, europium doped glasses were synthesized using different CaO concentrations (figure 2.1.) and different  $\text{Eu}_2\text{O}_3$  concentrations (figure 2.2.)

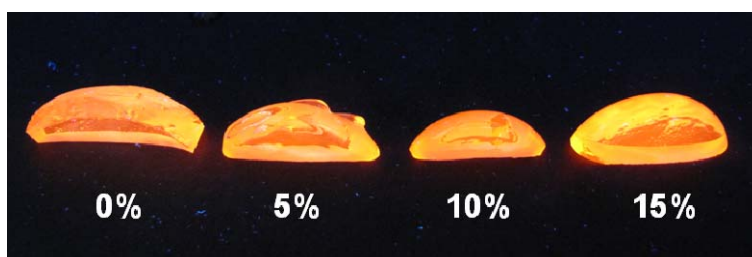


**Figure 2.1.** Glasses synthesized with 7% of  $\text{Eu}_2\text{O}_3$  and with different CaO concentrations: 0 (C1), 5 (C2), 10 (C3) and 15 (C4) wt%, under UV-light (ca. 370 nm).

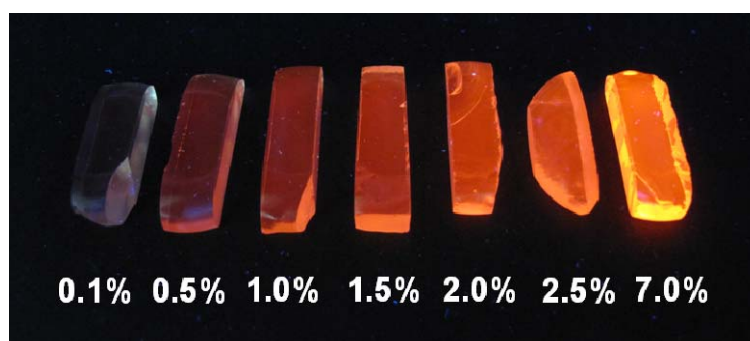


**Figure 2.2.** Glasses synthesized with different  $\text{Eu}_2\text{O}_3$  concentrations: 0.1 (E1), 0.5 (E2), 1.0 (E3), 1.5 (E4), 2.0 (E5), 2.5 (E6) and 7.0 (C3) wt%, under UV-light (ca. 370 nm).

An orange luminescent colour is observed in all the synthesized glasses. This colour is in agreement with what is found in the literature for europium in the trivalent state.<sup>11,53</sup> Observing all the synthesized glasses under the UV-light, no significant changes in luminescence are detected for glasses of group A, with different CaO concentrations, but it is observed that luminescence increases with  $\text{Eu}_2\text{O}_3$  concentration as expected.

#### 2.3.1. Physical properties

The glass transition temperature ( $T_g$ ) and the Coefficient of Thermal Expansion (CTE) of the base glass **E0** (74%  $\text{SiO}_2$ , 16%  $\text{Na}_2\text{O}$  and 10%  $\text{CaO}$ ) were determined using a dilatometer. The linear thermal expansion can be found in section 9.1.2, Supplementary Material. This glass

has a  $T_g$  value of 537°C and a CTE of 98.5 ( $\times 10^{-7} \cdot ^\circ\text{C}^{-1}$ ) in a temperature range of 25-300°C. Densities ( $d$ ) of all glasses were determined, see Table 2.2.

**Table 2.2.** Densities values ( $d$ ) of all the synthesized glasses.

	Glass sample	CaO (wt%)	Eu <sub>2</sub> O <sub>3</sub> (wt%)	$d$ /g.cm <sup>-3</sup>
<b>Group A</b>	<b>C1</b>	<b>0.0</b>	7.0	1.782
	<b>C2</b>	<b>5.0</b>	7.0	2.066
	<b>C3</b>	<b>10.0</b>	7.0	2.242
	<b>C4</b>	<b>15.0</b>	7.0	2.305
<b>Group B</b>	<b>E0</b>	10.0	<b>0.0</b>	2.140
	<b>E1</b>	10.0	<b>0.1</b>	1.869
	<b>E2</b>	10.0	<b>0.5</b>	1.989
	<b>E3</b>	9.9	<b>1.0</b>	2.011
	<b>E4</b>	9.9	<b>1.5</b>	2.224
	<b>E5</b>	9.8	<b>2.0</b>	2.001
	<b>E6</b>	9.8	<b>2.5</b>	1.920

The refractive indices ( $n$ ) of the synthesized glasses with different CaO contents were determined using ellipsometry technique. These measurements and calculations were performed by Professor Hugo Águas from Cenimat. The modelling used to determine the refractive index can be found in section 9.1.3, Supplementary Material.

From this abovementioned data it is possible to calculate other physical parameters, such as molar refractivity ( $R_M$ ), Eu<sup>3+</sup> ion concentration ( $N$ ) and the interionic distance ( $r_i$ ) between europium ions. These parameters can be found on Table 2.3 according with the different CaO concentrations.

**Table 2.3.** Physical properties of glasses with different CaO concentrations. Refractive index ( $n_d$ ), density ( $d$ ), molar refractivity ( $R_M$ ), Eu<sup>3+</sup> ion concentration ( $N$ ), interionic distance ( $r_i$ ) and contribution of oxygen to the molar refractivity ( $R_M(\text{O}^{2-})$ ).

CaO (wt%)	$n$	$d$ /g.cm <sup>-3</sup>	$R_M \text{ exp}$ /cm <sup>3</sup> .mol <sup>-1</sup>	$N / 10^{20}$ ions.cm <sup>-3</sup>	$r_i$ /Å	$R_M(\text{O}^{2-})$ /cm <sup>3</sup> .mol <sup>-1</sup>
0	1.5253	1.782	13.91	4.27	13.3	5.7
5	1.5372	2.066	12.19	4.95	12.6	5.1
10	1.5479	2.242	11.39	5.37	12.3	4.9
15	1.5572	2.305	11.20	5.52	12.2	4.9

The interionic distances were calculated using the following equation:

$$r_i = \left( \frac{1}{N} \right)^{\frac{1}{3}} \quad (2.1)$$

and the molar refractivity was calculated using the Lorentz-Lorenz equation<sup>105</sup>

$$R_M = \left[ \frac{n^2 - 1}{n^2 + 2} \right] \frac{\overline{M}}{d} \quad (2.2)$$

where  $\overline{M}$  is the average molar weight of the glasses, taking into account the relative compositions of them. Molar refractivity can be considered as the sum of the contributions of each ion in the glass.<sup>105</sup> Therefore  $R_M$  can be calculated according to the following equations:

$$R_M = x_{Si^{4+}} R(Si^{4+}) + x_{Na^+} R(Na^+) + x_{Ca^{2+}} R(Ca^{2+}) + x_{Eu^{3+}} R(Eu^{3+}) + x_{O^{2-}} R(O^{2-}) \quad (2.3)$$

where  $x$  is the molar concentration. It is considered that cations have molar refractivities relatively independent of the medium, while anions can change considerably. Therefore, the cation values are held constant and were taken from the literature:  $R(Na^+) = 0.72 \text{ cm}^3$ ,  $R(Si^{4+}) = 0.04 \text{ cm}^3$ ,  $R(Ca^{2+}) = 1.33 \text{ cm}^3$  and  $R(Eu^{3+}) = 2.4 \text{ cm}^3$ .<sup>105, 106</sup> The anionic specie in the synthesized glass matrix is  $O^{2-}$ , subsequently  $R(O^{2-})$  are calculated using equation (2.3) and shown on table 2.3. It is observed that the contribution of oxygen to the molar refractivity  $R_M(O^{2-})$  decreases as the calcium concentration increases in the glass matrix. If some small losses occur in the glasses synthesis, the glass matrix should have always the same elements and this trend is going to be the same. These results suggest a greater ionic character of oxygen when calcium is absent, while its presence increases the covalent character.

### 2.3.2. UV/Vis/NIR Absorption Spectroscopy

Absorption spectra of group A and group B glasses, with different CaO concentrations and with different Eu<sub>2</sub>O<sub>3</sub> concentrations were measured (figure 2.3). The absorption peaks observed can be attributed to electronic transitions of Eu<sup>3+</sup> by comparison with attributions found in the literature in aqueous solutions.<sup>107</sup> It is known, according to Laporte selection rule, that all of these transitions are forbidden, since they are due to electronic transitions within the 4f subshell.<sup>11,36,60</sup> However the aforementioned transitions can be allowed for magnetic dipole (MD) or electric quadrupole radiation and also forbidden f-f electric dipole (ED) transitions appear from the admixture into the 4f<sup>N</sup> configuration of configurations of opposite parity. In practical terms, electric quadrupole transitions are too weak to be observed; therefore all the observed peaks are either MD or ED transitions. In figure 2.3 it is possible to observe that the absorbance increases with increasing CaO concentration and with Eu<sub>2</sub>O<sub>3</sub> concentration. A linear dependence between absorbance and Eu<sub>2</sub>O<sub>3</sub> weight fraction within the range studied (until 7% wt) was found, see section 9.1.4, Supplementary Material.

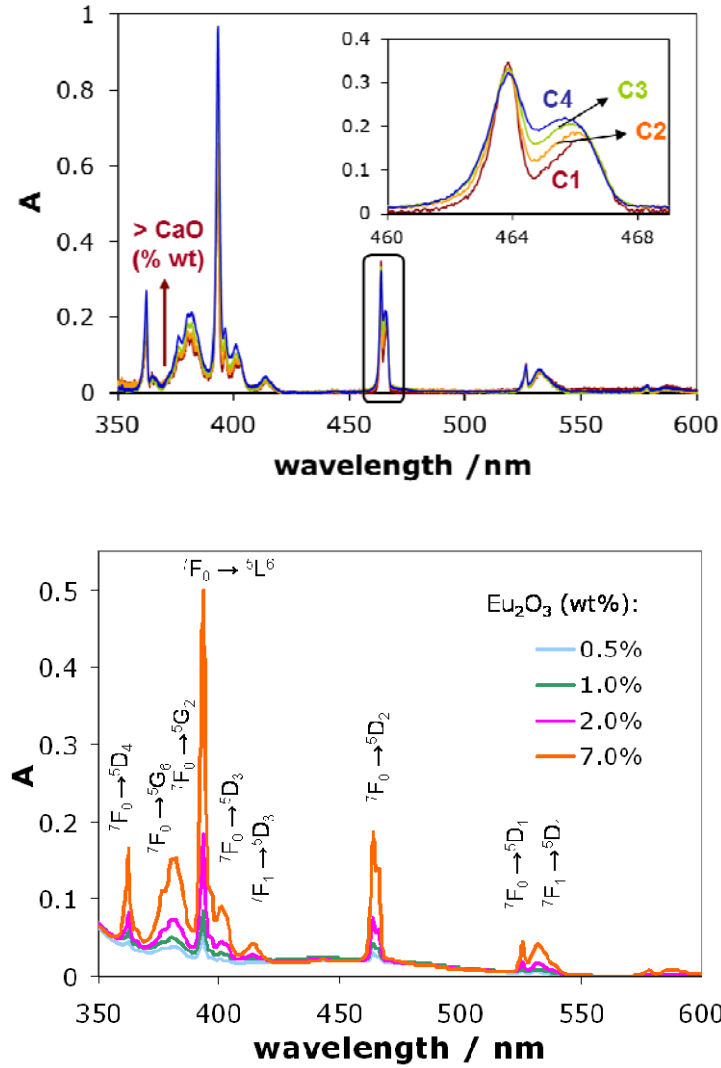


**Figure 2.3.** (Top) UV/VIS absorption spectra of  $\text{Eu}_2\text{O}_3$  (7 wt%) doped glasses with different CaO concentrations 0 (C1), 5 (C2), 10 (C3) and 15 (C4) wt%. (Bottom) UV/VIS absorption spectra of glasses doped with different  $\text{Eu}_2\text{O}_3$  concentrations 0.5 (E2), 1.0 (E3), 2.0 (E5) and 7% (C3) wt%, with the correspondent electronic transition.

An isosbestic point can be found at 463 nm, see insert on figure 2.3 on the top, suggesting the existence of two  $\text{Eu}^{3+}$  species. The absorption peaks observed can be attributed to electronic transitions of  $\text{Eu}^{3+}$  based on published results in aqueous solutions (see table 2.4).<sup>107</sup>

**Table 2.4.** Analysis of  $\text{Eu}_2\text{O}_3$  absorption spectroscopy in glasses with different CaO concentrations. Attribution of the energy levels to each absorption peak and the correspondent value found in the literature, in nm. These peaks were obtained with the bands decomposition in energy. ED – transition allowed by electric dipole mechanism, MD - transition allowed by magnetic dipole mechanism.

Energy Levels	Barycenter /nm				literature <sup>107</sup>	
	C1	C2	C3	C4		
${}^7F_1 \rightarrow {}^7F_6$	2196	2198	2198	2202	<b>2164</b>	<b>ED</b>
${}^7F_0 \rightarrow {}^7F_6$	2088	2092	2093	2097	<b>2008</b>	<b>ED</b>
	2016	2016	2017	2020		
	1866	1876	1879	1913		
${}^7F_2 \rightarrow {}^5D_0$	612	612	612	612	-	<b>ED</b>
${}^7F_1 \rightarrow {}^5D_0$	588	588	588	588	<b>591</b>	<b>MD</b>
${}^7F_0 \rightarrow {}^5D_0$	578	578	578	578	<b>579</b>	<b>MD</b>
${}^7F_1 \rightarrow {}^5D_1$	537	537	537	537	<b>535</b>	<b>ED</b>
	532	532	532	532		
${}^7F_0 \rightarrow {}^5D_1$	526	526	526	526	<b>525</b>	<b>MD</b>
	526	526	525	525		
${}^7F_0 \rightarrow {}^5D_2$	466	466	466	465	<b>465</b>	<b>ED</b>
	464	464	464	464		
${}^7F_1 \rightarrow {}^5D_3$	415	414	414	414	<b>416</b>	<b>ED</b>
${}^7F_1 \rightarrow {}^5L_6$	403	403	403	403	<b>400</b>	<b>ED</b>
${}^7F_0 \rightarrow {}^5L_6$	401	401	401	401	<b>394</b>	<b>ED</b>
	397	397	396	396		
	393	393	393	393		
${}^7F_1 \rightarrow {}^5L_7$	384	384	384	384	<b>383</b>	<b>ED</b>
${}^7F_0 \rightarrow {}^5G_2$	382	382	382	382	<b>380</b>	<b>ED</b>
	380	380	380	380		
${}^7F_0 \rightarrow {}^5G_4$	377	376	376	376	<b>375</b>	<b>MD</b>
${}^7F_1 \rightarrow {}^5D_4$	366	365	365	365	<b>366</b>	<b>ED</b>
${}^7F_0 \rightarrow {}^5D_4$	362	362	363	363	<b>361</b>	<b>ED</b>

In the visible part of the spectrum, transitions from  ${}^7F_0$  and  ${}^7F_1$  manifolds appear in close proximity, which at wavelengths below 400 nm give rise to a difference between peaks less than 5 nm. As a result the spectra appear overlapped and the peaks are difficult to distinguish without spectral decomposition. In the spectral region of the  ${}^7F_1 \rightarrow {}^5D_0$  and  ${}^7F_0 \rightarrow {}^5D_0$  transitions (ca. 580 nm), this difference is larger (above 10 nm) and the two peaks are easily distinguished. A very small absorption band around 610 nm, which in energy is about  $1000\text{ cm}^{-1}$  less than the  ${}^7F_0 \rightarrow {}^5D_0$  transition, is attributed to the  ${}^7F_2 \rightarrow {}^5D_0$  ED transition (it is not shown the spectra of figure 2.3 because the intensity is too low to be observed due to the high intensity of the other peaks). NIR transitions, see figure 2.4., can be assigned to  ${}^7F_0 \rightarrow {}^7F_6$  and  ${}^7F_1 \rightarrow {}^7F_6$ . Those transitions cannot be assigned to  ${}^7F_2 \rightarrow {}^7F_6$  or  ${}^7F_0 \rightarrow {}^7F_5$ , since these ones are expected to have energies around  $3000\text{ cm}^{-1}$ . A complete assignment of the NIR bands can be done, measuring the absorption spectra at different temperatures (the intensity of  ${}^7F_0 \rightarrow {}^7F_6$  transitions decrease, while  ${}^7F_1 \rightarrow {}^7F_6$  transitions increase with increasing temperature). Indeed, as temperature

increases, the absorption intensity of one band increases while the other 3 bands intensity decrease, see figure 2.4. So the 3 higher transitions are assigned to  ${}^7F_0 \rightarrow {}^7F_6$  while the remainder is assigned to  ${}^7F_1 \rightarrow {}^7F_6$ ,

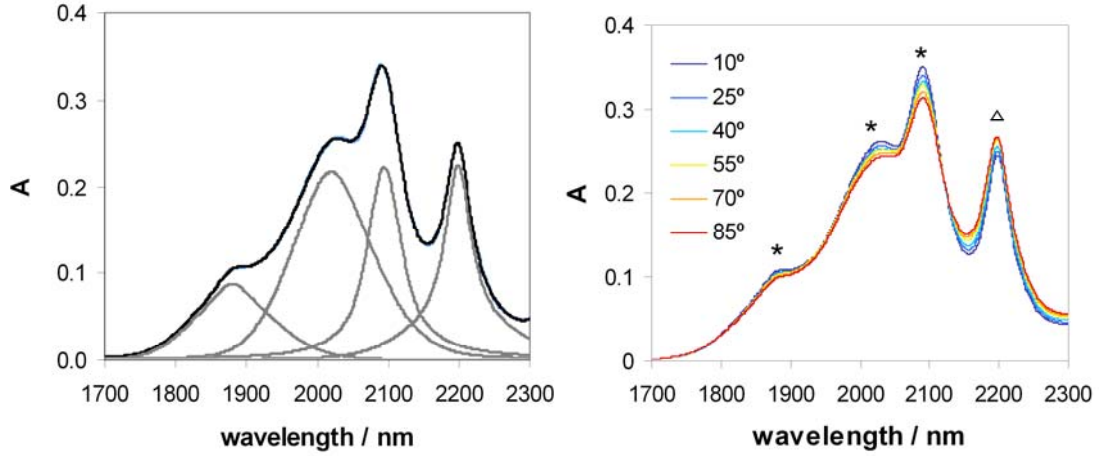


**Figure 2.4.** (Left side) NIR absorption spectrum of 7% wt Eu<sub>2</sub>O<sub>3</sub> doped glass (C3) and decomposition with four pseudo-Voigt bandshapes. The bands decomposition was made in energy. (Right side) NIR absorption spectra of 7% wt Eu<sub>2</sub>O<sub>3</sub> doped glass (C3) at different temperatures. \* represents the transitions that decrease with temperature and  $\Delta$  the one that increase with temperature.

In order to have an accurate calculation of the oscillator strength  $f_{\text{exp}}$ , to access the intensity of each electronic transition, it is necessary to have reliable data for wavelength dependent extinction coefficients. Such data, unfortunately, is not so easy to retrieve from absorption spectra taken from glass samples. At low wavelengths the glass matrix absorbs light, which prevents any possibility of studying the UV spectra of lanthanides in such hosts. Even in the visible region, problems arise from the baseline, due either to the presence of small impurities or light scattering from the glass. To overcome these experimental issues, the spectral band-shapes were decomposed and the area was calculated from those results.

To decompose the band shapes it was used Lorentzian curves (2.4), which suggest a natural broadening from the solute with little influence from the matrix (homogeneous broadening) and Gaussian curves (2.5) when the matrix influence in the electronic transition is strong (inhomogeneous broadening)

$$L(\nu, \sigma, \nu_{\text{max}}) = \frac{1}{\pi} \frac{\sigma/2}{(\nu - \nu_{\text{max}})^2 + (\sigma/2)^2} \quad (2.4)$$

$$G(\nu, \sigma, \nu_{\text{max}}) = \frac{1}{\sigma\sqrt{2\pi}} \exp\left[-\frac{1}{2}\left(\frac{\nu - \nu_{\text{max}}}{\sigma}\right)^2\right] \quad (2.5)$$

where  $\nu$  is the frequency,  $\sigma$  the band width and  $\nu_{\max}$  the frequency at the peak of the spectroscopic band. The decomposition of the absorption bands was made using the absorption spectra in wavenumber ( $\text{cm}^{-1}$ ) instead of wavelength.

When the bandshape can neither be fitted with equation (2.4) or equation (2.5), a transition between these two extreme cases is observed. The Voigth distribution can be applied to describe these cases, giving bandshapes that are a true mix between homogeneous and inhomogeneous broadening. The major drawback of Voigth distribution, however, is the inexistence of an analytical solution, which requires the careful use of numerical analysis procedures in order to correctly fit the experimental data. A pseudo-Voigth bandshape (equation 2.6) is therefore often used to solve this problem. Such bandshape is a linear combination of equations (2.4) and (2.5):

$$V_{pseudo}(\nu, \sigma, \nu_{\max}) = \alpha_L L(\nu, \sigma, \nu_{\max}) + \alpha_G G(\nu, \sigma, \nu_{\max}) = \alpha_L L(\nu, \sigma, \nu_{\max}) + (1 - \alpha_L) G(\nu, \sigma, \nu_{\max}) \quad (2.6)$$

where  $\alpha$  gives the contribution of each broadening process to the experimental bandshape.

All the electronic transitions analysed in the UV/Vis region are inhomogeneous and were decomposed using Gaussian curves; on the other hand the Near Infrared (NIR) transitions show also some degree of homogeneous broadening. The NIR transitions could then be decomposed with four pseudo-Voight bandshapes (see Figure 2.4 on the left side), indicating both homogeneous and inhomogeneous broadening.<sup>108</sup>

After the spectra decomposition it was possible to proceed to the calculations of the oscillator strength  $f_{\text{exp}}$ , based on experimental data, using equation 2.7:<sup>11</sup>

$$f_{\text{exp}} = 4.318 \times 10^{-9} \int \varepsilon(\nu) d\nu \quad (2.7)$$

where  $\varepsilon$  is the frequency dependent molar extinction coefficient and  $\nu$  is the energy (or wavenumber) in  $\text{cm}^{-1}$ . Experimental oscillator strength values ( $f_{\text{exp}}$ ) can be found in table 2.5. The values of  $f_{\text{cal}}$  that are discussed afterwards are also represented in table 2.5.



**Table 2.5.** Absorption band positions (in nm) and experimental ( $f_{exp}$ ) and calculated ( $f_{cal}$ ) oscillator strengths ( $\times 10^5$ ) for 7% Eu<sub>2</sub>O<sub>3</sub> doped glasses with different CaO concentrations (C1, C2, C3 and C4).

Transition	Band Position /nm	Oscillator strengths							
		C1		C2		C3		C4	
		$f_{exp}$	$f_{cal}$	$f_{exp}$	$f_{cal}$	$f_{exp}$	$f_{cal}$	$f_{exp}$	$f_{cal}$
$^7F_2 \rightarrow ^5D_0$	610	0.006	0.005	0.005	0.006	0.005	0.007	0.007	0.007
$^7F_1 \rightarrow ^5D_0$	588	0.020	-(a)	0.017	-(a)	0.018	-(a)	0.023	-(a)
$^7F_0 \rightarrow ^5D_0$	578	0.007	-(a)	0.005	-(a)	0.006	-(a)	0.008	-(a)
$^7F_1 \rightarrow ^5D_1$	533	0.110	0.126	0.111	0.138	0.123	0.158	0.133	0.173
$^7F_0 \rightarrow ^5D_1$	526	0.031	-(a)	0.032	-(a)	0.035	-(a)	0.037	-(a)
$^7F_0 \rightarrow ^5D_2$	465	0.274	0.266	0.304	0.292	0.348	0.333	0.380	0.364
$^7F_1 \rightarrow ^5D_3$	414	0.073	0.066	0.080	0.070	0.091	0.077	0.106	0.085
$^7F_1 \rightarrow ^5L_6$	403	0.130	0.091	0.127	0.094	0.117	0.123	0.116	0.165
$^7F_0 \rightarrow ^5L_6$	393	0.933	0.957	1.111	0.990	1.421	1.296	1.747	1.743
$^7F_1 \rightarrow ^5D_4$	366	0.048	0.027	0.050	0.028	0.053	0.030	0.058	0.033
$^7F_0 \rightarrow ^5D_4$	362	0.253	0.257	0.265	0.269	0.281	0.285	0.309	0.315

<sup>(a)</sup> Judd -Ofelt theory is only applied to electric-dipole transitions,<sup>70,71</sup> which is not the case in (a).

### Judd-Ofelt analysis of absorption spectra

In Table 2.6 are shown the experimental oscillator strength values ( $f_{exc}$ ) being the most intense ED transitions  $^7F_0 \rightarrow ^5L_6$  and  $^7F_0 \rightarrow ^7F_6$ . The  $^7F_0 \rightarrow ^5L_6$  is a hypersensitive electronic transition, and is greatly influenced by the crystal field of the surrounding medium.<sup>53,59,109,110,111</sup> The oscillator strengths for ED transitions can be rationalized according to the Judd-Ofelt theory as it was mentioned in chapter 1. Three phenomenological intensity parameters are considered ( $\Omega_\lambda$ , with  $\lambda=2, 4$  and  $6$ ), which are related with the dipole strength  $D$  of the electronic transition through equation 2.8:

$$D = \frac{1}{(2J+1)} \frac{(n^2+2)^2}{9n} e^2 \sum_{\lambda=2,4,6} \Omega_\lambda \left\langle f^N \Psi J \left\| U^{(\lambda)} \right\| f^N \Psi' J' \right\rangle^2 \quad (2.8)$$

$\left\langle f^N \Psi J \left\| U^{(\lambda)} \right\| f^N \Psi' J' \right\rangle$  are the reduced matrix elements and were previously calculated by Carnall et al.,<sup>107</sup>  $e$  is the elementary charge and  $n$  is the medium refraction index which should

be taken into account since the lanthanide ion is a dielectric medium and therefore, affected by polarizability interactions with the host glass.

The calculated oscillator strength,  $f_{\text{cal}}$ , can be calculated using the following equation, as it was demonstrated in chapter 1.

$$f_{\gamma_{F_J} \rightarrow \gamma_{L_J}} = \frac{8\pi n c}{3h X_{\gamma_{F_J}}(T)} \overline{\nu} D \quad (2.9)$$

Both experimental ( $f_{\text{exp}}$ ) and calculated ( $f_{\text{cal}}$ ) oscillator strengths for the Eu<sub>2</sub>O<sub>3</sub> doped glass samples with different CaO concentrations are given in Table 2.6. With these results, obtained from the absorption spectra, the Judd-Ofelt parameters were calculated (Table 2.6).

**Table 2.6.** Judd-Ofelt parameters (in  $10^{-20} \text{ cm}^2$ ) calculated for glasses with different wt% of CaO by fitting the experimental absorption.

Glass sample	CaO (wt%)	$\Omega_2 \pm 2.5$	$\Omega_4 \pm 2$	$\Omega_6 \pm 0.5$
C1	0	12.0	6.6	1.9
C2	5	11.2	5.9	1.6
C3	10	11.7	5.7	2.0
C4	15	12.3	6.1	2.9

These parameters are going to be discussed in the next subchapters.

### 2.3.3. Luminescence Spectroscopy

#### Steady-State Emission Spectra

Luminescence spectra of all the glasses were obtained exciting at 532 nm ( $^7F_1 \rightarrow ^5D_1$  transition), see Figure 2.5. These spectra are characterized by several peaks corresponding to transitions from Eu<sup>3+</sup>  $^5D_0$  state to  $^7F_n$  states ( $n = 0, 1, 2, 3, 4, 5, 6$ ). It is possible to observe that  $^5D_0 \rightarrow ^7F_2$  transition originates the most intense peak and non-permitted  $^5D_0 \rightarrow ^7F_0$  and  $^5D_0 \rightarrow ^7F_3$  peaks also appear in the spectrum, showing that J-J mixing is important on this system.<sup>59,111,112</sup> The  $^5D_0 \rightarrow ^7F_1$  transition presents three peaks, indicating three  $^7F_1$  Stark levels. This transition can give important information about the crystal field point group symmetry, depending on the number of peaks present on its emission band.<sup>53,100</sup>

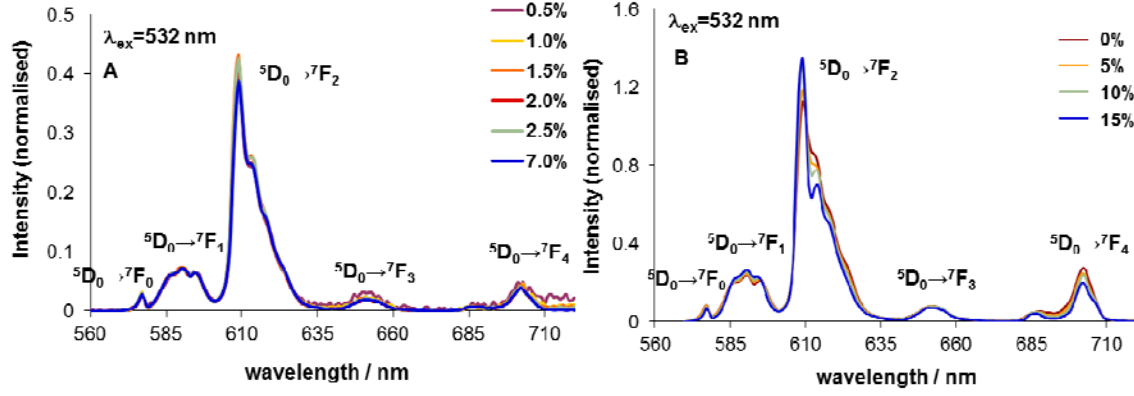


**Figure 2.5.** (A) Luminescence spectra of glasses with different Eu<sub>2</sub>O<sub>3</sub> concentrations (0.5, 1.0, 1.5, 2.0, 2.5 and 7.0%) and (B) luminescence spectra of 7% Eu<sub>2</sub>O<sub>3</sub> doped glasses with different CaO concentrations (0, 5, 10 and 15%),  $\lambda_{exc}=532$  nm. The spectra were normalised based on the total MD band area ( $^5D_0 \rightarrow ^7F_1$ ).

Comparing the normalized emission spectra for different Eu<sup>3+</sup> concentrations, no significant changes are observed. Main differences are indeed observed when CaO concentration is changed, mainly in the  $^5D_0 \rightarrow ^7F_2$  and  $^5D_0 \rightarrow ^7F_4$ , whilst other peaks remain almost unchanged. The emission of the state that is directly populated with 532 nm excitation,  $^5D_1$  state, is also observed, but its intensity is rather low compared with  $^5D_0$ .

#### Judd-Ofelt analysis via steady-state emission spectra: branching ratio

Emission spectra can also be analysed according to Judd-Ofelt theory. The probability of an ED transition in lanthanides ( $A_{ED}$ ) is given by:<sup>100</sup>

$$A_{ED} = \frac{64\pi^4 e^2 \bar{\nu}^3}{3h(2J+1)} \frac{n(n^2+2)^2}{9} \sum_{\lambda=2,4,6} \Omega_{\lambda} \left\langle f^N \Psi J \left\| U^{(\lambda)} \right\| f^N \Psi' J' \right\rangle^2 \quad (2.12)$$

where  $n$  is the refractive index of the medium,  $h$  the Planck's constant,  $e$  the electron charge in electrostatic unit,  $\bar{\nu}$  is the transition energy in cm<sup>-1</sup> and  $J$  the total angular momentum of the ground state.  $A_{ED}$  can be calculated through equation 2.12, when  $n$  and  $\Omega_{\lambda}$  are known. If those values are unavailable, it is possible to analyze individually each emission band.  $^5D_0 \rightarrow ^7F_2$  and  $^5D_0 \rightarrow ^7F_4$  emissions can be characterized under the Judd-Ofelt theory, since they are ED transitions and can be compared with the  $^5D_0 \rightarrow ^7F_1$  MD transition which for Eu<sup>3+</sup> is known to be almost independent of the environment and has a negligible ED mechanism; therefore, this MD transition is fairly constant.<sup>67</sup> The dependence of the magnetic dipole transition with the refractive index is

$$A_{MD} = \frac{64\pi^4 e^2 \bar{\nu}^3}{3h(2J+1)} n^3 D_{MD} \quad (D_{MDJ=1} = 9.4 \times 10^{-6} \text{ Debye}^2) \quad (2.13)$$

$$\beta_j = \frac{A_{ED}^j}{\sum_{i=1}^6 A_{ED}^i + A_{MD}^i} \quad (2.14)$$

$\beta_j$  is a branching ratio, giving the intensity of a  $j$  transition compared to other peaks of the luminescence spectra. It is, therefore, a value that can be accessed experimentally, and so a direct comparison between absorption spectra and luminescence spectra can be made. The branching ratio can be theoretically calculated, since  $A_{MD}$  value is independent of the medium.<sup>67</sup> Assuming  $D_{MD, J=1}$  taken from the literature, the remaining  $A$  are obtained in a simple way, see Table 2.7.

**Table 2.7.** Data analysis of the emission spectra of Figure 2.5 (B). Probability of  $^5D_0 \rightarrow ^7F_1$  MD transition ( $A_{MD, J=1}$ ), probability of different ED transitions ( $A_{ED}$ ) and experimental and calculated branching ratio ( $\beta_j$ ) for glass samples with different CaO concentrations.

Glass sample	CaO (wt%)	$A_{MD, J=1} / \text{ms}^{-1}$ a)	$A_{ED} / \text{ms}^{-1}$ b)		$\beta_j$			
			$^5D_0 \rightarrow ^7F_2$	$^5D_0 \rightarrow ^7F_4$	$^5D_0 \rightarrow ^7F_2$		$^5D_0 \rightarrow ^7F_4$	
					exp	calc	exp	calc
<b>C1</b>	0	50.8	166.1	19.3	0.67	0.70	0.08	0.08
<b>C2</b>	5	52.0	184.6	24.7	0.67	0.71	0.09	0.09
<b>C3</b>	10	53.1	192.5	27.9	0.66	0.70	0.09	0.10
<b>C4</b>	15	54.1	203.6	33.0	0.66	0.70	0.11	0.11

a) The  $A_{MD, J=1}$  value was calculated using  $D_{MD, J=1} = 9.4 \times 10^{-6} \text{ Debye}^2$ <sup>107</sup> and was used to calculate other parameters. b) Calculations performed using  $n$  values of table 2.3.

$\Omega_\lambda$  can now be calculated,<sup>100</sup> considering that MD mechanism is negligible for other transitions.

$$\Omega_\lambda = \frac{A_{J=\lambda}}{A_{J=1}} \frac{9n^2}{(n^2 + 2)^2} \left( \frac{\bar{\nu}_\lambda}{\bar{\nu}_{J=1}} \right)^3 \frac{D_{J=1}^{MD}}{\langle f^N \Psi J \| U^{(\lambda)} \| f^N \Psi J' \rangle} \quad (2.15)$$

$A_{J=\lambda}/A_{J=1}$  is an experimental value that can be calculated by the integral intensity ratio of each transition over the MD transition. The refraction index,  $n$ , can be retrieved from table 2.3 and  $U^{(\lambda)}$  from references 73 and 113.

The radiative lifetime of Eu<sup>3+</sup> can also be calculated using this available experimental data:

$$\tau_r = \frac{1}{\sum_{i=1}^6 A_{ED}^i + A_{MD}^i} \quad (2.16)$$

This is the expected luminescence lifetime if the luminescence quantum yield was one. Lower luminescence lifetimes indicate luminescence quenching of Eu<sup>3+</sup>.

However the most accurate way to perform  $\Omega_\lambda$  calculation is to consider the area of the emission peak rather than its intensity maximum, in order to account for different band shapes. Thus the experimental values shown in Table 2.8 are calculated with the area of the emission peaks. Previous studies showed that  $\Omega_2$  values should be significantly high, taking into account published results for  $I(^5D_0 \rightarrow ^7F_2)/I(^5D_0 \rightarrow ^7F_1)$  ratios.<sup>114</sup>

**Table 2.8.** Judd-Ofelt parameters (in  $10^{-20} \text{ cm}^2$ ) calculated for glasses with different wt% of CaO by fitting the experimental steady state emission

Glass sample	CaO (wt %)	$\Omega_2 \pm 0.5$	$\Omega_4 \pm 0.2$
C1	0	5.2	1.3
C2	5	5.7	1.6
C3	10	5.8	1.7
C4	15	6.0	2.0

$\Omega_2$  and  $\Omega_4$  values are calculated from emission spectra with a much higher accuracy than by absorption spectroscopy measurements since they are obtained using the MD transition, which is an internal calibrator of the emission spectra. Both Judd-Ofelt parameters increase with CaO concentration, but on the other hand there is a mismatch between these data and those obtained from the absorption spectra. This mismatch cannot be attributed to errors in the absorption spectra (which would be mainly from baseline corrections) since its difference is rather high. There is an inconsistency between the results, so this is going to be analyzed with the time-resolved data.

### Time-Resolved Luminescence

The luminescence decays, obtained using Flash Photolysis technique, spans across four timescale decades and two time regions are distinguished. It is observed in the microsecond timescale an internal conversion between  $^5D_1$  and  $^5D_0$ , but the relaxation of  $^5D_1$  also gives rise to decays at wavelengths such as 525 nm ( $^5D_1 \rightarrow ^7F_0$ ), 532 nm ( $^5D_1 \rightarrow ^7F_1$ ) and 550 nm ( $^5D_1 \rightarrow ^7F_2$ ), see figure 2.6 and figure 2.7. On the other hand, at 609 nm a time rise is clearly observed, with the growth starting from zero intensity (see figure 2.6).

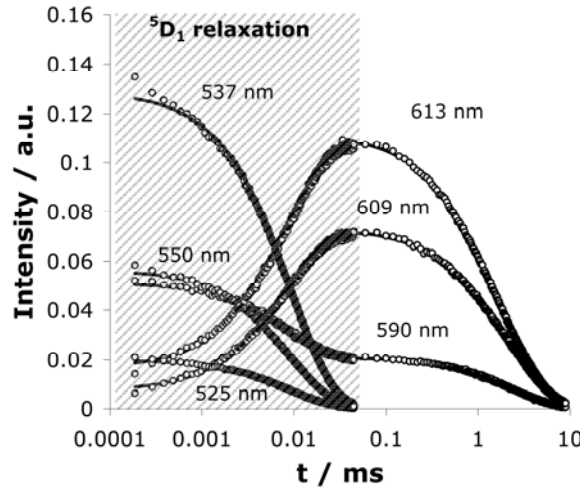


**Figure 2.6.** Luminescence decays at single wavelengths of glass C4, with 7% of Eu<sub>2</sub>O<sub>3</sub> and 15% CaO (wt %),  $\lambda_{\text{exc}}=532$  nm.

Figure 2.7 shows the energy levels identified from luminescence decays of Eu<sup>3+</sup>. It is observed the relaxation of <sup>5</sup>D<sub>1</sub> after excitation and the decays from <sup>5</sup>D<sub>0</sub> to <sup>7</sup>F<sub>n</sub> afterwards.

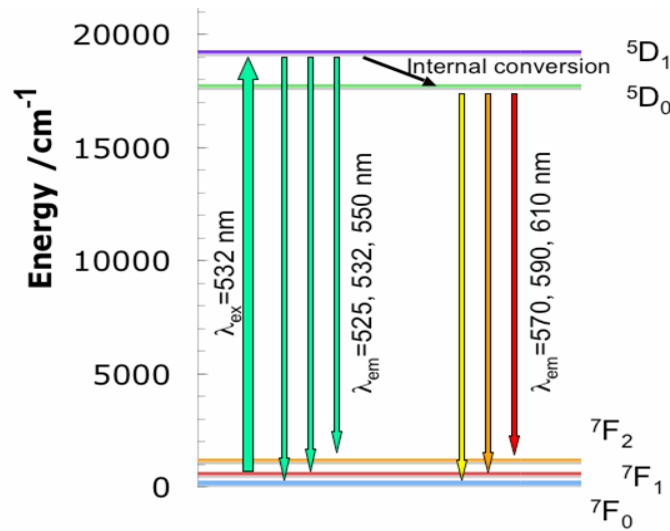


**Figure 2.7.** Schematic energy-level of Eu<sup>3+</sup>

Single exponential kinetics does not fully describe the Eu<sup>3+</sup> luminescence at each timescale. To obtain good residuals the decays had to be fitted with the sum of two exponentials for each wavelength:

$$I(t, \lambda) = a_1(\lambda)e^{-\frac{t}{\tau_1}} + a_2(\lambda)e^{-\frac{t}{\tau_2}} \quad (2.17)$$

where  $a$  are the pre-exponential values and  $\tau$  are the lifetimes. In order to understand what gives rise to these experimental results, luminescence decays of glass samples with different Eu<sub>2</sub>O<sub>3</sub> concentrations (**E2**- 0.5%, **E3**- 1%, **E5**- 2% and **C3**- 7% of Eu<sub>2</sub>O<sub>3</sub>) and with different CaO

concentrations (**C1**- 0%,**C2**- 5%,**C3**- 10% and **C4**- 15% of CaO) were performed on the ms timescale, from  $^5D_0$  excited state (see figure 2.8).

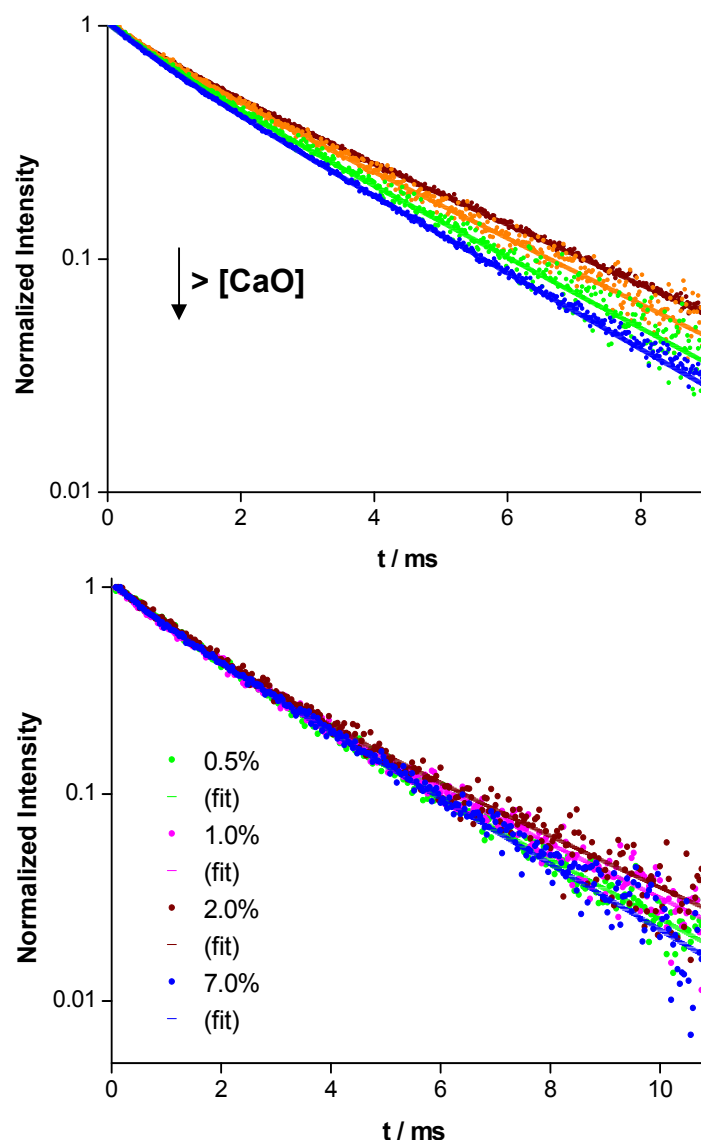


**Figure 2.8.** (Up) Luminescence decays of glasses with  $\text{Eu}^{3+}$  (7 wt%) and CaO (0 to 15%, wt%) at 609 nm. (Bottom) Luminescence decays of glasses with different  $\text{Eu}^{3+}$  concentrations (0.5, 1, 2 and 7%, wt%) at 609 nm.

Once more it is possible to observe that the luminescence decays obtained display a non-exponential relaxation back to the ground state and also that the kinetics changes with CaO and  $\text{Eu}_2\text{O}_3$  concentrations. Two different models can explain this deviation from exponential relaxation, the first one is the existence of homomolecular resonance energy transfer (RET) between  $\text{Eu}^{3+}$ , but this phenomenon was rejected because the luminescence decays are fairly independent of  $\text{Eu}^{3+}$  concentration, excitation and emission wavelength. The very low molar absorptivity of  $\text{Eu}^{3+}$  and therefore the negligibly low rate constant of RET in this case may justify the absence of homomolecular RET. The second model is the presence of more than one population of  $\text{Eu}^{3+}$  present in the glass. A distribution of locations for the europium in the glass matrix can exist, which would then give rise to a distribution of luminescence lifetimes and,

hence, to a non-exponential decay. This case has been pointed out in many studies where stretched exponential relaxations were used to explain the experimental data.<sup>115</sup> The impact of such distribution on the absorption spectra, however, would be discernible with a depart from Lorentzian band shapes to Gaussian band shapes. The NIR experiments do not support such assumption, since the absorption bands still preserve a strong Lorentzian character. Another possibility is that the number of populations is greatly reduced to about 2 or 3 species, which would reflect different locations in the glass matrix, and hence some crystallinity is retained at the nanoscopic level. In such case, the luminescence relaxation would be fitted with a sum of two or three exponentials, like it happens in our case study.

All the luminescence decays obtained for our glass samples were fitted using a sum two exponentials (equation 2.17) in order to obtain good residuals and two different lifetimes were calculated using luminescence decays at different wavelengths (in the 575-635 nm range with intervals of 1 nm) for each glass sample (table 2.9). The shortest component lifetime decreases from 1.6 ms (0.5% of Eu<sub>2</sub>O<sub>3</sub>, glass E2) to 0.9 ms (7% of Eu<sub>2</sub>O<sub>3</sub>, glass C3), showing a self-quenching effect. The longest lifetime component has only an appreciable effect for the higher europium concentration.

**Table 2.9.** Lifetimes,  $\tau_i$ , obtained by tetra-exponential decay fittings of the glasses 7% of Eu<sub>2</sub>O<sub>3</sub> and with different CaO concentrations and by bi-exponential decay fittings of glasses with 10% of CaO and different Eu<sub>2</sub>O<sub>3</sub> concentrations.

Glass sample	CaO (wt%)	Eu <sub>2</sub> O <sub>3</sub> (wt%)	<sup>5</sup> D <sub>1</sub> → <sup>5</sup> D <sub>0</sub>		<sup>5</sup> D <sub>0</sub> → <sup>7</sup> F <sub>n</sub>	
			$\tau_1/\mu\text{s}$	$\tau_2/\mu\text{s}$	$\tau_1/\text{ms}$	$\tau_2/\text{ms}$
C1	0	7	6.3	10.9	0.99	3.38
C2	5	7	7.8	12.2	0.91	3.09
C3	10	7	8.3	11.8	0.96	2.87
C4	15	7	5.4	11.2	0.91	2.67
E2	10	0.5	—	—	1.56	3.39
E3	10	1	—	—	1.48	3.54
E5	10	2	—	—	1.34	3.38

The pre-exponential factors of the decay from <sup>5</sup>D<sub>0</sub> show that each component has a different spectral signature (see Figure 2.9). The shortest decay (with a lifetime of about 0.9 ms) clearly has a higher ratio between <sup>5</sup>D<sub>0</sub>→<sup>7</sup>F<sub>2</sub> and <sup>5</sup>D<sub>0</sub>→<sup>7</sup>F<sub>1</sub> emission peaks than the component with longer lifetime (around 3 ms).



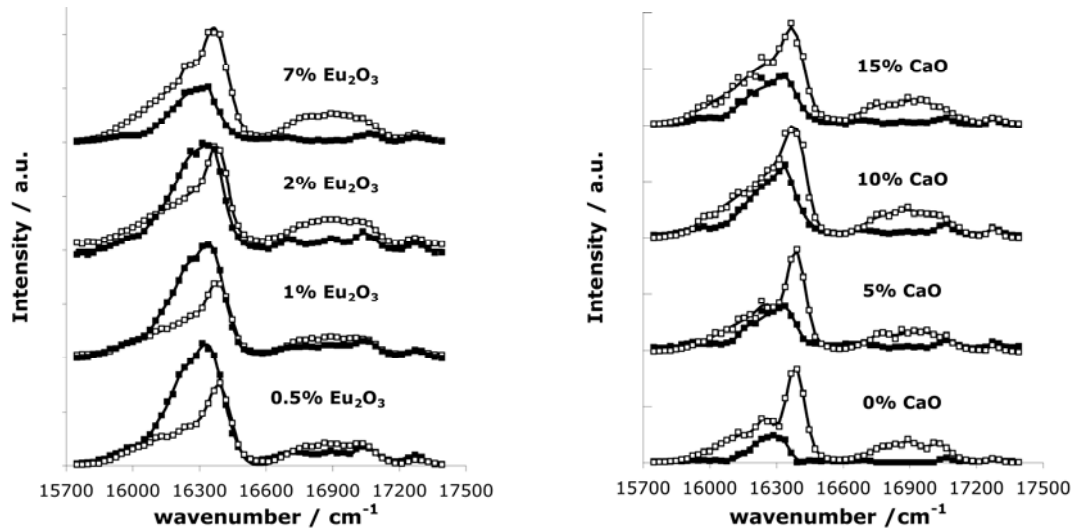


**Figure 2.9.** Luminescence pre-exponential factors spectrum using different conditions, according to bi-exponential analysis for the  $^5D_0 \rightarrow ^7F_n$  decay, for glass samples with different  $\text{Eu}_2\text{O}_3$  concentrations and with different CaO concentrations. White squares – Long component; Black squares – Short component.

Taking these pre-exponential factors as individual spectra of each component of the luminescence decay at different wavelengths, it is possible to estimate  $\Omega_2$  values (by calculating areas), which are presented in Table 2.10.

**Table 2.10.** Judd-Ofelt parameters (in  $10^{-20} \text{ cm}^2$ ) calculated for glasses with different wt% of CaO by fitting the time-resolved emission spectra.

Glass sample	CaO (wt%)	$\Omega_2$ short lifetime	$\Omega_2$ long lifetime
C1	0	10.6	4.5
C2	5	7.2	5.1
C3	10	11.6	4.7
C4	15	10.3	4.7

While the short component clearly shows a value consistent with the results from absorption spectroscopy, the long component is consistent with the steady-state emission data. This shows different bonds between  $\text{Eu}^{3+}$  and oxygen for the two species, with a more covalent character for the species prevalent in glass samples with lower europium concentration.

### 2.3.4. Spectroscopic measurements analysis and discussion

In the absorption spectra, the  $^7F_0 \rightarrow ^5D_2$  transition splits into two peaks and an isosbestic point is observed at 463 nm (see insert on Figure 2.3 on the top). Increasing CaO composition enhances the intensity of the 466 nm peak, and the separation between the two peaks decreases from 109 to 83  $\text{cm}^{-1}$ . The peak at 464 nm is less sensitive to the environment here

investigated, but it gets broader with its FWHM increasing from about 55 cm<sup>-1</sup> to 80 cm<sup>-1</sup>. The other peak (466 nm) also gets broader with increasing CaO concentration. Inhomogeneous broadening seems therefore to increase with CaO, indicating a more heterogeneous environment. The number of Stark levels is at least two, but the broadening may indicate more Stark levels buried within each peak.  ${}^7F_0 \rightarrow {}^5D_1$  transition does not split, but the asymmetrical broadening shows the presence of more than one Stark level. Decomposition of the peak is achieved with two inhomogeneous distributions, leading to the conclusion that two Stark levels are enough to characterize this transition from the experimental data available. Under such assumption, hexagonal, pentagonal or tetragonal group symmetry of the ligand crystal field is hinted (see table 2.11).<sup>53, 59, 99, 110, 111</sup>

**Table 2.11.** Number of energy J-sublevels in a given point symmetry vs. the quantum number J <sup>(a)</sup>

Symmetry	J						
	0	1	2	3	4	5	6
Icosahedral	1	1	1	2	2	3	4
Cubic O <sub>h</sub> , O, T <sub>d</sub> , T <sub>h</sub> , T	1	1	2	3	4	4	6
Hexagonal D <sub>6h</sub> , D <sub>6</sub> , C <sub>6v</sub> , C <sub>6h</sub> , C <sub>6</sub> , D <sub>3h</sub> , C <sub>3h</sub> , D <sub>3d</sub> , D <sub>3</sub> , C <sub>3v</sub> , S <sub>6</sub> , C <sub>3</sub>	1	2	3	5	6	7	9
Pentagonal D <sub>5h</sub> , C <sub>5h</sub> , C <sub>5v</sub> , C <sub>5</sub> , D <sub>5</sub>	1	2	3	4	5	7	8
Tetragonal D <sub>4h</sub> , D <sub>4</sub> , C <sub>4v</sub> , C <sub>4h</sub> , C <sub>4</sub> , D <sub>2d</sub> , S <sub>4</sub>	1	2	4	5	7	8	10
Low D <sub>2h</sub> , D <sub>2</sub> , C <sub>2v</sub> , C <sub>2h</sub> , C <sub>2</sub> , C <sub>s</sub> , S <sub>2</sub> , C <sub>1</sub>	1	3	5	7	9	11	13

(a) Table taken from reference 53.

The splitting of the  ${}^7F_0 \rightarrow {}^5D_2$  into two peaks indicates therefore a D<sub>3</sub>, D<sub>2d</sub>, C<sub>6v</sub>, C<sub>6</sub>, C<sub>4v</sub> or C<sub>4</sub> group symmetry for the present system. Since  ${}^7F_0$  is a non-degenerated state, the energy difference between the peaks directly measures the difference between Stark energy levels on the  ${}^5D_2$  and  ${}^5D_1$  state, indicating that for the case of  ${}^5D_2$  the effect of adding CaO directly changes the energy levels. However the forbidden  ${}^7F_0 \rightarrow {}^5D_0$  is also present on the absorption spectra. This transition appears due to J-J mixing with the ED transition  ${}^7F_2 \rightarrow {}^5D_0$ , a mechanism present for C<sub>s</sub>, C<sub>n</sub> and C<sub>nv</sub> symmetries. By comparison, only C<sub>6v</sub>, C<sub>6</sub>, C<sub>4v</sub> or C<sub>4</sub> group symmetry would be possible to explain the data. However the presence of an extra Stark level in the  ${}^7F_0 \rightarrow {}^5D_1$  transition cannot completely be ruled out. In such case, a C<sub>2v</sub> or C<sub>2</sub> group could also be a possibility. Examining now the emission spectra, the presence of the  ${}^5D_0 \rightarrow {}^7F_0$  peak is striking with the CaO addition, although with relatively low intensity, indicating a C<sub>s</sub>, C<sub>n</sub> or C<sub>nv</sub> symmetry group, however the three peaks for the  ${}^5D_0 \rightarrow {}^7F_1$  are only consistent with C<sub>2v</sub>, C<sub>2</sub> or C<sub>s</sub> point symmetry groups. In conclusion, while in the absorption spectra only 2 peaks seem to explain the  ${}^7F_0 \rightarrow {}^5D_1$  transition indicating an hexagonal, pentagonal or tetragonal group symmetry, the 3

peaks in the  ${}^5D_0 \rightarrow {}^7F_1$  of the emission points out a lower symmetry and from this analysis there can exist some incongruence between the two sets of experimental results.

The time-resolved spectra shows the existence of two different species that appear as the lanthanide concentration increases and curiously the time-resolved spectra show that  ${}^5D_0 \rightarrow {}^7F_1$  transition has a different behaviour for the short and long component. Indeed the three peaks, consistent with  $C_{2v}$ ,  $C_2$  or  $C_s$ , are observed for the species with longer lifetime, but the short lifetime species shows two peaks, congruent with  $C_{6v}$ ,  $C_6$ ,  $C_{4v}$  or  $C_4$  group symmetry. In sum the two species observed in time-resolved emission measurements belong to different point symmetry groups.

Concerning the lifetimes obtained from the luminescence decays a self-quenching effect is detected hinting for a mechanism in which excited state energy is transferred from one species to another species, in this case from species with shortest luminescence lifetime to species with longer luminescence lifetime. The best candidate for such effect is the formation of clusters of Eu<sub>2</sub>O<sub>3</sub> within the glass matrix.<sup>100,101,102</sup> The longest lifetime would be assigned to luminescence from these aggregates, while the shortest component would be due to Eu<sup>3+</sup> isolated in the glass matrix. Under such assumption, the self-quenching effect would arise from the energy-transfer of isolated Eu<sup>3+</sup> species to those in the aggregates that behave as traps of this energy. Evidence for the existence of such traps can be traced into the self-quenching effect. Under resonance energy transfer formalisms, the efficiency  $E$  of energy transfer is defined by the following equation:<sup>116</sup>

$$E = 1 - \frac{\tau_0}{\tau} = \frac{1}{1 + \left(\frac{R}{R_0}\right)^6} \quad (2.18)$$

where  $R_0$  is a critical distance in which  $E$  is equal to 0.5 (this means donor equal probability for emission and energy transfer processes). In a glass system there is no fixed distance  $R$  between donors and acceptors, a problem solved by Forster who derived the following equation:<sup>117</sup>

$$E = \sqrt{\pi} x e^{x^2} (1 - \text{erf}(x)) \quad (2.19)$$

with:

$$x = \frac{1}{2} \sqrt{\pi} \left(\frac{R_0}{R}\right)^3 \quad (2.20)$$

Analysing the self-quenching effect under such formalism enables the determination of  $R_0$  (see Figure 2.10). The obtained value, around 1 nm, is rather large for lanthanide ions where extinction coefficients are too low to allow values higher than 0.5 nm. This result corroborates

the conclusion that Eu<sup>3+</sup> aggregates act as traps, since their overall extinction coefficient will be higher (due to the presence of large numbers of europium ions) giving  $R_0$  with values that could reach magnitudes over 1 nm depending on the size of such aggregates. This phenomenological result may also point out to some intrinsic heterogeneous character of the Eu<sup>3+</sup> solubility in the glass, which could give rise to domains where local concentrations of the lanthanide are higher than the bulk concentration, in which case the  $R_0$  value is overestimated.

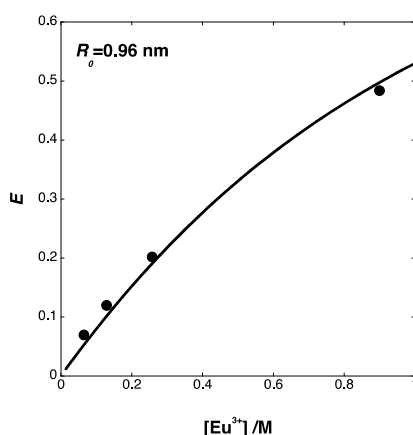


**Figure 2.10.** Fitting of the energy transfer efficiency calculated with the shortest component of the  $^5D_0 \rightarrow ^7F_n$  decay (see Table 2.9), using eq. 2.18 and eq. 2.19 for glasses changing Eu<sup>3+</sup> concentration.

By comparing between different CaO concentrations with 7% Eu<sub>2</sub>O<sub>3</sub>, the shortest lifetime is fairly constant while the longest lifetime changes. Since  $\Omega_2$  does not change appreciably (at least within experimental error), and according with the europium aggregate hypothesis, this would mean a change on the luminescence quantum yield in the aggregates when CaO concentration increases. The longest component has also less impact when CaO concentration increases. This result might indicate some disaggregation effect when CaO is added into the glass matrix, a process that could be linked with the higher covalent character of oxygen as seen from molar refractivity results. In this case, Ca<sup>2+</sup> would compete with Eu<sup>3+</sup> in order to form bonds with oxygen, decreasing the amount of europium aggregates in the glass.

The isolated Eu<sup>3+</sup> experiences a higher symmetry of the crystal field of the matrix, with higher covalent character bonds with oxygen compared with Eu<sup>3+</sup> aggregates. These differences explain why luminescence lifetimes of the two species are easily distinguishable in our experimental design. In other glasses where europium is not so strongly bonded to oxygen, the luminescence lifetimes would not be so different, which would give single exponential decays.

## **2.4. Conclusions**

To better understand how the europium concentration and the glass composition influence the europium distribution and the clustering behaviour, consequently how influences the photoluminescence colour two sets of Eu<sub>2</sub>O<sub>3</sub> doped luminescent glasses were synthesized. The first set was made using different CaO concentrations and the other with different Eu<sub>2</sub>O<sub>3</sub> concentrations.

Time resolved luminescence studies of Eu<sup>3+</sup> in soda-lime silicate glass shows the existence of two different species that appear as the lanthanide concentration increases. The results point out to the formation of Eu<sup>3+</sup> aggregates that act as traps of excitation energy within the matrix, rendering different Judd-Ofelt parameters between absorption and emission spectroscopy measurements. On the other hand some disaggregation effects seem to occur when CaO is added into the glass matrix. The isolated Eu<sup>3+</sup> experiences a higher symmetry of the crystal field of the matrix, with higher covalent character bonds with oxygen compared with Eu<sup>3+</sup> aggregates. These differences explain why luminescence lifetimes of the two species are easily distinguishable in our experimental design. In other glasses where europium is not so strongly bonded to oxygen, the luminescence lifetimes would not be so different, which would give single exponential decays. Therefore time-resolved luminescence measurements can only distinguish the two species in glasses displaying  $\Omega_2$  values higher than about  $10 \times 10^{-20} \text{ cm}^2$ . This study leads to a better understanding of this glass system, showing that europium ions have less clustering tendency when Eu<sub>2</sub>O<sub>3</sub> concentration decreases and when CaO concentration increases in a soda-lime silicate glass composition.

This knowledge can be useful for the development of luminescent glasses to be used in different areas, inclusive in artworks. Concluding it is not possible to use a very high europium concentration in this glass synthesis because the clustering of the lanthanide will increase and as a result photoluminescence will decrease. Still the increase of CaO content in the glass composition can decrease this clustering tendency. Artists normally search for intense colours, thus in the production of luminescent glasses to be used in the art field it has to be taken in account this clustering tendency when a very high concentration of europium is used.



## Chapter 3 – Synthesis of luminescent glasses using different lanthanides

In chapter 2 one lanthanide (europium) was used to obtain luminescent glasses and also to obtain a better structural understanding of this particular glass system. In this chapter the same glass composition was doped with a mixture of different lanthanide oxides in order to increase the luminescence colour palette and also to obtain white luminescence. Luminescence colour coordinates were calculated for all the synthesized glasses.

### 3.1. Lanthanide oxides in glass

“Smart materials” is a relatively new term for materials that are able to reversibly change their shape or colour in response to physical and/or chemical influences.<sup>8</sup> Besides the lanthanides numerous technological applications, such as catalysts in steels as dioxidizers and desulphurizers, as magnets in security applications, in light emitting diodes, in biomedical imaging and also in lasers,<sup>118,119,120</sup> lanthanides can also be applied in “smart materials” when doping glasses in order to give rise to different luminescent colours under a UV-light. Diverse investigations were made using different lanthanides in different materials exploring the development of materials with different luminescent colours.<sup>121,122,123,124,125,126,127,128,129,130,131,132</sup>

Photoluminescent glass material with different colours can be obtained by changing the lanthanide dopant and the composition of the glass matrix.<sup>11</sup> The production of glasses with different luminescent colours can be very attractive in the art field due to the diverse and strong colours that can be achieved.

In this chapter, studies of luminescence of glasses containing different lanthanide oxides are presented. The luminescence of terbium (III), cerium (III) and europium (III) doped glasses are going to be studied in more detail. Figure 3.1 illustrate that these lanthanides in oxidation state 3+ emit in the green, blue and red part of the spectra. Doping the glass with a mixture of these lanthanides, a varied colour palette can be produced and it is also possible to generate white luminescence. White luminescence in glass and ceramics was, in the last years, subject of several investigations due to its possible application in white light emitting diodes (W-LED).<sup>133,134,135</sup> The W-LED have been considered as new generation of illumination source, due to their many advantages when compared with incandescent and fluorescent lighting such as higher energy efficiency, longer life and reliability and low temperature of performance, reducing the energy consumption when this LED-based luminaries replace other lightning sources.<sup>136,137</sup>

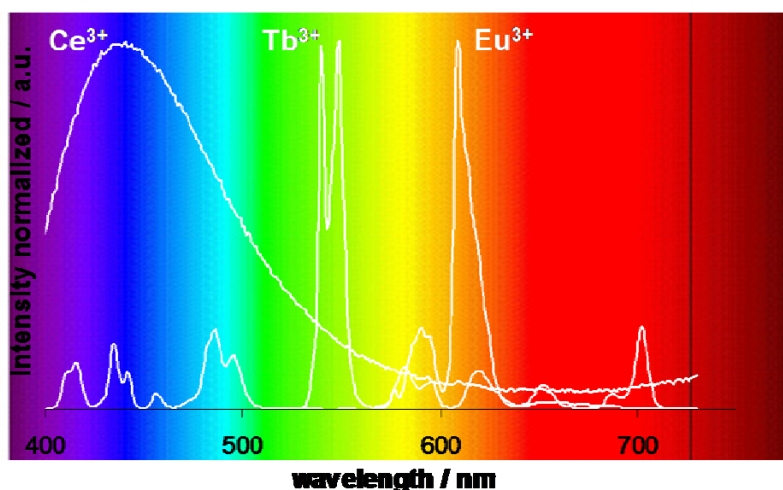


**Figure 3.1.** Electromagnetic spectrum in the visible region and emission spectra of  $\text{Ce}^{3+}$ ,  $\text{Tb}^{3+}$  and  $\text{Eu}^{3+}$  doped soda-lime silicate glasses ( $\lambda_{\text{exc}} = 377\text{nm}$ ).

In the case of  $\text{Tb}^{3+}$ , luminescence essentially arises from the  $^5\text{D}_4$  electronic level. Each emission line corresponds to a radiative deactivation from a  $^5\text{D}_4$  excited state to  $^7\text{F}_n$  ( $n=0$  to  $6$ ) “ground” state. A strong emission is observed, due to the transitions  $^5\text{D}_4 \rightarrow ^7\text{F}_6$  and  $^5\text{D}_4 \rightarrow ^7\text{F}_5$ , which are mainly in the green spectral region around  $490\text{ nm}$  and  $545\text{ nm}$ , respectively. But if  $^5\text{D}_4 \rightarrow ^7\text{F}_6$  transition shows some sensitivity to the environment on the other hand the transition  $^5\text{D}_4 \rightarrow ^7\text{F}_5$  has a strong magnetic dipole character which intensity is rather insensitive to the environment (it only changes with the medium refractivity index).<sup>11,53</sup> There are also  $\text{Tb}^{3+}$  emission lines at  $414$ ,  $436$  and  $460\text{ nm}$  that correspond to  $^5\text{D}_3 \rightarrow ^7\text{F}_5$ ,  $^5\text{D}_3 \rightarrow ^7\text{F}_4$  and  $^5\text{D}_3 \rightarrow ^7\text{F}_3$  electronic transitions, respectively.<sup>138</sup> Cerium in the trivalent state usually emits in the ultraviolet or in the blue spectral region. Electric-dipole transitions between the  $4f$  ground state and the  $5d$  excited state of  $\text{Ce}^{3+}$  are parity allowed and have large oscillator strength. Contrarily to what happens with the other lanthanides in the trivalent form, cerium shows a broad band in the luminescence spectra that corresponds to the  $5d$ - $4f$  emission.<sup>11,139</sup> Finally,  $\text{Eu}^{3+}$ , as it was mentioned in chapter 2, displays an intense orange luminescence with several emissions lines for wavelengths above  $570\text{ nm}$ . The most important emission lines are the  $^5\text{D}_0 \rightarrow ^7\text{F}_1$ , with a peak around  $590\text{ nm}$ , that is a magnetic dipole transition,<sup>11,67</sup> and the hypersensitive  $^5\text{D}_0 \rightarrow ^7\text{F}_2$  electronic transition that depends critically on the environment, with a peak around  $610\text{ nm}$ .

In this chapter several glasses doped with a mixture of different lanthanide oxides (essentially terbium, cerium and europium oxide) in different concentrations were synthesized in order to increase the colour palette and obtain white luminescence and therefore to develop new materials that may have several applications, but in particularly that could be used in the art field. The luminescence colour coordinates of all the synthesized glasses were determined.



### 3.2. Experimental Part

#### 3.2.1 Synthesis and samples preparation

Glasses doped with one lanthanide were synthesized adding into the same base composition of soda-lime-silicate glass, 74SiO<sub>2</sub>.16NaO.10CaO (wt %), 2% of the different lanthanide oxides, such as Eu<sub>2</sub>O<sub>3</sub>, Tb<sub>4</sub>O<sub>7</sub>, CeO<sub>2</sub>, Sm<sub>2</sub>O<sub>3</sub>, Dy<sub>2</sub>O<sub>3</sub> and Tm<sub>2</sub>O<sub>3</sub>. Mixtures of Eu<sub>2</sub>O<sub>3</sub>, Tb<sub>4</sub>O<sub>7</sub> and CeO<sub>2</sub> in different concentrations were also doped into the same composition, see table 3.1. Approximately 30 g batches were mixed and melted in platinum crucibles in an electric furnace at 1400 °C for 3 hours in air. The quantity of oxides used to prepare the different glass compositions can be found in section 9.2.1, Supplementary Material. Reagent grade SiO<sub>2</sub> (p.a., Fluka), CaCO<sub>3</sub> (p.a., Panreac), Na<sub>2</sub>CO<sub>3</sub> (p.a., Riedel de Haen) and the lanthanide oxides Eu<sub>2</sub>O<sub>3</sub>, Tb<sub>4</sub>O<sub>7</sub>, CeO<sub>2</sub>, Sm<sub>2</sub>O<sub>3</sub>, Dy<sub>2</sub>O<sub>3</sub> and Tm<sub>2</sub>O<sub>3</sub> (99.9%, Metall Rare Earth Limited) were used as starting materials in all the synthesized glasses. The melted glasses were quenched pouring them into a metal sheet at room temperature and further annealed at ca. 550°C for one hour. The glass samples were cut and carefully polished, for optical measurements, with 0.7 cm thickness and 0.8 cm width.

The glass compositions in the binary system were calculated in mol, to have the same lanthanide fraction in all the three binary systems (Eu<sub>2</sub>O<sub>3</sub>/Tb<sub>4</sub>O<sub>7</sub>, Eu<sub>2</sub>O<sub>3</sub>/CeO<sub>2</sub> and Tb<sub>4</sub>O<sub>7</sub>/CeO<sub>2</sub>).

**Table 3.1.** Composition of the soda-lime-silicate glasses doped with different lanthanide oxides (wt%). Glasses doped with only one (Mono system), with a mixture of two (Binary system) and with a mixture of three (Ternary system) lanthanides oxides- Tb<sub>4</sub>O<sub>7</sub>, Eu<sub>2</sub>O<sub>3</sub> and CeO.

Base Composition	Group	Glass sample	Composition (wt %)		
			Tb <sub>4</sub> O <sub>7</sub>	Eu <sub>2</sub> O <sub>3</sub>	CeO
74% SiO <sub>2</sub> + 16% Na <sub>2</sub> O + 10% CaO	Mono	M1_1	1.0	-	-
		M1_2	2.0	-	-
		M2_1	-	1.0	-
		M2_2	-	2.0	-
		M3_1	-	-	1.0
		M3_2	-	-	2.0
	Binary Eu+Tb	BET1	1.0	3.76	-
		BET2	1.0	1.85	-
		BET3	1.0	1.0	-
		BET4	2.0	2.0	-
		BET5	2.0	0.94	-
		BET6	2.0	0.62	-
	Binary Tb+Ce	BTC1	3.3	-	1.0
		BTC2	2.2	-	1.0
		BTC3	1.0	-	1.0
		BTC4	2.0	-	2.0
		BTC5	1.0	-	2.0
		BTC6	0.55	-	2.0
	Binary Eu+Ce	BEC1	-	4.0	1.0
		BEC2	-	2.0	1.0
		BEC3	-	1.0	1.0
		BEC4	-	2.0	2.0
		BEC5	-	1.0	2.0
		BEC6	-	0.68	2.0

74% SiO <sub>2</sub> + 16% Na <sub>2</sub> O + 10% CaO	Ternary [Tb]	TTb0.2	0.2	1.0	1.0
		TTb0.5	0.5	1.0	1.0
		TTb1	1.0	1.0	1.0
		TTb1.5	1.5	1.0	1.0
		TTb2	2.0	1.0	1.0
		TTb2.5	2.5	1.0	1.0
		TTb3	3.0	1.0	1.0
		TTb3.5	3.5	1.0	1.0
		TTb4.5	4.5	0.5	0.5
	Ternary [Eu]	TEu0.2	1.0	0.2	1.0
		TEu0.5	1.0	0.5	1.0
		TEu2	1.0	2.0	1.0
		TEu3	1.0	3.0	1.0
		TEu4.5	0.5	4.5	0.5
	Ternary [Ce]	TCe0.2	1.0	1.0	0.2
		TCe0.5	1.0	1.0	0.5
		TCe2	1.0	1.0	2.0
		TCe3	1.0	1.0	3.0
		TCe4.5	0.5	0.5	4.5

### 3.2.2. Measurements

Absorption spectra were recorded using a Varian Cary-5000 UV/VIS/NIR spectrophotometer over the 300-2300 nm wavelength range with a 1 nm resolution for all the glass samples. Luminescence spectra were measured using a SPEX Fluorolog-3 Model FL3-22 spectrofluorimeter, with 1 nm spectral resolution. Experiments were performed at room temperature (21°C). The emission spectra were corrected with the absorption value using equation 3.1.

$$I_{corr} = A \times I_{obs} (1 - 10^{-A}) \quad (3.1)$$

The glass transition temperature ( $T_g$ ), the softening temperature ( $T_s$ ) and the coefficients of thermal expansion (CTE) were measured using a Netvcshe Dil402PC dilatometer in a temperature range of 20-750°C, with a heating rate of 5 K.min<sup>-1</sup>. The  $T_g$  analyses were performed after cutting the samples with 0.5 cm thickness, 0.5 cm width and 2.5 cm length.

### 3.3. Different lanthanides in a Na<sub>2</sub>O-CaO-SiO<sub>2</sub> glass matrix: single, binary and ternary systems

Having in mind the production of glasses with new luminescent colours, in order to increase the luminescent colour palette and also to generate white luminescence with the purpose of being used in future art works or decorative objects, different glasses were synthesized with one of each lanthanide oxides: Eu<sub>2</sub>O<sub>3</sub>, Tb<sub>4</sub>O<sub>7</sub>, CeO<sub>2</sub>, Dy<sub>2</sub>O<sub>3</sub>, Tm<sub>2</sub>O<sub>3</sub> and Sm<sub>2</sub>O<sub>3</sub>; mixing two lanthanides oxides (binary system) - Eu<sub>2</sub>O<sub>3</sub>/Tb<sub>4</sub>O<sub>7</sub>, Eu<sub>2</sub>O<sub>3</sub>/CeO<sub>2</sub> and Tb<sub>4</sub>O<sub>7</sub>/CeO<sub>2</sub>; and mixing three lanthanide oxides (ternary system) - 1%Eu<sub>2</sub>O<sub>3</sub> + xTb<sub>4</sub>O<sub>7</sub> + 1%CeO<sub>2</sub>, xEu<sub>2</sub>O<sub>3</sub> +

$1\% \text{Tb}_4\text{O}_7 + 1\% \text{CeO}_2$  and  $1\% \text{Eu}_2\text{O}_3 + 1\% \text{Tb}_4\text{O}_7 + x\text{CeO}_2$ , where  $x$  corresponds to different lanthanide concentrations. To use the synthesized glasses in art or in other applications it is important to study the influence of the lanthanide concentration and the interaction between different lanthanides and how they influence colour under UV-light. A soda-lime silicate glass composition was chosen because it is similar to the composition used in utilitarian and decorative applications and also in architecture (Float glass).<sup>140, 141</sup> A less complex glass compared with what is used by the industry was synthesized, only with three components ( $\text{Na}_2\text{O}-\text{CaO}-\text{SiO}_2$ ) in order to be easier to understand the lanthanide behaviour in these glasses.

### 3.3.1. Glasses doped with one lanthanide – Single system

The glasses doped with one lanthanide are colourless under visible light, except the  $\text{CeO}_2$  and  $\text{Sm}_2\text{O}_3$  doped glasses that are slightly yellow, but under UV-light present different luminescent colours (Figure 3.2). The base glass used to synthesize those glasses is identical to the one described on chapter 2: 74%  $\text{SiO}_2$ , 16%  $\text{Na}_2\text{O}$  and 10%  $\text{CaO}$  (wt%). The luminescent colours obtained are in agreement with the colour found in the literature for each lanthanide in the trivalent state:  $\text{Eu}_2\text{O}_3$  - orange,  $\text{Tb}_4\text{O}_7$  - green,  $\text{CeO}_2$  - blue,  $\text{Dy}_2\text{O}_3$  - yellow,  $\text{Tm}_2\text{O}_3$  - violet and  $\text{Sm}_2\text{O}_3$  - orange.<sup>11, 53</sup>

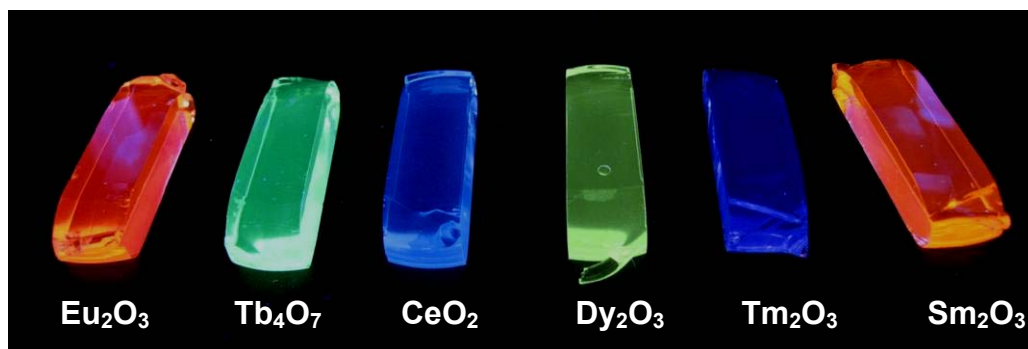


**Figure 3.2.** Glasses doped with 2% of different lanthanide oxides (wt %) under a UV light (365 nm).

The absorption and emission spectra of each lanthanide oxide doped glass are in agreement with data published in the literature and it is possible to attribute each peak to different electronic transitions (figure 3.3 and figure 3.4).<sup>11, 36, 53, 75, 142, 143</sup> Typical sharp peaks corresponding to f-f transitions are observed for all lanthanides (III) except in the case of  $\text{Ce}^{3+}$  where a broad band corresponding to 5d-4f transition is observed.

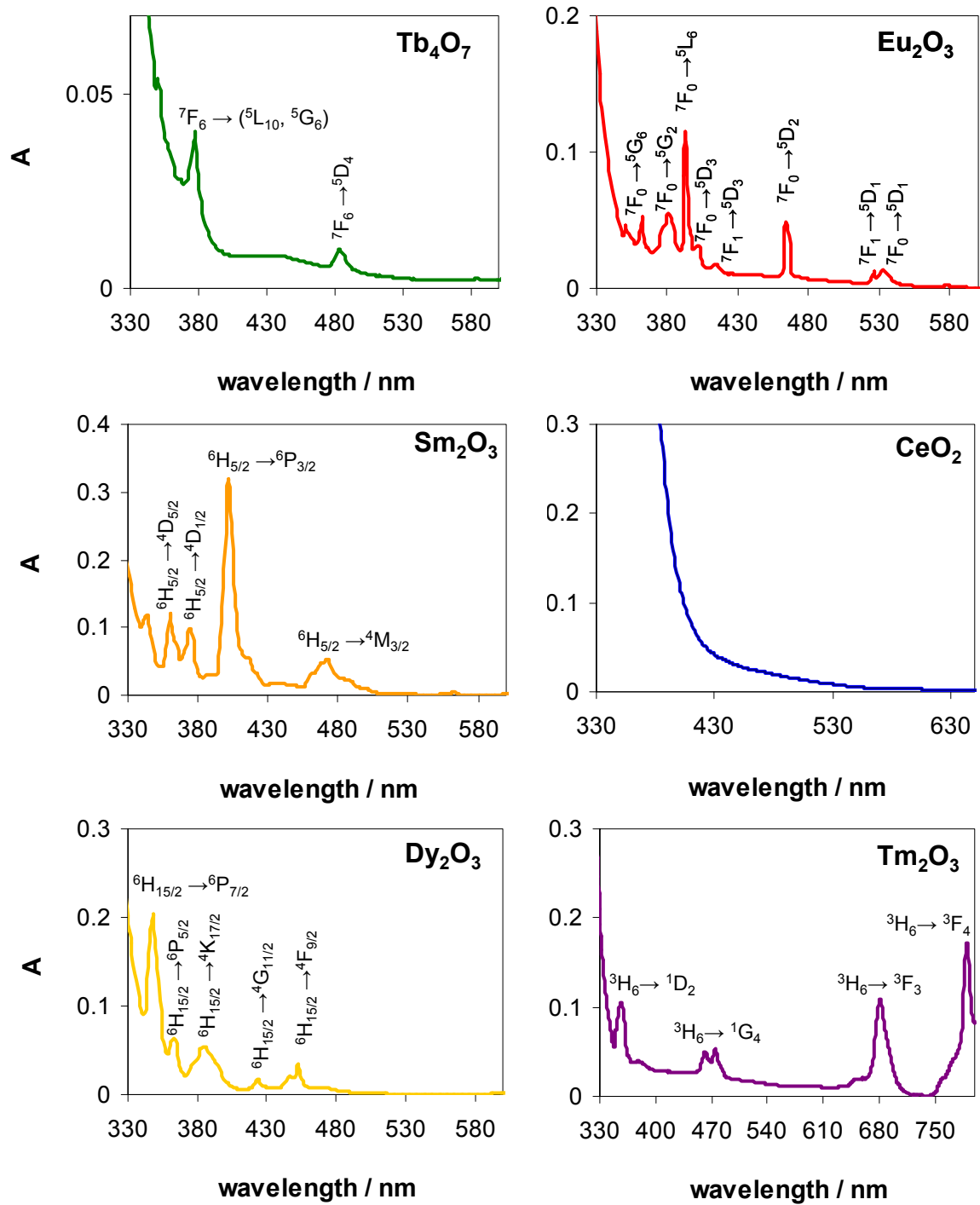


**Figure 3.3.** Absorption spectra of glass samples with different lanthanide oxides (Tb<sub>4</sub>O<sub>7</sub>, Eu<sub>2</sub>O<sub>3</sub>, Sm<sub>2</sub>O<sub>3</sub>, CeO<sub>2</sub>, Dy<sub>2</sub>O<sub>3</sub> and Tm<sub>2</sub>O<sub>3</sub>) and the correspondent electronic transitions.

As it was abovementioned cerium and samarium doped glasses present a yellow colour under interior illumination. In cerium doped glasses it always exist equilibrium between Ce<sup>3+</sup> and Ce<sup>4+</sup>. Cerium absorption peaks appear in the UV region, more specifically Ce<sup>3+</sup> at 314 nm and Ce<sup>4+</sup> at 240 nm, but with high cerium concentrations and with different glass compositions this absorption band becomes larger promoting the observed yellow colour.<sup>17, 144</sup> In the Sm<sub>2</sub>O<sub>3</sub>

doped glass the yellow colour is due the intense peak observed in figure 3.3, that is attributed to  ${}^6\text{H}_{5/2} \rightarrow {}^6\text{P}_{3/2}$ .

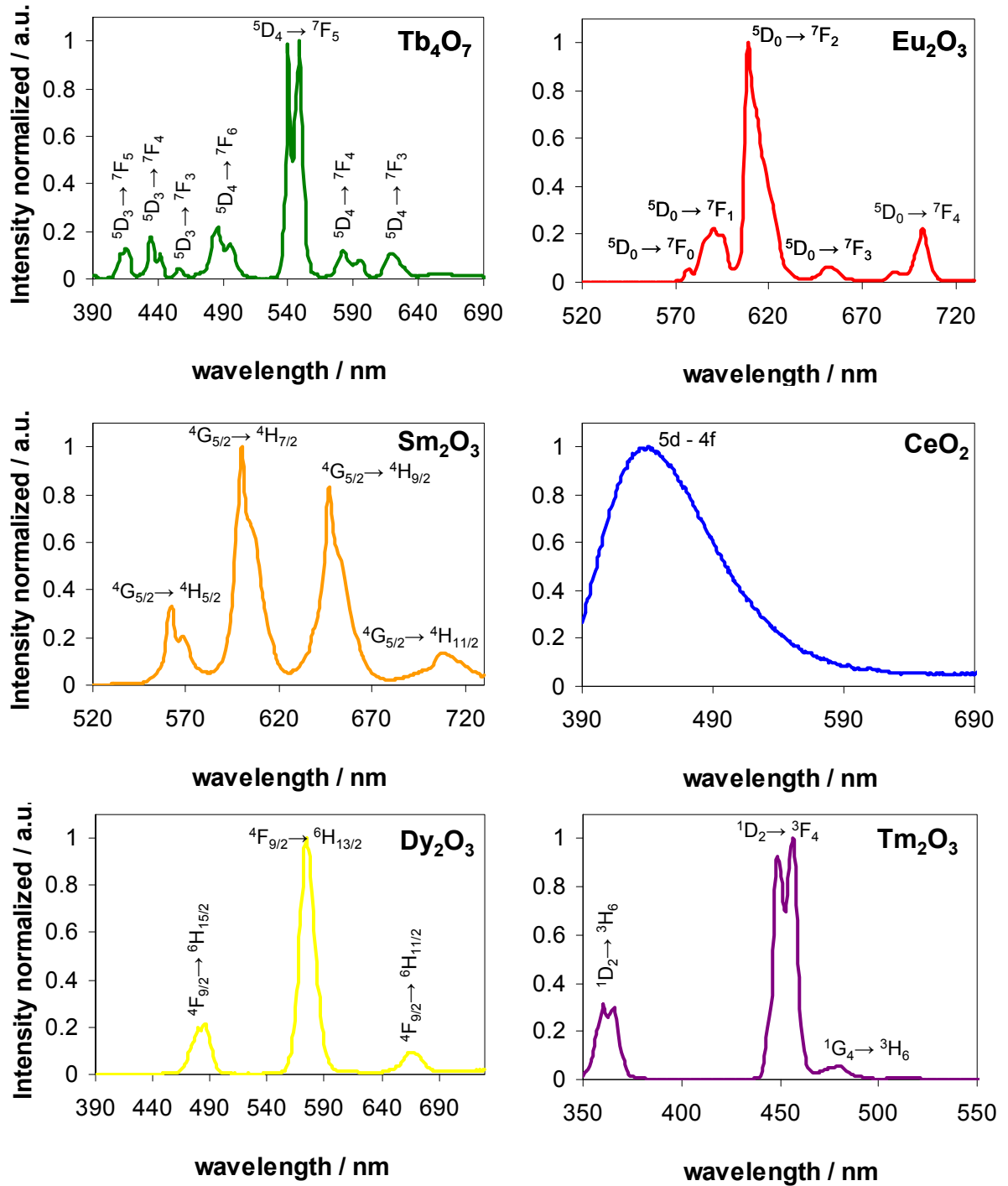


**Figure 3.4.** Luminescence spectra of glass samples with different lanthanide oxides, Tb<sub>4</sub>O<sub>7</sub>, Eu<sub>2</sub>O<sub>3</sub>, Sm<sub>2</sub>O<sub>3</sub>, CeO<sub>2</sub>, Dy<sub>2</sub>O<sub>3</sub> and Tm<sub>2</sub>O<sub>3</sub>, and the correspondent electronic transitions,  $\lambda_{\text{exc}}=377$  nm except in Tm<sub>2</sub>O<sub>3</sub> doped glass case where  $\lambda_{\text{exc}}=340$  nm was used.

A thermal characterization of all these luminescent glasses was made. Different types of glass expand and contract at different temperatures. This temperature change is known as the CTE (Coefficient of Thermal Expansion). The thermal expansion of solid glasses is controlled by the asymmetry of the amplitude of thermal vibrations in the glass and decreases when the rigidity of glass network increases.<sup>145,146</sup> Compatibility tests of the produced glasses were made using a dilatometer in a temperature range of 25-300°C. The CTE,  $T_g$  and  $T_s$  values obtained from the thermal expansion curves (see section 9.2.2., Supplementary Material) for the glasses with europium, samarium, dysprosium, terbium, cerium and thulium are shown in Table 3.2. These measurements were performed by Dr. Carlos Queiroz from Vicarte. Usually two glasses are considered compatible when the difference between their thermal expansion coefficients is less than  $0.5 \times 10^{-6} \text{ K}^{-1}$ .<sup>17</sup> The CTE values obtained were  $9.90 \times 10^{-6} \text{ K}^{-1}$  for the base glass (with no lanthanide oxide) and  $9.85 \times 10^{-6} \text{ K}^{-1}$ ,  $9.89 \times 10^{-6} \text{ K}^{-1}$ ,  $9.92 \times 10^{-6} \text{ K}^{-1}$ ,  $9.87 \times 10^{-6} \text{ K}^{-1}$ ,  $10.05 \times 10^{-6} \text{ K}^{-1}$  and  $9.45 \times 10^{-6} \text{ K}^{-1}$  for  $\text{Eu}_2\text{O}_3$ ,  $\text{Tb}_4\text{O}_7$ ,  $\text{CeO}_2$ ,  $\text{Dy}_2\text{O}_3$ ,  $\text{Tm}_2\text{O}_3$  and  $\text{Sm}_2\text{O}_3$  doped glasses, respectively. So the differences between these values are less than  $0.5 \times 10^{-6} \text{ K}^{-1}$ , except between the glasses doped with  $\text{Dy}_2\text{O}_3$  and  $\text{Tm}_2\text{O}_3$ . These results indicate that all the luminescent glasses are compatible with their base glass and with each other, except the glasses with  $\text{Dy}_2\text{O}_3$  and with  $\text{Tm}_2\text{O}_3$ , where the difference of the CTE values is higher than  $0.5 \times 10^{-6} \text{ K}^{-1}$ . This result is very important for the potential production of glass artworks, since if glasses are not compatible they will break when fused together. The compatible glasses with different luminescent colours can be fused together, increasing the artistic possibilities.

**Table 3.2.**  $T_g$  and CTE values obtain for the glass samples doped with different lanthanides. CTE values were taken from the 25-300°C temperature range.

Glass sample	$T_g$ /°C	$T_s$ /°C	CTE /°K <sup>-1</sup> x10 <sup>-6</sup>
Base glass (with no lanthanide oxide)	537.1	587.9	9.85
$\text{Eu}_2\text{O}_3$	537.9	591.5	9.89
$\text{Tb}_4\text{O}_7$	540.4	585.5	9.92
$\text{CeO}_2$	535.4	593.3	9.87
$\text{Dy}_2\text{O}_3$	539.8	601.7	10.05
$\text{Tm}_2\text{O}_3$	548.0	595.9	9.45
$\text{Sm}_2\text{O}_3$	541.4	590.5	9.90

### 3.3.2. Glasses doped with two lanthanides – Binary system

In order to achieve white luminescence and a vast number of luminescent colours,  $\text{Eu}_2\text{O}_3$ ,  $\text{Tb}_4\text{O}_7$  and  $\text{CeO}_2$  that emit red, green and blue, respectively (figure 3.5) were mixed and used to dope soda-lime silicate glasses. The referred lanthanides were already used in several studies with different glass compositions and other materials, that focus the production of white light in particularly W-LEDs.<sup>147,148,149,150,151,152</sup>

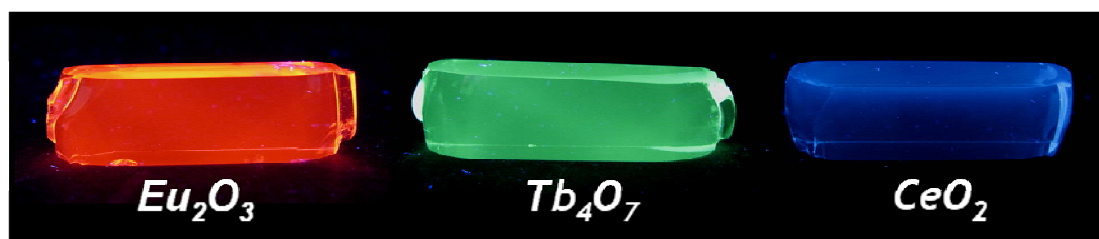


**Figure 3.5.** Glasses doped with 2% (wt) of different lanthanides,  $\text{Eu}_2\text{O}_3$ ,  $\text{Tb}_4\text{O}_7$  and  $\text{CeO}_2$ , under UV light (365 nm).

To use this glass in the art field it is important to investigate which colour can be obtained by an element and if that colour changes with other effects when several elements are mixed together. Glasses doped with three lanthanides are presented in the subchapter 3.3.3, but first in order to better understand these systems, a study of binary glasses ( $\text{Eu}_2\text{O}_3/\text{Tb}_4\text{O}_7$ ,  $\text{Eu}_2\text{O}_3/\text{CeO}_2$  and  $\text{Tb}_4\text{O}_7/\text{CeO}_2$ ) was made.

### ***Eu+Tb system***

Several luminescent colours were obtained doping the soda-lime silicate glass with different concentrations of  $\text{Eu}_2\text{O}_3$  and  $\text{Tb}_4\text{O}_7$  (Figure 3.6). Higher  $\text{Eu}_2\text{O}_3$  concentrations originate orange samples that become yellow and afterwards green when  $\text{Tb}_4\text{O}_7$  is added to the glass composition. The red and green colours are due to  $^5\text{D}_0 \rightarrow ^7\text{F}_2$  and  $^5\text{D}_4 \rightarrow ^7\text{F}_5$  electronic transition of  $\text{Eu}^{3+}$  ions and of  $\text{Tb}^{3+}$  ions, respectively.

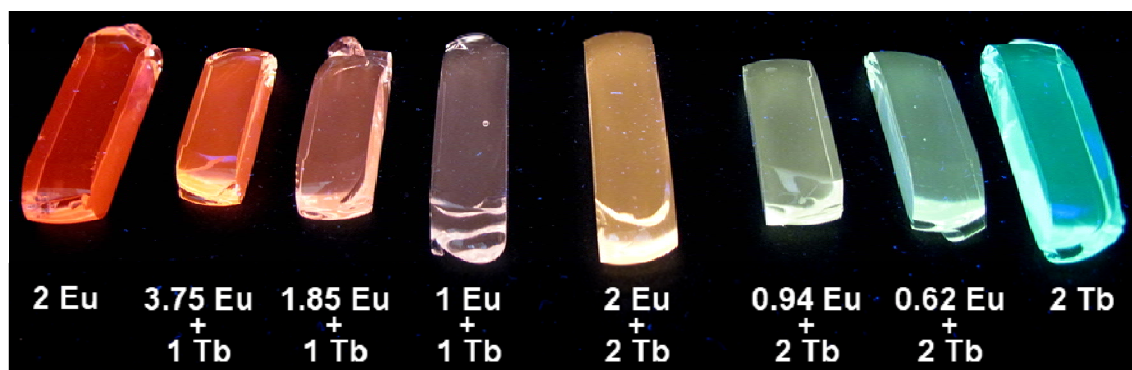


**Figure 3.6.** Glasses doped with different concentrations of  $\text{Eu}_2\text{O}_3$  and  $\text{Tb}_4\text{O}_7$  (wt%), under UV light (370 nm).

Photophysical processes between the two elements can influence colour under an UV-light when these two lanthanides are mixed together. It is known, for example, that energy transfer in solid materials enhances luminescent emission and excitation efficiency.<sup>153,154,155,156</sup> In fact the photoluminescence (PL) intensity of  $\text{Tb}^{3+}$  or  $\text{Eu}^{3+}$  in some materials is weak due to the forbidden f-f transitions and one of the strategies to enhance the emission is co-doping with ions that can act as sensitizers.<sup>152,153,154,155,156,157,158</sup> In this case energy transfer increases the colour intensity of one of the elements and decrease the colour intensity of the other. Several studies showed that  $\text{Tb}^{3+}$  can transfer energy to  $\text{Eu}^{3+}$ ,<sup>159,160,161,162</sup> but to understand what is happening in this case a spectroscopic study was performed.

Both ions are excited at 377 nm and give their characteristic emission in the visible spectrum. The incorporation of both europium and terbium oxides results in an enhancement of  $\text{Eu}^{3+}$  emission and decrease of  $\text{Tb}^{3+}$  emission indicating energy transfer from  $\text{Tb}^{3+}$  to  $\text{Eu}^{3+}$  (figure 3.7).

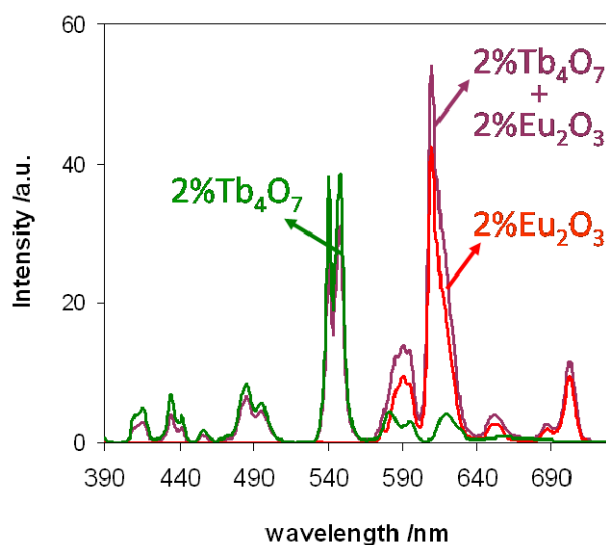


**Figure 3.7.** Luminescence spectra of glass samples with 2%  $\text{Tb}_4\text{O}_7$  (green), 2%  $\text{Eu}_2\text{O}_3$  (red) and 2%  $\text{Tb}_4\text{O}_7$  + 2%  $\text{Eu}_2\text{O}_3$  (purple),  $\lambda_{\text{exc}}=377$  nm.

An essential condition for the existence of energy transfer between two ions is the overlap of the emission spectra of the donor ( $\text{Tb}^{3+}$ ) with the excitation of the acceptor ( $\text{Eu}^{3+}$ )<sup>163</sup>, which condition is observed in figure 3.8 B where the transition  $^5\text{D}_4 \rightarrow ^7\text{F}_5$  of the  $\text{Tb}^{3+}$  emission spectrum overlap the absorption transition  $^7\text{F}_0 \rightarrow ^5\text{D}_1$  at 532 nm of  $\text{Eu}^{3+}$  excitation spectrum. By monitoring 700 nm  $\text{Eu}^{3+}$  emission, the excitation spectrum of sample doped with 2%  $\text{Eu}_2\text{O}_3$  + 2%  $\text{Tb}_4\text{O}_7$  in figure 3.8 A shows excitation of  $\text{Tb}^{3+}$  at 484 nm, while in the sample doped with only  $\text{Eu}^{3+}$  it is absent. This is explained with energy transfer from  $\text{Tb}^{3+}$  to  $\text{Eu}^{3+}$ .

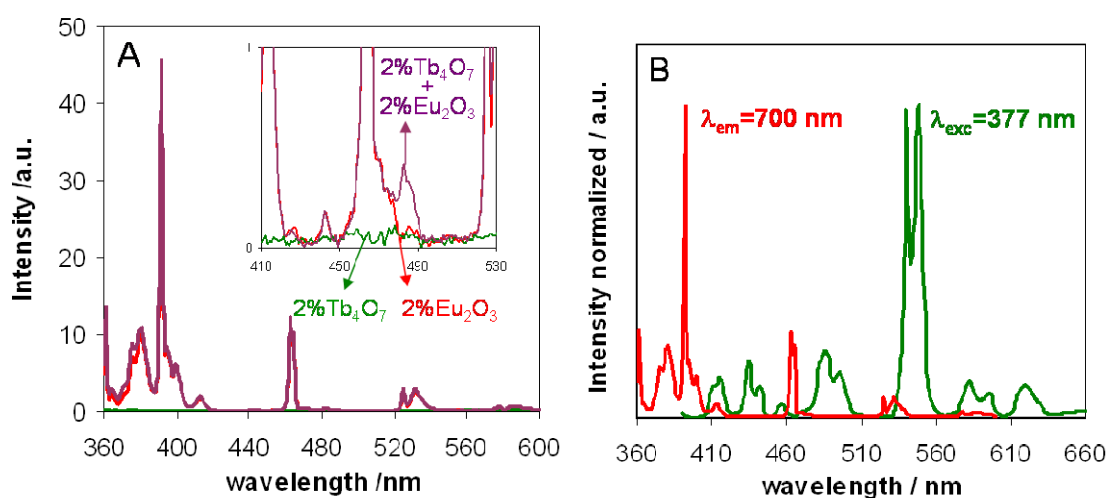


**Figure 3.8.** (A) Excitation spectra at 700 nm of glasses with 2%  $\text{Eu}_2\text{O}_3$  (red line), 2%  $\text{Tb}_4\text{O}_7$  (green line) and 2%  $\text{Eu}_2\text{O}_3$  + 2%  $\text{Tb}_4\text{O}_7$  (purple line). (B) Excitation spectrum of glass with 2%  $\text{Eu}_2\text{O}_3$ ,  $\lambda_{\text{em}}=700$  nm (red line) and luminescence spectrum of the glass sample with 2%  $\text{Tb}_4\text{O}_7$ ,  $\lambda_{\text{exc}}=377$  nm (green line).



The increment of  $\text{Eu}_2\text{O}_3$  concentration in glasses with 1% (wt) of  $\text{Tb}_4\text{O}_7$  (figure 3.9 A) and with 2% (wt) of  $\text{Tb}_4\text{O}_7$  (figure 3.9 B) quenches the  $\text{Tb}^{3+}$  emission. Differences on the emission intensity of  $\text{Eu}^{3+}$  and  $\text{Tb}^{3+}$  are represented in figure 3.10. As it was expected the luminescence intensity at 700 nm (that corresponds to the electronic transition  $^5\text{D}_0 \rightarrow ^7\text{F}_4$  of  $\text{Eu}^{3+}$ ) increases with  $\text{Eu}_2\text{O}_3$  concentration and is higher compared with what is observed in the absence of terbium (black line). Meanwhile the luminescence intensity at 549 nm, that corresponds to the  $\text{Tb}^{3+}$  electronic transition  $^5\text{D}_4 \rightarrow ^7\text{F}_5$ , decreases with the  $\text{Eu}_2\text{O}_3$  concentration (figure 3.10).

Two sets of glasses with different  $\text{Tb}_4\text{O}_7$  concentrations were made in order to explore different lanthanide molar fractions in the glass. If high  $\text{Eu}_2\text{O}_3$  concentrations are used, we would change the glass structure and possibly the glasses would not be compatible with those synthesized before. Therefore high  $\text{Eu}^{3+}$  molar fractions in the compatible binary glasses could not be produced. In addition, it is known that lanthanides oxides in this type of glass composition act as flux and therefore high concentrations of lanthanides decrease the glass stability.<sup>145,164</sup>

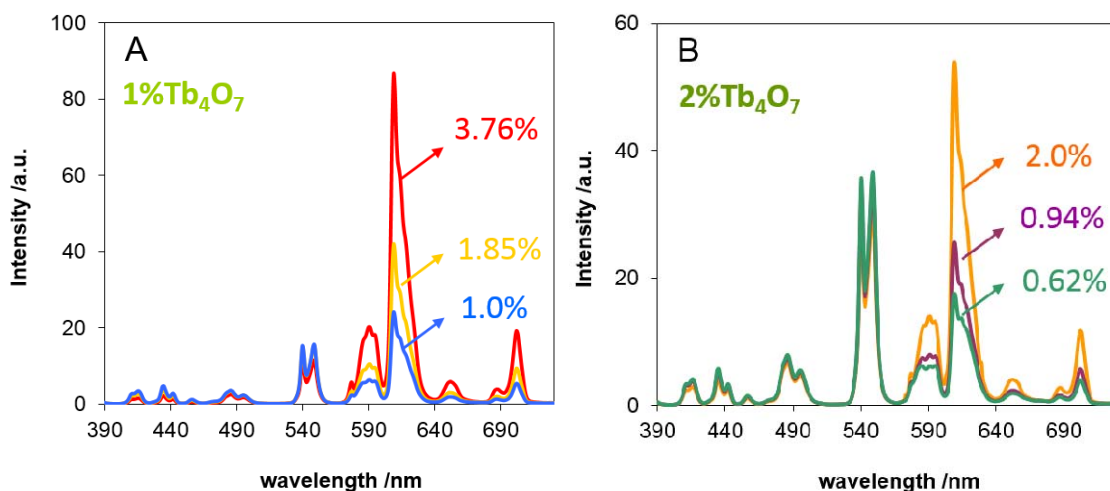


**Figure 3.9.** Luminescence spectra of different glass samples: (A) with 1% of  $\text{Tb}_4\text{O}_7$  and different  $\text{Eu}_2\text{O}_3$  concentrations, 3.76% (BET1), 1.85% (BET2) and 1.0% (BET3); (B) with 2% of  $\text{Tb}_4\text{O}_7$  and different  $\text{Eu}_2\text{O}_3$  concentrations, 2.0% (BET 4), 0.94% (BET 5) and 0.62% (BET 6),  $\lambda_{\text{exc}}=377$  nm.

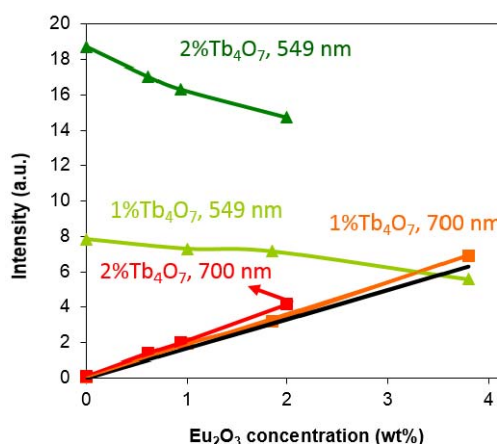
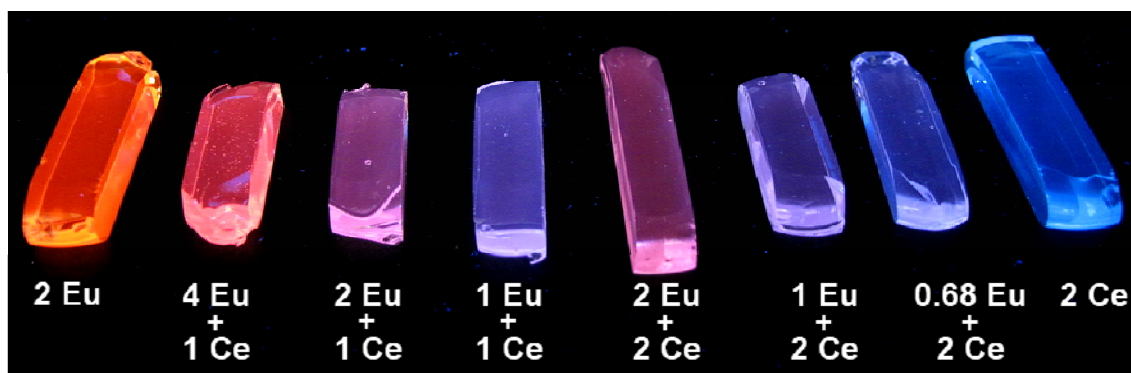


**Figure 3.10.** Luminescence intensity of  $\text{Tb}^{3+}$  emission at 549 nm (green lines) and  $\text{Eu}^{3+}$  emission at 700 nm (red lines) as function of  $\text{Eu}_2\text{O}_3$  concentration, for the glass samples doped with 1% (lighter lines) and 2 % of  $\text{Tb}_4\text{O}_7$  (darker lines). The black line corresponds to the intensities of  $\text{Eu}^{3+}$  at 700 nm without the presence of  $\text{Tb}_4\text{O}_7$ .

The previous results show that in this binary system  $\text{Tb}^{3+}$  transfers energy to  $\text{Eu}^{3+}$ , slightly enhancing the red luminescence in the glass samples but with a more significant  $\text{Tb}^{3+}$  luminescence quenching.

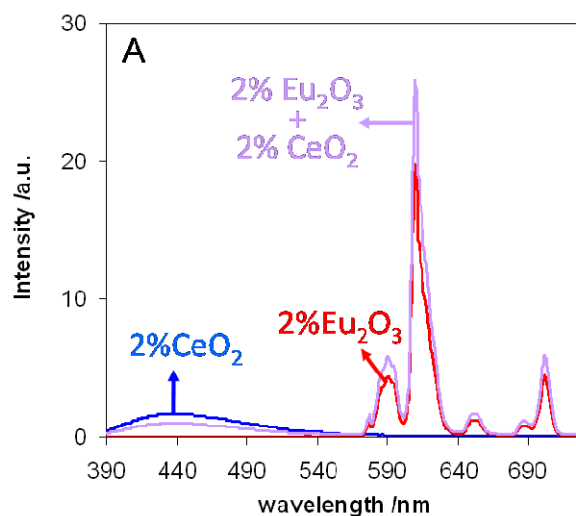
### Eu+Ce system

The colour palette can be further extended by introducing another binary system containing  $\text{Eu}_2\text{O}_3$  and  $\text{CeO}_2$  (figure 3.11). Higher  $\text{Eu}_2\text{O}_3$  concentrations originate orange samples that become pink and finally blue in the  $\text{CeO}_2$  glass. These red and blue colours are due to  $^5\text{D}_0 \rightarrow ^7\text{F}_2$  and 5d-4f electronic transition of  $\text{Eu}^{3+}$  ions and  $\text{Ce}^{3+}$  ions, respectively.



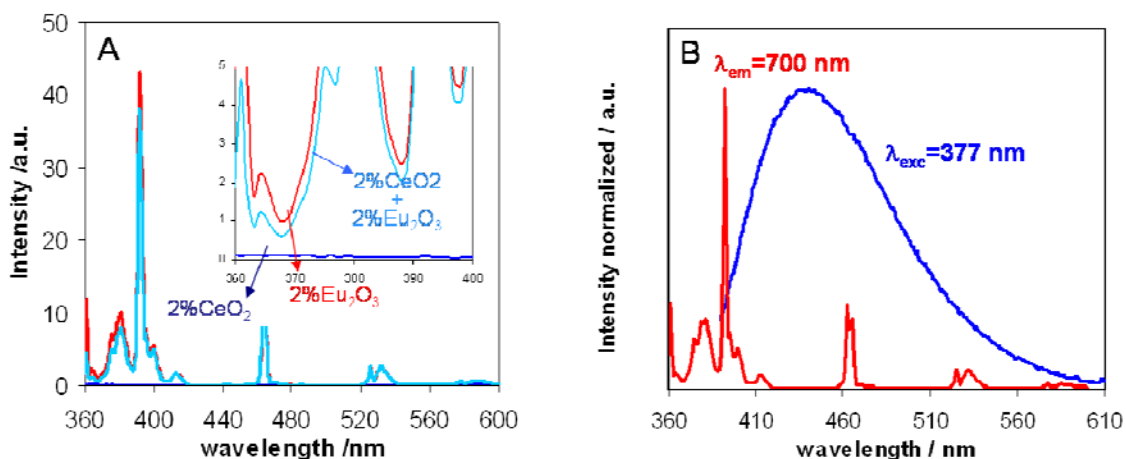
**Figure 3.11.** Glasses doped with different concentrations of  $\text{Eu}_2\text{O}_3$  and  $\text{CeO}_2$  (wt%), under UV-light (370 nm).

It is found in the literature that a small amount of  $\text{CeO}_2$  is often added as a sensitizer<sup>165,166,167</sup> and some studies already demonstrated that  $\text{Ce}^{3+}$  can transfer energy to  $\text{Eu}^{3+}$ .<sup>150,168,169,170</sup>  $\text{Eu}^{3+}$  and  $\text{Ce}^{3+}$  can also be excited at 377 nm and give their characteristic emission in the visible region as it is observed in figure 3.4. The incorporation of both europium and cerium oxide results in an enhancement of  $\text{Eu}^{3+}$  emission and quenching of  $\text{Ce}^{3+}$  emission indicating the existence of energy transfer, see figure 3.12.



**Figure 3.12.** Luminescence spectra of glass samples with 2%  $\text{CeO}_2$  (blue), 2%  $\text{Eu}_2\text{O}_3$  (red) and 2%  $\text{CeO}_2$  + 2%  $\text{Eu}_2\text{O}_3$  (violet),  $\lambda_{\text{exc}}=377$  nm.

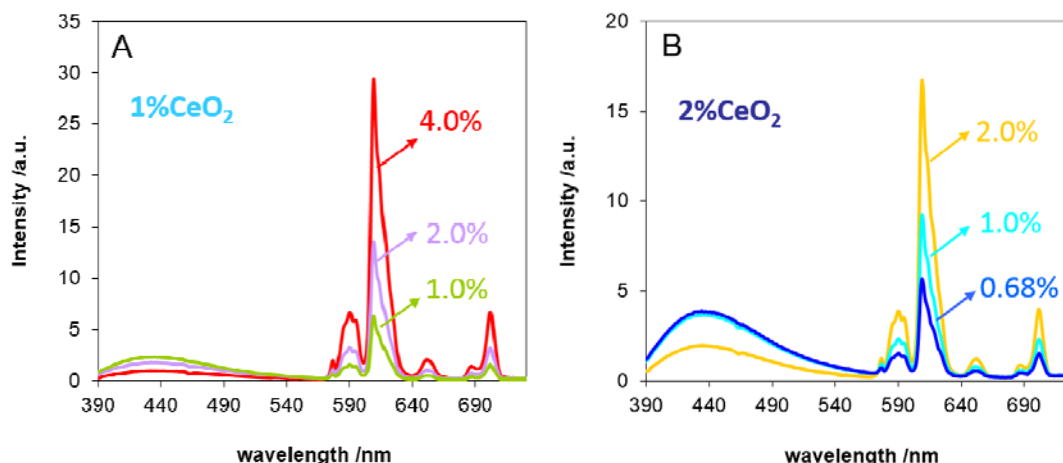
By monitoring 700 nm  $\text{Eu}^{3+}$  emission, the excitation spectrum of sample doped with 2% $\text{Eu}_2\text{O}_3$ +2%  $\text{CeO}_2$  in figure 3.13 A do not show any additional excitation besides those that corresponding to  $\text{Eu}^{3+}$ . Luminescence spectra results illustrated in figure 3.12 pointed out to an energy transfer from  $\text{Ce}^{3+}$  to  $\text{Eu}^{3+}$  and this system present an essential condition for the existence of energy transfer since the emission spectra of the donor ( $\text{Ce}^{3+}$ ) overlaps the absorption spectra of the acceptor ( $\text{Eu}^{3+}$ ), figure 3.13 B, but the excitation spectra at 700 nm in the presence of  $\text{Ce}^{3+}$  does not show this effect.



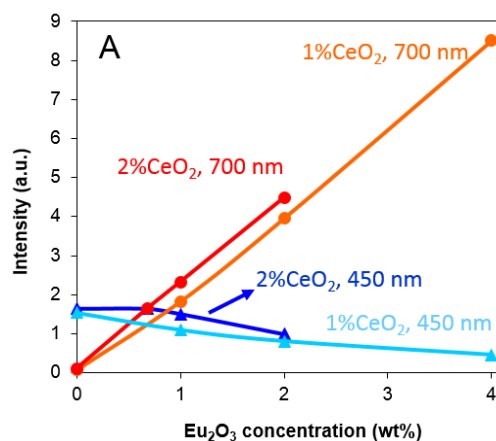
**Figure 3.13.** (A) Excitation spectra at 700 nm of glasses with 2%  $\text{Eu}_2\text{O}_3$  (red line), 2%  $\text{CeO}_2$  (dark blue line) and 2%  $\text{Eu}_2\text{O}_3$  + 2%  $\text{CeO}_2$  (light blue line). (B) Excitation spectra of glass with 2%  $\text{Eu}_2\text{O}_3$ ,  $\lambda_{\text{em}} = 700$  nm (red line) and luminescence spectrum of the glass sample with 2%  $\text{CeO}_2$ ,  $\lambda_{\text{exc}} = 377$  nm (blue line).

Nevertheless cerium influences the  $\text{Eu}^{3+}$  PL intensity. Emission spectra were measured for two composition sets: a) 1%  $\text{CeO}_2$  and different  $\text{Eu}_2\text{O}_3$  concentrations (1, 2, 4%, wt) and b) 2%  $\text{CeO}_2$  and different  $\text{Eu}_2\text{O}_3$  concentrations (0.68, 1, 2%, wt), see figure 3.14. Figure 3.15 shows the emission intensity vs  $\text{Eu}_2\text{O}_3$  concentration at 450 nm and 700 nm. As it was expected, the luminescence intensity at 700 nm increases with  $\text{Eu}_2\text{O}_3$  concentration and is higher compared with what it is observed in the absence of cerium (black line). Meanwhile the luminescence intensity at 450 nm that corresponds to the  $\text{Ce}^{3+}$  emission decreases with the  $\text{Eu}_2\text{O}_3$  concentration.

The samples with 0 and with 2%  $\text{Eu}_2\text{O}_3$  containing different  $\text{CeO}_2$  concentrations (1 and 2%) at 450 nm have almost the same PL intensity, suggesting that  $\text{Ce}^{3+}$  can act as a self-quencher. One possible explanation is the concentration quenching due to the aggregation of cerium and as a result part of the  $\text{Ce}^{3+}$  ions are self-quenched by nearby  $\text{Ce}^{3+}$  ions,<sup>139,171,172,173</sup> therefore very high concentrations of  $\text{Ce}^{3+}$  suppress the blue luminescence. In this soda-lime silicate binary system  $\text{Ce}^{3+}$  seems to influence the  $\text{Eu}^{3+}$  PL, enhancing the red luminescence. Probably energy-transfer does occur, but since the excitation spectra is not probing wavelengths below 360 nm it is not evident the effect.



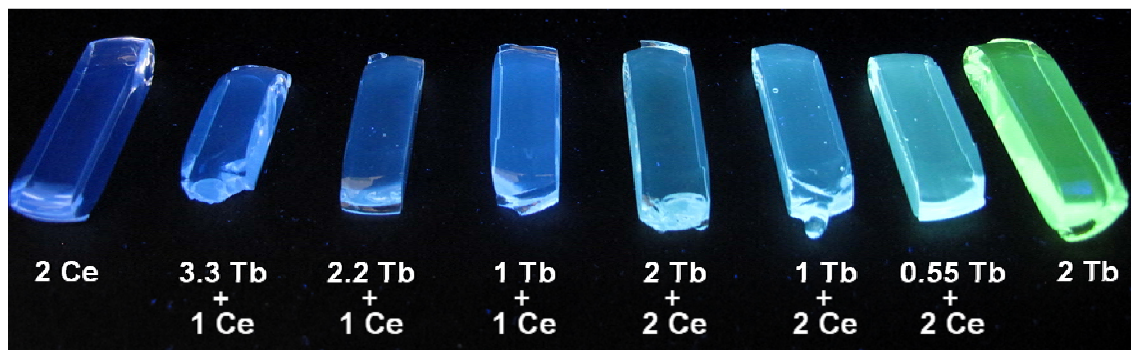
**Figure 3.14.** Luminescence spectra of different glass samples: (A) with 1% of  $\text{CeO}_2$  and different  $\text{Eu}_2\text{O}_3$  concentrations, 4.0% (BEC1), 2.0% (BEC2) and 1.0% (BEC3); (B) with 2% of  $\text{CeO}_2$  and different  $\text{Eu}_2\text{O}_3$  concentrations, 2.0% (BEC 4), 1.0% (BEC 5) and 0.68% (BEC 6),  $\lambda_{\text{exc}}=377$  nm.



**Figure 3.15.** Luminescence intensity of  $\text{Ce}^{3+}$  emission at 450 nm (blue lines) and  $\text{Eu}^{3+}$  emission at 700 nm (red and orange line) as function of  $\text{Eu}_2\text{O}_3$  concentration, for the glass samples doped with 1% (lighter lines) and 2 % of  $\text{CeO}_2$  (darker lines). The black line represents the  $\text{Eu}^{3+}$  intensity at 700 nm without  $\text{CeO}_2$ .

### Tb+Ce system

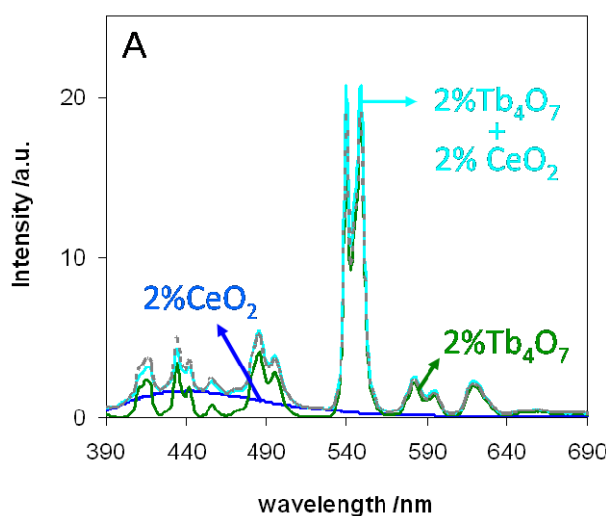
The same glass composition was doped with different concentrations of  $\text{Tb}_4\text{O}_7$  and  $\text{CeO}_2$  (Figure 3.16). Higher  $\text{CeO}_2$  contents give rise to blue samples that become green  $\text{Tb}_4\text{O}_7$  glass.



**Figure 3.16.** Glasses doped with different concentrations of  $\text{CeO}_2$  and  $\text{Tb}_4\text{O}_7$  (wt%), under UV light (370 nm).

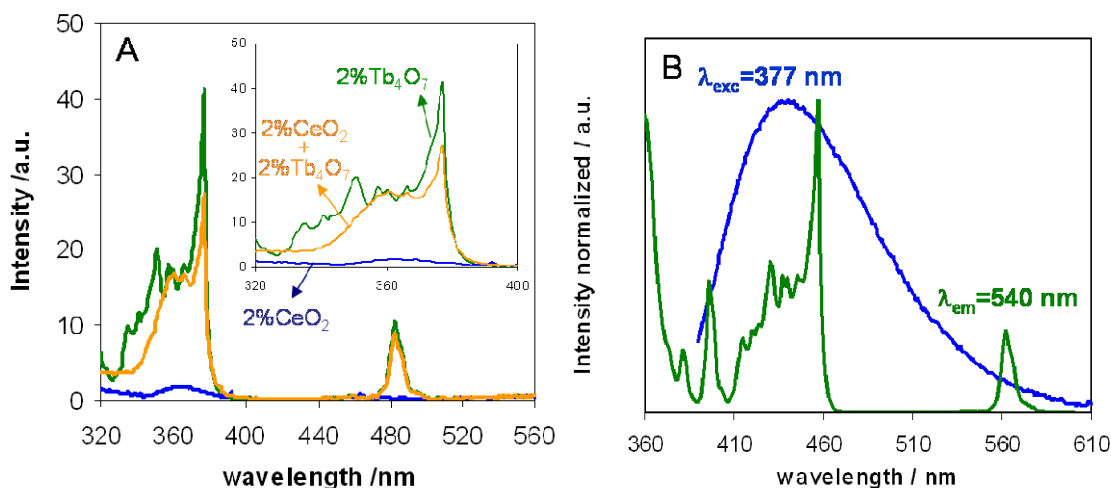
Several studies have been already made with cerium and terbium doped materials, where energy transfer processes between  $\text{Ce}^{3+}$  and  $\text{Tb}^{3+}$  was investigated.<sup>150,153,155,157,169</sup> In the majority of those works,  $\text{Ce}^{3+}$  transfers energy to  $\text{Tb}^{3+}$ , but some reports do not observe this process. Zorenko et al., for example, reported, in single-crystalline films of  $\text{Tb}_3\text{Al}_5\text{O}_{12}:\text{Ce},\text{Eu}$ , a process of energy transfer from  $\text{Tb}^{3+}$  ions to  $\text{Ce}^{3+}$  and  $\text{Eu}^{3+}$  ions and from  $\text{Ce}^{3+}$  ions to  $\text{Eu}^{3+}$ .

Figure 3.17 show the emission spectra of glasses doped with cerium and terbium. The luminescence spectra of the glass doped with 2%  $\text{Tb}_4\text{O}_7$  + 2%  $\text{CeO}_2$  (light blue full line) is very similar to the spectra obtained with the sum of the spectrum of glass doped with 2%  $\text{CeO}_2$  with the one with 2%  $\text{Tb}_4\text{O}_7$  (grey dashed line).



**Figure 3.17.** Luminescence spectra of glass samples with 2%  $\text{Tb}_4\text{O}_7$  (green), 2%  $\text{CeO}_2$  (blue), 2% $\text{Tb}_4\text{O}_7$  + 2%  $\text{CeO}_2$  (light blue) and sum of 2%  $\text{CeO}_2$  and  $\text{Tb}_4\text{O}_7$  luminescence spectra (grey dashed line),  $\lambda_{\text{exc}}=377\text{nm}$ .

The excitation spectrum ( $\lambda_{\text{em}}=620\text{ nm}$ ,  $\text{Tb}^{3+}$  emission line) of the glass sample doped with 2%  $\text{CeO}_2$  + 2% $\text{Tb}_4\text{O}_7$  presented in figure 3.18 A show a excitation at 360 nm attributed to  $\text{Ce}^{3+}$ .  $\text{Tb}^{3+}$  is also directly excited in that area but the band shape is different. This suggests the existence of energy transfer from  $\text{Ce}^{3+}$  to  $\text{Tb}^{3+}$ . Figure 3.18 B show the excitation spectrum of terbium doped glass,  $\lambda_{\text{em}}=540\text{ nm}$ , and the emission spectrum of cerium doped glass,  $\lambda_{\text{exc}}=377\text{ nm}$ , in order to illustrate the spectra overlap in several electronic transitions.



**Figure 3.18.** (A) Excitation spectra at 620 nm of glasses with 2% Tb<sub>4</sub>O<sub>7</sub> (green line), 2% CeO<sub>2</sub> (blue line) and 2% Eu<sub>2</sub>O<sub>3</sub> + 2% CeO<sub>2</sub> (orange line). (B) Excitation spectra of glass with 2% Tb<sub>4</sub>O<sub>7</sub>,  $\lambda_{em}=700$  nm (green line) and luminescence spectrum of the glass sample with 2% CeO<sub>2</sub>,  $\lambda_{exc}=377$  nm (blue line).

The luminescence spectra were measured for two different sets of glass samples: A) 1% CeO<sub>2</sub> with different Tb<sub>4</sub>O<sub>7</sub> concentrations (1, 2.2, 3.3%, wt) and B) 2% CeO<sub>2</sub> with different Tb<sub>4</sub>O<sub>7</sub> concentrations (0.55, 1, 2%, wt), see figure 3.19. Figure 3.20 shows the emission intensity vs Tb<sub>4</sub>O<sub>7</sub> concentration at 450 nm and 617 nm, which are wavelengths that correspond to Ce<sup>3+</sup> (<sup>5</sup>D<sub>4</sub>→<sup>7</sup>F<sub>3</sub>) and Tb<sup>3+</sup> emission (<sup>5</sup>D<sub>4</sub>→<sup>7</sup>F<sub>3</sub>), respectively. Observing figure 3.20, at 450 nm Ce<sup>3+</sup> show the same behaviour as in the Eu<sup>3+</sup>/Ce<sup>3+</sup> system, illustrating again that increasing CeO<sub>2</sub> concentration gives rise to self-quenching effects. At 617 nm the intensity increases with terbium concentration, as it was expected, and is higher than what it is observed in the absence of cerium (black line). Therefore, Ce<sup>3+</sup> aggregation and Ce<sup>3+</sup>/Tb<sup>3+</sup> energy-transfer play a role in the measured luminescence spectra of this set of glass samples.

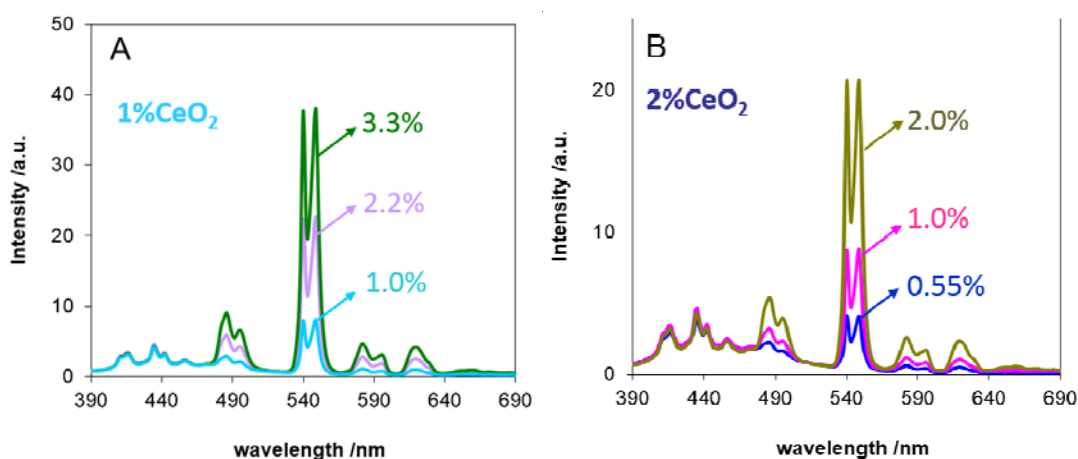


**Figure 3.19.** Luminescence spectra of different glass samples: (A) with 1% of CeO<sub>2</sub> and different Tb<sub>4</sub>O<sub>7</sub> concentrations, 3.3% (BTC1), 2.2% (BTC2) and 1.0% (BTC3); (B) with 2% of CeO<sub>2</sub> and different Tb<sub>4</sub>O<sub>7</sub> concentrations, 2.0% (BTC4), 1.0% (BTC5) and 0.55% (BTC6),  $\lambda_{exc}=377$  nm.

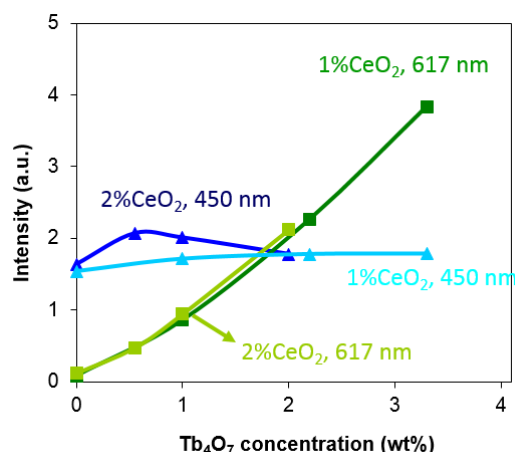


**Figure 3.20.** Luminescence intensity of  $\text{Ce}^{3+}$  emission at 450 nm and  $\text{Tb}^{3+}$  emission at 619 nm as function of  $\text{Tb}_4\text{O}_7$  concentration, for the glass samples doped with 1% and 2% of  $\text{CeO}_2$ . The black line corresponds to the intensity of  $\text{Tb}^{3+}$  at 617 nm without the presence of  $\text{CeO}_2$ .

Summarizing soda-lime silicate glasses were prepared containing  $\text{Eu}_2\text{O}_3/\text{Tb}_4\text{O}_7$ ,  $\text{Eu}_2\text{O}_3/\text{CeO}_2$  and  $\text{Tb}_4\text{O}_7/\text{CeO}_2$  and different luminescent colours were obtained. The spectroscopic measurements showed an enhancement of the red luminescence when cerium and terbium are present and an enhancement of the green luminescence when cerium is present. It was also possible to observe self-quenching of  $\text{Ce}^{3+}$ . These effects have an influence in the colour of luminescence, as explained below.

### 3.3.3. Glasses doped with three lanthanides – Ternary system

Glass samples were doped with different concentrations of mixtures of  $\text{Eu}_2\text{O}_3$ ,  $\text{Tb}_4\text{O}_7$  and  $\text{CeO}_2$ , in which only one lanthanide oxide was varied as follows: ( $x\text{Eu}_2\text{O}_3 + 1\%\text{Tb}_4\text{O}_7 + 1\%\text{CeO}_2$ ),  $\text{CeO}_2$  ( $1\%\text{Eu}_2\text{O}_3 + 1\%\text{Tb}_4\text{O}_7 + 1\%\text{CeO}_2$ ) or  $\text{Tb}_4\text{O}_7$  ( $1\%\text{Eu}_2\text{O}_3 + x\text{Tb}_4\text{O}_7 + 1\%\text{CeO}_2$ ). For the samples with 4.5% of one lanthanide, the concentration of the other two in the ternary system was decreased by 0.5%, to maintain the total lanthanide concentrations below 6% (wt). It is only changed the concentration of one lanthanide, in order to obtain a “semi-binary” system. Different luminescent colour were obtained, see figure 3.21. In the samples doped with different  $\text{CeO}_2$  contents it is observed that using high cerium concentrations such as 4.5% the luminescence is quenched, as explained in the sub-chapter 3.3.2.



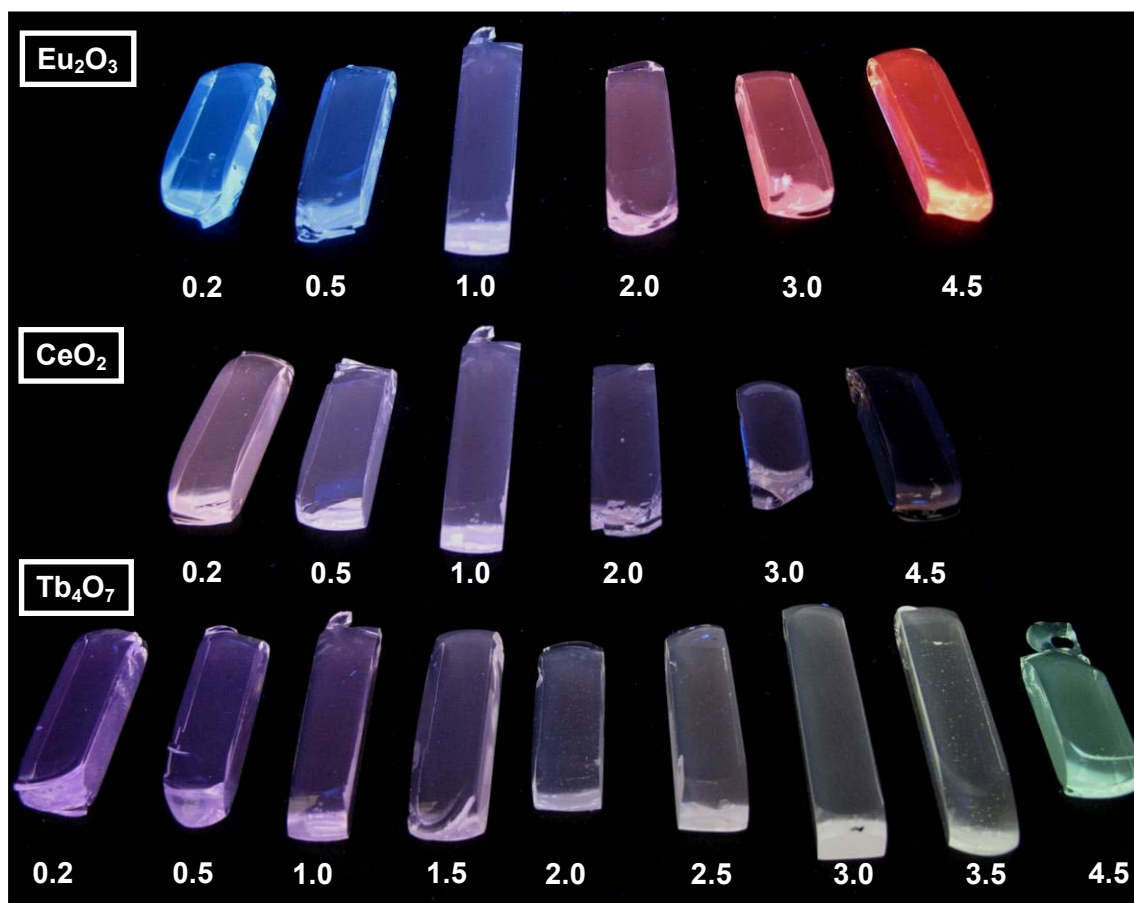


**Figure 3.21.** Glasses doped with  $\text{Eu}_2\text{O}_3$ ,  $\text{CeO}_2$  and  $\text{Tb}_4\text{O}_7$ , changing  $\text{Eu}_2\text{O}_3$  concentration ( $x\text{Eu}_2\text{O}_3 + 1\%\text{Tb}_4\text{O}_7 + 1\%\text{CeO}_2$  and  $4.5\%\text{Eu}_2\text{O}_3 + 0.5\%\text{Tb}_4\text{O}_7 + 0.5\%\text{CeO}_2$ ),  $\text{Tb}_4\text{O}_7$  concentration ( $1\%\text{Eu}_2\text{O}_3 + x\text{Tb}_4\text{O}_7 + 1\%\text{CeO}_2$  and  $0.5\%\text{Eu}_2\text{O}_3 + 4.5\%\text{Tb}_4\text{O}_7 + 0.5\%\text{CeO}_2$ ) and  $\text{CeO}_2$  concentration ( $1\%\text{Eu}_2\text{O}_3 + x\text{Tb}_4\text{O}_7 + 1\%\text{CeO}_2$  and  $0.5\%\text{Eu}_2\text{O}_3 + 0.5\%\text{Tb}_4\text{O}_7 + 4.5\%\text{CeO}_2$ ), wt%, under a UV-light (370 nm).

Spectroscopic measurements were made to study the composition influence in the luminescence colour. Emission spectra of Eu/Tb/Ce doped glasses excited at 377 nm are shown in figure 3.22. The bands observed in figure 3.22 correspond to the electronic transitions of  $\text{Eu}^{3+}$ ,  $\text{Tb}^{3+}$  and  $\text{Ce}^{3+}$ , already attributed in figure 3.4. The emission spectra are organized in three groups of glasses: A – different  $\text{Eu}_2\text{O}_3$  concentrations, B – different  $\text{Tb}_4\text{O}_7$  concentrations and C – different  $\text{CeO}_2$  concentrations. To compare the PL intensity of the trivalent lanthanide ions in the different glass groups' three wavelengths were chosen where the emission is mainly due to one of the lanthanides: 450 nm for  $\text{Ce}^{3+}$ , 549 nm for  $\text{Tb}^{3+}$  and 700 nm for  $\text{Eu}^{3+}$ .



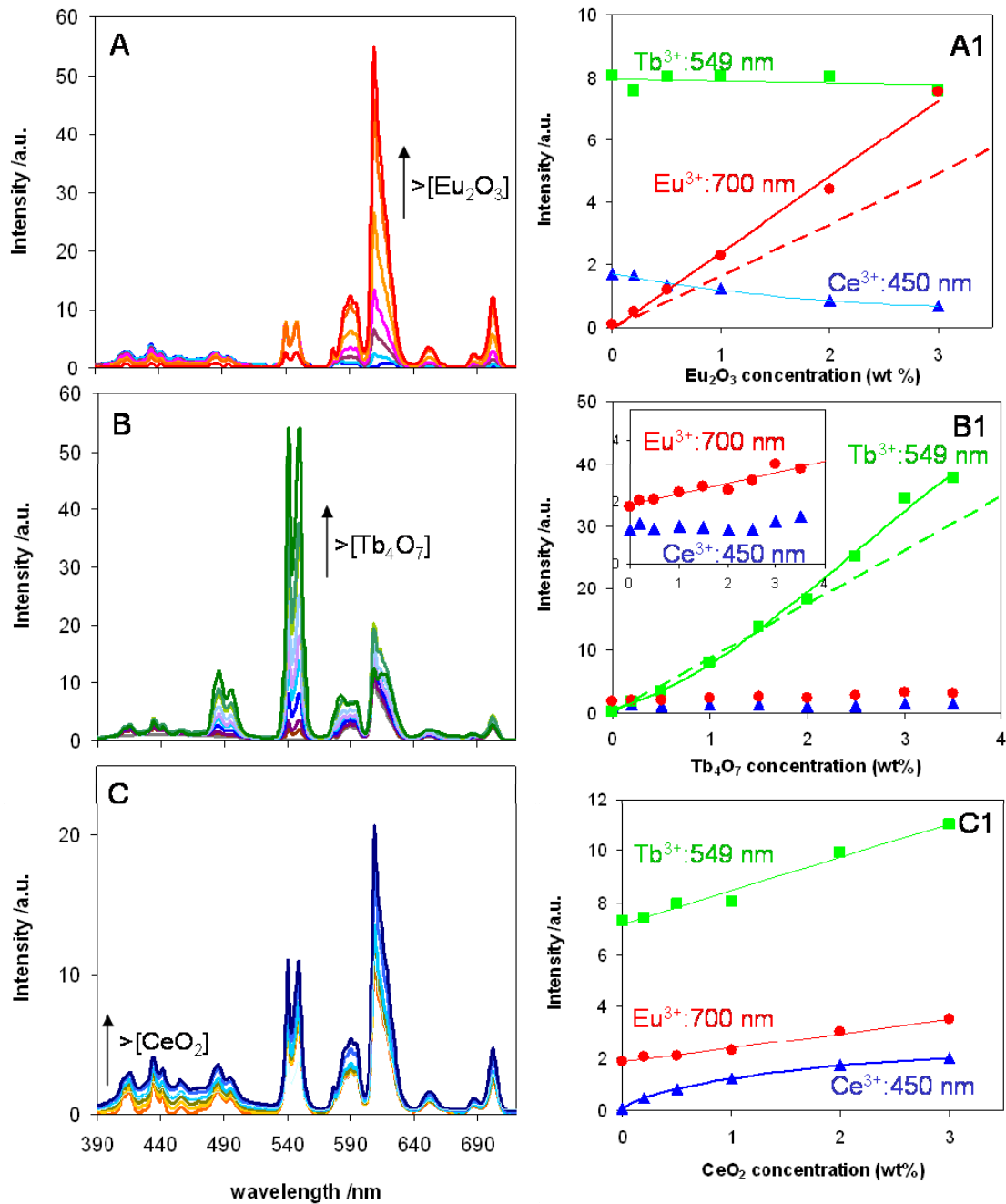


**Figure 3.22.** Luminescence spectra of several glass samples doped with different concentrations of  $\text{Eu}_2\text{O}_3$ ,  $\text{CeO}_2$  and  $\text{Tb}_4\text{O}_7$  as indicated in figure 3.21. Luminescence intensity of  $\text{Ce}^{3+}$  emission at 450 nm (blue triangles), of  $\text{Tb}^{3+}$  emission at 549 nm (green squares) and of  $\text{Eu}^{3+}$  emission at 700 nm (red circles) as function of  $\text{Eu}_2\text{O}_3$  concentration (A1),  $\text{Tb}_4\text{O}_7$  concentration (B1) and  $\text{CeO}_2$  concentration (C1). Dashed lines represent the intensity of  $\text{Eu}^{3+}$  (red) and of  $\text{Tb}^{3+}$  (green) in the absence of the other two lanthanides.

Figure 3.22 A1 shows the PL intensity behaviour of the different ions with the increase of the  $\text{Eu}_2\text{O}_3$  concentration and, as expected, the peak at 700 nm has higher intensities compared with what it was expected for glass samples without terbium and cerium. Figure 3.22 B1 correspond to the PL intensity of the  $\text{Eu}/\text{Tb}/\text{Ce}$  doped samples with different  $\text{Tb}_4\text{O}_7$  concentrations. The  $\text{Tb}^{3+}$  intensity at 549 nm increases, with higher intensities compared to that expected for samples without cerium and europium, while the  $\text{Eu}^{3+}$  intensity at 700 nm also shows a small increment.

Figure 3.22 C1 shows the PL intensities of the glass samples with different  $\text{Ce}^{3+}$  concentrations. The intensity that corresponds to  $\text{Ce}^{3+}$  at 450 nm increases with  $\text{CeO}_2$  concentration although at higher concentrations this intensity reaches a plateau, possibly due to the cerium self-quenching already discussed above. These results are in agreement with what was observed in the binary systems: cerium and terbium enhance the europium red luminescence, cerium enhance the terbium green luminescence and high  $\text{CeO}_2$  concentrations gives rise to self-quenching. These effects are relevant for future glass synthesis: it shows that synthesizing glasses with these elements, red luminescence will be enhanced due to energy transfer and very high amounts of  $\text{CeO}_2$  leads to cerium luminescence quenching.

Next, the luminescence colour coordinates in a CIE chromaticity diagram are calculated. The goal is to study two questions: is it possible to estimate which luminescent colours can be produced for a given composition? Are excited-state processes relevant for luminescence colour coordinates? These questions are going to be discussed in the next sub-chapter.

### 3.3.4. Luminescence Colour Coordinates

Colour characterization has been commonly done by emission or absorption spectrometry. But a spectra gives an objective measure of the interaction of light with matter and do not take in account factors such as the impact on the human eye of the subjective perception of hue, saturation and relative luminescence.<sup>174</sup> During the years different methods to define colour were developed.<sup>175</sup> It is established that all colours can be defined using three parameters and consequently represented in three dimensional coordinate systems.<sup>32</sup>

The 1931 CIE (Commission Internationale de l' Eclairage) standard observer defines a system that classifies colour according to the human visual organization,<sup>175</sup> but in these cases the experiments only covered about  $2^\circ$  angle of vision. More experiments were performed using a  $10^\circ$  angle with lower levels of illumination giving rise to the 1964 CIE standard observer. To reflect properly the colour of luminescence the CIE 1964 xy chromaticity coordinates can be used.<sup>174,176</sup> The x, y, z coordinates are given by:<sup>174</sup>

$$x = \frac{X}{X + Y + Z}; y = \frac{Y}{X + Y + Z}; z = \frac{Z}{X + Y + Z} \quad (3.4)$$

where X, Y and Z are the tristimulus values (equation 3.5):

$$X = \int E(\lambda) \overline{x}_{10}(\lambda) d\lambda \quad Y = \int E(\lambda) \overline{y}_{10}(\lambda) d\lambda \quad Z = \int E(\lambda) \overline{z}_{10}(\lambda) d\lambda \quad (3.5)$$

being  $E(\lambda)$  the spectral energy emitted and  $\overline{x}_{10}(\lambda)$ ,  $\overline{y}_{10}(\lambda)$  and  $\overline{z}_{10}(\lambda)$  the three colour-matching functions (Figure 3.23), that correspond to the three primary colours red, green and blue, for

any wavelength  $\lambda$  in the human visual range of 380 through 780 nm, also called as red, green and blue cones.<sup>177</sup> The 1964 10 °CIE standard colorimetric observer data for a full set of 1nm was determined using a colour perception average of different observers between 380 and 780 nm and can be taken from <http://www.cis.rit.edu/mcsl/online/cie.php>. But z can be calculated using x and y:  $z=1-(x+y)$ , therefore the colour coordinates can be represented only by x and y.

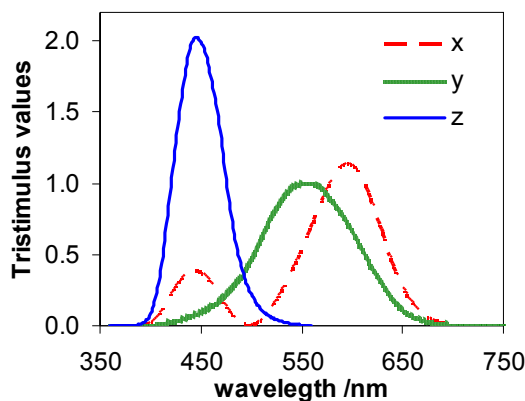


**Figure 3.23.** Colour matching functions,  $x_{10}(\lambda)$ ,  $y_{10}(\lambda)$  and  $z_{10}(\lambda)$  of the 1964 CIE standard observer

With this information the luminescence colour coordinates can be calculated for all the glasses using the emission spectra and can be represented in a bi-dimensional colour diagram. Luminescence colour coordinates for the samples doped with one lanthanide were calculated (Figure 3.24).

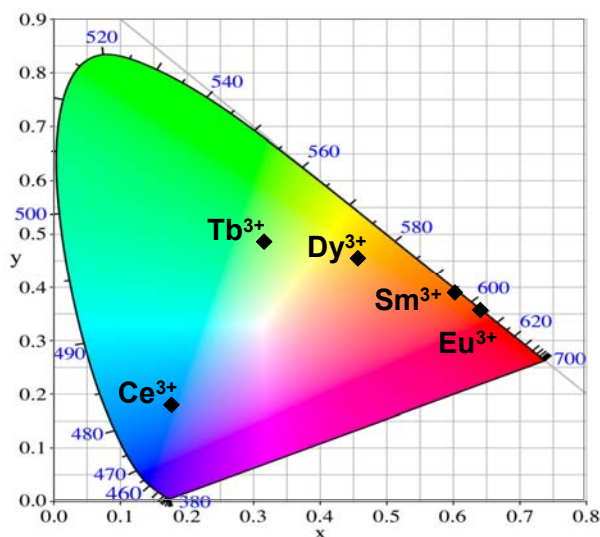


**Figure 3.24.** CIE diagram with the colour coordinates of glass samples doped with 2 % (wt) of different lanthanides:  $\text{Eu}_2\text{O}_3$ ,  $\text{Sm}_2\text{O}_3$ ,  $\text{Dy}_2\text{O}_3$ ,  $\text{Tb}_4\text{O}_7$  and  $\text{CeO}_2$  ( $\lambda_{\text{exc}} = 377 \text{ nm}$ ).

CIE chromaticity diagram can be used to understand which luminescent colours are accessible for a given composition range. Using  $\text{Eu}^{3+}$ ,  $\text{Tb}^{3+}$  and  $\text{Ce}^{3+}$  it is possible to obtain glasses with all luminescent colours that are inside the triangular area observed in the CIE diagram of figure 3.25 and consequently it is also possible to obtain white luminescent glasses.

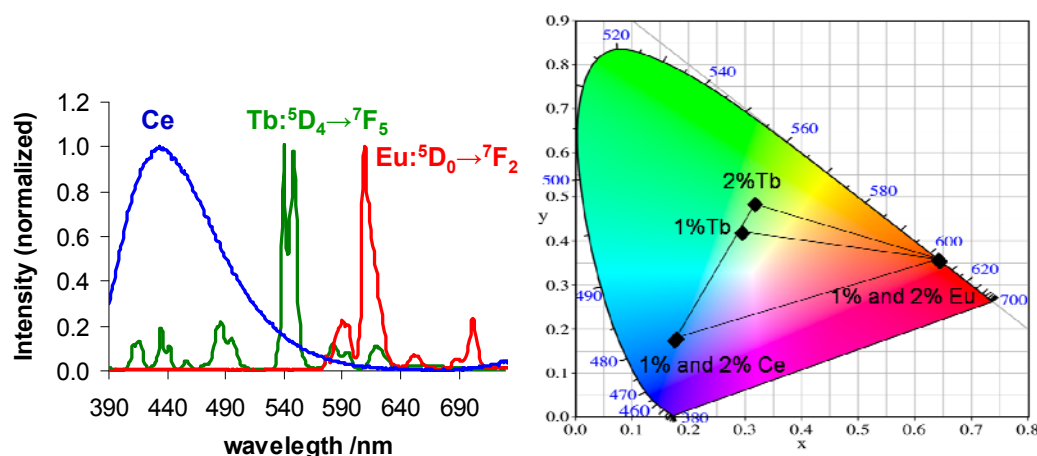


**Figure 3.25.** (Left side) Luminescence spectra of glass samples doped with 2% (wt %) of  $\text{CeO}_2$  (blue line),  $\text{Tb}_4\text{O}_7$  (green line) and  $\text{Eu}_2\text{O}_3$  (red line). (Right side) CIE diagram with the colour coordinates of the glass samples with 1 and 2% of  $\text{Tb}_4\text{O}_7$ , 1 and 2% of  $\text{CeO}_2$  and 1 and 2% of  $\text{Eu}_2\text{O}_3$ .

The luminescence colour coordinates should be the same for the several lanthanides in different concentrations, as it happens in  $\text{Ce}^{3+}$  and  $\text{Eu}^{3+}$  cases, because the spectrum shape is the same and what changes is the intensity. But in the terbium case the colour coordinates are different for 1% and 2% of  $\text{Tb}_4\text{O}_7$ . Analysing carefully the normalized emission spectra of the two samples (section 9.2.3, Supplementary Material) it is observed that the transitions in the blue part of the spectrum have different relative intensities, so the colour coordinates are not going to be the same. It is important to pay attention to this detail when analysing the binary and ternary systems.

Glasses doped with two lanthanide oxides colour coordinates were calculated from the emission spectra, see figure 3.26. All the colour coordinates are in the triangles lines, as it was expected, since we are just using two lanthanides in the glass synthesis and changing their concentration.

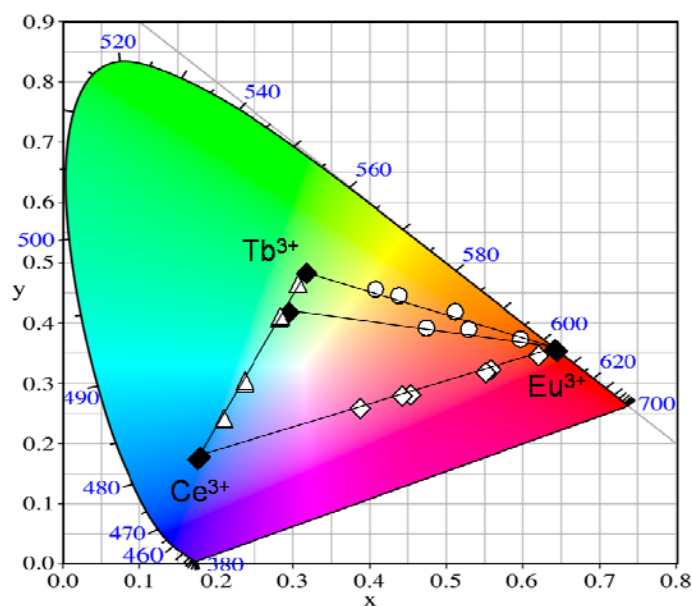


**Figure 3.26.** CIE diagram with the colour coordinates of the binary system glass samples (table 3.1): Black squares – doped with one lanthanide; white rhombus –  $\text{Eu}^{3+}/\text{Ce}^{3+}$  system; white triangles –  $\text{Tb}^{3+}/\text{Ce}^{3+}$  system; white circles –  $\text{Eu}^{3+}/\text{Tb}^{3+}$  system ( $\lambda_{\text{exc}} = 377 \text{ nm}$ ).

With the mixture of two lanthanides a large range of colours can be obtained. The colour coordinates observed in figure 3.28 are influenced not only by the lanthanides composition fraction used in each glass but also from the excited-state processes that occur in each system. Is it possible to understand if an excited-state process is occurring comparing the lanthanides fraction used in the glass synthesis with the fraction calculated from the obtained colour coordinates?

To answer this question the lanthanides fraction is going to be calculated using the colour coordinates are going to be made using equations 3.6 and 3.7:

$$x = x_{L1}f_{L1} + x_{L2}f_{L2} \quad (3.6)$$

$$y = y_{L1}f_{L1} + y_{L2}f_{L2} \quad (3.7)$$

where  $x$  and  $y$  are the sample colour coordinates,  $x_{L1}$ ,  $x_{L2}$ ,  $y_{L1}$  and  $y_{L2}$  are the colour coordinates of the glass samples doped only with lanthanide L1 or lanthanide L2 and  $f_{L1}$  and  $f_{L2}$  the lanthanides luminescence fraction. The calculated lanthanides luminescence fraction are in section 9.2.4, Supplementary Material, and are also represented in figure 3.28 for all the binary systems in study (A-Eu<sup>3+</sup>/Tb<sup>3+</sup>, B-Eu<sup>3+</sup>/Ce<sup>3+</sup> and C-Tb<sup>3+</sup>/Ce<sup>3+</sup>) compared with their molar fractions.

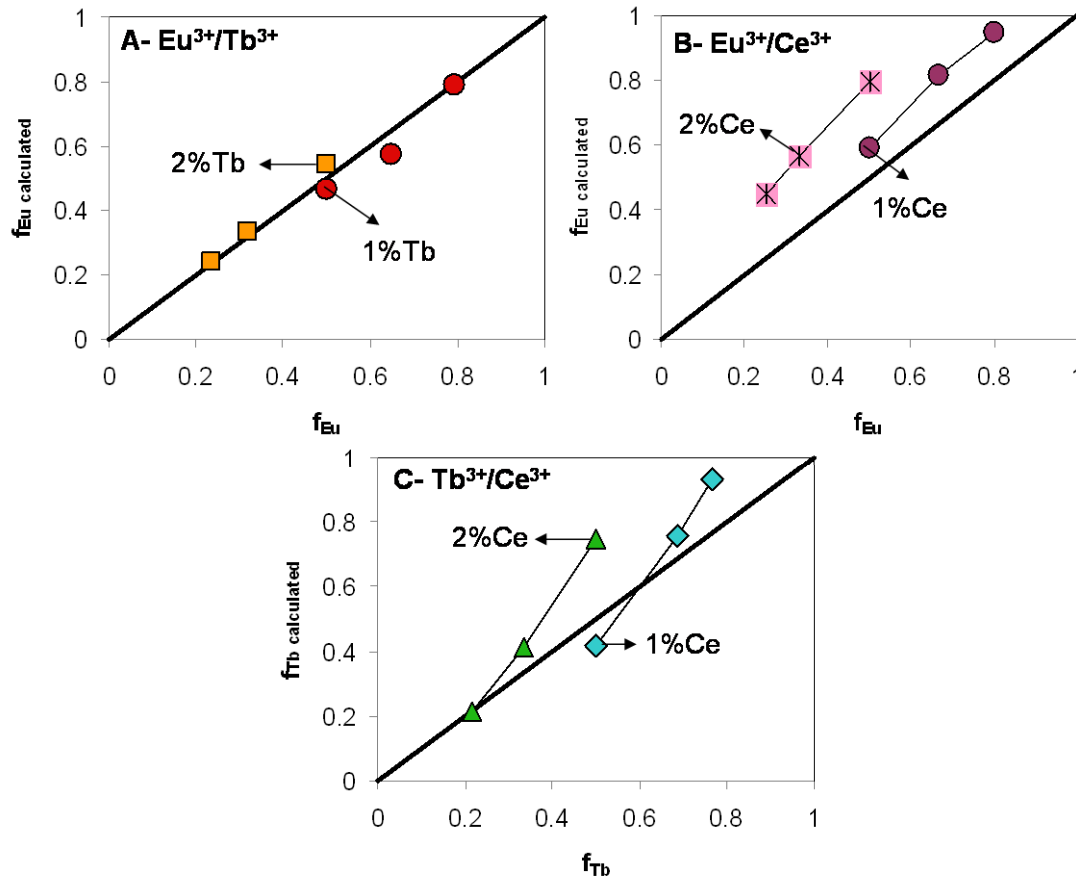


**Figure 3.27.** (A)  $f_{Eu}$  calculated from the colour coordinates vs  $f_{Eu}$  used in the glass synthesis, for the binary system  $Eu^{3+}/Tb^{3+}$ , with two different  $Tb_4O_7$  concentrations: 1% (red circles) and 2% (orange squares). (B)  $f_{Eu}$  calculated from the colour coordinates vs  $f_{Eu}$  used in the glass synthesis, for the binary system  $Eu^{3+}/Ce^{3+}$ , with two different  $CeO_2$  concentrations 1% (purple circles) and 2% (pink squares). (C)  $f_{Tb}$  calculated from the colour coordinates vs  $f_{Tb}$  used in the glass synthesis, for the binary system  $Tb^{3+}/Ce^{3+}$ , with two different  $CeO_2$  concentrations 1% (green triangles) and 2% (blue rhombus).

Figure 3.27 illustrate the lanthanide fraction calculated from the colour coordinates (equations 3.6 and 3.7) versus the lanthanide molar fraction used in the glass synthesis. Figure 3.27A allows us to compare the calculated europium fraction ( $f_{Eu}$  calculated) with the europium molar fraction that was used to synthesize the glass samples ( $f_{Eu}$ ). The obtained values are very close to  $f_{Eu}$  indicating that the colour coordinates are not affected by excited-state processes between  $Tb^{3+}$  and  $Eu^{3+}$ . In the case of  $Eu^{3+}/Ce^{3+}$  and  $Tb^{3+}/Ce^{3+}$  systems the calculated  $f_{Eu}$  and  $f_{Tb}$ , respectively, are higher than those used in the synthesis. This indicates that energy-transfer from  $Ce^{3+}$  to  $Eu^{3+}$  and  $Tb^{3+}$  in the two binary systems indeed affect the colour coordinates.

After studying the binary systems it is possible to proceed to the ternary system with a mixture of three lanthanides. The luminescence colour coordinates were determined for all the glass samples of this system (Table 3.1): Glasses doped with  $Eu_2O_3$ ,  $CeO_2$  and  $Tb_4O_7$ , changing  $Eu_2O_3$  concentration ( $xEu_2O_3 + 1\%Tb_4O_7 + 1\%CeO_2$  and  $4.5\%Eu_2O_3 + 0.5\%Tb_4O_7 + 0.5\%CeO_2$ ),  $Tb_4O_7$  concentration ( $1\%Eu_2O_3 + xTb_4O_7 + 1\%CeO_2$  and  $0.5\%Eu_2O_3 + 4.5\%Tb_4O_7 + 0.5\%CeO_2$ )

and  $\text{CeO}_2$  concentration ( $1\%\text{Eu}_2\text{O}_3 + x\text{Tb}_4\text{O}_7 + 1\%\text{CeO}_2$  and  $0.5\%\text{Eu}_2\text{O}_3 + 0.5\%\text{Tb}_4\text{O}_7 + 4.5\%\text{CeO}_2$ ), wt%. The obtained colour coordinates are represented in figure 3.28.

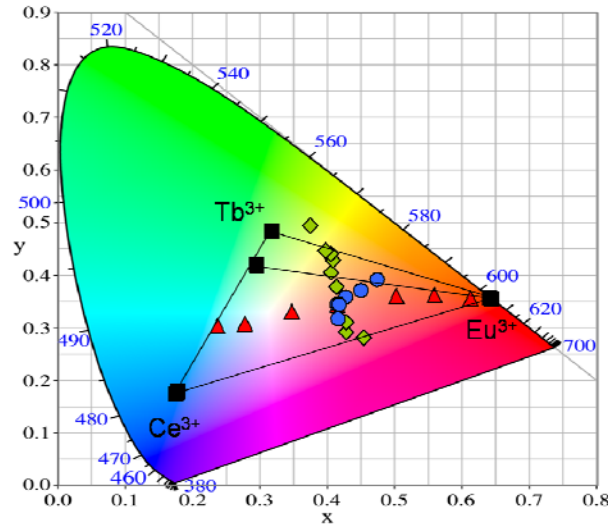


**Figure 3.28.** CIE diagram with the colour coordinates of the ternary system glass samples (table 3.1): Black squares – doped with one lanthanide; green rhombus – changing  $\text{Tb}_4\text{O}_7$  concentration; red triangles – changing  $\text{Eu}_2\text{O}_3$  concentration; blue circles – changing  $\text{CeO}_2$  concentration ( $\lambda_{\text{exc}} = 377 \text{ nm}$ ).

Several colours were obtained which is very significant to the development of new luminescent colours. Concerning the white luminescence, only one sample in figure 3.28 is near the colour coordinates  $x=0.33$ ,  $y=0.33$ :  $1\%\text{Tb}_4\text{O}_7 + 0.5\% \text{Eu}_2\text{O}_3 + 1\% \text{CeO}_2$  with colour coordinates around  $x=0.34$  and  $y=0.33$ . But the luminescent colour change with the excitation light source, so different colours can be obtained using other excitation wavelengths.<sup>176</sup> This fact is illustrated in figure 3.29, where the  $\lambda_{\text{exc}}$  used was 373 nm. With this excitation wavelength other colours are obtained and more samples are very close of the white luminescence.

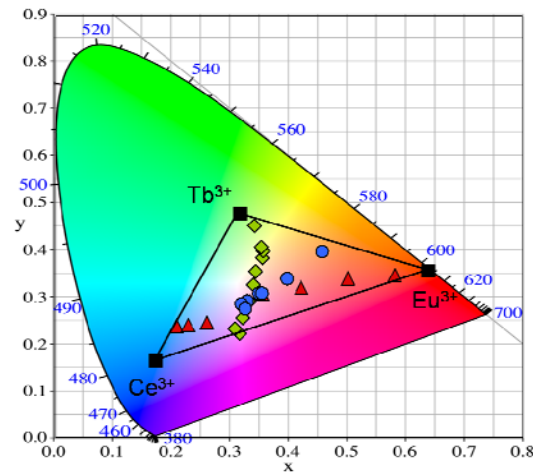


**Figure 3.29.** CIE diagram with the colour coordinates of the ternary system glass samples (table 3.1): Black squares – doped with one lanthanide; green rhombus – changing  $\text{Tb}_4\text{O}_7$  concentration; red triangles – changing  $\text{Eu}_2\text{O}_3$  concentration; blue circles – changing  $\text{CeO}_2$  concentration ( $\lambda_{\text{exc}} = 373 \text{ nm}$ ).

The same calculations made in the binary system were also performed using equations 3.8, 3.9 and 3.10, in order to observe if any excited-state processes affect the colour coordinates.

$$x = x_{Ce}f_{Ce} + x_{Tb}f_{Tb} + x_{Eu}f_{Eu} \quad (3.8)$$

$$y = y_{Ce}f_{Ce} + y_{Tb}f_{Tb} + y_{Eu}f_{Eu} \quad (3.9)$$

$$1 = f_{Ce} + f_{Tb} + f_{Eu} \quad (3.10)$$

where  $x$  and  $y$  are the sample colour coordinates,  $x_{Eu}$ ,  $x_{Tb}$ ,  $x_{Ce}$ ,  $y_{Eu}$ ,  $y_{Tb}$  and  $y_{Ce}$  the colour coordinates of the glass samples doped only with one lanthanide and  $f_{Eu}$ ,  $f_{Tb}$  and  $f_{Ce}$  the lanthanides fraction. The calculated lanthanides fractions are in section 9.2.4, Supplementary Material, and are also represented in figure 3.30.

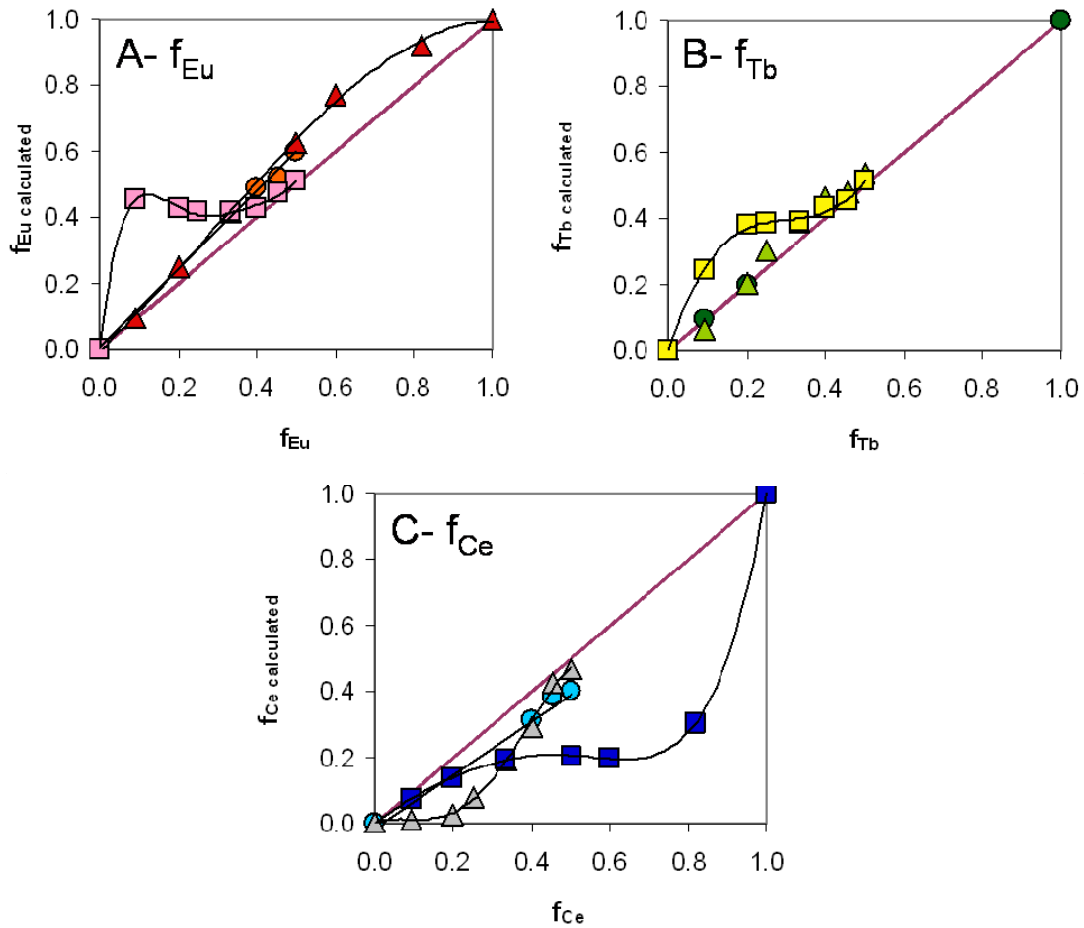


**Figure 3.30.** (A)  $f_{Eu}$  calculated from the colour coordinates vs  $f_{Eu}$  used in the glass synthesis, for the ternary system changing Eu (red triangles), Tb (orange circles) and Ce concentration (pink squares) (B)  $f_{Tb}$  calculated from the colour coordinates vs  $f_{Tb}$  used in the glass synthesis, for the ternary system changing Eu (light green triangles), Tb (dark green circles) and Ce concentration (yellow squares) (C)  $f_{Ce}$  calculated from the colour coordinates vs  $f_{Ce}$  used in the glass synthesis, for the ternary system changing Eu (grey triangles), Tb (light blue circles) and Ce concentration (dark blue squares).



As it was referred the luminescence colour coordinates of the samples doped only with terbium, change with the  $\text{Tb}_4\text{O}_7$  concentration (figure 3.26). For that reason the colour coordinates correspondent to the ternary glasses with high  $\text{Tb}_4\text{O}_7$  contents were not used in this analysis. Observing figure 3.30 A the  $f_{\text{Eu}}^{\text{calculated}}$  values are higher than  $f_{\text{Eu}}$ , except for high  $\text{CeO}_2$  concentrations, indicating that europium luminescence enhancement by the presence of the other two lanthanide ions affects the colours coordinates in the ternary systems. Concerning the  $f_{\text{Tb}}^{\text{calculated}}$  (figure 3.30 B), these values are very similar, except for low cerium concentrations, due to the  $\text{Ce}^{3+}/\text{Tb}^{3+}$  energy-transfer. Increasing the  $\text{CeO}_2$  concentration it occur the same problem referred before. The  $f_{\text{Ce}}^{\text{calculated}}$  values are all lower than  $f_{\text{Ce}}$  (figure 3.30 C), inclusive with the increase of  $\text{CeO}_2$  concentration. This result indicates the decrease of  $\text{Ce}^{3+}$  luminescence in europium and terbium presence and also with high cerium concentrations. All of the observations taken from figure 3.30 are in accordance with what was discussed previously. Only energy-transfer from  $\text{Tb}^{3+}$  to  $\text{Eu}^{3+}$  has a minor impact on the colour coordinates. The CIE diagram and the luminescence colour coordinates allowed us to understand what colours could be obtained using europium, terbium and cerium oxides in a glass composition. It was also possible to detect the enhancement and quenching of the luminescence of the different lanthanides showing that the colour coordinates calculation can also be a tool to understand the impact of excited-state processes. Finally it is also important to have in mind that the initial fractions of lanthanides may not be exactly the same that exists in glass after fusing it at  $1400^\circ\text{C}$ , due to oxides losses at that temperature or due to the existence of different oxidations states in the glass samples.

### 3.4. Conclusions

Lanthanide ions doped soda-lime silicate glasses gave rise to a diverse luminescent colour palette. Using europium, terbium and cerium that emit red, green and blue, respectively, several colours were created and it was also demonstrated that white luminescence can be obtained. The same glass sample has different colours by changing the excitation light, allowing higher tunability of luminescent colours and higher possibilities of obtaining the white luminescence.

The spectroscopic measurements of the lanthanides doped samples indicated the presence of excited-state processes such as energy transfer and also self-quenching of  $\text{Ce}^{3+}$ . It was shown that synthesizing glasses with these elements red luminescence will be enhanced due to energy transfer and it is not possible to use very high amounts of  $\text{CeO}_2$  because it suppresses the luminescence.

The large range of produced colours was demonstrated and represented by the luminescence colour coordinates of all the synthesized glasses. In this chapter it was shown that using the CIE chromaticity diagram and the colour coordinates it can be estimated which luminescent colour can be produced for a given composition. Moreover it is possible to detect if an excited-state process is occurring by calculating the lanthanides factors and compare them with the

ones used in the glass synthesis. Nevertheless the energy transfer process, for example, has to be significant to influence the colour coordinates and therefore to influence the factors calculation. This work also presents a practical strategy to detect if excited-states processes are occurring in a given system.

## Chapter 4 – Luminescent aluminoborosilicate glass with lead halide nanoparticles and cuprous ion

In this chapter the main goal is to show glass photoluminescence without using rare earths. The strategy involved the synthesis of aluminoborosilicate glasses, where the formation of lead halide nanoparticles is described. These glasses are photoluminescent at room temperature, when halides (chloride, bromide or iodide) are added to the glasses containing  $\text{Pb}^{2+}$ . Using the same base glass composition, photoluminescent aluminoborosilicate glasses with  $\text{Cu}^+$  are also synthesized and described. Different photoluminescent colours are achieved by changing the copper concentration in the presence of lead halide nanoparticles. The luminescent colour coordinates were determined for all the synthesized glasses.

### 4.1. Luminescent glasses without lanthanide oxides

Glasses doped with lanthanide oxides are commonly used to produce luminescent glasses, but due to their high cost other alternatives are being investigated. Different approaches were studied, such as the formation of luminescent nanoparticles in the glass matrix (e.g.  $\text{ZnSe}$ ,  $\text{ZnS}$ ,  $\text{Cd}_{1-x}\text{Mn}_x\text{S}$ ,  $\text{PbS}$  and  $\text{Ag}$  nanoparticles)<sup>86,87,89,178</sup> or the glass synthesis with d transition metals in a determined oxidation states (e.g.  $\text{Cu}^+$  and  $\text{Mn}^{2+}$ ). In this thesis two different strategies were used to obtain luminescent glasses: the formation of lead halide nanoparticles and the synthesis of glasses with  $\text{Cu}^+$ . A essential feature to achieve this goal is the use of multi-component glass, i.e., including several “network formers” such as Si or B, “network modifiers” that act essentially as to counter-ions for negatively charged defects, usually alkali metals but also Pb, and “intermediate” metals (between the two “extreme” cases) such as Ca or Al.<sup>15</sup> Silver photochromic glasses are one example of multi-component glass since they allow the segregation of silver halide colloids essential for the photochromic effect (formation of silver nanoparticles). Multi-component glass is, therefore, the most promising materials for the development of luminescent glass by forming luminescent centres such as lead halide particles.<sup>17</sup>

Lead halides have many interesting properties due to their unique interactions with light. Indeed, it is known that lead halides can undergo processes such as photolysis and photoluminescence, which are generically related with photo-induced electron-transfer processes.<sup>179,180,181</sup> Several studies focusing on these aspects are available, with special relevance for photoluminescence spectroscopy motivated by applications of lead halides crystals in scintillator detectors of high-energy radiation (such as  $\gamma$  and X-rays).<sup>179,182</sup> The photoluminescence behavior of lead halides

has been attributed to the electron-transfer from the halide to lead, in a similar way to what is observed on silver halide.<sup>181,183,184</sup> Like silver halides, light irradiation with adequate intensity and wavelength can give rise to lead metallic nanoparticles (these nanoparticles have been matter of big interest due to their applications in photography<sup>179</sup>). However in many cases a transient  $\text{Pb}_2^{3+}$  species (STEL, self-trapped electron center, while the halide gives rise to a self-trapped hole, STH,  $\text{X}_2^-$ ) is formed, see figure 4.1, within the crystal where through a back electron-transfer process gives rise to a self-trapped exciton (STE) responsible for the photoluminescence.<sup>183,184,185,186</sup>

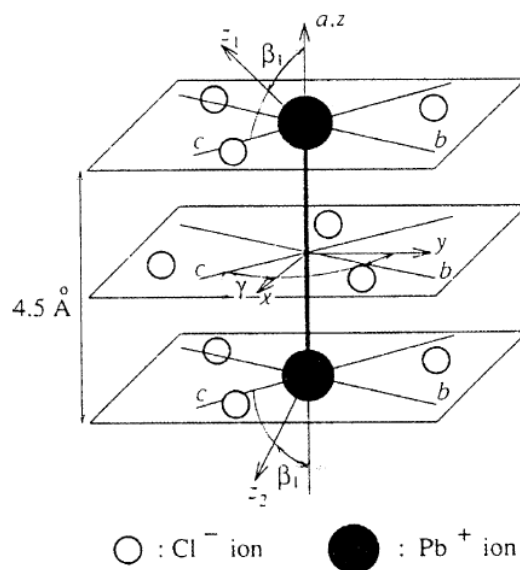


**Figure 4.1.** Schematic model of the  $\text{Pb}_2^{3+}$  STEL center in  $\text{PbCl}_2$  and the orientation of the coordinate axes. This scheme was taken from Nistor, Phys. Rev. B, 48 (1993) 9575-9580.<sup>181</sup>

At room temperature, thin films of these crystals have limited stability, due to moisture attack, a problem which may be overcome with suitable protective films.<sup>179</sup> A glass matrix can be a more stable solution to obtain lead halide nanoparticles at room temperature. To the best of our knowledge the majority of lead halides photoluminescence studies were performed at very low temperatures.<sup>180,183,184,186,187,188,189,190</sup>

Glass preparation, including silicate glass, containing nanocrystalline particles of lead halides,<sup>191,192</sup>  $\text{PbS}$ <sup>193</sup> or  $\text{PbWO}_4$ <sup>191,194</sup> were described in the past, normally with the aim to obtain scintillation materials. Lead halides on borate glass are known to undergo the formation of crystallites in controlled conditions, in some cases using a multicomponent glass matrix.<sup>186,191</sup> Moreover, these particles offer an opportunity to do experimental studies of photoinduced charge-transfer processes on transparent glass.

Other element that can give rise to luminescent glasses is copper.  $\text{Cu}^+$  exhibit a characteristic luminescence assigned to the electronic transition  $3d^9 4s^1 \rightarrow 3d^{10}$ . Over time crystals and glasses doped with  $\text{Cu}^+$  have received some attention by several investigators due to their possible applications for example in laser and photonic technology, for X-ray imaging, in thermoluminescence dosimeter phosphors and as blue component of full colour

electroluminescent display devices.<sup>79</sup> Contrarily to what happens with trivalent lanthanide ions, which have sharp emission lines weakly influenced by the environment influence, in  $\text{Cu}^+$  case, due to the 3d-4s transitions, the emission spectrum usually consists of a broad band strongly dependent of the surrounding environment. For this reason  $\text{Cu}^+$  luminescence becomes very attractive not only in the technological field, e.g. tunable laser emission,<sup>80,195</sup> but also in the art field, allowing higher tunability of luminescent colours. On the other hand, in some cases the luminescence of transition metal ions in oxide glasses can be very weak. One of the major reasons of this low intensity is concentration quenching. The optical absorption and luminescent properties of  $\text{Cu}^+$  in different hosts can be found in the literature such as in alkali sulphates,<sup>79</sup> phosphates,<sup>79</sup> zeolites<sup>196</sup> and in different glasses such as borate,<sup>197,198,199</sup> phosphate<sup>197,200</sup> and silicate glasses.<sup>77,78,201,202</sup>

In order to obtain luminescent glasses without using lanthanides and with luminescent colours more dependent of the surrounding composition, in this chapter aluminoborosilicate glasses with metals, such as lead halides and copper, were synthesized and the photoluminescence obtained was characterized. These glass systems allows us to produce glasses with lead halides with luminescence under a UV-light, at room temperature, while in the past this photoluminescence was obtained at cryogenic conditions.<sup>180,183,184,186,187,188,189,190</sup>  $\text{Pb}^{2+}$  in the presence of chloride or bromide is responsible for a broad emission band at 435 nm, resulting in a blue luminescence, while  $\text{Cu}^+$  gives rise to a broad emission band at 600 nm, resulting in a yellow luminescence. These two elements were introduced in the glass matrix in order to obtain different luminescent colours by changing their relative concentrations. Luminescence colour coordinates were calculated for the synthesized glasses.

## **4.2. Experimental Part**

### **4.2.1. Synthesis and samples preparation**

A multi-component glass composition was taken from the literature:<sup>17</sup> 54.15%  $\text{SiO}_2$ , 16.04%  $\text{B}_2\text{O}_3$ , 9.12%  $\text{Al}_2\text{O}_3$ , 1.91%  $\text{ZrO}_2$ , 4.31%  $\text{PbO}$ , 6.62%  $\text{BaO}$ , 2.31%  $\text{Li}_2\text{O}$ , 3.01%  $\text{Na}_2\text{O}$ , 1.40%  $\text{K}_2\text{O}$ , 0.03%  $\text{CuO}$ , 0.50%  $\text{Cl}$ , 0.10%  $\text{F}$  and 0.50%  $\text{Br}$ , wt%) and a luminescent glass was synthesized. To study this luminescence, several glasses were synthesized containing different components (table 4.1). Glasses 1 and 3 were also doped with different  $\text{CuO}$  concentrations (table 4.2).

**Table 4.1.** Synthesized glasses and the different components used in each glass.

Glasses	Oxides and halogens in the glass composition					
	Base glass: SiO <sub>2</sub> +B <sub>2</sub> O <sub>3</sub> +Al <sub>2</sub> O <sub>3</sub> + Li <sub>2</sub> O+Na <sub>2</sub> O+K <sub>2</sub> O	BaO	ZrO <sub>2</sub>	PbO	CuO	Halogens (F+Cl+Br)
1	✓	✓	✓	✓	✓	✓
2	✓	✓	✓	✓	X	✓
3	✓	✓	✓	✓	✓	X
4	✓	✓	X	✓	X	✓
5	✓	✓	✓	X	X	✓
6	✓	✓	X	X	X	✓
7	✓	✓	X	✓	X	X
8	✓	✓	X	X	X	X
9 (base glass)	✓	X	X	X	X	X
10	✓	X	X	✓	X	X
11	✓	X	X	✓	X	✓
12	✓	X	X	X	✓	X
13	✓	X	X	✓	✓	X

**Table 4.2.** Glasses 1 and 3 (without halides) with different CuO concentrations (wt %).

Glass samples		CuO (wt%)
1	3 – without halides	
1a	3a	0.00
1b	3b	0.00375
1c	3c	0.0075
1d	3d	0.015
1e	3e	0.030
1f	3f	0.045
1g	3g	0.06

Additionally in this chapter aluminoborosilicate glasses were synthesized using the following base composition: 55.84 SiO<sub>2</sub>, 16.55 B<sub>2</sub>O<sub>3</sub>, 9.41 Al<sub>2</sub>O<sub>3</sub>, 6.82 BaO, 3.1 Na<sub>2</sub>O, 1.45 K<sub>2</sub>O, 2.38 Li<sub>2</sub>O and 4.45 PbO (wt %); the different halogens (X), fluoride, chloride, bromide and iodine, were added to the glass composition with a molar ratio (r) of X/Pb=1.33. The quantity of oxides used to prepare the different glass compositions can be found in section 9.3.1, Supplementary Material. Reagent grade SiO<sub>2</sub> (p.a., Fluka), B<sub>2</sub>O<sub>3</sub> (99%, Acros Organics), Al<sub>2</sub>O<sub>3</sub> (p.a. Merk), ZrO<sub>2</sub> (p.a., Riedel-de Haën), Pb<sub>3</sub>O<sub>4</sub> (97%, Panreak), BaO (Aldrich), Li<sub>2</sub>CO<sub>3</sub> (p.a., Fluka), Na<sub>2</sub>CO<sub>3</sub> (p.a., Riedel de Haen), K<sub>2</sub>CO<sub>3</sub> (p.a., Panreak), CuO (p.a. Merk), NaCl (p.a., Panreak), NaF (Merk), NaBr (Merk) and NaI (Merk) were used as starting materials.

In this synthesis, approximately 30 g batches were made, mixing was done in a Shaker powder mixer (turbula T2F), and melted inside platinum crucibles in an electric furnace at 1300 °C for 1.5 hours in air, see figure 4.2. To be easier to pour the glasses, the temperature was increased to 1400°C and then the melted glasses were quenched pouring them into a metal sheet at room temperature, and further annealed at about 650°C for 15 minutes. The glass samples were cut and carefully polished, for optical measurements, with 0.6 cm thickness and 0.9 cm width.

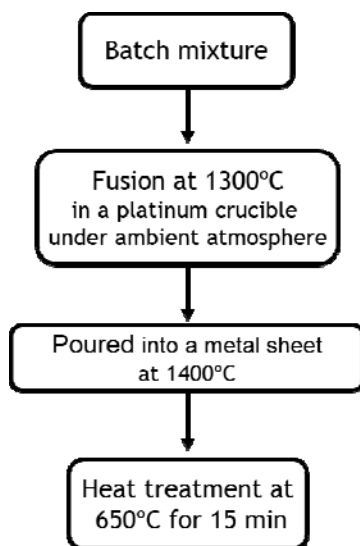


**Figure 4.2.** Synthesis conditions of the different aluminoborosilicate glasses studied.

#### **4.2.2. Measurements**

Different techniques were used in order to better understand the luminescence and structure of the synthesized glasses. Equipment descriptions are given bellow:

**Spectroscopic Measurements** - UV/Vis absorbance spectra were recorded using a Varian Cary-5000 UV/VIS/NIR spectrophotometer over the 300-2300 nm wavelength range with a 1 nm resolution. Luminescence spectra were measured using a SPEX Fluorolog-3 Model FL3-22 spectrofluorimeter, with 5 nm slits. Experiments were performed at room temperature (293 K) and at 77K.

**Transmission electron microscopy (TEM)** - Images were obtained with a Hitachi H9000, operated microscope at 300 kV. The samples were ground, suspended in ethanol, dropped and evaporated on a copper grid.

**Energy dispersive X-ray spectroscopy (EDS)** - Analyses were carried out with a ThermoNoran device in a semiquantitative way with a resolution of 138 eV.

**X-ray Diffraction experiments (XRD)** - X-ray powder diffractometer Philips X'Pert MPD using Cu K $\alpha$  radiation,  $\lambda=1.540598$  Å, with step width 0.02°.

**Raman spectroscopy** - Labram 300 Jobin Yvon spectrometer, equipped with a solid state laser operating at 532 nm.

**Glass transition temperature ( $T_g$ ) and coefficients of thermal expansion (CTE) measurements** – These values were obtained with a Dilatometer Netvcshe Dil402PC ) from 25 to 700°C with a heating rate of 5 K.min<sup>-1</sup>. To do these analyses the samples were cut and polished with 0.5 cm thickness, 0.5 cm width and 2.5 cm length.

**Time-resolved luminescence spectra** - Flash Photolysis equipment LKS.60 nanosecond laser photolysis spectrometer from Applied Photophysics, with a Brilliant Q-Switch Nd-YAG laser from Quantel, using the third harmonics ( $\lambda_{ex}$  = 355 nm, laser pulse half width equal to 6 ns).

**Single photon counting (SPC)** - Time-correlated single-photon counting (TCSPC) option on the FluoroLog-3 spectrofluorimeter (Horiba Jobin Yvon). A sample, placed in a single sample chamber static thermostated cuvette holder maintained at 293 K, was excited with vertically polarized 372 nm pulses from a NanoLED (fwhm <1.0 ns), at a repetition rate of 100 kHz. Measurements were done by collecting repeated sequences of 60 s vertically (parallel) and 60 s horizontal (perpendicular) polarized fluorescence emission. Individual photons were detected by a Hamamatsu R928 photomultiplier tube and arrival times were stored in 4096 channels (0.8 ns channel width) of an IBH Data Station Hub photon counting module. Data rate was set proportional to the source repetition rate up to ~2% to avoid photon pileup artifacts. Typical measurements involved accumulation of a maximum count per channel of at least 10000 in the difference function IVV-GIVH. The instrument response function (fwhm <1.0 ns) was obtained at 372 nm with a suspension of Ludox (colloidal silica beads) in water. The G factor was obtained by measuring two additional decays, IHV(t) and IHH(t), and the value used in later analysis was created from the average of several repeated measurements. Both luminescence decays and time-resolved luminescence anisotropy were measured at room temperature.

#### **4.3. Synthesis and characterization of luminescent glasses in aluminoborosilicate glass using different metals: lead halides and CuO**

Luminescent aluminoborosilicate glasses doped with lead halides and with CuO were synthesized and afterwards characterized. During an investigation concerning photochromic glasses, a multi-component glass was synthesized and a luminescent glass was obtained, using a composition taken from the literature,<sup>17</sup> (glass **1** - 54.15% SiO<sub>2</sub>, 16.04% B<sub>2</sub>O<sub>3</sub>, 9.12% Al<sub>2</sub>O<sub>3</sub>, 1.91% ZrO<sub>2</sub>, 4.31% PbO, 6.62% BaO, 2.31% Li<sub>2</sub>O, 3.01% Na<sub>2</sub>O, 1.40% K<sub>2</sub>O, 0.03% CuO, 0.50% Cl, 0.10% F and 0.50% Br, wt%). see Figure 4.3.





**Figure 4.3.** Glass sample 1, under a UV light (365 nm).

To initiate the study of this luminescence some components were removed from the glass composition in order to understand its origin, as shown in table 4.3.

**Table 4.3.** Different components used in the synthesized glasses, besides the base glass ( $\text{SiO}_2 + \text{B}_2\text{O}_3 + \text{Al}_2\text{O}_3 + \text{Alkaline oxides}$ ), ✓ when the components are added to the base glass, X when they are not. The correspondent colour at day light and the colour obtained exciting the glasses with a 370 nm UV-light.

Glasses	Oxides and halogens in the glass composition					Daylight	Luminescence
	BaO	ZrO <sub>2</sub>	PbO	CuO	Halogens (F+Cl+Br)	Colour	(370 nm)
1	✓	✓	✓	✓	✓	blue	pink / white
2	✓	✓	✓	X	✓	-	Blue
3	✓	✓	✓	✓	X	blue	yellow
4	✓	X	✓	X	✓	-	blue
5	✓	✓	X	X	✓	-	-
6	✓	X	X	X	✓	-	-
7	✓	X	✓	X	X	-	-
8	✓	X	X	X	X	-	-
9 (base glass)	X	X	X	X	X	-	-
10	X	X	✓	X	X	-	-
11	X	X	✓	X	✓	-	blue
12	X	X	X	✓	X	blue	green
13	X	X	✓	✓	X	blue	yellow

The results summarized in table 4.3 demonstrate that the essential components for the blue luminescence are PbO and the halogens mixture Z (F+Cl+Br) and for the yellow luminescence CuO and PbO.

Two independent sources of luminescence are found in these glasses, one that gives rise to a blue luminescence, where lead and a mixture of halogens have a very important role, and other that gives rise to a yellow luminescence, where CuO seems to be the major responsible of these luminescence. In a first approach the blue and yellow luminescence are going to be studied separately in the next sub-chapters 4.3.1 and 4.3.2.

#### 4.3.1. Luminescent aluminoborosilicate glasses doped with different lead halides

As it was aforementioned and as it is shown in figure 4.4, lead oxide and the halides  $Z=F+Cl+Br$  used in the glass synthesis are essential to obtain the blue luminescence.

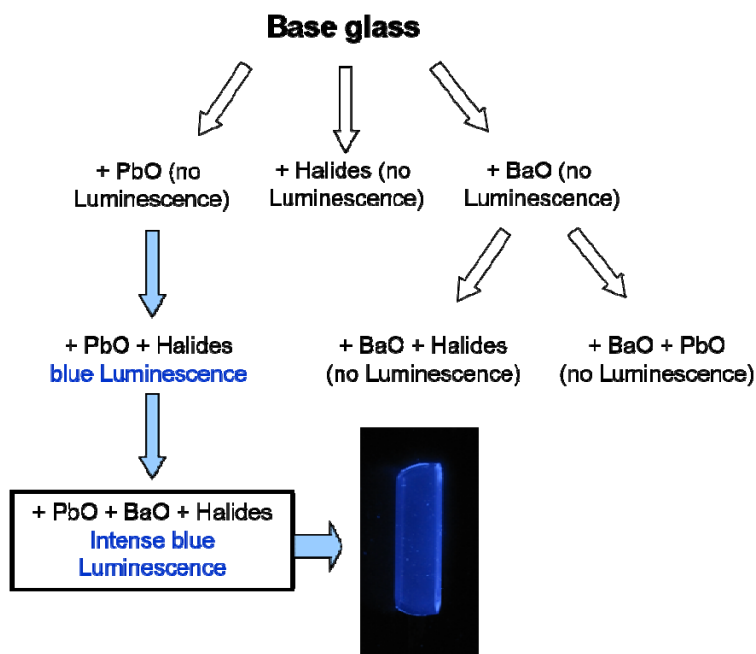


**Figure 4.4.** Essential components to obtain blue luminescence in an aluminoborosilicate glass and glass sample **4**, under UV light (365 nm).

The base glass **9** (BG) with  $SiO_2$ ,  $B_2O_3$ ,  $Al_2O_3$  and alkaline oxides and glass **8** containing BaO,  $SiO_2$ ,  $B_2O_3$ ,  $Al_2O_3$  and alkaline oxides, do not reveal any luminescence. But results exhibited in figure 4.5 show that adding both lead and the halogens Z to this two compositions a broad emission band at 435 nm (2.85 eV) appears, giving rise to a blue luminescence (glass **4** and **11**). All the mentioned glasses are uncoloured under daylight.

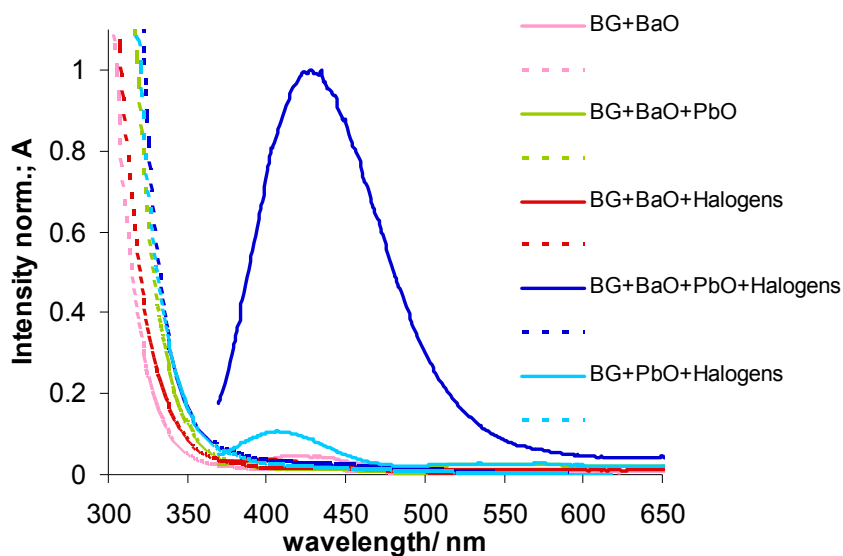


**Figure 4.5.** Absorption spectra (dashed lines) and emission spectra (full lines) of glass the BG (base glass) +BaO (pink), BG + BaO + PbO (green line), BG + BaO + Halogens (red line), BG + BaO + PbO+ Halogens (strong blue line) and of BG + PbO + Halogens (light blue line).

Figure 4.5 show the UV-visible absorption spectra of the different synthesised glasses. The energy correspondent to the inherent ultraviolet absorption edge of glasses decreases when PbO is added to the base composition. It is assumed that the transition of a valence electron of a network anion to an excited state is the responsible for the saturation of the absorption in the UV region in glass materials.<sup>16</sup> The shift to lower energies observed in figure 4.5. can be related to the formation of nonbridging oxygen, which bind excited electrons less strongly than bridging oxygen.<sup>203</sup> In the same figure the emission band at 435 nm that gives rise to blue luminescence is also shown. This band only exists when both lead and halides are in the glass matrix, although this luminescence is stronger when BaO is also added. BaO should contribute to the lead halide nanoparticles aggregation, adding to the multicomponent glass composition required to such effects.

TEM and Raman measurements of glasses containing both lead and halides, were made in order to checkout heterogeneities at the nanometer scale and to better follow the structural changes in these glasses with the different elements. In TEM analysis in fact it is possible to detected nanostructures with diameters ranging from 3 to 10 nm. TEM results suggest that lead and the halides that exist in the glass sample are segregated in the glass matrix as nanoparticles aggregates (figure 4.6).

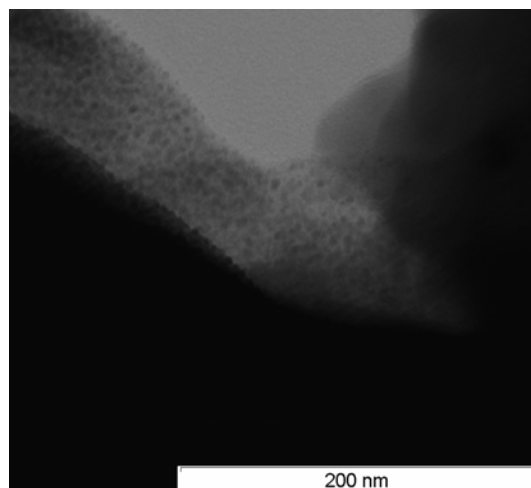


**Figure 4.6.** TEM image of glass sample 1 after the glass thermal treatment at 650°C.

Concerning the Raman analysis, the spectra of the synthesized glasses (section 9.3.2, Supplementary Material), exhibit the usual features of this type of glass: a band between 300 and 600  $\text{cm}^{-1}$  representing the overall connectivity of the network (bending or rocking of Si-O-Si), as well as the degree of the borosilicate network polymerization; several bands between 900 and 1200  $\text{cm}^{-1}$  representing various silicate vibration modes or different types of bridging and/or non-bridging units, and a band between 1300 and 1500  $\text{cm}^{-1}$  that is characteristic of trigonal borate.<sup>204,205,206,207,208,209,210</sup> Concerning the region between 900 and 1200  $\text{cm}^{-1}$ , several sub-bands are well known to overlap in this region, corresponding to structural silicate groups  $Q^n$  (where  $n$  is the number of bridging oxygens per silicate tetrahedron).<sup>204,205,209</sup> The band around 780  $\text{cm}^{-1}$  may be due to the presence of alkali metaborate units or to motions of Si against its tetrahedral oxygen cage.<sup>204,208, 211, 212</sup> Within the range between 700 and 1100  $\text{cm}^{-1}$ , Si-O stretching bands appear indicating different degrees of polymerization of the silicate chain.<sup>213</sup>

To find out which halogen was responsible for this blue luminescence, a less complex glass with the following composition 55.84  $\text{SiO}_2$ , 16.55  $\text{B}_2\text{O}_3$ , 9.41  $\text{Al}_2\text{O}_3$ , 6.82  $\text{BaO}$ , 3.1  $\text{Na}_2\text{O}$ , 1.45  $\text{K}_2\text{O}$ , 2.38  $\text{Li}_2\text{O}$  and 4.45  $\text{PbO}$  (wt%) doped with only one halogen was synthesized. Different halogens (F, Cl, Br and I) were used to dope this glass composition, using sodium halides as raw materials (this synthesis is described in the experimental part 4.2.1). In figure 4.7 are shown the produced glasses with different lead halides under a UV-light. Different luminescent colours can be obtained using different halogens in this glass synthesis.

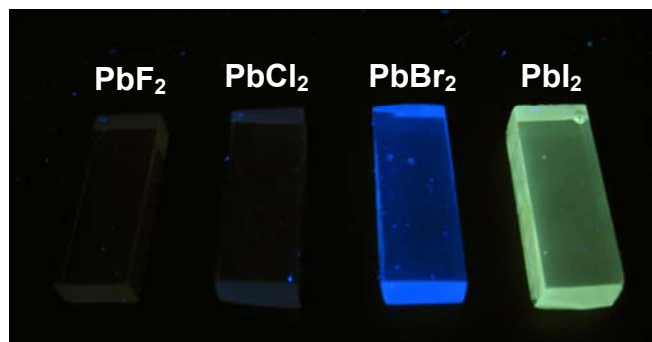


**Figure 4.7.** Aluminoborosilicate glasses doped with lead oxide and with different sodium halides (molar ratio X/Pb=1.33) under a UV-light (364 nm)

TEM was used to observe possible heterogeneities on these glasses doped with different halogens and once more nanostructures are observed in the glasses doped with Cl and Br, with diameters ranging from 3 to 10 nm (figure 4.8). However, in the case of  $\text{PbI}_2$  doped glass it was not possible to identify any particles in the TEM image, figure 4.8. Several attempts to acquire such images were made, and indeed in the beginning of the TEM measurements some particles were seen in the glass sample, but when the incident beam is focused to reach the sample the particles disappear and the image could not be acquired. Probably the electron beam disrupt the  $\text{PbI}_2$  particles, and therefore it was not possible to acquire a direct proof of their existence yet. Nevertheless, there is some heterogeneity in the TEM image and the correspondent selected area diffraction (SAED) pattern shows the existence of crystalline particles (see white spots in figure 4.8 in the inset).

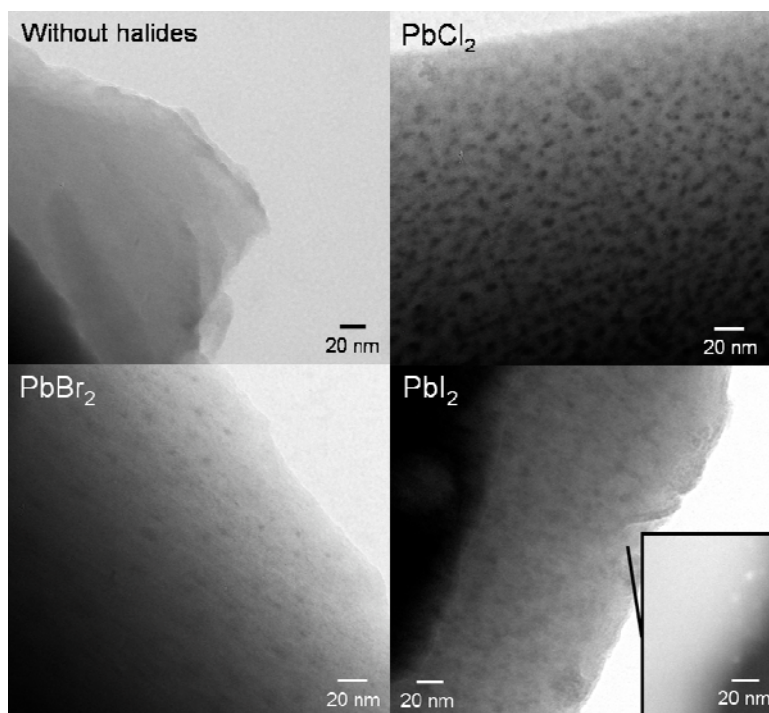


**Figure 4.8.** TEM image of the glass sample doped with no halide and with different halides (Cl, Br and I) in X/Pb molar ratio of 1.33. An image of the SAED pattern of  $\text{PbI}_2$  doped glass is shown in the inset.

XRD studies were also performed to study the nano-heterogeneous character of the aluminoborosilicate glass doped with halides. The XRD pattern of all samples show a broad band that corresponds to the amorphous glass background, but small peaks with very low intensity appears in the halides doped samples pattern, suggesting the presence of a crystalline phase in these glasses. In the sample without halides these small peaks are not present (figure 4.9). The XRD of  $\text{PbBr}_2$  sample will be discussed in more detail later.

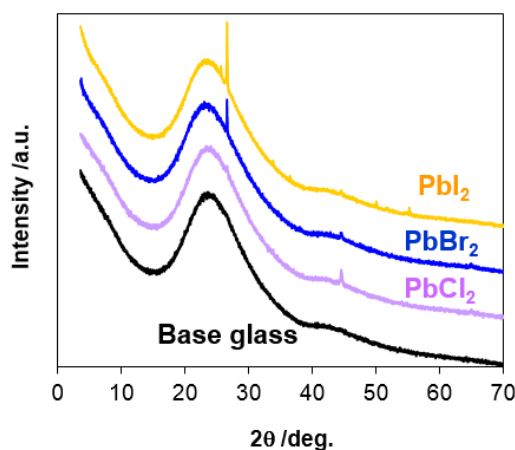


**Figure 4.9.** XRD of the base glass, without halogens (black line), with  $\text{PbCl}_2$  (violet line), with  $\text{PbBr}_2$  (blue line) and with  $\text{PbI}_2$  from 0 to 70°.

These glass materials have luminescence at room temperature, exciting at wavelengths higher than 350 nm. Exciting the glass samples at 350 nm a strong blue luminescence is obtained with  $\text{PbBr}_2$  and a yellow luminescence with  $\text{PbI}_2$  due to a broad emission band at 435 nm (2.85 eV) and 530 nm (2.34 eV), respectively (figure 4.10). In the case of  $\text{PbCl}_2$  the luminescence is less intense and no luminescence was obtained for  $\text{PbF}_2$ , see figure 4.10. This figure also illustrates the luminescent colour coordinates, which were determined using the emission spectra.

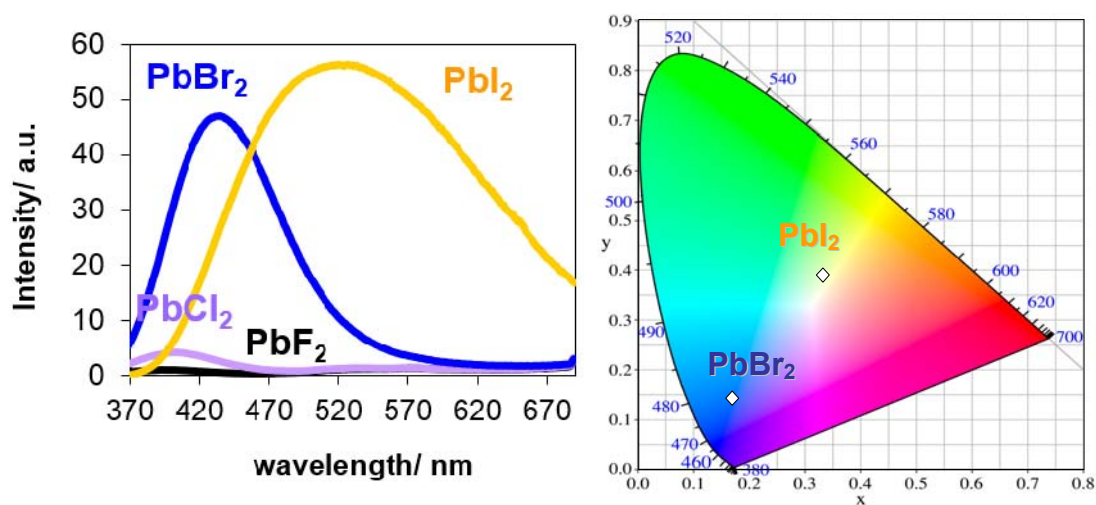


**Figure 4.10.** Emission spectra of aluminoborosilicate glasses doped with different lead halides,  $\text{PbF}_2$ ,  $\text{PbCl}_2$ ,  $\text{PbBr}_2$  and  $\text{PbI}_2$  ( $\lambda_{\text{exc}}=350$  nm). CIE diagram with colour coordinates of the luminescent samples doped with  $\text{PbBr}_2$  and  $\text{PbI}_2$ .

Figure 4.11 shows the UV-Vis absorption spectra of the four glasses. The absorption observed in the UV region is common in glasses and is attributed to the electronic transition between valence bands and conduction bands.<sup>16</sup> This absorption edge that goes into the gap states is called the Urbach edge and can be described by the Urbach formula:<sup>16,189</sup>

$$\alpha(E, T) = \alpha_0 \exp\left(-\sigma \frac{E_0 - E}{k_B T}\right) \quad (4.1)$$

where  $\alpha$  is the absorption coefficient,  $\sigma$  is the steepness parameter,  $E_0$  is the Urbach energy and  $E$  is the photon energy. The formula predicts a linear relationship between  $\ln(\alpha)$  and the photon energy for the low energy tail of the glass exciton band. This type of dependence is observed in figure 4.11, where a gradual shifting to lower energies within the halide series occurs. This shift can be justified with the increasing of the polarizability and with the electronic affinity decreasing, and as a result the required excitation energy of electronic transition is smaller.<sup>214</sup>

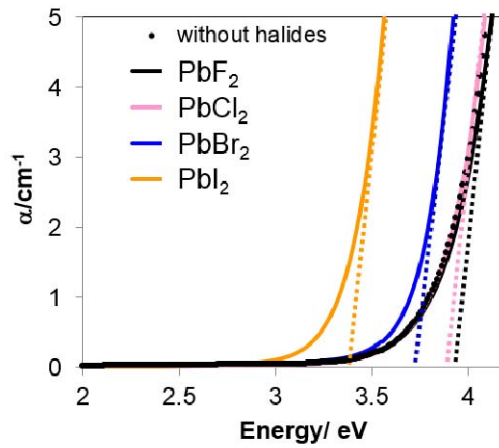


**Figure 4.11.** Absorption spectra of glasses without halides and of glasses containing different lead halides, ( $\text{PbF}_2$ ,  $\text{PbCl}_2$ ,  $\text{PbBr}_2$  and  $\text{PbI}_2$ ). Extrapolation of the linear part of the represented spectra to obtain the  $E_{\text{gap}}$ .

The illustrated absorption spectra show features typical of semiconductor spectroscopy (figure 4.11). A schematic energy diagram of these systems can be found in figure 4.12.

**E<sub>g</sub>** is the energy gap, which is the energy separation between the valence and conduction bands that is typically in the range between 0 and about 4 eV for semiconductors.  $E_v$  is the energy correspondent to the valence band and  $E_c$  to the conduction band;  $E_i$  and  $E_f$  are the initial and final energy.<sup>215</sup>

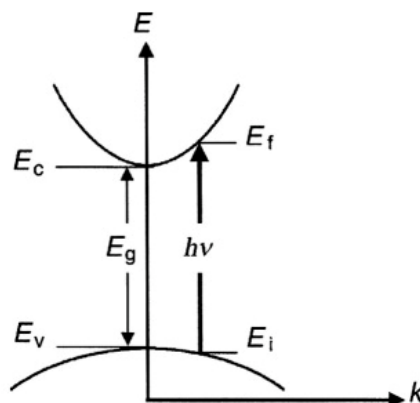


**Figure 4.12.** Energy diagram between valence and conduction bands. (Source: B. G. Yacobi, Semiconductor Materials: An Introduction to Basic Principles, Kluwer p.83, 2003).

A gradual shifting within the halide series exits not only in the absorption spectra but also in the emission spectra, see figures 4.10 and 4.11. Figure 4.13 illustrates the relation between the absorption and emission bands energy with the halogens electron affinity, showing that both absorption and emission bands shift towards lower energies when the electron affinity decreases.

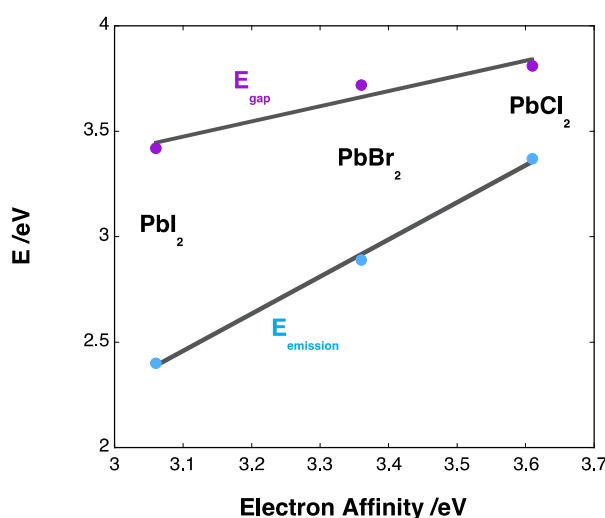


**Figure 4.13.** Electron affinity values of the different halogens used to dope the aluminoborosilicate glass and correspondent  $E_{gap}$  of absorption and  $E_{emission}$  (energy at the maximum of emission).

Luminescent decays were also determined, using Flash Photolysis technique. It is observed that the luminescence decays are in the submicrosecond timescale, non-exponential and strongly dependent on the anion, see figure 4.14. The previous results suggest that lead and the halogens that exist in the glass sample are segregated in the glass matrix as  $PbX_2$ . As it was abovementioned, in many cases a transient  $Pb_2^{3+}$  species (STEL, self-trapped electron



center, while the halide gives rise to a self-trapped hole,  $\text{STH}, \text{X}_2^-$ ) is formed within the crystal which through a back electron-transfer process gives rise to a self-trapped exciton (STE) responsible for the photoluminescence. All the results observed in figure 4.13. and 4.14 are consistent with charge-transfer from the halide to  $\text{Pb}^{2+}$ .

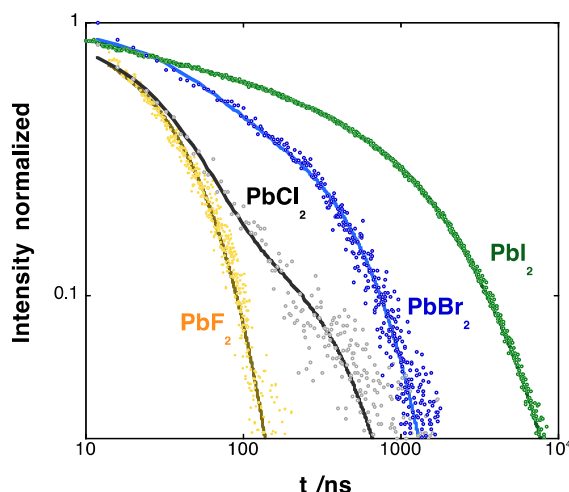


**Figure 4.14.** Luminescence decays of aluminoborosilicate glasses doped with different lead halides synthesized with molar ratio  $\text{X}/\text{Pb}=1.33$  ( $\lambda_{\text{exc}}=355$  nm).

### ***PbBr<sub>2</sub>***

To better understand the spectroscopy of these materials  $\text{PbBr}_2$  glass sample was studied in more detail, since it is this lead halide that gives rise to the blue luminescence initially discussed. The nano-heterogeneous character of the aluminoborosilicate glass doped with bromide (with molar ratio  $\text{Br}/\text{Pb}=1.33$ ) was studied by TEM and XRD (figures 4.15 and 4.16). The TEM image of the glass doped with  $\text{PbBr}_2$ , as it was shown before, reveals the presence of small (ca. 5 nm) particles (Figure 4.15 A), suggesting that lead and halogens that exist in this glass are segregated in the glass matrix as nanoparticles aggregates. In contrast the glass without any halogen does not show any meaningful heterogeneity (figure 4.15 B).

In XRD analysis a broad band that corresponds to the amorphous glass background largely dominates the XRD pattern of glasses doped with bromide and without any halogen (Figure 4.16). However small peaks at  $26.6^\circ 2\theta$  (very low intensity, with low statistical meaning) and at  $44.5^\circ 2\theta$  (more pronounced) appears in the  $\text{PbBr}_2$  glass pattern, suggesting the presence of a crystalline phase in these glass. The base glass pattern, without any halogen, does not show any small peaks. It is known that  $\text{PbBr}_2$ , in normal conditions, crystallize into an orthorhombic structure.<sup>216</sup> This do not seem to be in agreement with the present results, but the peaks observed are very small and the data does not have enough details to reach an accurate conclusion.

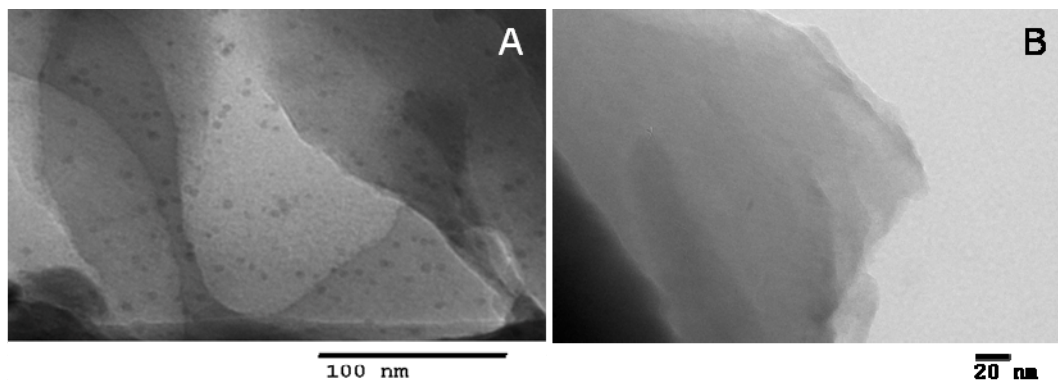


**Figure 4.15.** TEM image of the glass sample doped with bromide (A) and TEM image of the glass sample without halides.

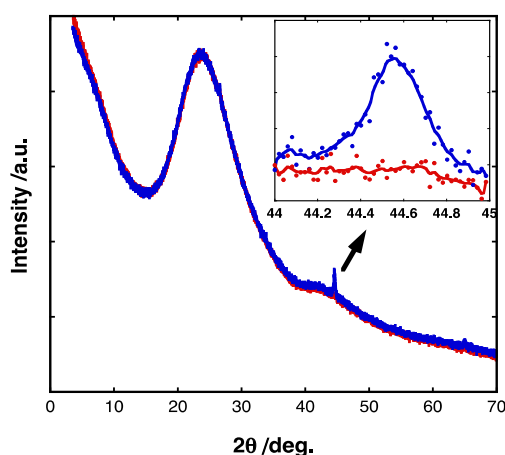


**Figure 4.16.** XRD of glasses with  $\text{PbBr}_2$  (blue line) and without any halogen (red line), from 0 to 70° and expansion of the areas where the small peaks exists.

It is important to refer that EDS analysis was also performed in order to verify the composition in and out of the nanoparticles. But the spectra did not show any differences between these two locations because of the small size of the nanoparticles. This technique did not detect any Br in the glass matrix, even analyzing a larger area, suggesting that Br was lost in the glasses synthesis. To resolve this problem XRF analysis were performed and Br was detected, see section 9.3.3., Supplementary Material. Therefore the Br concentration in the glass is not detectable by EDS. Raman spectroscopy was also performed; detecting only slight changes in the Br doped and undoped glasses (Figure 4.17). This was predictable, because  $\text{PbBr}_2$  undergoes vibrational transitions below  $100\text{ cm}^{-1}$ , out of the range of our equipment.<sup>179</sup> Importantly, this indicates that the addition of bromide does not change the overall glass structure, lending support to the segregation of bromide within the glass matrix as lead bromide nanocrystals.

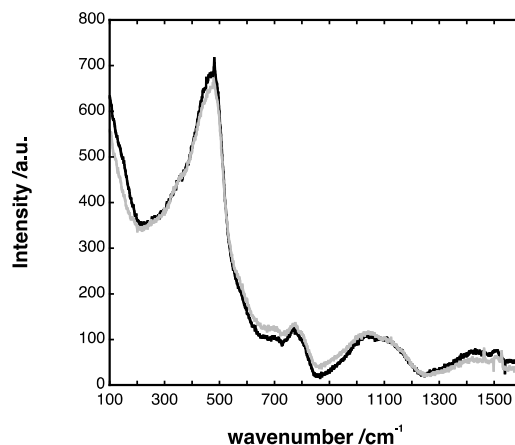


**Figure 4.17.** Raman spectra of glass without halogen (grey line) and with Br (black line).

The glass transition temperature ( $T_g$ ) and the coefficients of thermal expansion (CTE) values of these glasses were also determined, see table 4.4, but again only slight changes can be observed, suggesting that no modifications occur in the glass structure when Br is added.

**Table 4.4.**  $T_g$  and CTE values obtained for the glass samples without and with bromide. CTE was taken from the 30-400°C temperature range.

	Glass sample without halides	Glass sample with Br
$T_g$ /°C	495.3	494.2
CTE /K <sup>-1</sup>	$6.53 \times 10^{-6}$	$6.51 \times 10^{-6}$

Figure 4.18 shows the UV-Vis absorption spectra of the two glasses. A shift of the absorption band towards lower energies (about 0.2 eV) is observed when glass with Br, is compared with glass without Br. The shift to lower energies could be related to the formation of non-bridging oxygen, which binds excited electrons less strongly than bridging oxygen.<sup>203</sup>

However, the most dramatic change is observed when the samples are irradiated at  $\lambda_{ex}=370$  nm (3.35 eV). While glass without Br does not show a significant photoluminescence, glass with Br gives rise to a broad emission centered at 430 nm (2.85 eV), see figure 4.18 that depends highly on the temperature. The seemingly structure in the emission at room temperature shows at 77 K several peaks separated by about 0.17 eV exhibiting a much larger intensity (about 1 order of magnitude, spectra without normalization can be found in section 9.3.4., Supplementary Material).

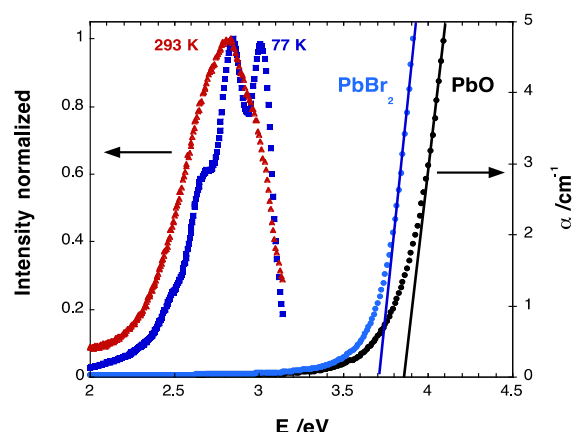


**Figure 4.18.** Absorption coefficient of glass without halide (black line, PbO) and glass with bromide (blue line, PbBr<sub>2</sub>) and emission spectra of glass with PbBr<sub>2</sub> at 293 and 77 K ( $\lambda_{\text{exc}}$ =370 nm).

The appearance of structure in the emission spectra may be related with vibrational coupling of the charge-transfer. The spacing between each peak is periodical, about 0.175 eV (1410 cm<sup>-1</sup>), relatively far from the vibrational transitions of PbBr<sub>2</sub> (around 100 cm<sup>-1</sup>). The Raman spectra already discussed, shows a broad peak centered around 1400 cm<sup>-1</sup>, attributed to O-B-O bending modes. If a relation exists between this vibrational mode and the luminescence spectra, this means that the glass matrix phonon mode couples with the electronic transition that gives rise to photoluminescence.<sup>217,218</sup>

Other luminescence studies were performed. Steady-state luminescence anisotropy was also measured at room temperature and a value of 0.19 was obtained independently of excitation wavelength, between 350 and 410 nm. This reveals the crystalline nature of the particles, because otherwise the luminescence anisotropy would be zero (value obtain for amorphous materials).

Time-resolved measurements were also performed and as it was previously said the results showed that the luminescence decay is in the submicrosecond timescale (figure 4.14). Time-resolved luminescence spectra were measured with the Flash Photolysis equipment using the third harmonics ( $\lambda_{\text{ex}}$  = 355 nm, laser pulse half width equal to 6 ns). Within the explored timescale, from about 20 to 2000 ns, the emission spectra shape and position do not show any difference with time (figure 4.19). This result is important since it indicates that a single active centre is responsible for the photoluminescence.

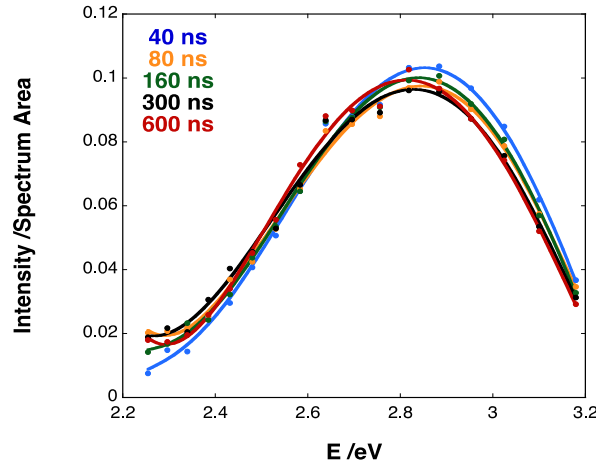


**Figure 4.19.** Normalized time-resolved emission spectra of Br doped glass, with the area of the emission peak between 2.2 and 3.2 eV ( $\lambda_{\text{exc}}=355$  nm).

A better time-resolution was achieved with a single photon counting (SPC) equipment in collaboration with Dr. Suzana Andrade. Luminescence decays of glass with  $\text{Br}^-$ , see figure 4.20, were measured at room temperature and at 77 K. At room temperature, two major results were observed: the luminescence decay is highly non-exponential and the luminescence anisotropy is time-independent within the accuracy of the measurement. Indeed, the time-resolved luminescence anisotropy confirms the steady-state result with an average value of 0.19.

It is important to explain the nature of this highly non-exponential decay. Mechanisms such as energy-transfer would require stretch exponential components with an exponent equal to 0.5,<sup>219</sup> but that is ruled out from the anisotropy measurements and shape of the luminescent decay (it cannot be fitted to such models). Phenomenological, three different functions were tested to fit the decay:

1°. The sum of exponentials was tested, but it was only successful when 4 exponentials were added and it did not fit the prompt pulse luminescence (which would require more exponentials). Therefore this type of approach does not give any reasonable insight.

2°. Another type of kinetics was also explored, namely stretched exponential kinetics. The sum of 2 stretched exponentials, equation (4.2), however, is able to fit the luminescence decay reducing from 8 to 6 the number of adjustable parameters, and it already predicts some amount of prompt luminescence. A stretched exponential is normally connected with local heterogeneity in the glass, giving rise to a distribution of local sites for the luminescent probe.<sup>220,221,222</sup>

$$I(t) = a_1 e^{-\left(\frac{t}{\tau_1}\right)^{\alpha_1}} + a_2 e^{-\left(\frac{t}{\tau_2}\right)^{\alpha_2}} \quad (4.2)$$

According to Dag and Lifshitz results analyzed within this framework for  $\text{PbI}_2$  nanocrystals were consistent with relaxation to low energy states.<sup>187</sup> This probably is not our case, since the luminescence spectra (and the anisotropy) do not change with time, but, at least, it provides a

good insight into the long component. Nevertheless the physical meaning of the sum of 2 stretched exponentials is difficult to grasp within this case: the shortest component has an exponent of about 0.3 and characteristic time of about 6 ns.

3°. Iwanaga *et al* discussed  $\text{PbBr}_2$  crystals luminescence mechanisms in great detail, as pointed out in the introduction.<sup>183,185</sup> The formation of a  $\text{STEL}(\text{Pb}_2^{3+})/\text{STH}$  pair followed by a STE is considered to be the main mechanism. Their luminescence decay followed equation (4.3):

$$I(t) = a.t^{-1} \left( 1 - e^{-\frac{t}{\tau}} \right) \quad (4.3)$$

with a decay time of about 1.2  $\mu\text{s}$ . However visual inspection of the decay shows linear dependence between  $\log(I)$  and  $\log(t)$  for short times, while equation (4.3) predicts such dependencies at long timescales up to 100 ms. Hence, in the third attempt to fit the decay, the following modified equation was tested, including mix order kinetics (first and second order) and an extra exponential that accounts for the initial part of the decay (few nanoseconds):

$$I(t) = \frac{a_1 \exp(-k_1 t)}{1 - a_2 \exp(-k_1 t)} + a_3 \exp\left(-\frac{t}{\tau}\right) \quad (4.4)$$

with:

$$a_1 = I_0 \frac{k_1 [X]_0}{k_1 + k_2 [X]_0}$$

$$a_2 = \frac{k_2 [X]_0}{k_1 + k_2 [X]_0}$$

This equation, in practice, gives rise to a power law (earlier times) and an exponential decay (longer times). It nicely fits the experimental results with 5 adjustable parameters.

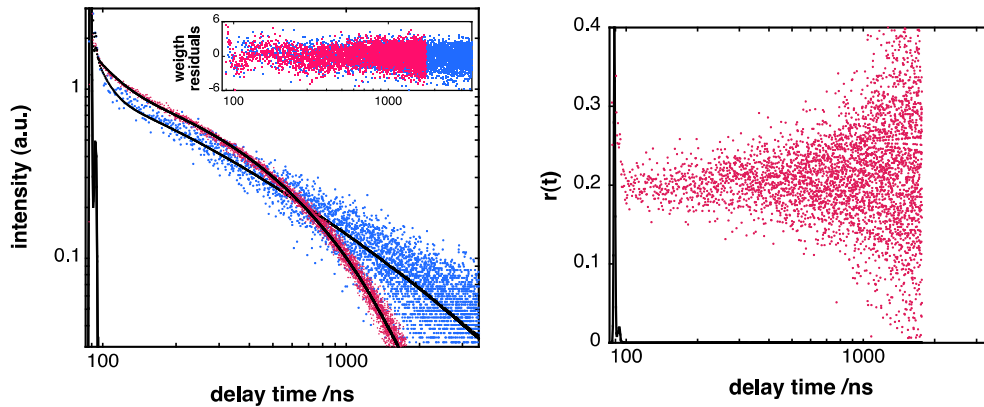


**Figure 4.20.** Luminescence decays at 298 K (red points) and 77 K (blue points) at 440 nm fitted with equation 4.4 ( $\lambda_{\text{ex}} = 372$  nm). Anisotropy decay at 298 K, at 440 nm with  $\lambda_{\text{ex}} = 372$  nm.

In table 4.5 are the fitting results, highlighting a short component in both decays at 77 K and 298 K.

**Table 4.5.** Fitting results of the luminescence decays (figure. 4.20) with equation 4.4

T /K	$a_1$	$a_2$	$k_1 / \mu s^{-1}$	$k_2[X]_0 / \mu s^{-1}$	$a_3$	$\tau / ns$
77	0.034±0.002	0.966±0.009	0.24±0.03	6.9±2.3	—	—
298	0.300±0.009	0.51±0.03	1.90±0.05	2.0±0.3	0.38±0.26	23.4±9.3

The shortest exponential component could be linked with the intrinsic luminescence from the glass itself. This luminescence is normally highly temperature dependent and should vanish at room temperature. At 77 K, however, this short component disappears, which leads us to attribute it to the PbBr<sub>2</sub> particles in the glass. On the other hand, the mixed second order kinetics exhibits the usual behavior, with higher first order kinetics ( $k_1$ ), demonstrated in the long tail observed on figure 4.20. The pre-exponential factor  $a_2$  is dependent on the degree of second order kinetics, which is clearly higher at 77 K. Therefore, STH/STEL radiative recombination reported previously<sup>183,184,185</sup> is also observed in the present PbBr<sub>2</sub> nanocrystals. However a first-order non-radiative process also occurs, being more pronounced at 298 K, which is linked to confinement effects due to the very small sizes of the particles (4 nm) allowing non-radiative electron recombination between STH/STEL center by thermal barrier crossing. In this case aluminoborosilicate glasses with strong blue luminescence containing lead bromide nanoparticles, with 4 nm, were produced. The use of a glass matrix was important to obtain this luminescence at room temperature and not only at low temperatures. Anisotropy and XRF results reveal the crystalline nature of the particles. Time-resolved luminescence measurements of these aggregates show, however, non-exponential decays that it seems to be connected with the electron-phonon coupling of the particles on a non-homogeneous nano-environment and with the intrinsic radiative relaxation of the exciton.

#### 4.3.2 Aluminoborosilicate glass doped with different copper concentrations

This study had the intention of investigate copper luminescence in these glasses and to explore the possibility of producing different luminescent colours using other metals as alternative to lanthanide oxides. The base glass (BG) doped with PbO and CuO (glass **13**), presents a very pale blue colour and yellow luminescence colour under UV-light, see figure 4.21. The blue colour is attributed to the presence of Cu<sup>2+</sup>,<sup>17,35</sup> while the yellow luminescence is attributed to Cu<sup>+</sup> indicating that both copper oxidations states, Cu<sup>+</sup> and Cu<sup>2+</sup>, are present since it is known from the literature that Cu<sup>+</sup> doped materials can emit different colour from blue to near infrared, due to its broad shifts of the emission band.<sup>77,78,196,197,198,199,200,201,202,223</sup>



**Figure 4.21.** Glass sample **13** (BG+PbO+CuO), left: under daylight; right: under a UV-light (370 nm)

Nevertheless, the yellow luminescence is only evident when PbO is added in the glass matrix, see figure 4.22. Without PbO the PL intensity is very weak and green. These results are going to be discussed in the following sub chapters.

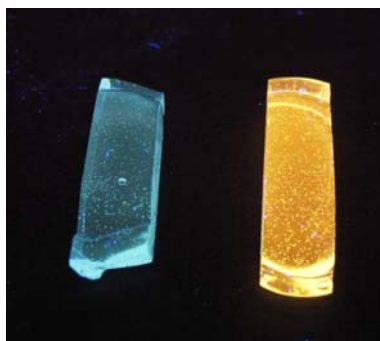


**Figure 4.22.** Left side: Glass samples **12**, BG + CuO. Right side: Base glass + PbO+CuO, under a UV-light (370 nm).

Doping the base glass with 0.03% of CuO (wt%) leads to luminescent glass (glass **12**), but the addition of lead oxide (glass **13**) was essential to obtain a more intense yellow luminescence, figure 4.23.



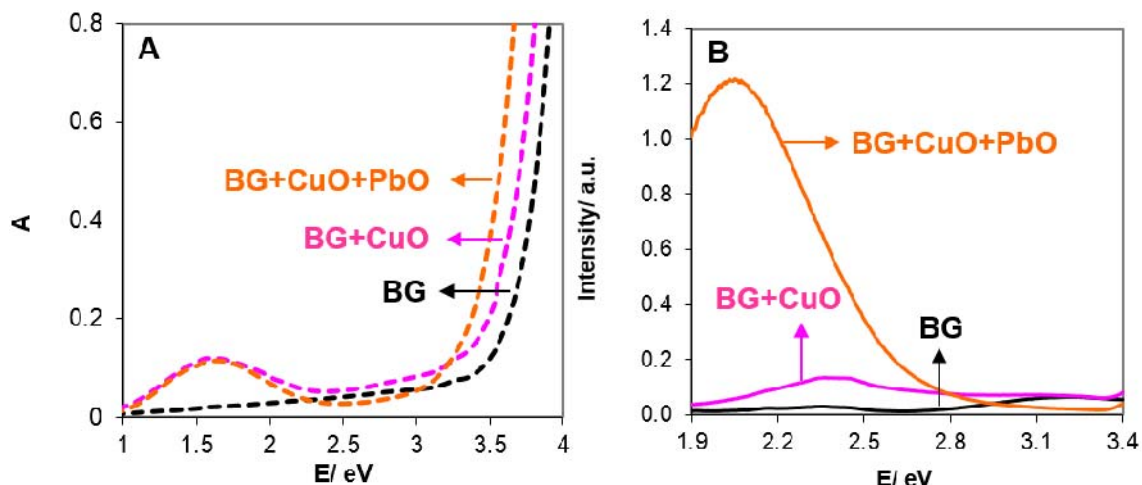


**Figure 4.23.** (A) Optical Absorption spectra of the base glass – BG (black line), of BG + CuO (pink line) and of BG + CuO +PbO (orange line). (B) Luminescence spectra of the base glass – BG (black line), of BG + CuO (pink line) and of BG + CuO +PbO (orange line),  $\lambda_{exc}=370$  nm .

Figure 4.23 A show the absorption spectra of CuO doped glass. The absorption spectrum of the base aluminoborosilicate glass is shown (black line) for comparison with the doped glasses where a band at 1.6 eV (775 nm) only appears when CuO is present. This absorption band is responsible for the blue colour of the glass sample that corresponds to  $^2E \rightarrow ^2T_2$  transition of  $Cu^{2+}$ .<sup>224</sup> Like in the previous study with lead halide doped glasses, in these samples the energy correspondent to the inherent ultraviolet absorption edge of glasses also decreases when PbO is added to the CuO doped base composition. As it was already said this difference can be related to the formation of nonbridging oxygen<sup>203</sup> or as it was referred in the literature due to a band of  $Cu^+$  that absorbs in the UV part of the spectra.<sup>77,201</sup>

Concerning the luminescence spectra, an intense band at 2.05 eV (605 nm) attributed to  $3d^9 4s^1 \rightarrow 3d^{10}$   $Cu^+$  transition<sup>198</sup> is observed, giving rise to the yellow luminescence. This band is much more intense when the base glass includes both PbO and CuO, so lead definitely has an important role.  $Cu^{2+}$  reduction induced by PbO could explain the result, however the absorption band at 1.6 eV, correspondent to  $Cu^{2+}$ , decreases only slightly in the PbO presence. This small difference in the absorption spectra does not justify such large differences in the luminescence when PbO is added to the glass matrix. The increase of the luminescence can also be explained with the formation of  $Cu^+$  dimers, since it is known that monovalent copper tends to form pairs in glasses.<sup>77, 225, 226</sup> The emission band of glass **13** (BG+PbO+CuO) can be decomposed in three Gaussian curves, see figure 4.24. The decomposition curve at 2.40 eV is similar to the emission spectra of glass **12** (BG+CuO) suggesting the bands at 2.05 eV and 1.99 eV are only observed when PbO is added. Probably the band at 2.40 eV correspond to single  $Cu^+$  and at 2.05 eV and 1.99 eV to dimers, since isolated copper monomers and dimers have specific luminescent properties.<sup>225</sup> The band at lower energy usually correspond to the  $\sigma(4s) \rightarrow \sigma^*(3d)$  transition of the  $Cu^+$  dimer (figure 4.25).<sup>77,226</sup>

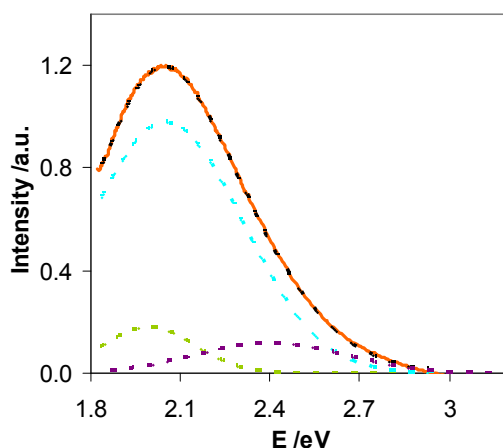


**Figure 4.24.** Luminescence spectrum of glass **13** - BG + CuO + PbO (full orange line) and decomposition with three Gaussian curves (blue, green and purple dashed lines),  $\lambda_{\text{ext}}=370$  nm. The fitted curve is represented with a dashed black line.

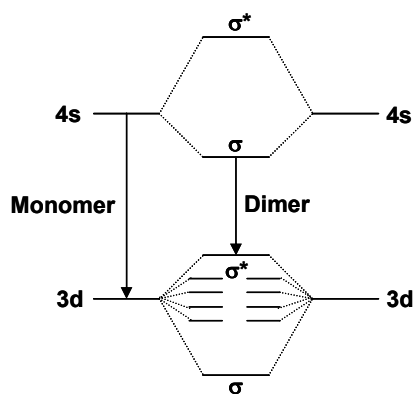
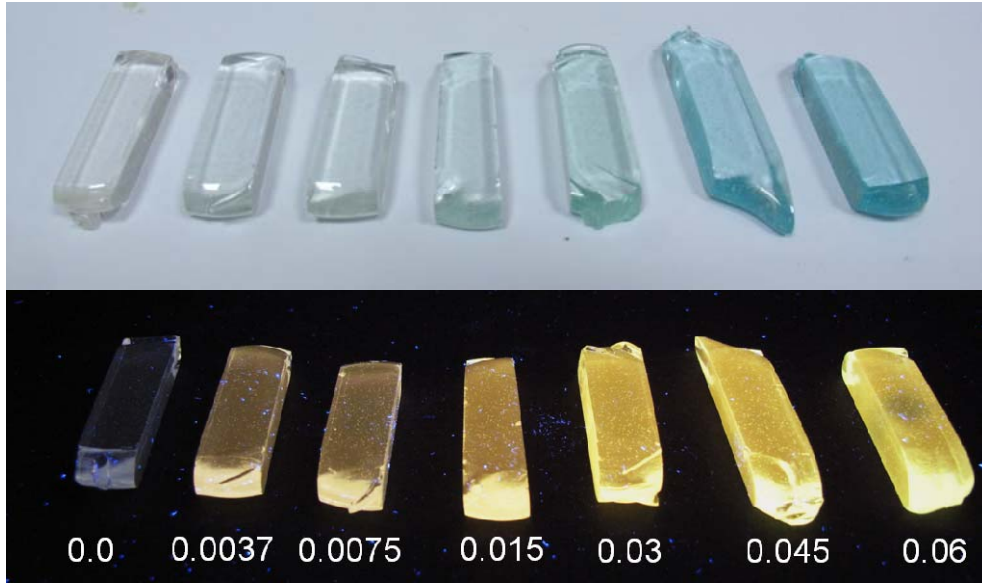


Figure 4.25. Schematic energy level diagram for  $\text{Cu}^+$  monomer and dimer.

For glass composition **3** (base glass+PbO+ZrO<sub>2</sub>+BaO) different CuO concentrations were used, see figure 4.26. Having in mind the existence of both oxidation states,  $\text{Cu}^+$  and  $\text{Cu}^{2+}$ , all the glass samples with  $[\text{Cu}^+]/[\text{Cu}^{2+}]$  fractions were measured using VIS/NIR absorption spectroscopy to calibrate the concentration effect on the luminescence colour. It is known that  $[\text{Cu}^+]/[\text{Cu}^{2+}]$  ratio depends of different factors such as temperature, annealing time, contact with atmospheric oxygen and composition,<sup>14,227,228</sup> but in our case all of these conditions were the same, except the CuO concentration used in the synthesized glasses.

The blue colour of  $\text{Cu}^{2+}$  and the yellow luminescence intensity attributed to  $\text{Cu}^+$  increases with the concentration of CuO (figure 4.26). The absorption coefficient spectra were obtained subtracting to all glasses the one with 0% CuO (figure 4.27). As it was expected the absorption band correspondent to  $\text{Cu}^{2+}$  increases with the CuO concentration.



**Figure 4.26.** Aluminoborosilicate glass **3** (base glass+PbO+ZrO<sub>2</sub>+BaO) doped with different CuO concentrations, (up) under daylight, (down) under a UV-light (365 nm).

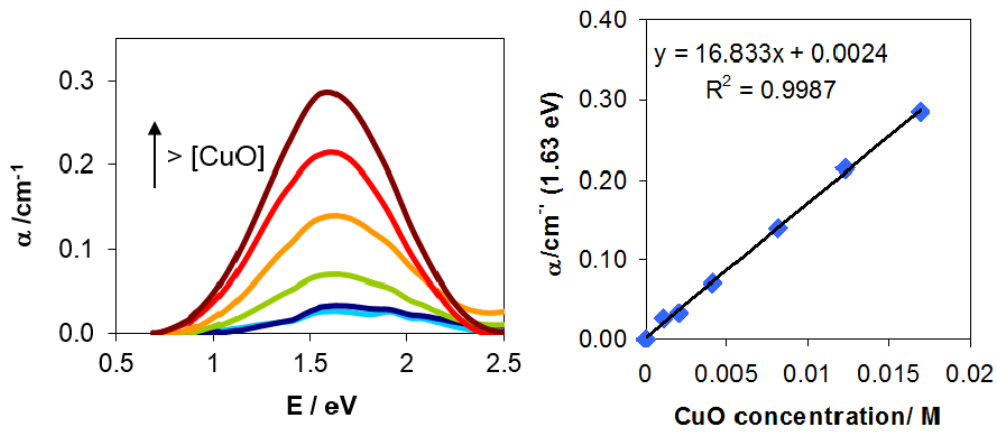


**Figure 4.27.** Left side: Optical absorption spectra of glass samples **3** with different CuO concentrations 0.0% (**3a**), 0.00375% (**3b**), 0.0075% (**3c**), 0.015% (**3d**), 0.03% (**3e**), 0.045% (**3f**) and 0.06% (**3g**), wt %. Right side: Dependence of the absorbance at the maximum of the absorption spectra (1.63 eV) with the CuO concentration (mol).

The molar extinction coefficient of Cu<sup>2+</sup> ions at 1.63 eV (760 nm),  $\varepsilon_{Cu^{2+}}$  can be taken from the dependence of A (1.63eV) with the CuO concentration in M through the Lambert-Beer law, equation 4.5.

$$A = \frac{\varepsilon_{Cu^{2+}}}{1 + K} l[CuO] \quad (4.5)$$

where  $\varepsilon_{Cu^{2+}}$  is the molar extinction coefficient of  $Cu^{2+}$ ,  $K = \frac{[Cu^+]}{[Cu^{2+}]}$ ,  $l$  is the thickness of the

glass sample and  $[CuO]$  is the CuO concentration.  $\frac{\varepsilon_{Cu^{2+}}}{1 + K}$  in these glass samples is  $17 \text{ M}^{-1} \cdot \text{cm}^{-1}$ .

This value is lower compared with other values found in the literature for  $\varepsilon_{Cu^{2+}}$  (in the range of  $30 - 60 \text{ M}^{-1} \cdot \text{cm}^{-1}$ )<sup>227,229,230</sup> indicating a large value for  $K$  due to the existence of both  $Cu^{2+}$  and  $Cu^+$  oxidation states in these glass samples.

Concerning the luminescence, this set of glasses with different CuO concentrations exhibit a broad emission band, centred at 2.05 eV (605 nm) when excited at 355 nm (Figure 4.28). Changing the copper content does not induce big changes in the shape of the emission spectrum. To compare all the emission spectra, they were corrected with the absorption value at 355 nm.

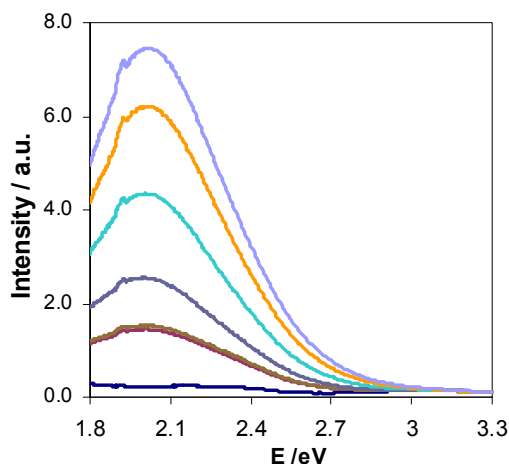


**Figure 4.28.** Luminescence spectra of glass sample **3** with different CuO concentrations 0.0% (**3a**), 0.00375% (**3b**), 0.0075% (**3c**), 0.015% (**3d**), 0.03% (**3e**), 0.045% (**3f**) and 0.06% (**3g**), wt%, exciting at 355 nm.

The yellow luminescent colour is observed in all the synthesized glasses (with luminescence chromaticity coordinates around  $x=0.49$  and  $y=0.44$ ). All this emission bands can be decomposed using three Gaussian curves (the equation can be found in chapter 2) with maximums at 1.91 (650 nm), 2.06 (602 nm) and 2.34 eV (530 nm).

To do these decompositions the band position and bandwidth values remained constant and only the pre-exponential values changed for the different samples. The normalized pre-exponential factors are shown in figure 4.29. The increase of CuO concentration does not originate strong changes in the contribution of each band. The band at 2.34 eV (530 nm) is related to the monomer, since it is positioned at higher energies close to what is found in the literature for this species (around 2.5 eV).<sup>231</sup> The other two bands are attributed to dimers in different environments.

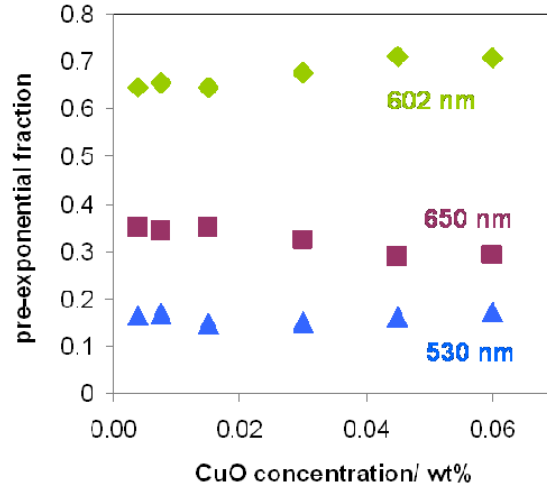


**Figure 4.29.** Relation between the normalized pre-exponential factors of the different Gaussian bands used to decompose the luminescence spectra and CuO concentration.

The luminescence decays of glass samples doped with different copper concentrations are not single-exponential (an example is shown in figure 4.30). Instead, a sum of three exponentials is required in line with the gaussian decomposition of the steady-state emission spectra shown above (4.6):

$$I(t, \lambda) = a_1(\lambda)e^{-\frac{t}{\tau_1}} + a_2(\lambda)e^{-\frac{t}{\tau_2}} + a_3(\lambda)e^{-\frac{t}{\tau_3}} \quad (4.6)$$

where  $a$  are the pre-exponential factors and  $\tau$  are the lifetimes.

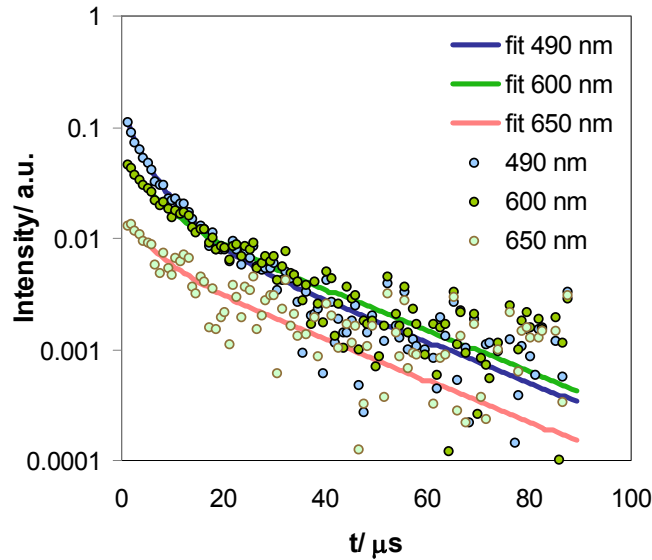


**Figure 4.30.** Luminescence decays of the glass sample **3g** doped with 0.06% CuO at 490, 600 and 650 nm.

Table 4.6 shows the lifetimes obtained for glass samples with different CuO concentrations. These values are practically constant for the different samples, around 1.5  $\mu$ s, 6  $\mu$ s and 26  $\mu$ s.

This deviation from exponential relaxation can be related to the existence of  $\text{Cu}^+$  monomers and two different dimer species in the samples.

**Table 4.6.** Lifetimes obtained by three-exponential decay fittings ( $\lambda_{\text{exc}}=355$  nm) for glass sample **3** (BG+CuO+PbO+BaO+ZrO<sub>2</sub>) with different CuO concentrations, 0.00375% (**3b**), 0.0075% (**3c**), 0.03% (**3e**), 0.045% (**3f**) and 0.06% (**3g**), wt %.

Sample	CuO(wt%)	$\tau_1/\mu\text{s}$	$\tau_2/\mu\text{s}$	$\tau_3/\mu\text{s}$
<b>3b</b>	0.00375	1.6	8.2	29.4
<b>3c</b>	0.0075	1.0	4.3	24.1
<b>3e</b>	0.030	1.5	6.1	19.9
<b>3f</b>	0.045	1.8	8.2	32.2
<b>3g</b>	0.06	1.4	5.3	23.5

The lifetime values were obtained by analysing luminescence decays at emission wavelengths 490, 600 and 650 ( $\lambda_{\text{exc}}=355$  nm). Figure 4.31 show the normalized pre-exponentials obtained when the decays of the glass doped with 0.06% CuO were fitted. At 650 nm the contribution of the species with a lifetime of 1.4  $\mu\text{s}$  is zero, as expected if this component is due to  $\text{Cu}^+$  monomer. The other two lifetimes are attributed to dimer species.

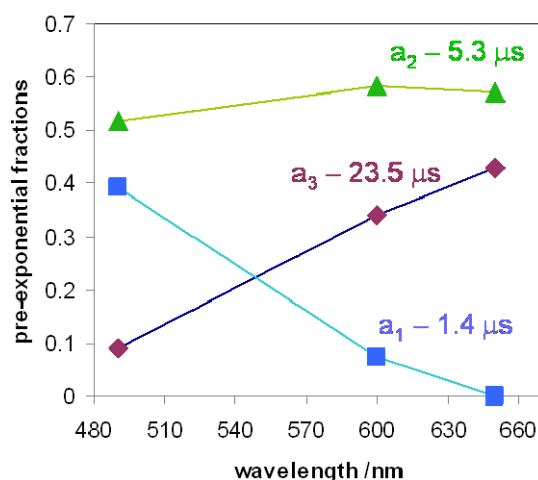


**Figure 4.31.** Relation between the relative pre-exponential factors obtained by three-exponential decay fittings for  $\tau = 1.4$  (blue squares) 5.3 (green triangles) and 23.5  $\mu\text{s}$  (purple rhombus) at different wavelengths for the glass sample **3** doped with 0.06% CuO.

During these experiments, the samples were irradiated with laser pulses from the Laser Flash Photolysis equipment. As a result, coloured spots appeared in the glass showing almost no luminescence under a UV-light, see inset of figure 4.32. The irradiation with the flash photolysis laser apparently oxidizes  $\text{Cu}^+$  to  $\text{Cu}^{2+}$  as it can be seen in figure 4.32 the increase of the absorption band correspondent to  $\text{Cu}^{2+}$ . Nevertheless, the influence of high energy lasers in glass is already reported in the literature.<sup>40,232,233,234</sup> The laser irradiation can generate different

types of defects in a glass matrix, such as non-bridging oxygen hole centers (NBOHCs), E' centers, and trapped electron centers.<sup>232</sup> The NBOHCs give rise to absorption bands at ca. 440 and 620 nm, therefore the increase of the absorption band in figure 4.32 can also be related with the formation of these defects.

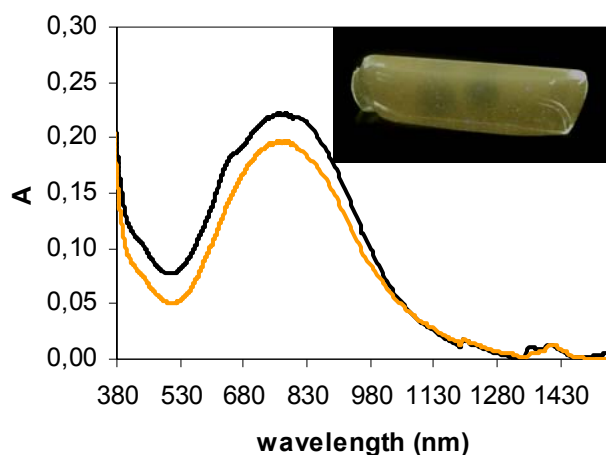


**Figure 4.32.** Absorption spectra of glass sample **3e**, in the region with yellow luminescence (yellow line) and in the hole without luminescence (black line). Inset - Glass sample **3e** after irradiation with the flash photolysis laser (355 nm).

After heating the samples at 400°C, these holes disappeared, the luminescence is recovered. This is potentially very useful in different applications, as highlighted by one of the artists from the Vicarte unit (see chapter 6), since it is possible to obtain a luminescent material and to quench that luminescence at chosen spots. This effect also has the advantage of being reversible, since it is possible to recover the luminescence properties after the thermal treatment.

Only one luminescent colour was produced with this glass set. Having in mind the blue luminescence obtained with lead and with different halogens (Z: F+Cl+Br) using this multicomponent glass composition, the batches that gave these two luminescence's were mixed together in order to create different luminescent colours and consequently to increase the colour palette. Therefore different CuO concentrations were used in glass **1** (base glass+PbO+ZrO<sub>2</sub>+BaO+CuO+Z) keeping the same concentration of lead oxide, to obtain several luminescence colours with the mixture of the yellow luminescence of Cu<sup>+</sup> and the blue luminescence of lead halides (figure 4.33).



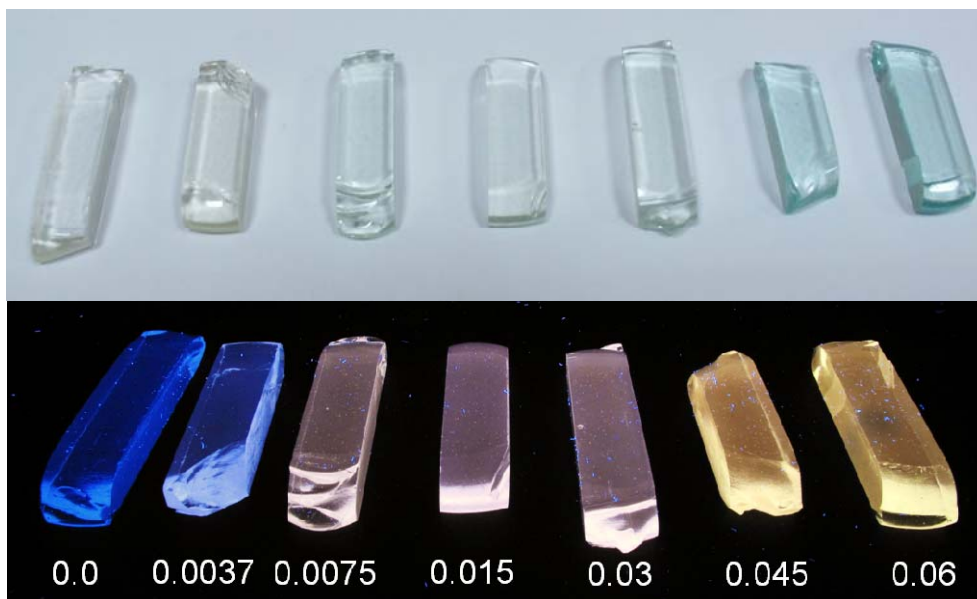


**Figure 4.33.** Aluminoborosilicate glass 1 (base glass+PbO+ZrO<sub>2</sub>+BaO+CuO+Z) doped with different CuO concentrations, (up) under daylight, (down) under a UV-light (365 nm).

The absorption coefficient spectra were once more obtained subtracting to all glasses the spectrum corresponding to the 0% CuO sample. Figure 4.34 illustrate the increase of the absorption band at 1.6 eV, correspondent to Cu<sup>2+</sup>, with the CuO concentration.

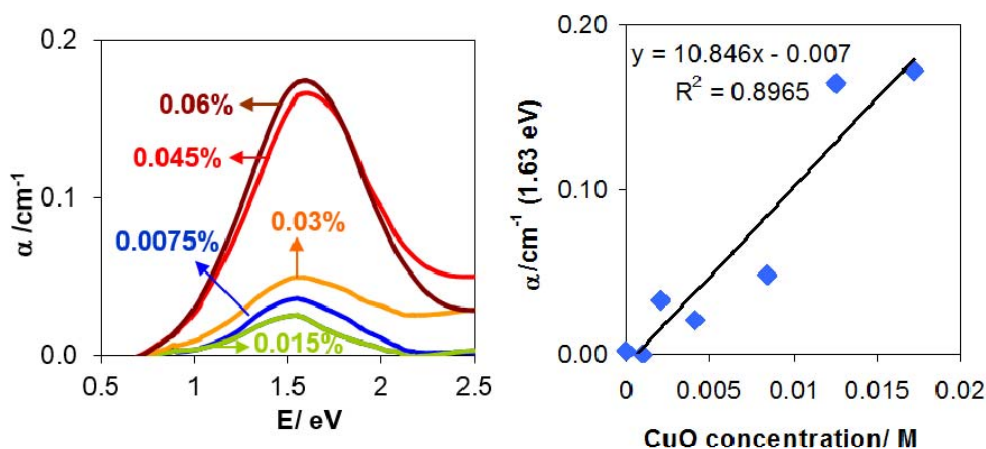


**Figure 4.34.** Optical absorption spectra of glass sample 1 with different CuO concentrations 0.0% (1a), 0.00375% (1b), 0.0075% (1c), 0.015% (1c), 0.03% (1e), 0.045% (1f) and 0.06% (1g), %wt. Right side: Dependence of the absorbance at the maximum of the absorption spectra (1.63 eV) with the CuO concentration (M).

The  $\frac{\epsilon_{Cu^{2+}}}{1+K}$  in these glass samples is 11 M<sup>-1</sup>.cm<sup>-1</sup>, lower than the one obtained for the glasses without halides, indicating the formation of more Cu<sup>+</sup>. The emission spectra Pb<sup>2+</sup> in the presence of halides (Cl+Br+F) is responsible for a broad emission band at 2.85 eV (435 nm), resulting in a blue luminescence, while Cu<sup>+</sup> gives rise to a broad emission band at 2.07 eV (600 nm), figure 4.35.



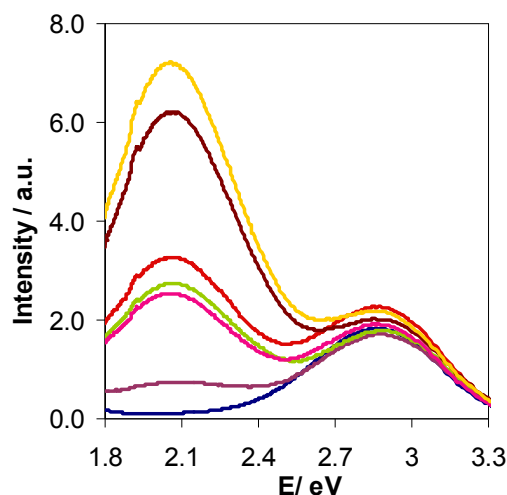


**Figure 4.35.** Luminescence spectra of glass sample **1** with different CuO concentrations 0.0% (**1a**), 0.00375% (**1b**), 0.0075% (**1c**), 0.015% (**1d**), 0.03% (**1e**), 0.045% (**1f**) and 0.06% (**1g**), wt% ( $\lambda_{\text{exc}}=355$  nm).

Luminescence colour coordinates were calculated from the emission spectra and are represented in a CIE chromaticity diagram in figure 4.36. Using this glass composition different luminescent colour can be produced along the chromaticity line, including white luminescence changing the concentration of lead halides and CuO. White luminescence can be obtained using a copper concentration between 0.0035 and 0.0075% (wt). This method presents, therefore, an interesting way of achieving this goal without using lanthanides.

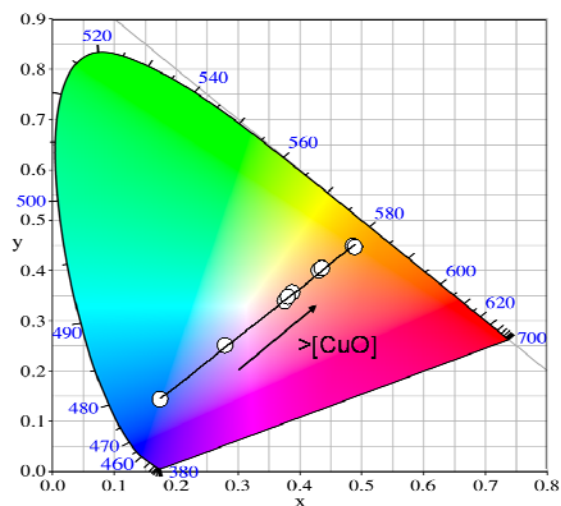


**Figure 4.36.** CIE ( $x$ ,  $y$ ) chromaticity diagram with the colour coordinates of luminescence of glass **1** with different CuO concentrations.

#### **4.4 Conclusions**

Due to the high cost of lanthanides alternatives to synthesize luminescent glasses with other cheaper metals were explored. Doping the aluminoborosilicate glass with lead and halogens gave rise to blue luminescence (with bromide) and yellow (with iodide). Using different techniques such as TEM, XRF and anisotropy, crystalline nanoparticles could be recognized, that were attributed to lead halide nanoparticles, with sizes around 4 nm.

The use of copper was also very useful to obtain other colours of luminescence. CuO doped aluminoborosilicates have yellow luminescence under UV-light. However the PbO presence is crucial to obtain an intense luminescence. This can be related to the development of dimers when PbO is present in the glass matrix. The steady state and time resolved luminescence support the idea of the existence of both monomers and dimers in the synthesized glass samples, indicating the existence of two different species of dimers, probably  $\text{Cu}^+-\text{Cu}^+$  and aggregates. With a mixture of lead halides and CuO in the same glass it is possible to obtain different luminescent colours.

## Chapter 5 – Sol-gel glass materials with gold nanoparticles

As mentioned in chapter 1, gold ruby glass was used in artworks and decorative objects for centuries. These glasses are still used by artists at VICARTE and therefore new methods to develop ruby glass are explored within the interface between science and art. In conventional processes, a portion of gold is added to the clear glass and to produce a red object it is necessary a fine heating control in order to obtain a desired colour. For this reason different protocols are constantly being explored to obtain gold ruby glass. In this chapter the focus is given on an innovative way to produce gold nanoparticles on glass materials using sol-gel synthesis with an ionic liquid, [bmim][BF<sub>4</sub>], avoiding the use of a reductive atmosphere (e.g. H<sub>2</sub> or CO) or other chemical reagents. The dependence of the nanoparticles size in this glass system with the sintering process is characterized and a mechanism for the nanoparticles formation is proposed.

### 5.1. Synthesis of gold nanoparticles in different materials

Metal nanoparticles have attracted considerable interest in several research fields, such as in biological and biomedical applications, in catalysis, optoelectronics, nanoelectronics and also storage systems.<sup>235,236,237,238,239,240,241</sup> The use of these nanoparticles for the coloration of several materials dates back several centuries ago, for example gold nanoparticles which give rise to the ruby color are used since 4th–5th B.C. by the Romans to color glass,<sup>35</sup> but even nowadays modern commercial glassmakers still employ metallic dispersions of copper, silver and gold to obtain different colours in decorative glasses. Metal nanoparticles have unique optical properties: when incident light frequency matches the intrinsic electron oscillation frequency, light will be absorbed resulting in the surface plasmon resonance (SPR).<sup>242</sup> Silver and gold nanoparticles, for instance, absorb the visible light and this absorption depends on different factors such as the morphology, size, the concentration of the noble metal nanoparticles, and the dielectric constant of the surrounding medium.<sup>242,243,244</sup>

The synthesis of gold nanoparticles is obtained by the reduction of a gold salt. The most popular synthesis route, for decades, is the citrate reduction of HAuCl<sub>4</sub> in water, called the Turkevich Method.<sup>245,246,247</sup> But gold nanoparticles can also be synthesized in different materials and deposited on surfaces for several purposes.<sup>240,248</sup> For example sol-gel synthesis containing gold nanoparticles is investigated not only due to its importance in the materials science field<sup>23,24,25</sup> but also in biological and pharmaceutical fields in the synthesis of bioactive glasses.<sup>28,29</sup> Sol-gel route synthesis of glass offers a flexible way to obtain new glass materials since it has low

processing temperatures and it is relatively easy to introduce several reagents.<sup>20,21,100,249</sup> This flexibility can be useful in the use of sol-gel incorporating ionic-liquids, the so-called silica ionogels, opening up to different routes and structures in glass synthesis.<sup>250,251,252,253,254,255,256</sup> The main concern during the synthesis of sol-gel gold nanoparticles is to control the aggregation in order to synthesize nanoparticles of desired sizes obtaining glass materials with the required colour. The reducing agent has a crucial role in the nanoparticles formation process.<sup>37,44,240,257,258,259,260</sup> Nucleation can be produced through different reduction agents. Halsbeck et al., for example, have studied the tin influence in the nanoparticles formation,<sup>42</sup> but other elements such as antimony, lead or europium can also be used.<sup>17</sup> Besides the conventional reductive agents other reduction methods have been also used to obtain the gold reduction such as synchrotron radiation, used by Eichekbaum et al., gamma radiation by Ruivo et al. and Zeng et al., which showed that gold was reduced and afterwards gold nanoparticles were formed in a silicate glass after being irradiated with different irradiation sources such as a femtosecond laser, nanosecond laser and X-rays, followed by a thermal treatment.<sup>37,40,41</sup> Ionic liquids (IL) that can be defined as salts that are liquid at low temperature, below than 100°C,<sup>261</sup> display very interesting properties, such as strong thermal stability and ability to stabilize "exotic" redox states.<sup>262,263,264,265</sup> In the case of transition metals, the ionic liquids have been considered in the last few years as stabilizers of metal nanoparticles in solution as an alternative to more traditional methods.<sup>266,267,268,269,270,271</sup> The nanoparticles stabilization in ionic liquids may be due to the intrinsic ionic charge, high polarity, high dielectric constant, and supramolecular network of ionic liquids that gives an electrostatic protection (a protective shell) to the metal nanoparticles.<sup>267</sup> In some cases, it was found that in solution, ionic liquids such as 1-butyl-3-methylimidazolium hexafluorophosphate and 1-(3-aminopropyl)-3-ethylimidazolium bromide could reduce the metal salt to obtain the nanoparticles and afterwards stabilize them.<sup>272,273</sup> Other studies demonstrate a different route to prepare metal nanoparticles by directly heating, for example  $\text{HAuCl}_4 \cdot 3\text{H}_2\text{O}$  in an ionic liquid.<sup>270,274</sup> However only a few studies of gold nanoparticles formation in an ionogel were made.<sup>260</sup> Having this in mind, in this chapter glass materials containing gold nanoparticles were prepared at low temperatures using the sol-gel route with an ionic liquid (1-Butyl-3-methylimidazolium tetrafluoroborate, [bmim][BF<sub>4</sub>]). With the sol-gel process route it is possible to obtain solid matrices with gold nanoparticles that can be used in several technological applications such as catalysts, optical devices and non-linear optical materials, but can also be used for decorative purposes and in art works.<sup>23,275</sup> In this work the ionic liquid was used not only as a porogen in the sol-gel synthesis but also as a reductive agent, avoiding the use of a reductive atmosphere (e.g. H<sub>2</sub> or CO) or other chemical reagents. Ionic liquids have the advantage, when used in the ionogel synthesis, to be able to control the particle aggregation and packing within the template, important factor to control the nanoparticles size and organization.<sup>260</sup> This study takes profit from the ability to use a sol-gel route to obtain a glass material containing gold and an ionic liquid. The effect of sintering the ionogel at different temperatures ( $T_{\text{sint}}$ ) or times ( $t_{\text{sint}}$ ) on the optical properties, shape, size, and distribution of gold nanoparticles is also discussed. The

thermal decomposition of [bmim][BF<sub>4</sub>] in the ionogel is investigated using calorimetric and spectroscopic techniques, and by analysis of volatile compounds released by the sol-gel material during sintering. With these results a mechanism for the formation of the gold nanoparticles is proposed.

## 5.2. Experimental Part

### 5.2.1. Sol-gel preparation and densification

Gold samples were synthesized according to a typical preparation procedure in which tetramethyl orthosilicate (TMOS) is used as the silica precursor when mixed with alcohol and water at the molar proportion of 1:15:50 respectively (see figure 5.1.).<sup>22</sup> Briefly 2.0 ml of a gold solution  $5.0 \times 10^{-4}$  M were mixed with 1.3 ml of 2-propanol (*i*-PrOH) and 0.32 ml of TMOS. The solution was acidified with 0.25 ml of HCl (0.5 M), stirred for 5 min and left to solidify at room temperature (synthesis A). In synthesis B, a small amount (20  $\mu$ l) of the ionic liquid was dissolved on the gold salt solution previously to the sol-gel mixture formation. A water soluble ionic liquid, [bmim][BF<sub>4</sub>] was used. After gelation, samples produced accordingly to synthesis A (without ionic liquid) were heat treated in air at 400°C during 60 min, with a heating rate of 180°C/h, the so-called sintering step. In order to determine the influence of the temperature on the gold nanoparticles formation, the gels containing [bmim][BF<sub>4</sub>] (synthesis B) were heat treated in air at different temperatures (50, 150, 200, 250, 300, 350, 365, 375, 390, 400, 415, 425 and 450°C) and at 400°C during different times (15, 30 and 120 min), with an increment of 180°C/h.

The following reagents and solvents were used without further purification: tetramethyl orthosilicate (TMOS, Fluka, 98%), gold (III) chloride hydrate (HAuCl<sub>4</sub>·3H<sub>2</sub>O, Sigma-Aldrich, p.a.,  $\geq 49\%$  Au), concentrated hydrochloric acid (Aldrich, 37%), 2-propanol (*i*-PrOH, Fluka, p.a.) and 1-butyl-3-methylimidazolium tetrafluoroborate ([bmim][BF<sub>4</sub>], Alfa Aesar  $\geq 98\%$ ).

In figure 5.1 the two synthesis processes are described.

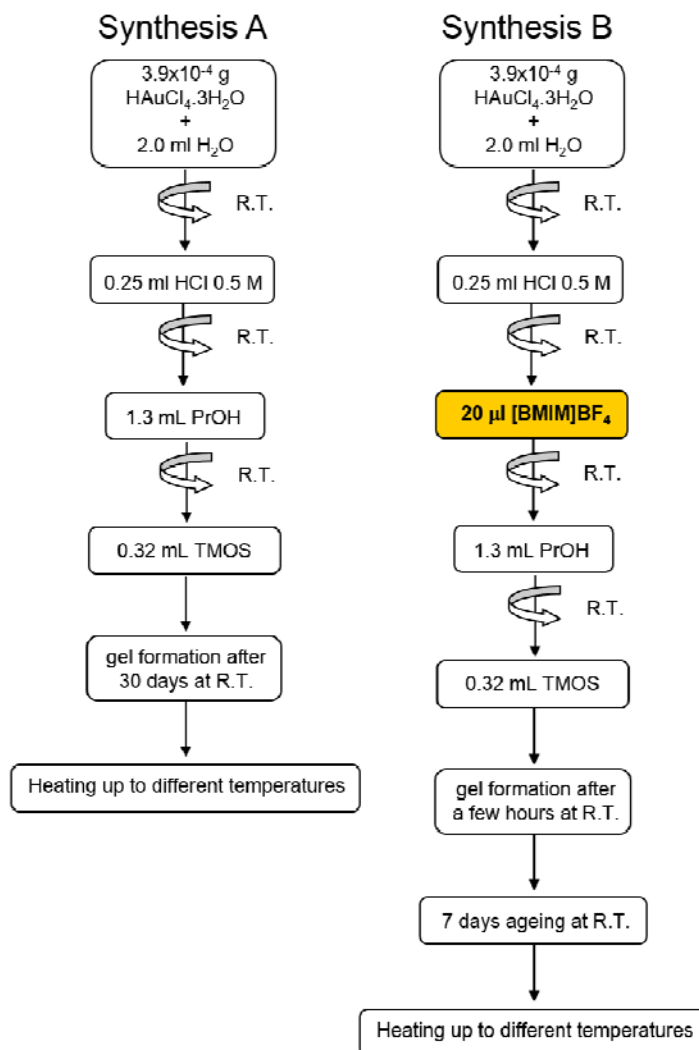


**Figure 5.1.** Schematic diagram of the sol-gel synthesis containing chloroauric acid (A) and containing chloroauric acid and the ionic liquid [bmim][BF<sub>4</sub>] (B).

### 5.2.2. Measurements

The samples characterization was made using several techniques:

**Transmission electron microscopy (TEM)** - images were obtained with a *Hitachi H-8100* microscope operating at 200 kV. The samples were ground in a mortar grinder RM200 from Retsch ( $\leq 32 \mu\text{m}$ ), suspended in ethanol, dropped and evaporated on a Formvar-coated copper grid. The images were obtained with a point-to-point resolution of 2.7 Å.

**Energy dispersive X-ray spectroscopy (EDS)** - carried out with a ThermoNoran device in a semiquantitative way with a resolution of 138 eV.

**Optical absorption spectroscopy** - UV/Vis absorbance spectra were performed using a UV-Vis-NIR spectrophotometer Varian Cary 5000 (using a spectral range from 300 to 800 nm). Several absorption spectra were taken of the sol-gel monoliths. To determine the spectra of the gold nanoparticles, a comparison was made with samples synthesized without chloroauric acid, in order to subtract the background. Several surface plasmon resonance (SPR) spectra were obtained, and the wavelength with higher intensity was determined. From those measurements,

a standard deviation was determined and shown in the data shown in the subchapter 5.3.1 displayed as error bars.

**Porosity** - tests were made by mercury intrusion porosimeter using a Micromeritics, Autopore, model IV 9500. The samples were grounded in a mortar grinder RM200 from Retsch ( $\leq 32 \mu\text{m}$ ) and then analyzed. Mercury was filled from a filling pressure of 0.5 psia and intruded to a maximum pressure of 30 000 psia.

**Thermogravimetry (TGA) and differential scanning calorimetry (DSC) analysis** - performed using a *Simultaneous Thermal Analyser STA 449 F3 Jupiter* in nitrogen (50 ml/min) from 20 to 900°C. To do these analyses the samples were grinded in an agata mortar, placed in platinum crucibles and heated at a rate of 5 K.min<sup>-1</sup>.

**Micro-energy dispersive X-ray fluorescence ( $\mu$ -EDXRF)** - were made using a portable spectrometer *ArtTAX Pro* which consists of an air-cooled low-power X-ray tube with a molybdenum target, a silicon drift detector electro- thermally cooled with a resolution of 160 eV at 5.9 keV (Mn-K $\alpha$ ) and a measurement head fixed on a tripod with a motor-driven XYZ stage for sample positioning. This system is combined with a color CCD camera that provides a magnified digital image of the area under investigation. The primary X-ray beam is focused by means of polycapillary X-ray minilens and the excitation and detection paths can be purged with helium to allow the detection of low-Z elements. Measurements were carried out directly on the surface of the samples without any previous preparation using always the same conditions: voltage 40 kV, intensity 0.6 mA and 360 s of live time measurement.

**Headspace-solid phase microextraction (HS-SPME) and Gas chromatography/mass spectrometry (quadrupole) analysis, GC/qMS** - HS-SPME-GC/qMS was used in collaboration with Professor Marco Gomes da Silva from FCT/UNL. HS-SPME was performed introducing the sol-gel sample obtained from synthesis B in a 4 mL vial. The vial was then immediately sealed with a Teflon lined rubber septum / aluminium cap. The vial samples were equilibrated at 260°C during the sorption step. The manual SPME holder and the SPME fibres were purchased from Supelco (Bellefonte, PA, USA). A 100  $\mu\text{m}$  PDMS fibre was used. Prior to use, the fibre was conditioned following the manufacturer's recommendations. The fibre was exposed to the sample headspace during a suitable sorption period of 30 min at 260°C and introduced into the GC injection port to allow thermal desorption of the analytes at a temperature of 250°C for a 1.0 min period. Splitless injection mode was performed for 1 min period. The GC/qMS system consisted of an Hewlett Packard 5890 series II model GC system. The GC/qMS instrument was equipped with a Hewlett Packard 5972 mass selective detector (MSD) series II and ChemStation software. The MS detector was operated with a transfer line temperature of 250°C, the detector voltage was 1.7 kV, and a mass scan range of 40–400 Da was used. Spectra were matched with Mass Spectra Library NIST version 2.0, 2005 ChemStation software. The analytical system operated with a BPX5 (5% phenyl polysilphenylene-siloxane) column; 30 m  $\times$  0.25 mm i.d.  $\times$  0.25  $\mu\text{m}$  film thickness ( $d_f$ ). The column was from SGE International (Ringwood, Australia). The oven temperature program for GC/qMS analyses began at 50°C, held for 1 min,

raised to 125°C at 4°C/min, then to 250°C at 6°C/min and held for 10 min at 250°C. Helium was used as carrier gas at a flow rate of 1.3 mL/min.

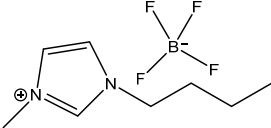
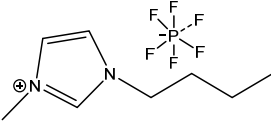
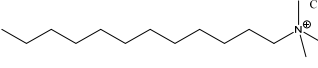
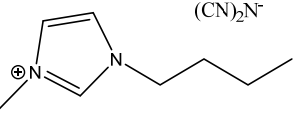
**Fourier transform infrared spectroscopy (FT-IR)** - analyses were performed on a *Nicolet Nexus* spectrophotometer coupled to a *Continuum* microscope with a *Thermo Nicolet MCT* detector cooled by liquid nitrogen, optimized for the spectral region of 4000 cm<sup>-1</sup> to 650 cm<sup>-1</sup>.

Spectra were collected in transmission mode, in 50-100 μm areas resolution setting 4 cm<sup>-1</sup> and 128 scans, using a diamond compression cell. The CO<sub>2</sub> absorption band at ca. 2300-2400 cm<sup>-1</sup> was removed from the spectra.

### 5.3. Synthesis of sol-gel glass with gold nanoparticles using an ionic liquid as a reduction agent

Silica gel samples were synthesized according to a typical sol-gel preparation procedure using TMOS, *i*-propanol and water, taking into account the proportions used in an ionogel synthesis found in the literature.<sup>22,249, 276</sup> The objective was to synthesize sol-gel materials with optical properties induced by the formation of gold nanoparticles. Therefore, gold(III) chloride was added into the preparation of the sol-gel. A reduction atmosphere or a reducing agent, such as sodium citrate, would also be necessary to reduce gold in order to obtain the gold nanoparticles.<sup>23,240,245,249</sup> On the other hand, ionic liquids are known to stabilize metal nanoparticles or other reduced metal states<sup>266,267,268,269,270</sup> and, in some cases, they can be the reducing agent of the metal salt as well.<sup>272,273</sup> The selection of the ionic liquid should take into account these aspects, providing simultaneously the porogen and the sacrificial reducing agent for gold reduction and formation of gold nanoparticles. Experiments with different ionic liquids were performed as shown in table 5.1.

**Table 5.1.** Different ionic liquids used in the sol-gel synthesis, their chemical formula, structure and solubility in water. Sol-gel characteristics before the heat treatment and after the heat treatment at 300°C

Ionic liquid	Chemical Formula	Structure	Water solubility	Before Heat treatment	After heat treatment (300°C)
1-Butyl-3-methylimidazolium tetrafluoroborate <b>Bmim[BF<sub>4</sub>]</b>	[C <sub>8</sub> H <sub>15</sub> N <sub>2</sub> ] <sup>+</sup> BF <sub>4</sub> <sup>-</sup>		✓	Transparent	Vitreous aspect
1-Butyl-3-methylimidazolium hexafluorophosphate <b>Bmim[PF<sub>6</sub>]</b>	[C <sub>8</sub> H <sub>15</sub> N <sub>2</sub> ] <sup>+</sup> PF <sub>6</sub> <sup>-</sup>		X	Did not formed sol-gel	-
Dodecyl trimethyl ammonium chloride <b>Aliquat®</b>	C <sub>15</sub> H <sub>34</sub> N.Cl		X	Heterogeneous Two phases	black
1-Butyl-3-Methyl-Imidazolium Dicyanamide <b>Bmim[DCA]</b>	C <sub>10</sub> H <sub>15</sub> N <sub>5</sub>		X	Heterogeneous white	black



Water-immiscible ionic liquids, such as 1-butyl-3-methylimidazolium hexafluorophosphate, dodecyl trimethyl ammonium chloride or 1-butyl-3-methyl-imidazolium dicyanamide, were not suitable because the first one did not form sol-gel and the others gave rise to a two-phase system, therefore homogeneous sol-gel materials were not possible to be synthesized. Focusing on [bmim] based ionic-liquids, [bmim][BF<sub>4</sub>] was selected since it is a well-known water-soluble ionic-liquid, which was previously reported for the synthesis of ionogels.<sup>276,277</sup> Using synthesis B of figure 5.1 (with ionic liquid) and following the different steps usually used in a sol-gel synthesis<sup>21,22</sup> a transparent and yellowish ionogel is formed after a few hours followed by the formation of a monolith with cylindrical shape after seven days aging, see figure 5.2. Those monoliths were afterwards sintered in air, with 50°C steps from 150°C to 450°C, for 60 minutes.

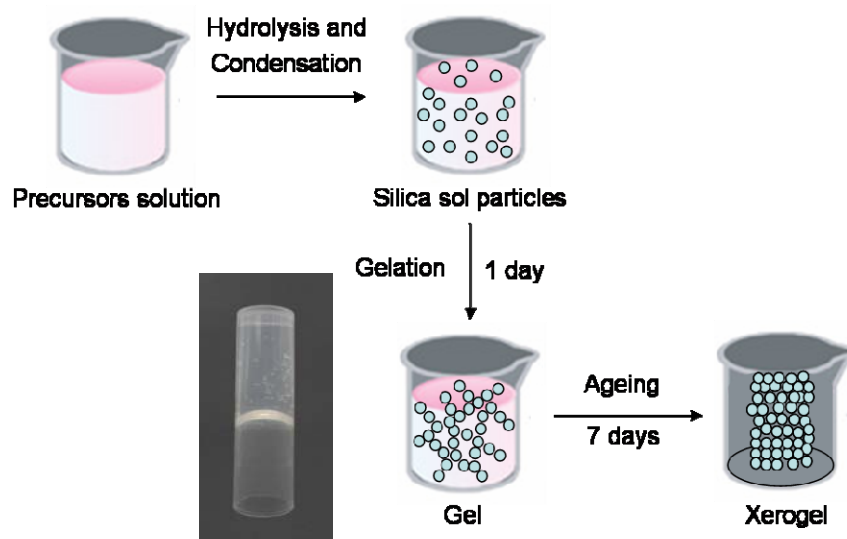


**Figure 5.2.** Different steps of the sol-gel process used in synthesis B, with the ionic liquid.

The different steps shown in figure 5.2 are commonly used in the sol-gel synthesis and are explained in detail in chapter 1.

The control synthesis A (without [bmim][BF<sub>4</sub>]) rendered a gelation step that took around 30 days and in this case a brittle material was obtained that gave rise to transparent and yellowish fragments. Sintering this sample at 400°C for 60 minutes did not give rise to the formation of gold nanoparticles (figure 5.3). This result is consistent to what is found in the literature, that a reducing agent is essential for the gold nanoparticles formation process.<sup>37,44,240,257,258,259</sup>



**Figure 5.3.** Glass monoliths obtained from synthesis A, without ionic liquid, sintered at 400°C.

Using synthesis B, with ionic liquid, a transparent red monolith glass was obtained when the sample was heat-treated at 400°C during 60 min suggesting that gold nanoparticles were formed at this temperature, while at lower temperatures, like 350°C, no change of optical properties was observed (figure 5.4). Above 450°C the samples became black and opaque, probably due to ionic liquid degradation forming carbon materials.

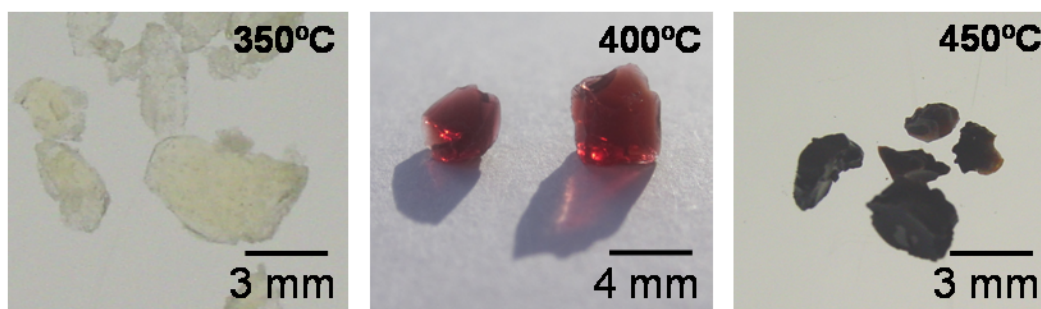


**Figure 5.4.** Glass monoliths obtained from synthesis B, with ionic liquid, sintered at 350°C, 400°C and 450°C.<sup>(6)</sup>

The presence of the ionic liquid was thus responsible for both lowering the gelation time of samples and for the reduction process. Generally, the gel synthesis from silicon alkoxides requires an acid catalyst that accelerates the hydrolysis of alkoxide to hydroxyl groups, and a base that catalyzes the condensation in order to obtain the siloxane link. Ionic liquids can work as a catalyst for both processes because their anions are good Lewis bases and their cations behave as a Brönsted acid. Therefore the small amount of ionic liquid, which was introduced in this synthesis, worked out as an accelerator of the gel formation process. When used as a solvent, the [bmim][BF<sub>4</sub>]:Si ratio is usually higher than the one used in the present work. Some authors (Liu et al, 2005; Karout and Pierre, 2009)<sup>276,277</sup> were able to produce transparent silica gels using [bmim][BF<sub>4</sub>] on molar proportions to silica higher than 0.4. In the present case, we

<sup>(6)</sup> The photographs of the sol-gel samples sintered at 350°C and 450°C were taken by the undergraduated student Carla Almeida.

thought that such high proportions of ionic-liquid are not required to synthesize the gold nanoparticles in the sol-gel matrix, because our first purpose is not to use the ionic liquid as a solvent, but to use it as a reductive agent; therefore a much lower ratio (1:0.05) was used in this work. This low quantity of ionic-liquid is not commonly used and only a few studies were reported. Shi et al, 2005, described a study of silica-gel using small amounts of ionic-liquid, showing that the average pore diameter increases with the ionic liquid quantity, but no conclusions about the gel formation time was reported.<sup>278</sup> Karout and Pierre, 2007, also synthesized silica xerogels and aerogels with different ionic-liquid concentrations, showing that the ionic-liquid influences the gel-time even in small quantities.<sup>279</sup> Curiously in this study the gelation time increased with the molar ratio of ionic-liquid to Si atoms (from nIL/nSi= 0 to 1.62), although the same authors on other study synthesized silica aerogels using different ionic-liquids as gelation catalysts.<sup>277</sup> Settling the synthesis composition, the sintering temperature effect on the optical properties, shape, size, and distribution of gold nanoparticles was studied in order to optimize the condition in which gold nanoparticles are formed. After the first temperature study, where samples were sintered in 50°C steps from 150°C to 450°C, the sol-gel samples with ionic liquid were now sintered at 350°C, 365°C, 375°C, 390°C, 400°C, 415°C and 425°C for 60 minutes. Red colored glass is obtained for sintering temperatures above 365°C, although at 365°C and 375°C the red colour still appears in an heterogeneous way, see figure 5.5., becoming more homogeneous at 390°C. This indicates that the ionic liquid is not dispersed in the sol-gel in a homogeneous way and that the reduction starts where the ionic liquid is more concentrated.

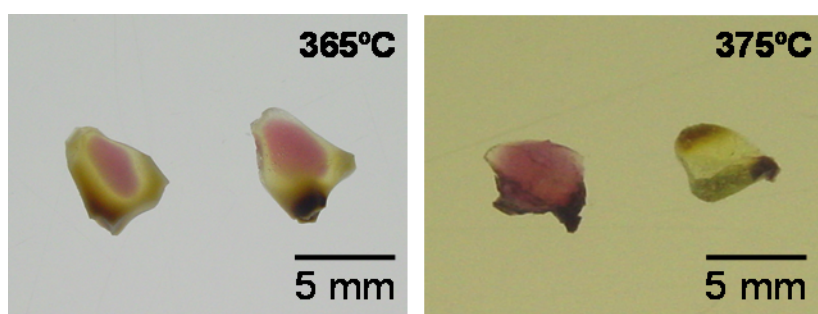


**Figure 5.5.** Sol-gel obtained from synthesis B, with ionic liquid, sintered at 365°C and 375°C.<sup>(7)</sup>

### 5.3.1. Monoliths characterization by UV-VIS absorption spectroscopy

In figure 5.6 the UV-Vis absorption spectrum of the red glass monoliths containing gold nanoparticles is shown. The spectra are normalized because the synthesized monoliths are irregular giving rise to different absorption intensities depending of light incidence position in the sample. These spectra were obtained after subtracting the background from the sol-gel. The

<sup>(7)</sup> The photographs of the sol-gel samples sintered at 350°C and 450°C were taken by the undergraduated student Carla Almeida.

spectrum presents the expected characteristic surface plasmon resonance (SPR) band of gold nanoparticles.<sup>44</sup>

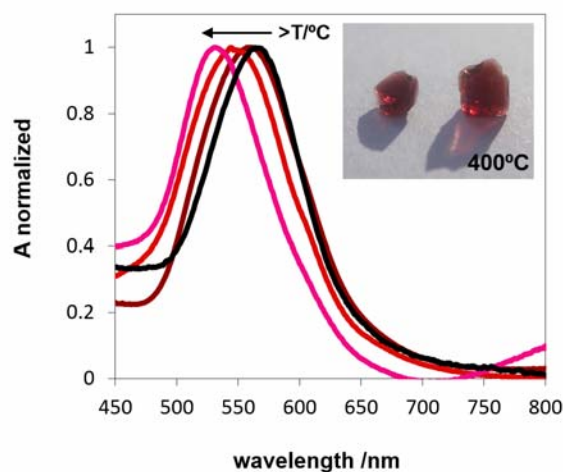


**Figure 5.6.** Experimental UV–Vis absorption spectrum of glass monolith samples with Au nanoparticles (after subtracting the background from the sol-gel), produced after the thermal treatment of the ionogel at 365, 375, 400 and 425°C (arrow indicates the increase of the sintering temperature) during 60 min. An image of the glass monoliths obtained at 400°C is shown in the inset.

These experiments were made not only sintering at different temperatures ( $T_{\text{sint}}$ ) but also during different times at 400°C ( $t_{\text{sint}}$ ), as shown in figure 5.7.

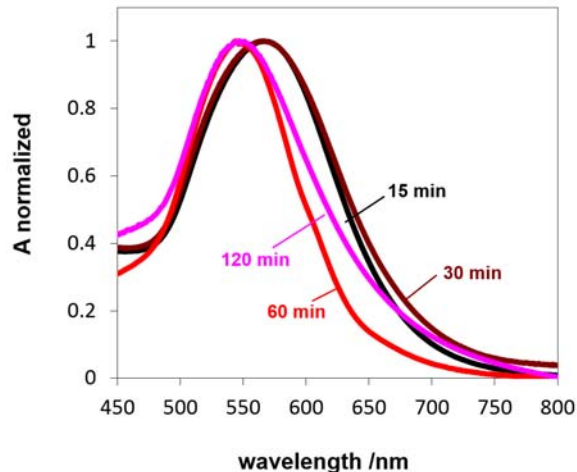


**Figure 5.7.** Experimental UV–Vis absorption spectrum of glass monolith samples with Au nanoparticles (after subtracting the background from the sol-gel), produced after the thermal treatment of the ionogel at 400°C during different times (15, 30, 60 and 120 min).

Both the parameters have an impact on the absorption spectra (table 5.2). The shift on absorbance maximum promoted by the temperature and time is also represented on Figure 5.8. The absorption band shifts to shorter wavelengths at higher sintering temperatures and with longer sintering times. This shift in the absorption band may be attributed to the presence of smaller gold nanoparticles. Also the bandwidth is relatively high, as can be found in other glass materials,<sup>23,248</sup> indicating a high polydispersity of the gold nanoparticles when compared to

those normally synthesized in aqueous solution using known standard methods such as the Turkevich method. However since it is not a direct result, TEM experiments were performed afterwards to determine the sizes and shapes of the gold nanoparticles.

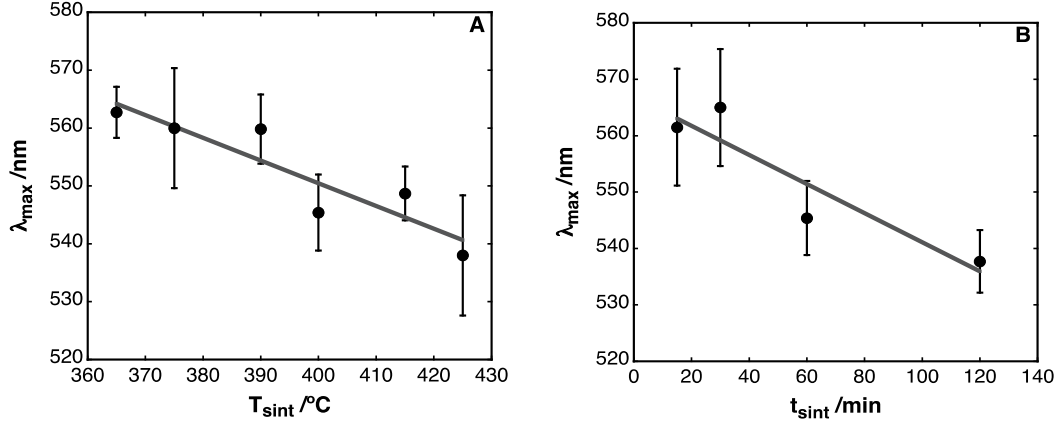


**Figure 5.8.** Plot of the wavelength corresponding to the maximum absorbance of the SPR band for samples sintered at different temperatures ( $T_{\text{sint}}$ ) for 60 minutes (A) and sintered at 400°C for different times ( $t_{\text{sint}}$ ) (B). Error bars corresponds to one standard deviation, see section 5.2.2. for details.

**Table 5.2.** Band position at the maximum of intensity ( $\lambda_{\max}$ ) of the gold nanoparticles taken from the absorption spectra, number of particles seen in TEM images (N), average diameter and the size standard deviation (log normal distribution,  $\sigma$ ) for different sintering temperatures ( $T_{\text{sint}}$ ) and times ( $t_{\text{sint}}$ ).

$T_{\text{sint}}$ /°C	$t_{\text{sint}}$ /min	$\lambda_{\max}$ /nm	N	Diameter /nm	$\sigma$	Average Pore Diameter (4V/A, nm)
375	60	$560 \pm 10$	23 <sup>a)</sup>	36.2	0.32	-
400	60	$545 \pm 7$	33 <sup>b)</sup>	32.0	0.26	41.7
425	60	$538 \pm 10$	87 <sup>c)</sup>	27.6	0.27	58.5
400	15	$562 \pm 10$	7 <sup>d)</sup>	51.9	0.46	39.6
400	30	$565 \pm 10$	31 <sup>e)</sup>	33.7	0.29	45.3
400	120	$538 \pm 6$	52 <sup>f)</sup>	39.1	0.30	52.4

N were found in the following areas: a)  $8 \mu\text{m}^2$ , b)  $8 \mu\text{m}^2$ , c)  $6 \mu\text{m}^2$ , d)  $8 \mu\text{m}^2$ , e)  $9 \mu\text{m}^2$  and f)  $10 \mu\text{m}^2$

### 5.3.2. TEM and EDS Measurements

The measurements were performed for two different sets of glass monoliths. One set shows the effect of changing  $T_{\text{sint}}$ , while another set shows the impact of changing  $t_{\text{sint}}$ . Table 5.2 summarizes those results, by showing the average diameter of the gold nanoparticles and also the standard deviation assuming a log normal distribution of sizes. Examples of images of the gold nanoparticles obtained through TEM technique are displayed in figure 5.9 (more images may be found in section 9.4.1, Supplementary Material). TEM images were taken from several parts of the grinded samples in order to have information of different areas. The particles are

highly polydispersed, with sizes ranging from 10 nm to 70 nm, and many times with non-spherical shapes (see section 9.4.1, Supplementary Material, some examples). Nevertheless, EDS measurements always confirmed that the nanoparticles observed by TEM were essentially constituted by gold as expected (Figure 5.10). Some small traces of other elements, such as carbon and oxygen, are also found but interestingly other elements such as chlorine or fluorine are not observed.

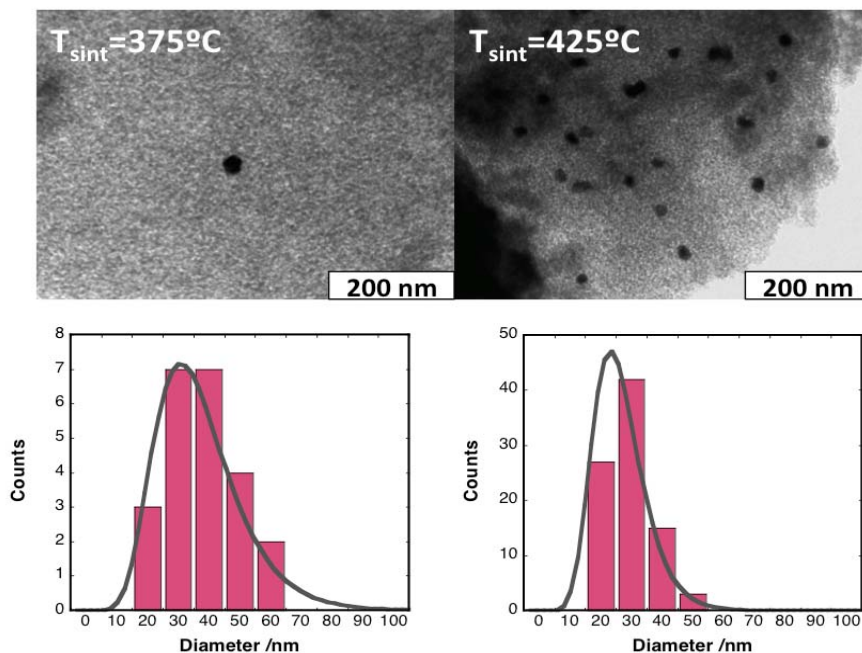


**Figure 5.9.** TEM image and size distribution analysis of Au nanoparticles in glass produced after the thermal treatment of the ionogel at 375 and 425°C during 60 minutes. The size distribution was determined with a log normal distribution using the statistic data obtained from the histograms here shown as well.

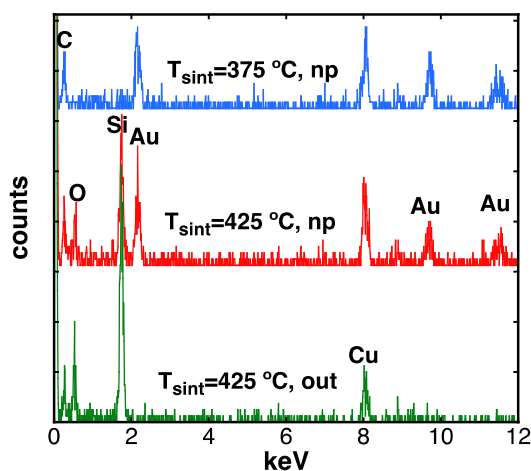


**Figure 5.10.** EDS analysis of the nanoparticles (np, red and blue line) with two different  $T_{\text{sint}}$  (375 and 425°C) and in an area without nanoparticles (out, green line).

The TEM images confirm the presence of gold nanoparticles. It is important to refer that the frequency of their presence greatly increases with  $T_{\text{sint}}$ , as can be seen from the particle count  $N$  on table 5.2, from the TEM images shown on figure 5.10 or from figure 5.11 that show the



nanoparticles number per  $\mu\text{m}^2$  in function of the  $T_{\text{sint}}$  and the  $t_{\text{sint}}$ . Increasing the temperature a higher number of nanoparticles are formed, indeed at  $T_{\text{sint}}=425^\circ\text{C}$  a high number of particles could be seen on a single image while at lower temperatures many regions gave a null result. The same effect was also seen with  $t_{\text{sint}}$  (see figure 5.11). It is also possible to detect the existence of a higher number of spherical shaped particles at  $T_{\text{sint}}=425^\circ\text{C}$  and  $t_{\text{sint}}=120$  min, see TEM images in section 9.4.1 in Supplementary material.

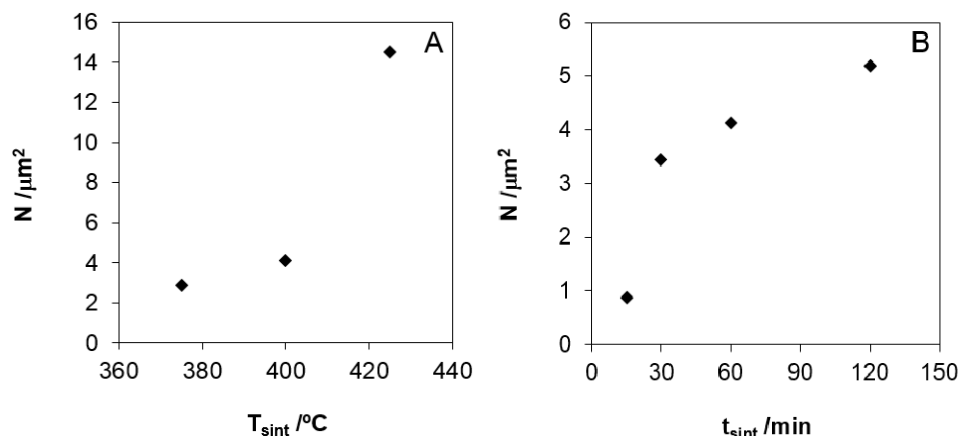


**Figure 5.11.** Number of gold nanoparticles per  $\mu\text{m}^2$  found by TEM for samples sintered at different temperatures ( $T_{\text{sint}}$ ) for 60 minutes (A) and sintered at  $400^\circ\text{C}$  for different times ( $t_{\text{sint}}$ ) (B).

The position of the SPR band correlates with the average diameter obtained from the TEM images, shifting to the blue when the size decreases as expected. This effect is particularly evident when  $T_{\text{sint}}$  is changed. When  $t_{\text{sint}}$  is varied this effect is not evident (table 5.2 and figure 5.12) but the average diameter decreases following a similar trend observed in the SPR band within experimental error. It also must be pointed out that for  $t_{\text{sint}}=15$  min TEM measurements are not statistically meaningful.

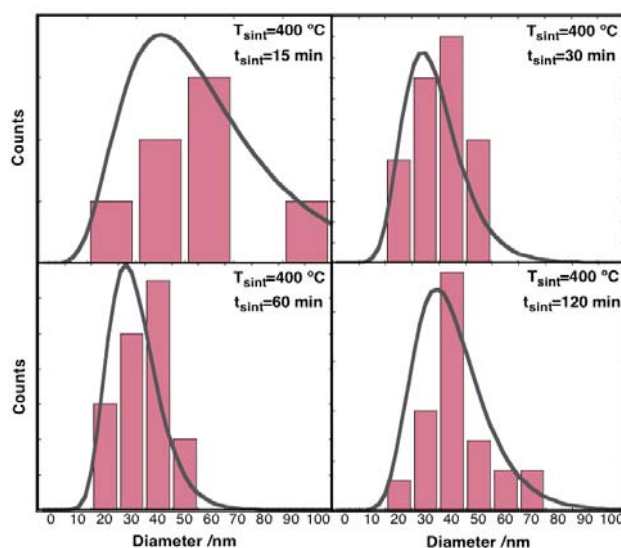


**Figure 5.12.** Histograms of TEM images and size distribution analysis of Au nanoparticles in glass produced after the thermal treatment of the ionogel at  $400^\circ\text{C}$  with different sintering times. The size distribution was determined with a log normal distribution using the statistic data obtained from the histograms here shown as well.

It is therefore possible to conclude that more gold nanoparticles can be found and that they are smaller when the samples are sintered at higher temperatures. This goes in disagreement to what is usually found in the literature.<sup>23,280,281,282,283</sup> This issue will be discussed after analyzing all the data.

Porosimetry tests were also performed, see table 5.2. The obtained gold nanoparticles have comparable diameters with the average pore diameters obtained with the porosimetry tests. These results suggest that the ionic liquid act as porogen for the gold nanoparticles formation.

The method here presented has a significant difference to other methods that may be found in the literature.<sup>245,249,257,258</sup> Here the sol-gel with the ionic liquid (ionogel) is the porogen for the *in-situ* production of metal nanoparticles at temperatures around 400°C. The ionic liquid should provide the reductive environment without the necessity of introducing reductive gases (e.g. H<sub>2</sub> or CO) or other chemical reagents, as well as the porogen. The gold nanoparticles here synthesized also do not have protective layers (such as silica) as in other examples from the literature.<sup>249,284</sup>

To better understand the process behind the gold nanoparticles formation, in the next sub chapters the thermal degradation mechanism of the ionic liquid and how it may allow the synthesis of glasses with gold nanoparticles, here described, is discussed.

### 5.3.3 Ionic liquid decomposition

The composition of the synthesized sol-gel includes two anions, BF<sub>4</sub><sup>-</sup> and Cl<sup>-</sup>, and both could therefore react with bmim<sup>+</sup> during the IL decomposition. On table 5.3, values reported for the thermal decomposition of [bmim] based ionic liquids found in the literature are listed.<sup>251,285</sup> It can be seen on table 5.3 that the decomposition temperature is highly dependent on the anion, while the encapsulation of the IL on a sol-gel has a minor effect.<sup>251,255</sup>

**Table 5.3.** Thermal decomposition of different [bmim] based ionic liquids and comparison with the thermal processes observed in sol-gel with ionic liquid. T<sub>starts</sub> is when the decompositions starts and T<sub>middle</sub> is the middle temperature value of the decomposition temperatures range. These values were taken from the TGA analysis.

compound	T <sub>middle</sub> /°C	T <sub>start</sub> /°C
[bmim][Cl] <sup>285</sup>	264	150
[bmim][BF <sub>4</sub> ] <sup>285</sup>	361	290
<i>Sol-gel produced in this work (synthesis B)</i>	265	240
	395	330
[bmim][TF <sub>2</sub> N] <sup>285</sup>	422	330
[bmim][TF <sub>2</sub> N] ionogel <sup>251</sup>	—	370



Thermogravimetric analysis (TGA) and differential scanning calorimetry analysis (DSC) were performed to samples made according with both synthesis routes. Synthesis A (without ionic liquid) gave rise to results shown in figure 5.13, essentially showing the thermal solvent removal until a temperature of about 200°C. Above 600°C it is possible to observe small exothermic peaks that should be connected with crystallization processes that occur at that temperature.

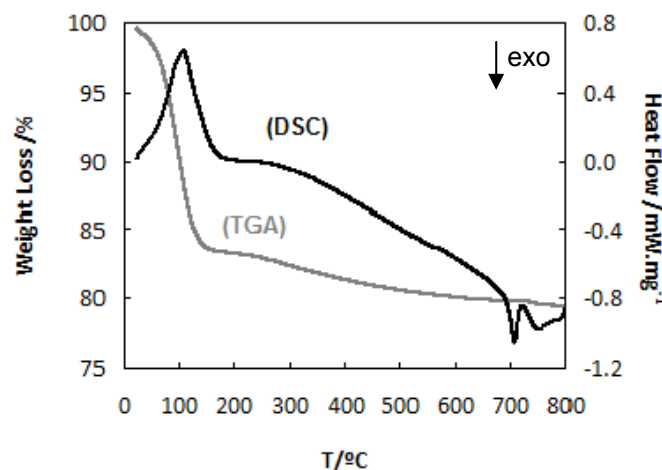


**Figure 5.13.** TGA (grey line) and DSC (black line) measurements of the material synthesized according to synthesis A, without the ionic liquid [bmim][BF<sub>4</sub>].

Synthesis B (with ionic liquid), however, showed many features that are shown in figure 5.14. DSC analysis shows an endothermic peak at around 114°C, which is correlated with a strong mass decrease seen in TGA, pointing out to the volatilization of the solvents present in the material. This effect is also seen in synthesis A. However, between 240 and 425°C several mass losses are observed stepwise, without any meaningful changes in the DSC result (see also table 5.3 where those temperatures are shown). Between 240 and 300°C a first mass loss is observed, followed by a second similar process at the range between 330 and 425°C. Interestingly, it is in the second temperature range that gold nanoparticles are formed which indicates that this mass loss is correlated with the red color formation. It is only possible to observe an exothermic peak at 425°C. This is coincident with the fact that above this temperature the material becomes black and opaque and also it is coincident with the [bmim][BF<sub>4</sub>] decomposition temperature reported in the literature. This should mean that at this temperature the small amount of ionic liquid that is in the sample finally degrades completely, leaving behind some carbon compounds which gradually are oxidized at higher temperatures leading to a small mass increase afterwards (indeed in other studies performed with europium above 700°C the samples are white and opaque with the presence of carbonates, that were confirmed by FTIR spectroscopic measurements, see section 9.4.2, Supplementary Material).

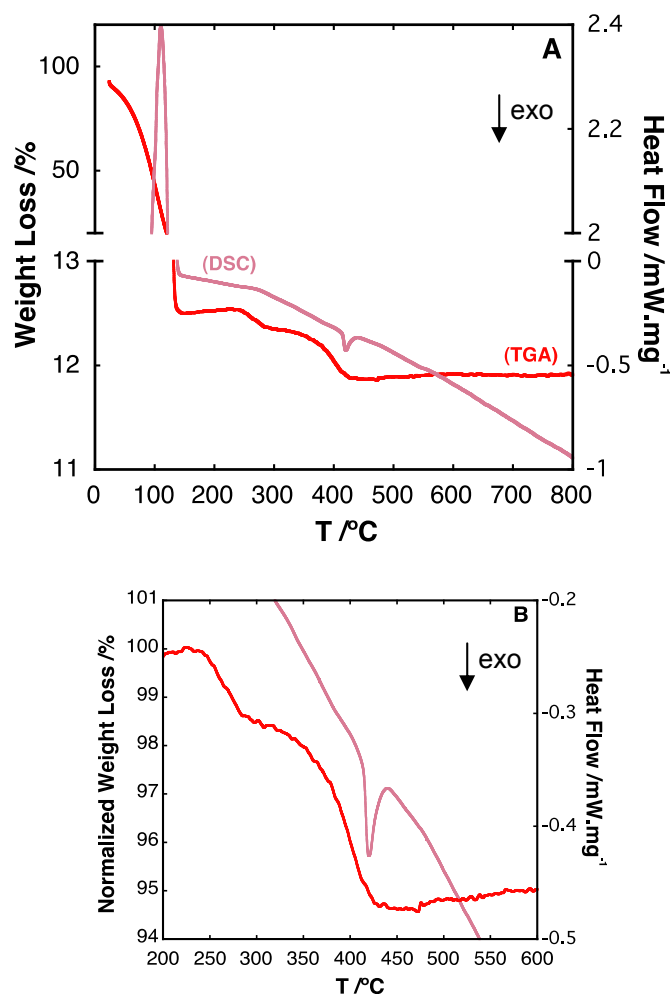


**Figure 5. 14.** TGA (red line) and DSC (pink line) measurements of the material synthesized according to synthesis B, with ionic liquid. Graphic A shows the full results of both experiments, while graphic B focus on the region where two mass losses steps are seen. In graphic B the TGA result is renormalized at  $T=230^{\circ}\text{C}$

$\mu$ -EDXRF analyses were performed in glass samples obtained by synthesis B, with different  $T_{\text{sint}}$ . In figure 5.15 (A), from  $50^{\circ}\text{C}$  to  $150^{\circ}\text{C}$  the broad band that exists in the 11 keV regions decreases significantly, which is connected with the fact that the sample is losing solvent. Chlorine concentration decreases about 80% during this process. At  $365^{\circ}\text{C}$  the peak correspondent to chlorine totally disappears. In figure 5.15 (B) is shown the chlorine intensity determined by XRF spectrometry of the samples with different  $T_{\text{sint}}$ . The remaining chlorine that still exists when the sample is sintered at  $150^{\circ}\text{C}$  disappears when the sample is sintered at  $250^{\circ}\text{C}$ . It is important to remember that all the samples analyzed by  $\mu$ -EDXRF were sintered at the different temperatures during one hour, but in the other hand in the TGA analysis it was used a heating rate of  $5\text{ K}\cdot\text{min}^{-1}$  without any dwell. The mechanism for the chlorine removal can be interpreted considering the HS-SPME-GC/qMS results.

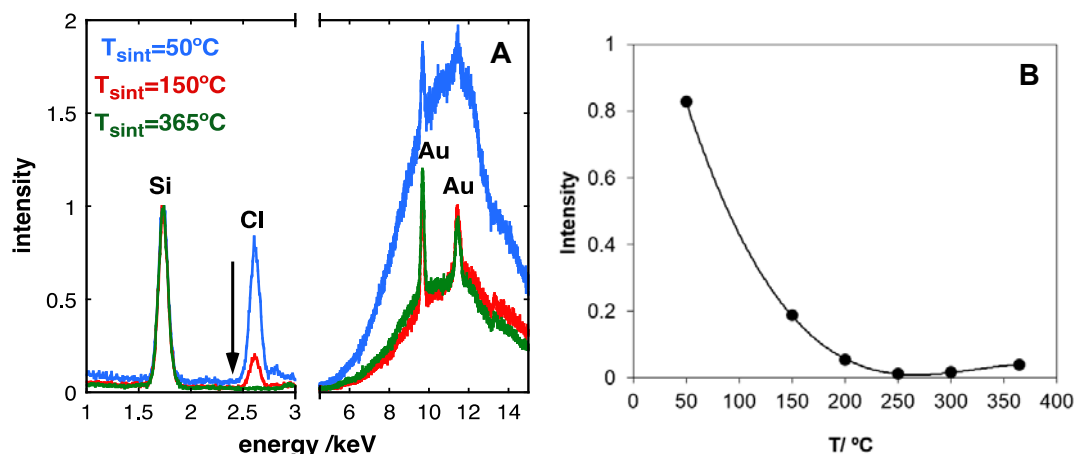


**Figure 5.15.** (A)  $\mu$ -EDXRF analysis of the glass samples sintered at different temperatures: 50°C, 150°C and 365°C, normalized in the Si peak. (B) Chlorine intensity taken from the XRF spectra (normalized in the Si peak) of the samples with different  $T_{\text{sint}}$ .

The GC/qMS analysis after HS-SPME (performed in collaboration with Professor Marco Gomes da Silva from FCT/UNL), allow the identification of chloromethane, 1-chloro-butane, N-methyl-imidazole and N-butyl imidazole as the major components. The mass spectra obtained for each compound was analyzed and were compared with NIST library: Chloromethane (retention time ( $t_r$ )= 1.8 min,  $m/z$  = 50 (100%) [ $M^+$ ], 52 (34%) [ $M^+$ ]; 1-chloro-butane,  $t_r$ = 2.9 min,  $m/z$  = 41 (60%), 56 (100%), 63 (5%), 92 and 94 both below 1% [ $M^+$ ]; N-methyl-imidazole,  $t_r$ = 7.9 min,  $m/z$  = 42 (19%), 54 (25%), 82 (100%) [ $M^+$ ]; N-butyl-imidazole,  $t_r$ = 17.3 min,  $m/z$  = 41 (40%), 55 (58%), 68 (27%), 81 (89%), 82 (100%), 97 (92%), 124 (56%) [ $M^+$ ]. These compounds were detected when the sample was treated at 250 °C and also at 350 °C. Although it cannot be excluded the presence of *i*-propanol in the sintering process, its presence was not confirmed due to possible coelution with the haloalkane's pair identified.

The temperature in which a weight loss occurs at the range between 240 and 260°C, is compatible with the [bmim][Cl] decomposition temperature (see table 5.3). GC/qMS results show that after sintering at 250°C four of the decomposition products are butylimidazole, methylimidazole, chlorobutane and chloromethane. These products are in accordance with the mechanism proposed earlier for the decomposition of [bmim][Cl], see figure 5.16, and it also explains the mass loss and the  $\mu$ -EDXRF result showing the disappearance of chlorine element. The other weight loss, of about 3.8%, could correspond to the [bmim][BF<sub>4</sub>] decomposition.

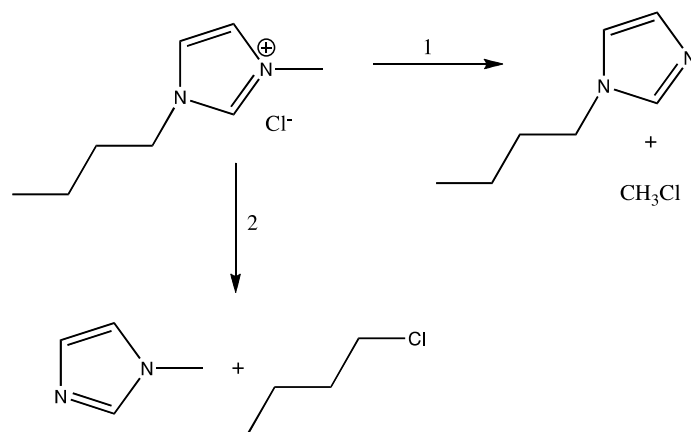


**Figure 5.16.** Mechanism proposed for the thermal degradation of [bmim][Cl] <sup>286</sup>

The decomposition products obtained after sintering, like butyl imidazole or methyl imidazole, provides the reducing conditions that could explain the appearance of gold nanoparticles above 365°C.

#### 5.3.4 Formation of gold nanoparticles

What is, therefore, the chemical process that triggers the reduction of gold? Having in mind that the gold nanoparticles were only formed in the presence of the ionic liquid we conclude that the ionic liquid is very important as porogen in the sol-gel synthesis and also has an important role in the formation of the gold nanoparticles. In the first step, the solvent present in the ionogel is removed, including water, *i*-propanol, methanol and HCl, reducing drastically the amount of chlorides present in the ionogel, as it is possible to see in the  $\mu$ -EDXRF analysis (figure 5.15). The remaining chlorides should be coordinating Au(III) at around 150°C (see figure 5.15), being part of the ionic liquid as  $\text{AuCl}_4^-$  anions.<sup>287</sup> Above 240°C the reaction of the imidazolium cation with the remaining chloride takes place according to figure 5.16. This leads to the formation of several volatile compounds seen with GC/qMS, and completely depletes the material from chloride anions. No indication of gold reduction is seen at this stage, which leaves us to conclude that Au(III) coordinates probably with imidazole compounds (methylimidazole and butylimidazole) at higher temperatures. Nevertheless, the amount of chloride available for these reactions is not enough to decompose completely all imidazolium cations, therefore [bmim][BF<sub>4</sub>] ionic liquid should exist until its degradation temperature. Above 365°C we start to see the formation of gold nanoparticles, which is accompanied by another weight loss but with no sign of ionic liquid degradation in the DSC (see figure 5.15). The ionic liquid in here can provide the porogen for the formation of the gold nanoparticles, but it also assures the fluidity necessary for gold aggregation and the reducing environment. Besides that, the remaining imidazole compounds that were formed can still stabilize the gold nanoparticles.<sup>288</sup> Zhang et al. stated that chloroauric acid can be thermal decomposed undergoing into gold particles <sup>289</sup> and the

nanosized particles could be related to confinement effects.<sup>260</sup> In the present case, only above 365°C we are able to see the gold nanoparticles, indicating the gold reduction above this temperature. Chlorine is absent at these temperatures (figure 5.15), and therefore the thermal process giving rise to the gold nanoparticles should follow a different route involving other coordinating species. The kinetics of the proposed processes is much faster at higher temperatures, leading both to more nanoparticles, but also to smaller sizes. Above 425°C the degradation of [bmim][BF<sub>4</sub>] takes place and the final product is black, and therefore this synthesis cannot take place above this threshold. The influence of  $t_{\text{sint}}$  is not clear at this stage. TEM measurements are not conclusive towards the evolution of the nanoparticle sizes, while absorption spectra seem to indicate a size decrease. Other effects may cause this result (e.g., change of the local refraction index due to changes of the material density).

#### 5.4. Conclusions

An innovative way to obtain nanoparticles on glass materials using sol-gel synthesis with an ionic liquid, [bmim][BF<sub>4</sub>] is shown in this chapter. The ionic liquid thermal decomposition study demonstrate that [bmim][BF<sub>4</sub>] has an important role not only as porogen in the sol-gel synthesis but also in the formation of the gold nanoparticles avoiding the use of a reductive atmosphere (e.g. H<sub>2</sub> or CO) or other chemical reagents. In the samples doped with ionic liquid it was possible to observe gold nanoparticles formation after sintering at 365°C, but in the sample without the ionic liquid no gold nanoparticles were formed, even at higher temperatures. Samples containing the ionic liquid were heated at different temperatures and during different times to study the effect of sintering process on the optical properties, shape, size and distribution of gold nanoparticles. These samples were investigated using several techniques, in particular UV-VIS absorption spectroscopy and TEM/EDS. It was shown that higher temperatures and higher times gave rise to more nanoparticles, but also to smaller sizes, due to the kinetics of these reduction processes.

The reduction is achieved by the [bmim][BF<sub>4</sub>] decomposition products after thermal treatment, present in the sol-gel above 240°C, that suffers a total degradation at 425°C. According to all the experimental data obtained, principally the TGA/DSC,  $\mu$ -EDXRF and GC/qMS - HS-SPME analysis it is proposed that a first ionic liquid decomposition step, where the imidazole compounds are released, generate a reductive environment that makes possible the gold nanoparticles production at temperatures between 350 and 425°C.

This work presents a new, practical and non-expensive strategy to produce and to control the dimension of gold nanoparticles into a sol-gel matrix which can be a strategy to obtain different colours changing the gold nanoparticle diameter. For example temperatures as 400°C give rise to red samples but at 365°C the samples were pink. These ruby monoliths can be used for decorative purposes.<sup>290, 291</sup> Examples of sol-gel monoliths used in artworks can already be found in the literature. Although the application of sol-gel in glass objects to obtain red films will make

these materials more simply to be applied and therefore more attractive for the artists. We expect that luminescent glasses can also be obtained using this strategy, since with this method it may be possible to synthesize glass materials reducing other metals in order to achieve more unusual oxidation states, such as  $\text{Eu}^{2+}$  or  $\text{Cu}^+$ .

## 6. Impact of the produced materials in art

### 6.1. Developed materials

This thesis shows the research and development of new glass materials designed to be used in artworks. Photoluminescent glasses doped with different lanthanides were developed, followed by a detailed structural understanding of the concentration influence of a particular lanthanide (europium) and of the glass composition in the lanthanide distribution in a glass matrix. Following this strategy, a diverse luminescent colour palette using different lanthanide oxides in soda-lime silicate glasses was achieved. Using europium, terbium and cerium that emit red, green and blue, respectively, several colours were accessible and, amongst them, it was also demonstrated that white luminescence is reachable by changing the lanthanides concentration and also changing the light excitation wavelength. The spectroscopic measurements of the lanthanides doped samples indicated the presence of excited-state processes such as energy transfer from  $\text{Tb}^{3+}$  to  $\text{Eu}^{3+}$ , from  $\text{Ce}^{3+}$  to  $\text{Eu}^{3+}$  and from  $\text{Ce}^{3+}$  to  $\text{Tb}^{3+}$  and also self quenching of  $\text{Ce}^{3+}$ , similar to what is observed in more detail for  $\text{Eu}^{3+}$ . These results are relevant for future glass synthesis since they have given important information such as the impact of the enhancement of red luminescence due to energy transfer in the final luminescence colour. The CIE chromaticity diagram and the colour coordinates is a very important tool to estimate which luminescent colours are obtained for a given composition with a mixture of lanthanides. Excited-state processes may therefore have an important impact in the final photoluminescence colour.

Another approached involved aluminoborosilicate luminescent glasses where different photoluminescence colours were also developed. In these multicomponent glasses luminescence is obtained without the use of lanthanides, giving the opportunity of avoiding these more expensive reagents using instead inexpensive reagents, such as lead halides and copper. It was possible to obtain blue luminescence doping the glasses with lead and halides due to the formation of lead halide nanoparticles. A yellow luminescence colour was also obtained due to the formation of  $\text{Cu}^+$ . The mixture of these two luminescence sources in different concentrations enables the production of several colours, including again white luminescence.

An innovative method of producing gold ruby glasses was also explored in this thesis with gold nanoparticles using the sol-gel synthesis with an ionic liquid,  $[\text{bmim}][\text{BF}_4]$ . The ionic liquid thermal decomposition study demonstrate that  $[\text{bmim}][\text{BF}_4]$  have an important role not only as template in the sol-gel synthesis but also in the formation of the gold nanoparticles avoiding the

use of a reductive atmosphere (e.g.  $H_2$  or  $CO$ ) or other chemical reagents. It is a new, practical and non-expensive strategy to produce and to control the dimension of gold nanoparticles into a sol-gel matrix which can be a strategy to obtain different colours changing the gold nanoparticle diameter.

## **6.2. Vicarte glass artists' interview**

This work is part of an ongoing collaboration between the research unit Vicarte and the photochemistry group of the associated laboratory Requimte. These groups join specialists in art, science, technology, history, archaeology and conservation. In this collaboration, where scientists and artists are working together, is very important for the scientists to understand what are the artists major concerns, what kind of products they are looking for and also to produce the new materials that will meet their requirements. In this thesis this collaboration allowed the preparation of new glass for artworks with an interesting palette of colours.

It is important to understand the importance of the development of new materials, in particularly those developed in this thesis, in the art field. Therefore, three artists working in glass were asked to give their opinions on the synthesized materials: Teresa Almeida, professor at the Faculty of Fine Art, Oporto University, Fernando Quintas, professor at the Faculty of Fine Art, Lisbon University and Robert Wiley, invited professor at the Faculty of Sciences and Technology, New University of Lisbon. For all the mentioned artists this collaboration between art and science is very important for a better understanding of the materials and in finding out what new possibilities may arise. Different opinions were obtained for the use of the different synthesized materials.

### **6.2.1. Teresa Almeida**

The artist Teresa Almeida has several artworks with luminescent glasses (figure 6.1). For Teresa Almeida luminescent glasses under a UV-light are very interesting due to the duality, the same art piece can give rise to two different readings, one under daylight, a monochromatic surface, and the other under UV-light, polychromatic surface. For her it is very important to have a diverse colour palette to use in her artworks, although the white luminescence that is intensely investigated, due to the numerous applications, is not interesting for Teresa Almeida, since she prefers to work with other colours, as she is interested in the dichotomy between monochromatic and polychromatic surfaces. For her the disadvantage of using luminescent glass, that commonly is doped with lanthanides, are the high cost of lanthanides oxides, consequently the possibility of using luminescent glasses doped with other metals is very attractive if their properties are similar to those with lanthanides. For Teresa Almeida the result obtained for the quenching of  $Cu^+$  luminescence by the laser is very exciting, because it allows to control the areas without luminescence in a luminescent glass. Normally in artworks,



obtained using the casting technique, it is difficult to control these areas when the glass is fused. She thinks that this can also be useful for publicity purposes to write a message in the luminescent glass. Concerning the ruby glass obtained using the sol-gel technique Teresa Almeida said that due to the small sizes normally obtained and due to the difficulty to fuse it with other glasses is not very appealing to her. So it is important to explore a way to synthesize glass pieces with bigger dimensions using a similar method.

### **6.2.2. Robert Wiley**

Robert Wiley has completely different opinions. For him luminescent glasses are not very interesting since it seems like a trick that is easy to use, although in his opinion it stimulates the public interest and has numerous possibilities in industry for visual and graphical communication. These glasses can be useful, for example, in educational objects. Besides their potential, luminescent glass is still a dangerous road for an artist, in Robert Wiley's opinion. Normally this artist does not have a lot of interest in colours, he prefers to see glass as water or ice; for him "glass is a door inside another world". But he also said that this opinion can be due to the low quantities of luminescent glass that he had access to explore the material possibilities. If he had kilos of this glass he could do more experiments, but the high cost of lanthanide doped glasses do not allow it. This problem can be solved with the use of d transition metals to obtain luminescent glasses. Besides his opinion, he already performed some experiments with luminescent glasses (figure 6.2). Concerning the ruby glass using the sol-gel technique, Robert Wiley opinion is that it has big limitations, as it is not very handy and it has a high cost. However he mentioned that these materials could be useful in jewellery or in decorative arts using the glass monoliths or depositing the sol-gel as a coating.

### **6.2.3. Fernando Quintas**

In Fernando Quintas opinion the use of luminescent glass is a very useful visual tool to seduce and to capture the observer attention and he already made several experiments with luminescent float glasses (figure 6.3). He said that are a lot of artists all over the world, so is the singularity and the authenticity that makes the difference, therefore everything that can help the artist to singularize his artwork is important. For Fernando Quintas the artworks need to have an immediate impact, as he said: "...the artist only has a few seconds to capture the observer's attention". As a professor he still added that luminescent glasses are also useful to capture the fine art students attention to science and therefore contribute for an increase of the plastic options of all students.

All the luminescent colours obtained in this thesis interest Fernando Quintas, inclusive the white luminescence. The artist in question thinks that white luminescent glasses can be very useful in architecture in Portugal. As the architects currently do not like to use many colours and normally try to reach a formal austerity in their projects, white luminescence can be well accepted by

architects since at night it complements and accentuates the austerity and clarity of the forms. “Artists fight to have art pieces in architecture and public spaces, so maybe white luminescence can be used to seduce the architect to collaborate more with artists”.

Fernando Quintas found interesting all the materials produced in this thesis, inclusive the ruby glass, because for him artists live with what is not expectable and all the elements that are different can be overlapped and very useful to show the artist creativity. For Fernando Quintas the collaboration between artists and scientists is extremely important, since artists commonly only use the materials but do not produce them. So this collaboration, in his opinion, is important for artists to discover the materials possibilities and viability, having a strong impact in the art evolution.

In this artists opinion most of all the produced glasses can be used and can increase the aesthetic value of an artwork or of design objects. Even Robert Wiley who did not show a great interest in luminescent glasses stated that it can cause an impact in the observers and it can also be used with other purposes in mind.

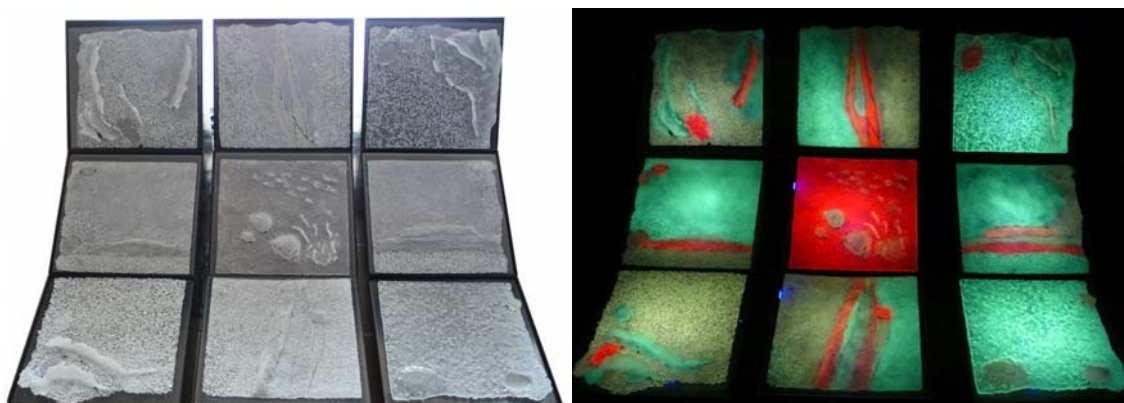


**Figure 6.1.** “Pâte de verre” artwork, using  $Tb^{3+}$ ,  $Eu^{3+}$  and  $Dy^{3+}$  doped glasses; Teresa Almeida, 2009. Left: shown under daylight; right: shown under UV-light (ca. 370 nm).



**Figure 6.2.** Result of an experiment made with europium doped borosilicate glass (lampwork) under UV-light (ca. 370 nm); Robert Wiley, 2012.

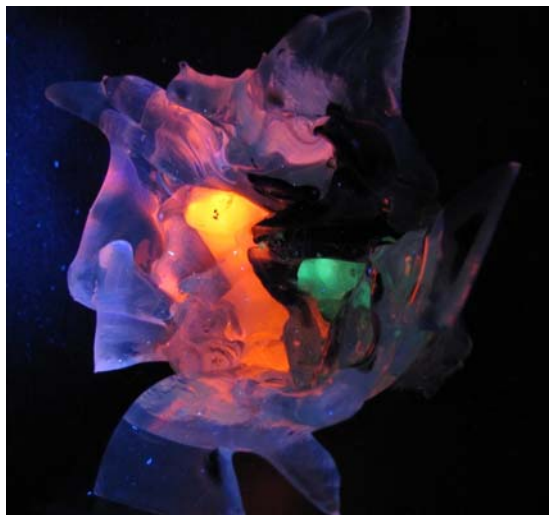


**Figure 6.3.** Tests for float glass luminescence , using  $\text{Sm}^{3+}$ ,  $\text{Tb}^{3+}$  and  $\text{Ce}^{3+}$  doped glasses, under a UV-light (ca. 370 nm); F. Quintas, 2011.

### 6.3. Insights given by Vicarte artists and directions for future work

The interaction between artists and scientists was very fruitful for the development of new glass materials. The use of the synthesized luminescent glasses already gave rise to different artworks made by Vicarte members, where sculptures and glass panels were made using luminescent glasses doped with one lanthanide (figure 6.1, 6.2 and 6.3). Materials with special optical properties are constantly being explored in our laboratories. Another example is the photochromic glass with silver nanoparticles, which change colour on exposure to sunlight, (figure 6.4). Spectroscopic studies of this glass system can be found in section 9.5.1, Supplementary Material.

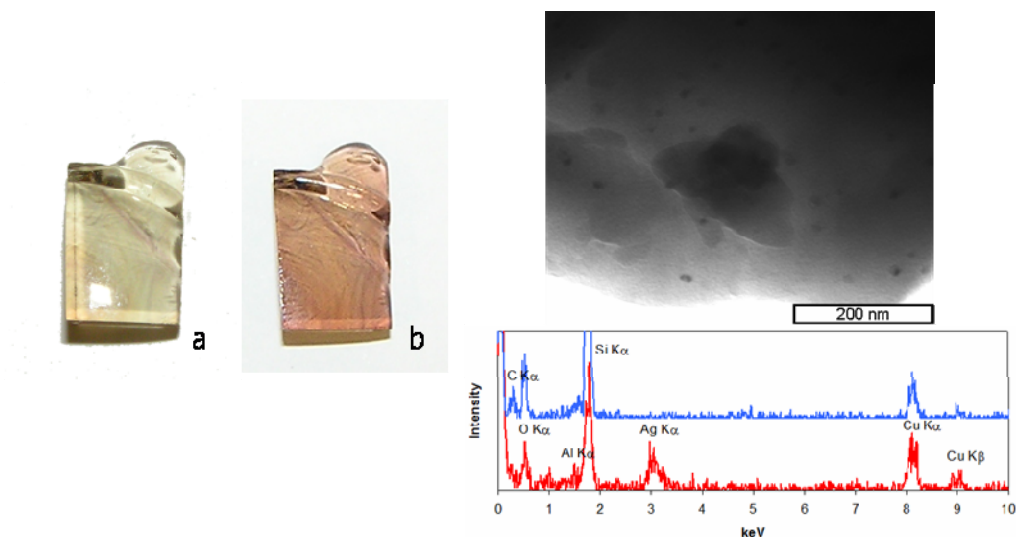


**Figure 6.4.** Glass sample before (a) and after (b) being exposed to daylight and TEM image and EDS measurement of the same glass. EDS analysis of the nanoparticle region (red spectra) and in regions without nanoparticles (blue spectra) show the existence of silver mainly within nanoparticles.

All the produced materials have strong possibilities to be used in the art field and in architecture and therefore to be produced in an industrial level. In the case of luminescent glasses with lanthanide oxides, all the interviewed artists agree that these materials promote an immediate impact in the observers and therefore the several luminescent colours produced in this thesis can be applied in artworks, design objects, publicity or even to didactic objects. Even the white luminescence, as the artist Fernando Quintas referred, may have a strong impact in architecture, since the architects, nowadays, do not like to use many colours in their work and normally try to reach a formal austerity and white luminescence probably can be applied in this type of works. Besides the numerous applicability's of lanthanide doped glasses, it was referred several times in this thesis that a disadvantage of these glasses is the lanthanides high cost. This disadvantage also revealed to be a problem for the interviewed artists. Due to the high cost of these materials, it is difficult to produce these luminescent glasses in a big scale and therefore to produce artworks with big dimensions or even to explore this luminescence to afterwards produce art works. This problem can be solved with the synthesis of luminescent glasses using cheaper elements. In this thesis the luminescence of lead halides and  $\text{Cu}^+$  was explored in aluminoborosilicate glasses. Teresa Almeida made some tests with these materials and observed that this type of luminescent glass can be applied in artworks using kiln casting or "pâte de verre" techniques. However it is important to extend this luminescence to commercial glass to be used in industry. In future work lead halides and  $\text{Cu}^+$  luminescence are going to be studied in different compositions, closer to the ones currently used in the glass industry. Other elements such as manganese can also be investigated to increase the colour palette without using lanthanide oxides.

The quenching of  $\text{Cu}^+$  luminescence by the laser revealed to be very interesting for the artists, in particularly for Teresa Almeida. This result presented a possible solution to control the areas without luminescence in a luminescent glass artwork and is also appealing for applications in design and publicity objects. This effect has to be investigate in more detail in order to really understand the possibilities of the luminescence quenching promoted by the laser irradiation, if is possible to have a fine control of the luminescent/no luminescent areas and which kind of luminescence is quenched, since this effect was not observed in the blue luminescence of  $\text{PbBr}_2$  doped glasses.

Concerning the ruby glass using the sol-gel technique Teresa Almeida e Robert Wiley shown lack of enthusiasm on using this materials in artworks due to their high cost, the small sizes and because these glasses are not very handy. It is necessary to explore these materials in order to make them appellative to the artists or even to industry. One solution is the deposition of the sol-gel as a film for a more straightforward application in glass objects; therefore is still necessary to study the gold nanoparticles formation in films using the method here reported. Different techniques of deposition can be explored, such as layer by layer, spray pyrolysis and spin coating to colour glasses with different sizes and shapes. Another solution is the production of aerogel that allows the synthesis of objects with bigger dimensions using the sol-gel

technique. The interviewed artists showed interest in perform some experiments with most of the materials produced in this thesis, for future application in their artworks.



## 7. References

- V. Tatton-Brown, C. Andrews, Before the Invention of Glassblowing. In H. Tait (Eds), Five Thousand Years of Glass, British Museum Press, 1991.
- <sup>2</sup> A. Shortland, L. Schachner, I. Freestone, M. Tite, *J. Archaeol. Sci.*, 33 (2006) 521-530.
- <sup>3</sup> J.V. Noble, *Amer. J. Archaeol.*, 73 (1969) 435-439.
- <sup>4</sup> S.C. Rasmussen, How Glass Changed the World. The History and Chemistry of Glass from Antiquity to the 13th Century, Springer, Heidelberg, New York, Dordrecht and London, 2012.
- <sup>5</sup> C.R. Kurkjian, W.R. Prindle, *J. Am. Ceram. Soc.*, 81 (1998) 795-813.
- <sup>6</sup> C. Shiess, The Light Artist Anthology-Neon and Related Media, ST Publications. Cincinnati, Ohio, 1994.
- <sup>7</sup> P.C. Reis, Pedro Cabrita Reis: On light and space, catalogue of exhibition at Museum Moderner Kunst Wien and Museu de Arte Contemporânea de Serralves, M. Sternberg and H. Tighe Eds., Charta, Milan, 1999.
- <sup>8</sup> A. Ritter, in *Smart Materials in Architecture, Interior Architecture and Design*, Birkhäuser – Publishers for Architecture, Basel, 2009.
- <sup>9</sup> T. Almeida, A. Ruivo, A. Pires de Matos, R. Oliveira, A. Antunes, *Journal of Cultural Heritage* 9 (2008) e138-e142.
- <sup>10</sup> T. Almeida, O vidro como material plástico: transparência luz, cor e expressão, PhD thesis, Aveiro University. 2011. <http://ria.ua.pt/bitstream/10773/5487/1/tese.pdf>.
- <sup>11</sup> C. Gorller-Walrand, K. Binnemans, Handbook on the physics and Chemistry of Rare Earths Vol. 25, Elsevier Science B.V., 1998, pp. 101-264.
- <sup>12</sup> Compilation of ASTM Standard Definitions, 7<sup>th</sup> edition, ASTM, Philadelphia, 1990.
- <sup>13</sup> R.H. Doremus, Glass Science, John Wiley & Sons, 2<sup>nd</sup> edition, New York, 1994.
- <sup>14</sup> A. Paul, Chemistry of Glasses, Chapman and Hall, 2<sup>nd</sup> edition, New York, 1990.
- <sup>15</sup> J. Shelby, Introduction to Glass Science and Technology, The Royal Society of Chemistry, Cambridge, 1997.
- <sup>16</sup> A. Varshneya, Fundamentals of Inorganic Glasses, Society of Glass Technology, 2<sup>nd</sup> edition, Sheffield, 2006.
- <sup>17</sup> J. Navarro, El Vidrio, 3<sup>rd</sup> edition, Consejo Superior de Investigaciones Científicas, Sociedad Española de Cerámica y Vidrio, Madrid, 2003.
- <sup>18</sup> S. Komarneni, S. Sakka, P. P. Phulé, R. M. Laine, Sol-gel synthesis and Processing, Ceramic Transitions, Volume 95, Ohio, 1998.
- <sup>19</sup> L. Klein, Sol-Gel technology for thin films, fibers, performs, electronics and specialty shapes, Noyes Publications, New Jersey, 1988
- <sup>20</sup> L. L. Hench, J. K. West, *Chem. Rev.*, 90 (1990) 33-72.
- <sup>21</sup> C.J. Brinker, G.W. Scherer, Sol-Gel Science: The Physics and Chemistry of Sol-Gel Processing, Academic Press, Boston, 1990.
- <sup>22</sup> J.D. Wright, N.A.J.M. Sommerdijk, Sol-Gel Materials Chemistry and Applications, CRC Press, Boca Raton, 2001.
- <sup>23</sup> M.G. Ventura, A.J. Parola, A. Pires de Matos, *J. Non-Cryst. Solids*, 357 (2011) 1342-1349.
- <sup>24</sup> X. Zhang, Q. Guo, D. Cui, *Sensors* 9 (2009) 1033-1053.
- <sup>25</sup> Y. Lu, Y. Yin, Z. Li, Y. Xia, *Nano Lett.* 2 (2002) 785-788.
- <sup>26</sup> H. Schmidt, *J. Sol-Gel Sci. Technol.* 40 (2006) 115–130.

- <sup>27</sup> S. Pandey, S.B. Mishra, *J. Sol-Gel Sci. Technol.*, 59 (2011) 73–94.
- <sup>28</sup> G. Lusvardi, G. Malavasi, V. Aina, L. Bertinetti, G. Cerrato, G. Magnacca, C. Morterra, L. Menabue, *Langmuir*, 26 (2010) 10303–10314.
- <sup>29</sup> V. Aina, T. Marchis, E. Laurenti, E. Diana, G. Lusvardi, G. Malavasi, L. Menabue, G. Cerrato, C. Morterra, *Langmuir*, 26 (2010) 18600–18605.
- <sup>30</sup> M. Sohrabi, S. Hesarak, A. Kazemzadeh, M. Alizadeh, *Mat. Sci Eng. C*, 33 (2013) 3730–3744.
- <sup>31</sup> T. Hayakawa, M. Nogami, *J. Appl. Phys.*, 90 (2001) 2200–2205.
- <sup>32</sup> R.J.D. Tilley, *Colour and the Optical Properties of materials*, Wiley, 2<sup>nd</sup> Edition, West Sussex, 2011.
- <sup>33</sup> R.M. Christie, *Colour Chemistry*, RCS, Cambridge, 2001.
- <sup>34</sup> B. Valeur, *Molecular Fluorescence: Principles and Applications*, Wiley VCH, Weinheim, Germany, 2001.
- <sup>35</sup> W.A. Weyl, *Coloured Glasses*. Society of Glass Technology, Sheffield, 1951.
- <sup>36</sup> W. T. Carnall, The absorption and fluorescence spectra of rare earth ions in solution. In K.A. Gschneidner, Jr and L. Eyring (Eds), *Handbook on the physics and Chemistry of Rare Earths*, Vol. 3, North-Holland Physics Publishing, 1979.
- <sup>37</sup> A. Ruivo, C. Gomes, A. Lima, M.L. Botelho, R. Melo, A. Belchior, A. Pires de Matos, *J. Cult. Herit.* 9 (2008) e134–e137.
- <sup>38</sup> A. Quaranta, R. Ceccato, C. Menato, N. Capra, R. Dal Mashio, *J. Non-Cryst. Solids*, 345&346 (2004) 671–675.
- <sup>39</sup> H. Schreiber, M. Stone, A. Swink, *J. Non-Cryst. Solids*, 352 (2006) 534–538.
- <sup>40</sup> H. Zeng, J. Qiu, Z Ye, C. Zhu, F. Gan, *J. Crystal Growth*, 267 (2004) 156–160.
- <sup>41</sup> M. Eichelbaum, K. Rademann, R. Müller, M. Radtke, H. Riesemeier, W. Görner, *Angew. Chem. Int. Ed.* 44 (2005) 7905–7909.
- <sup>42</sup> S. Halsbeck, K. Martinek, L. Steviano, F.E. Wagner, *Hyperfine Interact.*, 165 (2005) 89–94.
- <sup>43</sup> R. Rajaramakrishna, S. Karuthedath, R.V. Anavekar, H. Jain, *J. Non-Cryst. Solids*, 358 (2012) 1667–1672.
- <sup>44</sup> L.M. Liz-Marzán, *Langmuir*, 22 (2006) 32–41.
- <sup>45</sup> L. M. Liz-Marzán, *Mater. Today*, 7 (2004) 26–31.
- <sup>46</sup> A.M. Schwartzberg, J.Z. Zhang, *J. Phys. Chem. C* 112 (2008) 10323–10337.
- <sup>47</sup> N. Turro, *Molecular Photochemistry*, W.A. Benjamin, Inc., 1965.
- <sup>48</sup> A. Gilbert, J. Baggott, *Essentials of Molecular Photochemistry*, Blackwell Science Ltd, Oxford, 1995.
- <sup>49</sup> J. Qiu, A. Makishima, *Sci. Tech. Adv. Mater.* 4 (2003) 35–38.
- <sup>50</sup> P. Huang, C. Cui, H. Hao, *J. Sol-Gel Sci. Technol.*, 50 (2009) 308–313.
- <sup>51</sup> R. Sakai, T. Katsumata, S. Komuro, T. Morikawa, *J. Lumin.*, 85 (1999) 149–154.
- <sup>52</sup> S.V. Eliseeva, J.C.G. Bunzli, *Chem. Soc. Rev.*, 39 (2010) 189–227.
- <sup>53</sup> J. C. G. Bunzli, G.R. Chopin, *Lanthanide probes in life, chemical and earth sciences*, Elsevier, New York, 1989
- <sup>54</sup> T.S. Martins, P. Celso Isolani, *Quim. Nova*, 28 (2005) 111–117.
- <sup>55</sup> Y. Fan, S. Haung, J. Jiang, G. Li, P. Yang, H. Lian, Z. Cheng, J. Lin, *J. Colloid Interf. Sci.*, 357 (2011) 280–285.
- <sup>56</sup> M. Yamane, Y. Asahara, *Glasses for Photonics*, Cambridge University Press, Cambridge, 2004.



- <sup>57</sup> I. Billard, G. Moutiers, A. Labet, A. El Azzi, C. Gaillard, C. Mariet, K. Lutzenkirchen, *Inorg. Chem.*, 42 (2003) 1726-1733.
- <sup>58</sup> M. Peng, Z. Pei, G. Hong, Q. Su, *Chem. Phys. Lett.*, 371 (2003) 1–6.
- <sup>59</sup> C. Gorller-Walrand and K. Binnemans, Handbook on the physics and Chemistry of Rare Earths Vol. 23, Elsevier Science B.V., 1996, pp. 121-282.
- <sup>60</sup> B.M. Walsh, Judd-Ofelt theory: Principals and practices. In B. Di Bartolo and O. Forte (Eds), Advances in spectroscopy for lasers and sensing, Springer, Dordrecht, 2006.
- <sup>61</sup> T. Moeller, The Chemistry of the Lanthanides, Chapman & Hall LTD, London, 1965.
- <sup>62</sup> A.J. Bayramian, C.D. Marshall, J.H. Wu, J.A. Speth, S.A. Payne, G.J. Quarles, V.K. Castillo, *J. Lumin.*, 69 (1996) 85-94.
- <sup>63</sup> H. Lin, H. Liang, G. Zhang, Y. Tao, *J. Rare Earths*, 30 (2012) 1-5.
- <sup>64</sup> C. Bazzicalupi, A. Bencini, E. Berni, A. Bianchi, C. Giorgi, V. Fusi, B. Valtancoli, C. Lodeiro, A. Roque, F. Pina, *Inorg. Chem.*, 40 (2001) 6172-6179.
- <sup>65</sup> E. Brunet, H M H. Alhendawi, O. Juanes, L. Jiménez, J.C. Rodríguez-Ubis, *J. Mater. Chem.*, 19 (2009) 2494–2502.
- <sup>66</sup> I. Hemmil, V. Laitala, *J. Fluoresc.*, 15 (2005) 529-542.
- <sup>67</sup> C. Gorller-Walrand, L. Fluyt, A. Ceulemans, W. T. Carnall, *J. Chem. Phys.*, 95 (1991) 3099-3106
- <sup>68</sup> D. He, C.Yu, J. Cheng, S. Li L. Hu, *J. Alloy. Compd.*, 509 (2011) 1906–1909.
- <sup>69</sup> B.C. Jamalaiah, J. Suresh Kumar, A. Mohan Babu, T. Sasikala, L. Rama Moorthy, *Physica B*, 404 (2009) 2020–2024
- <sup>70</sup> B. R. Judd, *Phys. Rev.* 127 (1962) 750–761.
- <sup>71</sup> G. S. Ofelt, *J. Chem. Phys.* 37 (1962) 511-520.
- <sup>72</sup> C. K. Jørgensen, R. Reisfeld, *J. Less-Common Met.* 93 (1983) 107-112.
- <sup>73</sup> K. Binnemans, C. Gorller-Walrand, *J. Phys.: Condens. Matter*, 10 (1998) L167-L170.
- <sup>74</sup> M.P. Hehlen, M.G.Brik, K.W.Krämer, *J. Lumin.*, 136 (2013) 221–239.
- <sup>75</sup> P. Babu, H.J. Seo, K.H. Jang<sup>1</sup>, R. Balakrishnaiah, C.K. Jayasankar, A.S. Joshi, *J. Phys.: Condens. Matter.*, 17 (2005) 4859–4876.
- <sup>76</sup> N.V. Nikonorov, A.I. Sidorov, V.A. Tsekhomskii, T.A. Shakhverdov, *Optics and Spectroscopy*, 114, (2013) 379–383.
- <sup>77</sup> Q. Zhang, G. Chen, G. Dong, G. Zhang, X. Liu, J. Qiu, Q. Zhou, Q. Chen, D. Chen, *Chem. Phys. Lett.*, 482 (2009) 228–233.
- <sup>78</sup> E. Borsella, A. Dal Vecchio, M.A. Garcia, C. Sada, F. Gonella, R. Polloni, A. Quaranta, L.J.G.W. van Wilderen, *J. Appl. Phys.*, 91 (2002) 90-98.
- <sup>79</sup> R.R. Patil, S.V. Moharil, *Phys. stat. sol. (a)*, 187 (2001) 557–562.
- <sup>80</sup> P. Tresnakova, H. Malichova, J. Spirkova, M. Mika, *J. Phys. Chem. Solids*, 68 (2007) 1276–1279
- <sup>81</sup> Y. Kondo, Y. Kuroiwa, N. Sugimoto, T. Manabe, S. Ito, T. Tokizaki, A. Nakamura, *J. Non-Cryst. Solids*, 196 (1996) 90-94.
- <sup>82</sup> T. Sanada, K. Yamamoto, K. Kojima, N. Wada, *J. Sol-Gel Sci. Techn.*, 41 (2007) 237–243.
- <sup>83</sup> J. Lin, D.U. Sängner, M. Mennig, K. Bärner, *Thin Solid Films*, 360 (2000) 39-45.
- <sup>84</sup> I.E.C. Machado, L. Prado, L. Gomes, J.M. Prison, J.R. Martinelli, *J. Non-Cryst. Solids*, 348 (2004) 113–117.
- <sup>85</sup> J. Roqué, N. Poolton, J. Molera, A. Smith, E. Pantos, M. Vendrell-Saz, *Phys. Stat. Sol. (b)*, 243, No.6 (2006) 1337-1346.

- <sup>86</sup> N. Murase, *AIST Today*, Vol. 6, No.8 (2006) 22-23.
- <sup>87</sup> E.S. Freitas Neto, N.O. Dantas, S. A. Lourenço, *Phys. Chem. Chem. Phys.*, **14** (2012) 1493-1501.
- <sup>88</sup> L. El Mir, A. Amlouk, C. Barthou, *J. Phys. Chem. Solids*, **67** (2006) 2395-2399.
- <sup>89</sup> P. Yang, C. Song, M. Lu, X. Yin, G. Zhou, D. Xu, D. Yuan, *Chem. Phys. Lett.*, **345** (2001) 429-434.
- <sup>90</sup> K. Marimuthu, S. S. Babu, G. Muralidharan, S. Arumugam, C. K. Jayasankar, *Phys. Status Solidi A* **206** (2009) 131-139.
- <sup>91</sup> S.S. Babu, P. Babu, C.K. Jayasankar, W. Sievers, T. Tröster, G. Wortmann, *J. Lumin.*, **126** (2007) 109-120.
- <sup>92</sup> L. Kokou, J. Du, *J. Non-Cryst. Solids*, **358** (2012) 3408-3417.
- <sup>93</sup> K. Linganna, C.K. Jayasankar, *Spectrochim. Acta A* **97** (2012) 788-797.
- <sup>94</sup> J. Du, L. Kokou, *J. Non-Cryst. Solids*, **357** (2011) 2235-2240.
- <sup>95</sup> J. A. Johnson, C. J. Benmore, D. Holland, J. Du, B. Beuneu, A. Mekki, *J. Phys.: Condens. Matter* **23** (2011) 065404.
- <sup>96</sup> P. Krishnapuram, S. K. Jakka, C. Thummala, R. M. Lalapeta, *J. Molecular Structure* **1028** (2012) 170-175.
- <sup>97</sup> R. Rolli, K. Gatterer, M. Wachtler, M. Bettinelli, A. Speghini, D. Ajò, *Spectrochim. Acta A* **57** (2001) 2009-2017.
- <sup>98</sup> Q.Y. Zhang, K. Pita, S. Buddhudu, C.H. Kam, *J. Phys. D: Appl. Phys.* **35** (2002) 3085-3090.
- <sup>99</sup> R. Reisfeld, E. Zigansky, M. Gaft, *Molecular Physics*, **102** (2004) 1319-1330.
- <sup>100</sup> M. Ventura, C.A.T. Laia, A.J. Parola, *J. Phys. Chem.* **114** (2010) 18414-18422.
- <sup>101</sup> L. Yu, M. Nogami, *J. Sol-Gel Sci. Technol.* **43** (2007) 355-360.
- <sup>102</sup> V. C. Costa, M.J. Lochhead, K. L. Bray, *Chem. Mater.* **8** (1996) 783-790.
- <sup>103</sup> M. J. Lochhead, K.L. Bray, *Chem. Mater.* **7** (1995) 572-577.
- <sup>104</sup> G. Cormier, J.A. Capobianco, A. Monteil, *J. Non-Cryst. Solids* **152** (1993) 225-236.
- <sup>105</sup> G. Spierings, G. Melis, *J. Mater. Sci.* **16** (1981) 1059-1062.
- <sup>106</sup> J. Mochinaga, K. Igarashi, T. Aoki, Y. Iwadate, *Bull. Chem. Soc. Jpn.* **51** (1978) 3107.
- <sup>107</sup> W. T. Carnall, P. R. Fields, K. Rajnak, *J. Chem. Phys.* **49** (1968) 4450-4455.
- <sup>108</sup> T.R. Griffiths, D.A. Nerukh, S.A. Eremenkob, *Phys. Chem. Chem. Phys.* **1** (1999) 3199-3208.
- <sup>109</sup> K. Binnemans, C. Gorller-Walrand, *J. Rare Earths*, **14** (1996) 173-180.,
- <sup>110</sup> K. Binnemans, *Bull. Soc. Chim. Belg.* **105** (1996) 793-798.].
- <sup>111</sup> L.D. Carlos, A.L.L. Videira, *Phys. Rev. B*, **49** (1994) 11721-11728.
- <sup>112</sup> M. Tanaka, G. Nishimura, T. Kushuda, *Phys. Rev. B*, **49** (1994) 16917-16925.
- <sup>113</sup> M.H.V. Werts, R.T.F. Jukes, J.W. Verhoeven, *Phys. Chem. Chem. Phys.*, **4** (2002) 1542-1548.
- <sup>114</sup> Y. Nageno, H. Takebe, K. Morinaga, T. Izumitani, *J. Non-Cryst. Solids*, **169** (1994) 288-294.
- <sup>115</sup> G. Alombert-Goget, N. Gaumer, J. Obriot, A. Rammal, S. Chaussedent, A. Monteil, H. Portales, A. Chiasera, M. Ferrari, *J. Non-Cryst. Solids*, **351** (2005) 1754-1758.
- <sup>116</sup> J.R. Lakowicz, *Principles of Fluorescence Spectroscopy*, 3<sup>th</sup> edition, Springer, 2006.
- <sup>117</sup> Th. Förster, *Discuss. Faraday Soc.* **27** (1959) 7 - 17.
- <sup>118</sup> V.S. Sastri, J.C. Bünzli, V. Ramachandra Rao, G.V.S. Rayudu, J.R. Perumareddi, *Modern Aspects of Rare Earths and their Complexes*, Elsevier, Amsterdam, 2003.

- <sup>119</sup> J.C.G. Bunzli, S. Comby, A.S. Chauvin, C.D.B. Vandevyver, *J. Rare Earth.*, 25 (2007) 257 – 274.
- <sup>120</sup> S.K. Singh, A.K. Singh, S.B. Rai, *Nanotechnology*, 22 (2011) 275703.
- <sup>121</sup> Q. Lai, H. Lu, D. Wang, H. Wang, S. Feng, J. Zhang, *Macromol. Chem. Phys.* 212 (2011) 1435-1442.
- <sup>122</sup> W.J. Kim, M. Nyk, P.N. Prasad, *Nanotechnology*, 20 (2009) 185301.
- <sup>123</sup> Y. Qiao, Y. Lin, S. Zhang, J. Huang, *Chem. Eur. J.*, 17 (2011) 5180–5187.
- <sup>124</sup> C. Du, F. Lang, Y. Su, Z. Liu, *J. Colloid Interf. Sci.* 394 (2013) 94–99.
- <sup>125</sup> H. Li, Y. Ding, P. Cao, H. Liu, Y. Zheng, *J. Mater. Chem.* 22 (2012) 4056-4059.
- <sup>126</sup> V. Buissette, D. Giaume, T. Gacoin, J.P. Boilot, *J. Mater. Chem.*, 16 (2006) 529–539.
- <sup>127</sup> A.B. Dias, *Dalton Trans.* (2007) 2229–2241.
- <sup>128</sup> Y. Zhang, J. Hao, *J. Appl. Phys.* 113 (2013) 184112.
- <sup>129</sup> X. Rao, Q. Huang, X. Yang, Y. Cui, Y. Yang, C. Wu, B. Chen, G. Qian, *J. Mater. Chem.*, 22 (2012) 3210–3214.
- <sup>130</sup> Y. Jin, Chunxia Li, Z. Xu, Z. Cheng, W. Wang, G. Li, J. Lin, *Materials Chemistry and Physics* 129 (2011) 418– 423.
- <sup>131</sup> Y. Zhao, B. Yan, *Dalton Trans.*, 2012, 41, 5334–5342.
- <sup>132</sup> T. Grzyb, A. Szczeszak, J. Rozowska, J. Legendziewicz, S. Lis, *J. Phys. Chem. C* 2012, 116, 3219–3226.
- <sup>133</sup> R. Ye, H. Ma, C. Zhang, Y. Gao, Y. Hua, D. Deng, P. Liu, S. Xu, *J. Alloys Comp.* 566 (2013) 73–77.
- <sup>134</sup> D. Chen, Y. Yu, P. Huang, H. Lin, Z. Shan, Y. Wang, *Acta Materialia*, 58 (2010) 3035–3041.
- <sup>135</sup> Z. Lin, X. Liang, Y. Ou, C. Fan, S. Yuan, H. Zeng, G. Chen, *J. Alloys Comp.* 496 (2010) L33–L37.
- <sup>136</sup> M.R. Krames, *J. Display Technol.* 3 (2007) 160-175.
- <sup>137</sup> M. Pardha Saradhi, U. V. Varadaraju, *Chem. Mater.* 2006, 18, 5267-5272.
- <sup>138</sup> A.J. Silversmith, D.M. Boye, K.S. Brewer, C.E. Gillespie, Y. Lu, D.L. Campbell, *J. Lumin.*, 121 (2006) 14–20.
- <sup>139</sup> R. Reisfeld, A. Patra, G. Panczer, M. Gaft, *Optical Materials* 13 (1999) 81-88.
- <sup>140</sup> A. Ruivo, T. Almeida, F. Quintas, R. Wiley, M. Troeira, N. Paulino, C.AT. Laia, C.A. Queiroz, A. Pires de Matos. In *12<sup>th</sup> International AIC Colour Congress, Proceedings*, ed. by L. MacDonald, S. Westland and S. Wuerger (2013) 885-888.
- <sup>141</sup> F. Quintas, A. Ruivo, C. Queiroz, A. Pires de Matos. In *GLASSAC 11 – Glass Science in Art and Conservation: Innovative technologies in glass art, design and conservation from the 19<sup>th</sup> to the 21<sup>st</sup> century - the role of the sciences, Proceedings*, ed. by S. Rota and K. Wittstadt. Stuttgart: Fraunhofer Institute for Silicate Research and Fraunhofer-Verlag, (2011) 99-100.
- <sup>142</sup> B. Padlyak, A. Drzewiecki, *J. Non-Cryst. Solids*, 367 (2013) 58–69.
- <sup>143</sup> M. Elisa, B.A. Sava, I.C. Vasiliu, R.C.C. Monteiro, J.P. Veiga, L. Ghervase, I. Feraru, R. Iordanescu, *J. Non-Cryst. Solids*, 369 (2013) 55–60.
- <sup>144</sup> J.L. Rygel, C.G. Pantano, *J. Non-Cryst. Solids* 355 (2009) 2622–2629.
- <sup>145</sup> F. Lofaj, R. Satet, M.J. Hoffmann, A.R. de Arellano López, *J. Eur. Ceram. Soc.*, 24 (2004) 3377–3385.
- <sup>146</sup> W. Mitang, C. Jinshu, L. Mei, *J. Rare Earth.*, 28 (2010) 308-311.
- <sup>147</sup> C. Zhu, Y. Yang, X. Liang, S. Yuan, G. Chen, *J. Lumin.*, 126 (2007) 707–710.
- <sup>148</sup> L. Ren, X. Lei, X. Du, L. Jin, W. Chen, Y. Feng, *J. Lumin.*, 142 (2013) 150–154.

- <sup>149</sup> M. Nazarov, D.Y. Noh, J. Sohn, C. Yoon, *Opt. Mater.*, 30 (2008) 1387–1392.
- <sup>150</sup> Y. Zorenko, V. Gorbenko, T. Voznyak, M. Batentschuk, A. Osvet, A. Winnacker, *J. Lumin.*, 128 (2008) 652–660.
- <sup>151</sup> J. Sokolnicki, *J. Lumin.*, 134 (2013) 600–606.
- <sup>152</sup> P. Li, Z. Wang, Z. Yang, Q. Guo, X. Li, *J. Lumin.*, 130 (2010) 222–225.
- <sup>153</sup> D. Jia, J. Zhua, B. Wub, S. E, *J. Lumin.*, 93 (2001) 107–114.
- <sup>154</sup> A. Nag, T.R.N. Kutty, *Mater. Chem. Phys.* 91 (2005) 524–531.
- <sup>155</sup> J. Zheng, C. Guo, X. Ding, Z. Ren, J. Bai, *Curr. Appl. Phys.*, 12 (2012) 643–647.
- <sup>156</sup> Y. Chen, J. Wang, X. Zhang, G. Zhang, M. Gong, Q. Su, *Sensor Actuat. B – Chem.*, 148 (2010) 259–263.
- <sup>157</sup> J. Sokolnicki, *J. Phys. Condens. Matter.*, 22 (2010) 275301.
- <sup>158</sup> H.Y. Chung, C.H. Lu, C.H. Hsu, *J. Am. Ceram. Soc.*, 93 (2010) 1838–1841.
- <sup>159</sup> U. Caldiño, E. Álvarez, A. Speghini, M. Bettinelli, *J. Lumin.* 135 (2013) 216–220.
- <sup>160</sup> B.C. Joshi, *J. Non-Cryst. Solids*, 180 (1995) 217, B.
- <sup>161</sup> J.Y. Park, H.C. Jung, G.S.R. Raju, B.K. Moona, J.H. Jeonga, J.H. Kim, *Solid State Sci.* 12 (2010) 719–724.
- <sup>162</sup> S. Jiang, L. Li, C. Duan, X. Zhou, M. Yin, *J. Rare Earth.*, 28 (2010) 312–315.
- <sup>163</sup> D.L. Dexter, *J. Chem. Phys.*, 21 (1953) 836–849.
- <sup>164</sup> M. Wang, J. Cheng, M. Li, *J. Rare Earth*, 28 (2010) 308–311.
- <sup>165</sup> J. Bourcet, F. K. Fong, *J. Chem. Phys.*, 60 (1974) 34–39.
- <sup>166</sup> K.N. Shinde, I.M. Nagpure, S.J. Dhoble, *Synth. React. Inorg. Met.-Org. Chem*, 41 (2011) 107–113.
- <sup>167</sup> R. Sato, S. Takeshita, T. Isobe, T. Sawayama, S. Niikurab, *J. Solid State Sci. Technol.*, 1 (2012) R163–R168.
- <sup>168</sup> S. Zhan, Y. Gao, Y. Liu, H. Zhong, *J. Rare Earth.*, 30 (2012) 995–999.
- <sup>169</sup> C.G. Ma, S. Jiang, X. Zhou, *J. Rare Earth.*, 28 (2010) 40–42.
- <sup>170</sup> M. Batentschuk, A. Osvet, G. Schierning, A. Klier, J. Schneider, A. Winnacker, *Radiat. Meas*, 38 (2004) 539 – 543.
- <sup>171</sup> E. Cano, M.A. Garcia, M.A. Villegas, G. Battaglin, J. Llopis, J.M. Bastidas, *J. Sol-Gel Sci. Technol.*, 27 (2003) 293–299.
- <sup>172</sup> W.Y. Cong, W.M. Zheng, S.M. Li, Y.J. Wang, X.Y. Liu, H.B. Huang, X.Y. Meng, J.B. Zhai, *Phys. Status Solidi B* 249 (2012) 1585–1589.
- <sup>173</sup> L.F. Koao, H.C. Swart, R.I. Obed, F.B. Dejene, *J. Lumin.*, 131 (2011) 1249–1254
- <sup>174</sup> R.J. Mortimer, T.S. Varley, *Displays*, 32 (2011) 35–44.
- <sup>175</sup> R. S. Berns, Billmeyer and Saltzman's Principles of Color Technology, 3<sup>rd</sup> edition, John Wiley, New York, 2000.
- <sup>176</sup> L. Shen, X. Liu, B. Chen, E. Y. B. Pun, H. Lin, *J. Phys. D: Appl. Phys.*, 45 (2012) 115301.
- <sup>177</sup> R. Jagannathan, S.P. Manoharan, R.P. Rao, R.L. Narayanan, N. Rajaram, *B. Electrochem.*, 4 (1988) 597–600.
- <sup>178</sup> V.K. Tikhomirov, T. Vosch, E. Fron, V.D. Rodríguez, J.J. Velázquez, D. Kirilenko, G. Van Tendeloo, J. Hofkens, M. Van der Auweraer, V.V. Moshchalkov, *RSC Adv.*, 2 (2012) 1496–1501.
- <sup>179</sup> V.G. Plekhanov, *Prog. Mater. Sci.*, 49, (2004) 787–886.
- <sup>180</sup> W.C. De Gruijter, J. Kerksen, *Solid State Commun.*, 10 (1972) 837–841.

## References

---

- <sup>181</sup> S. V. Nistor, E. Goovaerts, D. Schoemaker, *Phys. Rev. B*, 48 (1993) 9575-9580.
- <sup>182</sup> M. Nikl, *Phys. stat. sol. (a)*, 178 (2000) 595-620.
- <sup>183</sup> M. Iwanaga, T. Hayashi, *J. Lumin.*, 102 (2003) 663-668.
- <sup>184</sup> M. Iwanaga, M. Watanabe, T. Hayashi, *Phys. Rev. B*, 62 (2000) 10766-107.
- <sup>185</sup> M. Iwanaga, M. Shirai, K. Tanaka, T. Hayashi, *Phys. Rev. B*, 66 (2002) 064304.
- <sup>186</sup> V. Babin, A. Krasnikov, M. Nikl, A. Stolovits, S. Zazubovich, *Phys. stat. sol. B*, 229 (2002) 1295-1304.
- <sup>187</sup> I. Dag, E. Lifshitz, *J. Phys. Chem.*, 100 (1996) 8962-8972.
- <sup>188</sup> H. Nakagawa, M. Terakami, K. Yasuda, *Radiation Measurements*, 33 (2001) 819-822.
- <sup>189</sup> C. Zaldo, J. García Solé, E. Diéguez, F. Agulló-López, *J. Chem. Phys.*, 83 (1985) 6197-6200.
- <sup>190</sup> M. Kitaura, H. Nakagawa, *J. Lumin.*, 72-74 (1997) 883-884.
- <sup>191</sup> W.A. Pisarski, T. Goryczka, J. Pisarska, W. Ryba-Romanowski, *J. Phys. Chem. B*, 111 (2007) 2427-2430.
- <sup>192</sup> J. Pisarska, R. Lisiecki, W. Ryba-Romanowski, G. Dominiak-Dzik, T. Goryczka, L. Grobelny, W.A. Pisarski, *J. of Non-Cryst. Solids*, 357 (2011) 1228-1231.
- <sup>193</sup> R.E. Lamaestre, H. Bernas, D. Pacifici, G. Franzo, F. Priolo, *Appl. Phys. Lett.*, 88 (2006) 181115.
- <sup>194</sup> H.A. ElBatal, A.M. Abdelghany, F.H. ElBatal, F.M. EzzEID, *Mater. Chem. Phys.*, 134 (2012) 542-548.
- <sup>195</sup> C. Parent, P. Boutinaud, G. Leflem, B. Moine, C. Pedrini, D. Garcia, M. Faucher, *Optical Materials*, 4 (1994) 107-113.
- <sup>196</sup> J. Dědeček, B. Wichterlová, *Phys. Chem. Chem. Phys.*, 1 (1999) 629-637.
- <sup>197</sup> B. Moine, C. Pedrini, E. Duloisy, P. Boutinaud, C. Parent, G. Le Flem, *J. Phys. IV*, 1 (1991) C7-289 – C7-292.
- <sup>198</sup> K. Annapurna, A. Kumar, R.N. Dwivedi, N. Sooraj Hussain, S. Buddhudu, *Mater. Lett.*, 45 (2000) 23-26.
- <sup>199</sup> B. Padyak, W. Ryba-Romanowski, R. Lisiecki, O. Smyrnov, A. Drzewiecki, Ya. Burak, V. Adamiv, I. Teslyuk, *J. of Non-Cryst. Solids*, 356 (2010) 2033-2037
- <sup>200</sup> M. Elisa, B. Sava, A. Diaconu, D. Ursu, R. Patrascu, *J. of Non-Cryst. Solids*, 355 (2009) 1877-1879.
- <sup>201</sup> S. Gomez, I. Urrea, R. Valiente, F. Rodriguez, *J. Phys.: Condens. Matter.*, 22 (2010) 295505.
- <sup>202</sup> Y. Fujimoto, M. Nakatsuka, *J. Lumin.*, 75 (1997) 213-219.
- <sup>203</sup> V. K. Shrikhande, V. Sudarsan, G. P. Kothiyal and S. K. Kulshreshtha, *J. Non-Cryst. Solids* 353 (2007) 1341-1345.
- <sup>204</sup> B.O. Mysen, D. Virgo, C.M. Scarfe, *Am. Mineral*, 65 (1980) 690-710.
- <sup>205</sup> P. Mcmillan, *Am. Mineral*, 69 (1984) 645-659.
- <sup>206</sup> S.A. Brawer, W.B. White, *J. Chem. Phys.*, 63 (1975) 2421-2432.
- <sup>207</sup> B.O. Mysen, D. Virgo, F.A. Seifert, *Am. Mineral* 70 (1985) 88-105.
- <sup>208</sup> F. Seifert, B.O. Mysen, D. Virgo, *Am. Mineral* 67 (1982) 696-717.
- <sup>209</sup> H. Li, P. Hrma, J. D. Vienna, M.X. Qian, Y.L. Su, D.E. Smith, *J. of Non-Cryst. Solids*, 331 (2003) 202-216.
- <sup>210</sup> T. Furukawa, W. White, *J. Material Science*, 16 (1981) 2689-2700.
- <sup>211</sup> X. Xue, J. Stebbins, M. Kanzaki, P. Mcmillan, B. Poe, *Am. Mineral*, 76 (1991) 8-

- <sup>212</sup> Z. Zheng, A.R. Liu, S.M. Wang, Y. Wang, Z.S. Li, W.M. Lau, L.Z. Zhang, *J. Mater. Chem.*, 15 (2005) 4555-4559.
- <sup>213</sup> S. Feller, G. Lodden, A. Riley, T. Edwards, J. Croskrey, A. Schue, D. Liss, D. Stentz, S. Blair, M. Kelley, G. Smith, S. Singleton, M. Affatigato, D. Holland, M.E. Smith, E.I. Kamitsos, C.P.E. Varsamis, E. Ioannou, *J. of Non-Cryst. Solids*, 356 (2010) 304-313.
- <sup>214</sup> X. Zheng, H. Tao, F. Chen, H. Guo, C. Lin, X. Zhao, *Chalcogenide Lett.*, 8 (2011) 371-376.
- <sup>215</sup> B. G. Yacobi, *Semiconductor Materials: An Introduction to Basic Principles*, Kluwer Academic Publishers, New York, 2003.
- <sup>216</sup> M. Lumberras, J. Protas, S. Jebbari, G.J. Dirksen, J. Schoonman, *Solid State Ionics*, 20 (1986) (1986) 295-304.
- <sup>217</sup> R.A. Marcus, *J. Phys. Chem.*, 93 (1989) 3078-3086.
- <sup>218</sup> J. Jortner, *J. Chem. Phys.* 64 (1976) 4860.
- <sup>219</sup> M. Inokuti, F. Hirayama, *J. Chem. Phys.*, 43 (1965) 1978-1989.
- <sup>220</sup> C.P. Lindsey, G.D. Patterson, *J. Chem. Phys.*, 73 (1980) 3348-3357.
- <sup>221</sup> W. Siebrand, T.A. Wildman, *Acc. Chem. Res.*, 19 (1986) 238-243.
- <sup>222</sup> C.A.T. Laia, S.M.B. Costa, D. Phillips, A. Beeby, *J. Phys. Chem. B*, 108 (2004) 7506-7514.
- <sup>223</sup> D. Chen, H. Miyoshi, T. Akai, T. Yazawa, *Appl. Phys. Lett.*, 86 (2005) 231908.
- <sup>224</sup> W. Eitel, *Silicate science, Volume VII, Glass science*, Academic Press Inc., London, 1976.
- <sup>225</sup> T. Lutz, C. Estournes, J.C. Merle, J.L. Guille, *J. Alloys Compd.* 262-263 (1997) 438-442.
- <sup>226</sup> J.D. Barrie, B. Dunn, G. Hollingsworth, J.I. Zink, *J. Phys. Chem.* 93 (1989) 3958-3963.
- <sup>227</sup> S. P. Singh, A. Kumar, *J. Mater. Sci.*, 30 (1995) 2999-3004.
- <sup>228</sup> N.V. Borisova, V.G. Konakov, T.G. Kostyreva, M.M. Shultz, *Glass Phys. Chem.*, 29 (2003) 28-34.
- <sup>229</sup> B.S. Bae, M.C. Weinberg, *J. of Non-Cryst. Solids*, 168 (1994) 223-231.
- <sup>230</sup> W. Thiemsohn, K. Keowkamnerd, P. Suwannathada, H. Hessenkemper, S. Phanichaphant, *Bull. Mater. Sci.*, 30 (2007) 487-495.
- <sup>231</sup> Y. Uchida, M. Yoshida, O. Nishiara, K. Matsui, *J. Sol-Gel Sci. and Tech.*, 26 (2003) 177-180.
- <sup>232</sup> K. Kadono, N. Itakura, T. Akai, M. Yamashita, T. Yazawa, *J. Phys.: Condens. Matter*, 22 (2010) 045901.
- <sup>233</sup> J. Sheng, Y. Wu, X. Yang, J. Zhang, *Int. J. Hydrogen Energ.*, 34 (2009) 1123-1125.
- <sup>234</sup> K. Kajihara, L. Skuja, M. Hirano, *Appl. Phys. Lett.*, 79 (2001) 1757-1759.
- <sup>235</sup> L. Dykman, N. Khlebtsov, *Chem. Sov. Rev.*, 41 (2012) 2256-2282.
- <sup>236</sup> P.M. Tiwari, K. Vig, V.A. Dennis, S.R. Singh, *Nanomaterials*, 1 (2011) 31-63.
- <sup>237</sup> X. Huang, P.K. Jain, I.H. El-Sayed, M.A. El-Sayed, *Nanomedicine*, 2 (2007) 681-693.
- <sup>238</sup> J. Rosa, J. Conde, J.M. Fuente, J.C. Lima, P.V. Baptista, *Biosens. Bioelectron.*, 36 (2012) 161-167.
- <sup>239</sup> G. Schmid, *Clusters & Colloids: From Theory to Application*, Wiley-VCH, Weinheim, 1994.
- <sup>240</sup> M.C. Daniel, D. Astruc, *Chem. Rev.*, 104(2004) 293-346.
- <sup>241</sup> M. Nogami, S.T. Selvan, H. Song, In: Nalwa HS (ed) *Handbook of Advanced Electronic and Photonic Devices*, Academic Press, San Diego, 2001.
- <sup>242</sup> A.M. Schwartzberg, J.Z. Zhang, *J. Phys. Chem. C*, 112 (2008) 10323-10337.
- <sup>243</sup> C. Sonnichsen, T. Franzl, T. Wilk, G. Von Plessen, J. Feldmann, *New J. Phys.*, 4 (2002) 93.1-93.8.

- <sup>244</sup> U. Kreibig, M. Vollmer, *Optical Properties of Metal Clusters*, Springer, Berlin, 1995.
- <sup>245</sup> J. Turkevich, P.C. Stevenson, J.A. Hillier, *Discuss Faraday Soc.*, 11(1951) 55-75.
- <sup>246</sup> J. Kimling, M. Maier, B. Okenve, V. Kotaidis, H. Ballot, A. Plech, *J. Phys. Chem. B*, 110 (2006) 15700-15707.
- <sup>247</sup> J.P. Rosa, J.C. Lima, P.V. Baptista, *Nanotechnology*, 22 (2011) 415202.
- <sup>248</sup> M. Epifani, C. Giannini, L. Tapfer, L. Vasanelli, *J. Am. Ceram. Soc.*, 83 (2000) 2385-2393.
- <sup>249</sup> Y. Kobayashi, M.A. Correa-Duarte, L.M. Liz-Marzán, *Langmuir*, 17 (2001) 6375-6379.
- <sup>250</sup> Y. Zhou, J.H. Schattka, M. Antonietti, *Nano Lett.* 4 (2004) 477-481.
- <sup>251</sup> M.A. Néouze, J. Le Bideau, P. Gaveau, S. Bellayer, A. Vioux, *Chem. Mater.*, 18 (2006) 3931-3936.
- <sup>252</sup> J. Le Bideau, P. Gaveau, S. Bellayer, M.A. Néouze, A. Vioux, *Phys. Chem. Chem. Phys.*, 9 (2007) 5419-5422.
- <sup>253</sup> R. Göbel, P. Hesemann, J. Weber, E. Möller, A. Friedrich, S. Beuermann, A. Taubert, *Phys. Chem. Chem. Phys.*, 11 (2009) 3653-3662.
- <sup>254</sup> R. Göbel, A. Friedrich, A. Taubert, *Dalton Trans.* 39 (2010) 603-611.
- <sup>255</sup> M.P. Singh, R.K. Singh, S. Chandra, *ChemPhysChem*, 11(2010) 2036-2043.
- <sup>256</sup> M. Antonietti, D. Kuang, B. Smarsly, Y. Zhou, *Angew. Chem. Int. Ed.*, 43 (2004) 4988-4992.
- <sup>257</sup> A.C. Templeton, W.P. Wuelfing, R.W. Murray, *Acc. Chem. Res.*, 33 (2000) 27-36.
- <sup>258</sup> G. Bognolo, *Adv. Colloid Interface Sci.*, 106 (2003) 169-181.
- <sup>259</sup> M.A. El-Sayed, *Acc. Chem. Res.*, 34 (2001) 257-264.
- <sup>260</sup> M.A. Firestone, M.L. Dietz, S. Seifert, S. Trasobares, D.J. Miller, N.J. Zaluzec, *Small*, 1 (2005) 754-760.
- <sup>261</sup> P. Wassercheid, W. Keim, *Angew. Chem. Int. Ed.*, 39 (2000) 3772-3789.
- <sup>262</sup> A.V. Mudring, A. Babai, S. Arenz, R. Giernoth, *Angew. Chem. Int. Ed.*, 44 (2005) 5485-5488.
- <sup>263</sup> C. Gaillard, A. Chaumont, I. Billard, C. Hennig, A. Ouadi, S. Georg, G. Wipff, *Inorg. Chem.*, 49 (2010) 6484-6494.
- <sup>264</sup> M.H.G. Precht, P.S. Campbell, J.D. Scholten, G.B. Fraser, G. Machado, C.C. Santini, J. Dupont, Y. Chauvin, *Nanoscale*, 2 (2010) 2601-2606.
- <sup>265</sup> J. Dupont, R.F. Souza, P.A.Z. Suarez, *Chem. Rev.*, 102 (2002) 3667-3696.
- <sup>266</sup> V. Bansal, S.K. Bhargava, *Ionic Liquids: Theory, Properties, New Approaches*, InTech, Croatia, 2011.
- <sup>267</sup> A. Safavi, S. Zeinali, *Colloids Surf. A: Physicochem. Eng. Aspects*, 362 (2010) 121-126.
- <sup>268</sup> J. Dupont, D. Scholten, *Chem. Soc. Rev.*, 39 (2010) 1780-1804.
- <sup>269</sup> A.I. Bhatt, Á. Mechler, L.L. Martin, A.M. Bond, *J. Mater. Chem.*, 17 (2007) 2241-2250.
- <sup>270</sup> Z. Li, Z. Liu, J. Zhang, B. Han, J. Du, Y. Gao, T. Jiang, *J. Phys. Chem. B*, 109 (2005) 14445-14448.
- <sup>271</sup> K. Richter, A. Birkner, A.V. Mudring, *Phys. Chem. Chem. Phys.*, 13 (2011) 7136-7141.
- <sup>272</sup> Y. Gao, A. Voigt, M. Zhou, K. Sundmacher, *Eur. J. Inorg. Chem.*, (2008) 3769-3775.
- <sup>273</sup> Z. Wang, Q. Zhang, D. Kuehner, A. Ivaska, L. Niu, *Green Chem.*, 10 (2008) 907-909.
- <sup>274</sup> L. Ren, L. Meng, Q. Lu, Z. Fei, P.J. Dyson, *J. Colloid Interf. Sci.*, 323 (2008) 260-266.
- <sup>275</sup> M.T. Laranjo, T.B.L. Kist, E.V. Benvenutti, M.R. Gallas, T.M.H. Costa, *J. Nanopart. Res.* 13 (2011) 4987- 4995.
- <sup>276</sup> Y. Liu, M.J. Wang, J. Li, Z.Y. Li, P. He, H.T. Liu, J.H. Li, *Chem. Commun.* (2005) 1778-1780.

- <sup>277</sup> A. Karout, A.C. Pierre, *J. Sol-Gel Sci. Technol.*, 49 (2009) 364-372.
- <sup>278</sup> F. Shi, Q. Zhang, D. Li, Y. Deng, *Chem. Eur. J.*, 11 (2005) 5279 – 5288.
- <sup>279</sup> A. Karout, A.C. Pierre *J. Non-Cryst. Solids*, 353(2007) 2900–2909.
- <sup>280</sup> S.T. Selvan, T. Hayakawa, M. Nogami, Y. Kobayashi, L.M. Liz-Marzán, Y. Hamanaka, A. Nakamura, *J. Phys. Chem. B*, 106 (2002) 10157-10162.
- <sup>281</sup> I. Tanahashi, Y. Manabe, T. Tohda, S. Sasaki, A. Nakamura, *J. Appl. Phys.*, 79 (1996) 1244-1249.
- <sup>282</sup> J. Qiu, X. Jiang, C. Zhu, M. Shirai, J. Si, N. Jiang, K. Hirao, *Angew. Chem. Int. Ed.*, 43 (2004) 2230-2234.
- <sup>283</sup> S.T. Selvan, Y. Ono, M. Nogami, *Mater. Lett.*, 37 (1998) 156-161.
- <sup>284</sup> E. Mine, A. Yamada, Y. Kobayashi, M. Konno, L.M. Liz-Marzan, *J. Colloid Interf. Sci.*, 264 (2003) 385-390.
- <sup>285</sup> C.P. Fredlake, J.M. Crosthwaite, D.G. Hert, S.N.V.K. Aki, J.F. Brennecke, *J. Chem. Eng. Data*, 49 (2004) 954-964.
- <sup>286</sup> Y. Hao, J. Peng, S. Hu, J. Li, M. Zhai, *Thermochim. Acta*, 501 (2010) 78-83.
- <sup>287</sup> M. Hasan, I.V. Kozhevnikov, M.R.H. Siddiqui, A. Steiner, N. Winterton, *Inorg. Chem.*, 38 (1999) 5637-5641.
- <sup>288</sup> P. Dash, R.W.J. Scott, *Chem. Commun.* (2009) 812-814.
- <sup>289</sup> J. Zhang, Y. Gao, R.A. Alvarez-Puebla, J.M. Buriak, H. Fenniri, *Adv. Mater.*, 18 (2006) 3233-3237.
- <sup>290</sup> E.D. Smy, *J. Sol-Gel Sci. Technol.*, 13 (1998) 233–236.
- <sup>291</sup> I. Michalou(di)s, *J. Non-Cryst. Solids*, 350 (2005) 61–66.



## 8. Publications

List of publications originated by the work in this thesis:

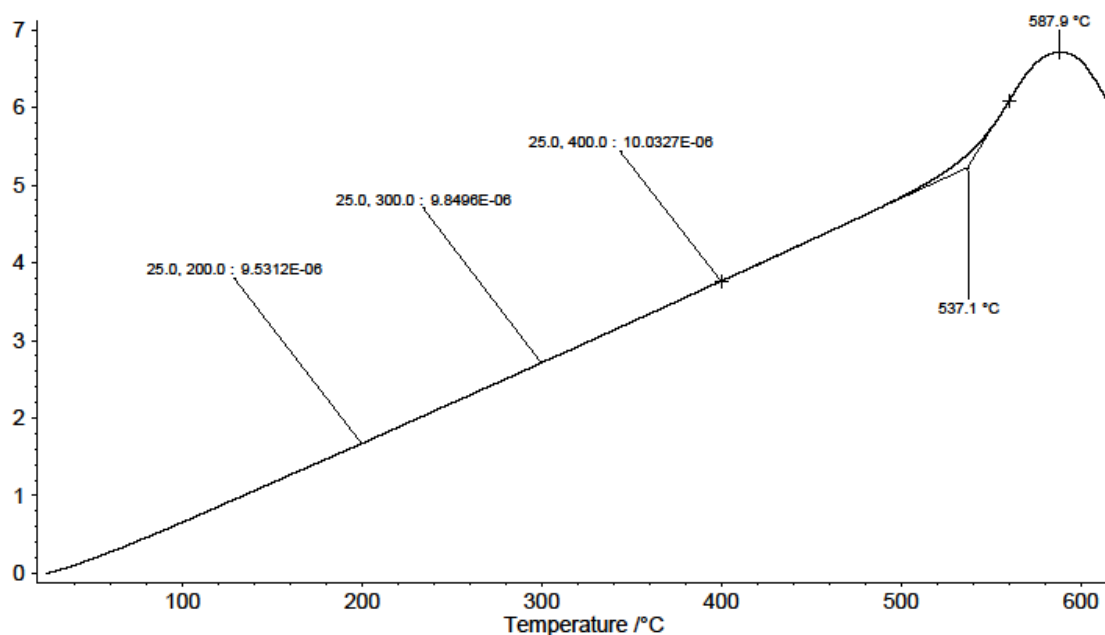
- A. Ruivo, T. Almeida, F. Quintas, R. Wiley, M. Troeira, N. Paulino, C.A.T. Laia, C.A. Queiroz, A. Pires de Matos. "Colours of Luminescent Glasses for Artworks" In 12th International AIC Colour Congress, Proceedings, ed. by L. MacDonald, S. Westland and S. Wuerger (2013) 885-888.
- A. Ruivo, M. G. Ventura, M. D.R. Gomes da Silva and C. A.T. Laia, "Synthesis of Gold Nanoparticles in Sol-Gel Glass Porogens Containing [bmim][BF<sub>4</sub>] Ionic Liquid", Journal of Sol Gel Science and Technology 68 (2013) 234-244.
- A. Ruivo, V. S. F. Muralha, H. Águas, A. Pires de Matos, C. A.T. Laia, "Time-resolved luminescence studies of Eu<sup>3+</sup> in soda-lime silicate glasses", Journal of Quantitative Spectroscopy and Radiative Transfer, in press.
- A. Ruivo, S. M. Andrade, J. Rocha, C. A.T. Laia, F. Pina, "Formation of photoluminescent lead bromide nanoparticles on aluminoborosilicate glass", Manuscript in preparation.



## Chapter 9 - Supplementary Material

9.1. Synthesis and characterization of luminescent  $\text{Eu}_2\text{O}_3$  doped glasses9.1.1.  $\text{Eu}_2\text{O}_3$  doped glass compositions and quantity of oxides used in the glass synthesis.**Table 9.1.** Composition of the europium doped soda-lime-silicate glasses studied (in wt %) and the quantity of oxides used to prepare 25 g of each glass.

	Glass sample	Composition (wt %)				Composition for a 25 g batch (g)			
		$\text{SiO}_2$	$\text{Na}_2\text{O}$	$\text{CaO}$	$\text{Eu}_2\text{O}_3$	$\text{SiO}_2$	$\text{Na}_2\text{O}$	$\text{CaO}$	$\text{Eu}_2\text{O}_3$
<b>Group A</b>	<b>C1</b>	76.5	16.5	<b>0.0</b>	7.0	19.13	<b>4.12</b>	0.00	1.75
	<b>C2</b>	72.4	15.6	<b>5.0</b>	7.0	18.10	<b>3.90</b>	1.25	1.75
	<b>C3</b>	68.2	14.8	<b>10.0</b>	7.0	17.05	<b>3.70</b>	2.50	1.75
	<b>C4</b>	64.2	13.8	<b>15.0</b>	7.0	16.05	<b>3.45</b>	3.75	1.75
<b>Group B</b>	<b>E0</b>	74.0	16.0	10.0	<b>0.0</b>	18.50	4.00	<b>2.50</b>	<b>0.00</b>
	<b>E1</b>	73.9	16.0	10.0	<b>0.1</b>	18.475	4.00	<b>2.50</b>	<b>0.025</b>
	<b>E2</b>	73.6	15.9	10.0	<b>0.5</b>	18.40	3.975	<b>2.50</b>	<b>0.125</b>
	<b>E3</b>	73.3	15.8	9.9	<b>1.0</b>	18.33	3.95	<b>2.47</b>	<b>0.25</b>
	<b>E4</b>	72.8	15.8	9.9	<b>1.5</b>	18.20	3.95	<b>2.48</b>	<b>0.37</b>
	<b>E5</b>	72.5	15.7	9.8	<b>2.0</b>	18.13	3.92	<b>2.45</b>	<b>0.50</b>
	<b>E6</b>	72.1	15.6	9.8	<b>2.5</b>	18.03	3.90	<b>2.45</b>	<b>0.62</b>

9.1.2. Linear thermal expansion of the base glass - glass sample E0 (74%  $\text{SiO}_2$ , 16%  $\text{Na}_2\text{O}$  and 10%  $\text{CaO}$ ). $dL/L_0 \cdot 10^{-3}$ **Figure 9.1.** Linear thermal expansion of glass sample E0, without  $\text{Eu}_2\text{O}_3$ .

### 9.1.3. Modelling used to determine the refractive index using ellipsometry technique

Ellipsometry spectra were measured using a Horiba Jobin Yvon UVISSEL ellipsometer, with a fixed 70° incidence angle, in the range of 1.5–6.5 eV to determine the refractive index,  $n$ , of the glasses. The modeling consisted of dividing the glasses into the bulk and surface regions. The glass material was modeled using the Classical Lorentz oscillator dispersion formula that describes the oscillations of electrons in dielectric materials and has been already used to fit oxide materials.<sup>a</sup> The surface properties were obtained by fitting the layer with a Bruggeman Effective Medium Approximation (BEMA) of 50% bulk material plus 50% voids.<sup>b</sup> The Lorentz oscillator model comprises four parameters that are required to describe the complex dielectric function of the material  $\tilde{\epsilon}$ .

$$\tilde{\epsilon} = \epsilon_{\infty} + \frac{(\epsilon_s - \epsilon_{\infty})\omega_0^2}{\omega_0^2 - \omega^2 - j\omega\Gamma_0} \quad (9.1)$$

where  $\epsilon_{\infty}$  is the dielectric constant when the energy tends to  $\infty$ ,  $\epsilon_s$  the static dielectric constant taken when the energy is zero,  $\omega_0$  the oscillator resonance energy and  $\Gamma_0$  the broadening term of the oscillation. The value of the refractive index was taken from the obtained values at the energy of 1.95 eV (635 nm).

### 9.1.4. Linear dependence between absorbance and Eu<sub>2</sub>O<sub>3</sub> concentration

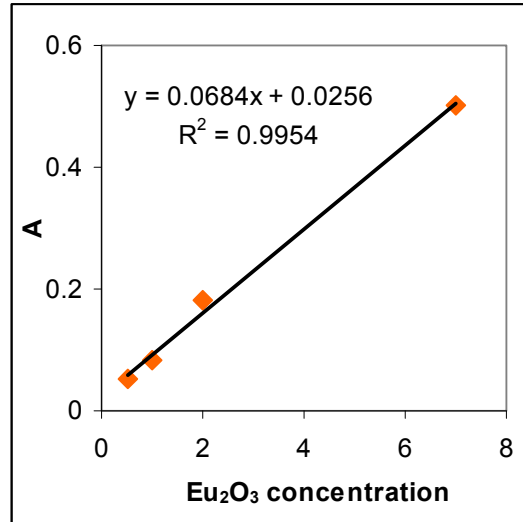


**Figure 9.2.** Dependence between absorbance and Eu<sub>2</sub>O<sub>3</sub> concentration (wt%) in soda-lime-silicate glasses

<sup>a</sup> E. Barrera-Calva, J. C. Martinez-Flores, L. Huerta, A. Avila, M. Ortega-Lopez, Sol. Energ. Mat. Sol. Cells 90 (2006) 2523-2531.

<sup>b</sup> H. Águas, A. Gonçalves, L. Pereira, R. Silva, E. Fortunato, R. Martins, Thin Solid Films 427 (2003) 345-349.

## 9.2. Synthesis of luminescent glasses using different lanthanides

### 9.2.1. Quantity of oxides used to prepare 30 g of each glass with different lanthanides

**Table 9.2.** Quantity of oxides used to prepare 30 g of the glasses synthesized in chapter 3 with different lanthanides.

Base Composition	Group	Glass sample	Composition for a 30 g batch (g)					
			SiO <sub>2</sub>	Na <sub>2</sub> O	CaO	Tb <sub>4</sub> O <sub>7</sub>	Eu <sub>2</sub> O <sub>3</sub>	CeO
74% SiO <sub>2</sub> + 16% Na <sub>2</sub> O + 10% CaO	Mono	M1_1	21.98	4.75	2.97	0.30	-	-
		M1_2	21.76	4.70	2.94	0.60	-	-
		M2_1	21.98	4.75	2.97	-	0.30	-
		M2_2	21.76	4.70	2.94	-	0.60	-
		M3_1	21.98	4.75	2.97	-	-	0.30
		M3_2	21.76	4.70	2.94	-	-	0.60
	Binary Eu+Tb	BET1	21.14	4.57	2.86	0.30	1.13	-
		BET2	21.58	4.66	2.91	0.30	0.56	-
		BET3	21.76	4.70	2.94	0.30	0.30	-
		BET4	21.31	4.61	2.88	0.60	0.60	-
		BET5	21.55	4.66	2.91	0.60	0.28	-
		BET6	21.62	4.67	2.92	0.60	0.19	-
	Binary Tb+Ce	BTC1	21.25	4.59	2.87	0.99	-	0.30
		BTC2	21.49	4.65	2.90	0.66	-	0.30
		BTC3	21.76	4.70	2.94	0.30	-	0.30
		BTC4	21.31	4.61	2.88	0.60	-	0.60
		BTC5	21.53	4.66	2.91	0.30	-	0.60
		BTC6	21.63	4.68	2.92	0.17	-	0.60
	Binary Eu+Ce	BEC1	21.09	4.56	2.85	-	1.20	0.30
		BEC2	21.53	4.66	2.91	-	0.60	0.30
		BEC3	21.76	4.70	2.94	-	0.30	0.30
		BEC4	21.31	4.61	2.88	-	0.60	0.60
		BEC5	21.53	4.66	2.91	-	0.30	0.60
		BEC6	21.61	4.67	2.92	-	0.20	0.60
	Ternary [Tb]	TTb0.2	21.72	4.69	2.93	0.06	0.30	0.30
		TTb0.5	21.65	4.68	2.92	0.15	0.30	0.30
		TTb1	21.53	4.66	2.91	0.30	0.30	0.30
		TTb1.5	21.42	4.63	2.90	0.45	0.30	0.30
		TTb2	21.31	4.61	2.88	0.60	0.30	0.30
		TTb2.5	21.20	4.58	2.87	0.75	0.30	0.30
		TTb3	21.09	4.56	2.85	0.9	0.30	0.30

	<b>TTb3.5</b>	20.98	4.54	2.83	1.05	0.30	0.30
	<b>TTb4.5</b>	20.98	4.54	2.83	1.35	0.15	0.15
<b>Ternary [Eu]</b>	<b>TEu0.2</b>	21.72	4.69	2.93	0.30	0.06	0.30
	<b>TEu0.5</b>	21.65	4.68	2.92	0.30	0.15	0.30
	<b>TEu2</b>	21.31	4.61	2.88	0.30	0.60	0.30
	<b>TEu3</b>	21.09	4.56	2.85	0.30	0.90	0.30
	<b>TEu4.5</b>	20.98	4.54	2.83	0.15	1.35	0.15
	<b>TCe0.2</b>	21.72	4.69	2.93	0.30	0.30	0.06
<b>Ternary [Ce]</b>	<b>TCe0.5</b>	21.65	4.68	2.92	0.30	0.30	0.15
	<b>TCe2</b>	21.31	4.61	2.88	0.30	0.30	0.60
	<b>TCe3</b>	21.09	4.56	2.85	0.30	0.30	0.90
	<b>TCe4.5</b>	20.98	4.54	2.83	0.15	0.15	1.35

**9.2.2. Linear thermal expansion of the base glass (74% SiO<sub>2</sub>, 16% Na<sub>2</sub>O and 10% CaO) doped with different lanthanide oxides (Eu<sub>2</sub>O<sub>3</sub>, Tb<sub>4</sub>O<sub>7</sub>, CeO<sub>2</sub>, Dy<sub>2</sub>O<sub>3</sub>, Tm<sub>2</sub>O<sub>3</sub> and Sm<sub>2</sub>O<sub>3</sub>).**

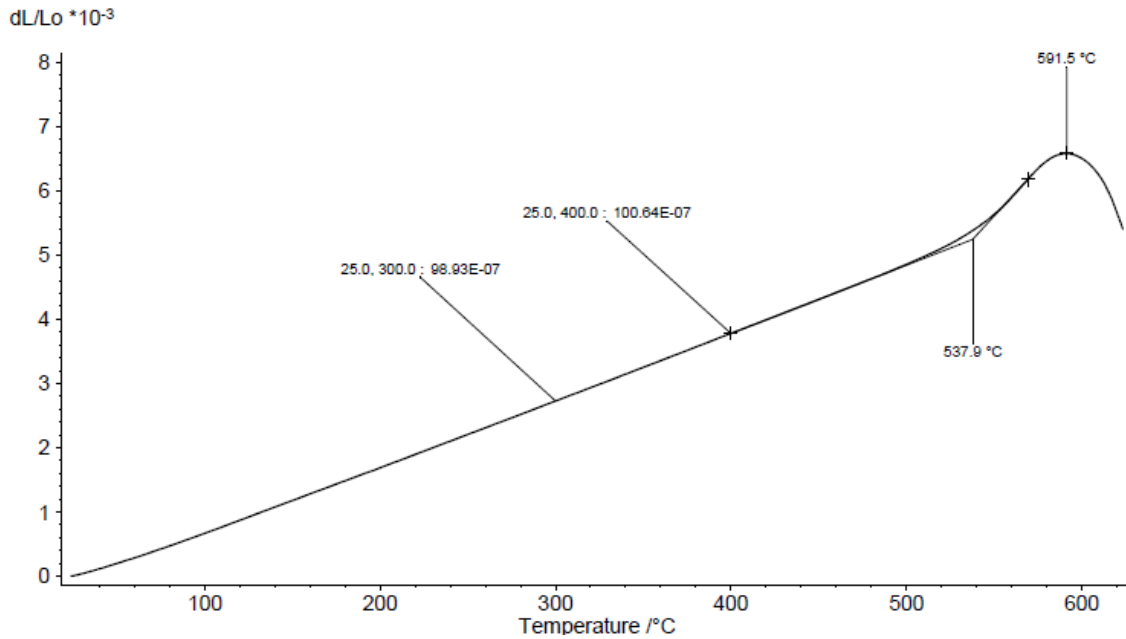


**Figure 9.3.** Linear thermal expansion of glass sample doped with 2% Eu<sub>2</sub>O<sub>3</sub> (wt %).

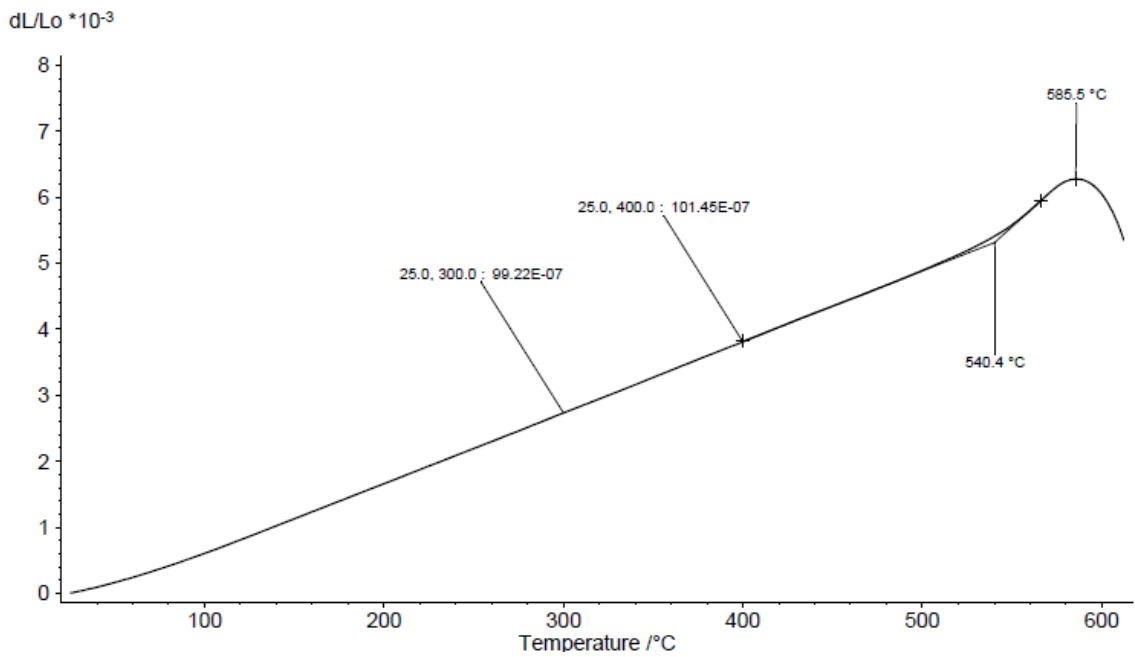


Figure 9.4. Linear thermal expansion of glass sample doped with 2%  $\text{Tb}_4\text{O}_7$  (wt %).

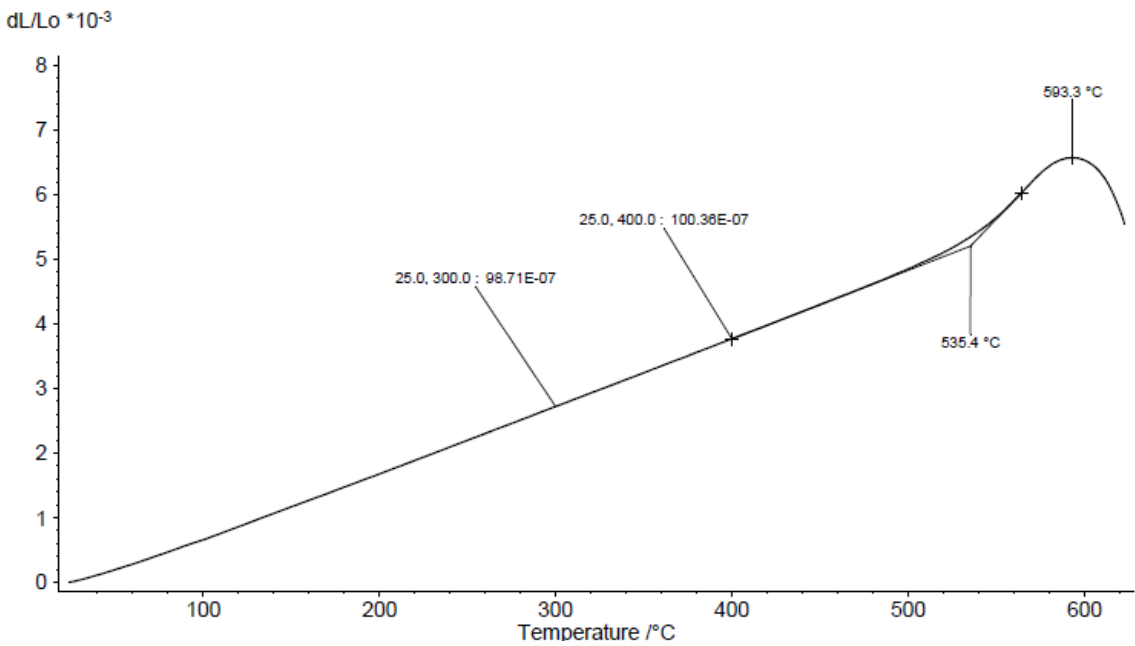


Figure 9.5. Linear thermal expansion of glass sample doped with 2%  $\text{CeO}_2$  (wt %).

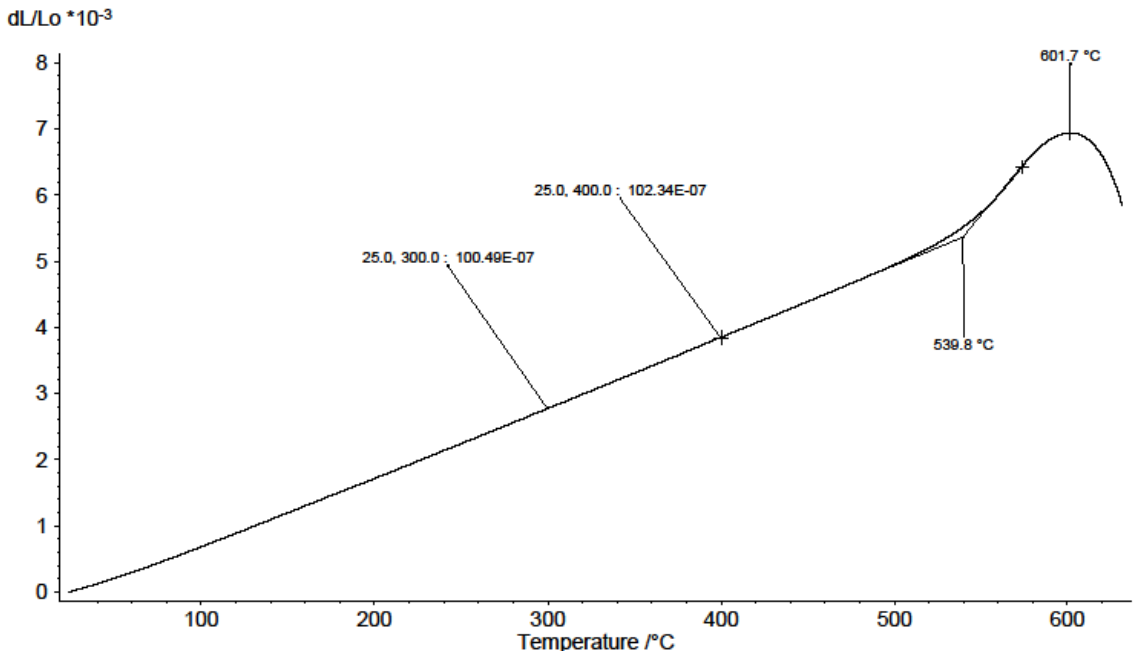


Figure 9.6. Linear thermal expansion of glass sample doped with 2% Dy<sub>2</sub>O<sub>3</sub> (wt %).

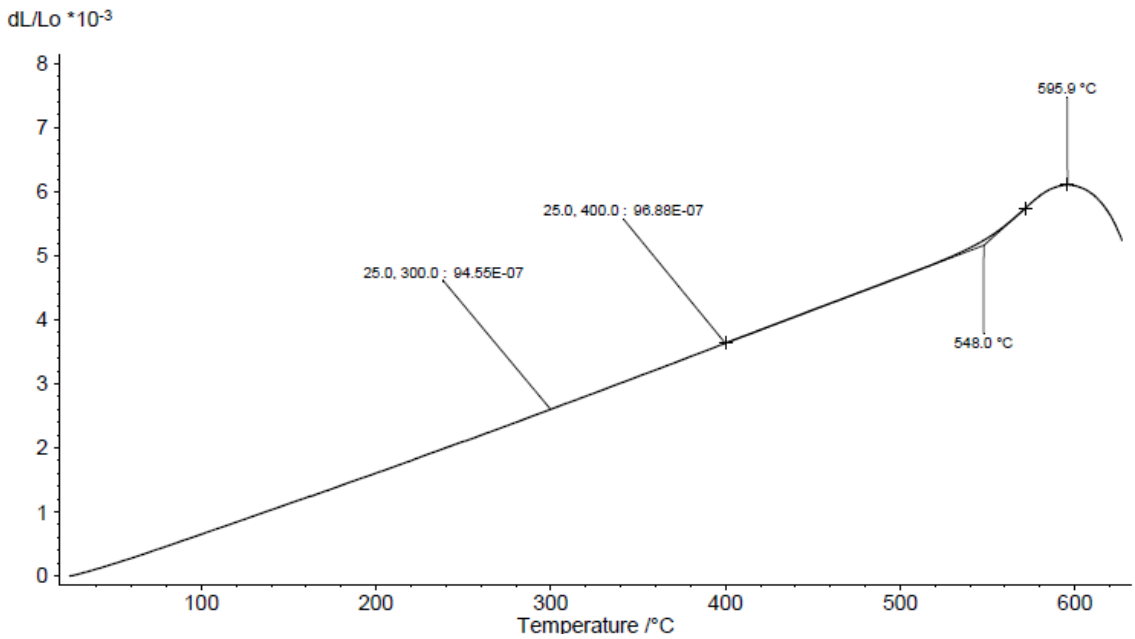
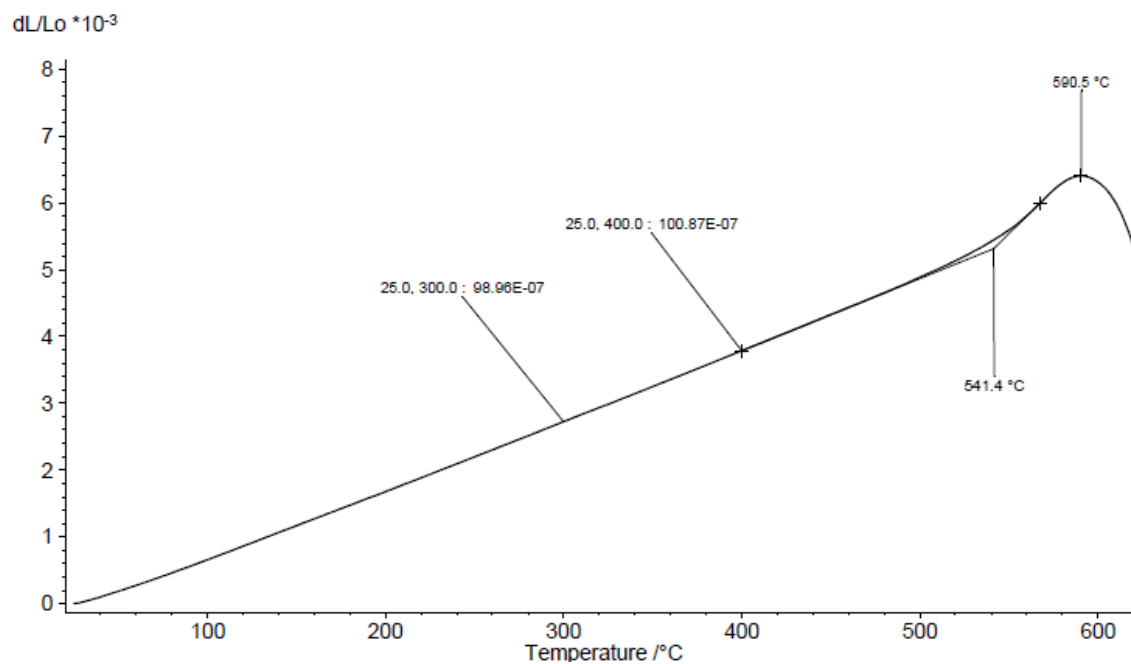


Figure 9.7. Linear thermal expansion of glass sample doped with 2% Tm<sub>2</sub>O<sub>3</sub> (wt %).





**Figure 9.8.** Linear thermal expansion of glass sample doped with 2%  $\text{Sm}_2\text{O}_3$  (wt %).

### 9.2.3. Normalized emission spectra of soda-lime silicate glass doped with 1% $\text{Tb}_4\text{O}_7$ and 2% $\text{Tb}_4\text{O}_7$ (wt%)

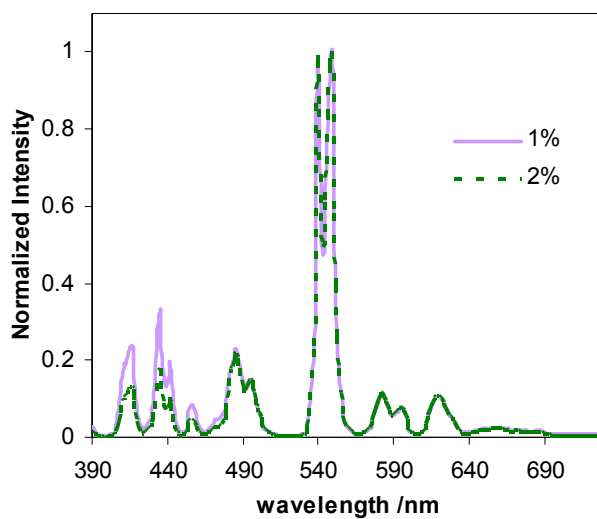


**Figure 9.9.** Normalized emission spectra of the glass samples doped with 1% (violet line) and 2% (green dashed line) of  $\text{Tb}_4\text{O}_7$ .

#### 9.2.4. Lanthanides fraction in the synthesized glasses

**Table 9.3.** Lanthanides fraction (europium-  $f_{Eu}$ , terbium-  $f_{Tb}$  and cerium-  $f_{Ce}$ ) and calculated lanthanides fraction in the binary glasses

Glass sample	Lanthanide fraction			Calculated lanthanide fraction		
	$f_{Eu}$	$f_{Tb}$	$f_{Ce}$	$f_{Eu\_cal}$	$f_{Tb\_cal}$	$f_{Ce\_cal}$
BET1	0.79	0.21	0	0.79	0.21	0
BET2	0.65	0.35	0	0.58	0.42	0
BET3	0.50	0.50	0	0.46	0.54	0
BET4	0.50	0.50	0	0.55	0.45	0
BET5	0.32	0.68	0	0.33	0.67	0
BET6	0.24	0.76	0	0.24	0.76	0
BTC1	0	0.22	0.78	0	0.21	0.79
BTC2	0	0.33	0.67	0	0.41	0.59
BTC3	0	0.50	0.50	0	0.75	0.25
BTC4	0	0.50	0.50	0	0.42	0.58
BTC5	0	0.69	0.31	0	0.76	0.24
BTC6	0	0.77	0.23	0	0.93	0.07
BEC1	0.80	0	0.20	0.95	0	0.05
BEC2	0.67	0	0.33	0.81	0	0.19
BEC3	0.50	0	0.50	0.59	0	0.41
BEC4	0.50	0	0.50	0.80	0	0.20
BEC5	0.33	0	0.67	0.57	0	0.43
BEC6	0.25	0	0.75	0.45	0	0.55

**Table 9. 4.** Lanthanides fraction (europium-  $f_{Eu}$ , terbium-  $f_{Tb}$  and cerium-  $f_{Ce}$ ) and calculated lanthanides fraction in the ternary glasses.

Glass sample	Lanthanide fraction			Calculated lanthanide fraction		
	$f_{Eu}$	$f_{Tb}$	$f_{Ce}$	$f_{Eu\_cal}$	$f_{Tb\_cal}$	$f_{Ce\_cal}$
TTb0.2	0.45	0.09	0.45	0.52	0.10	0.38
TTb0.5	0.40	0.20	0.40	0.49	0.10	0.31
TTb1	0.33	0.33	0.33	0.42	0.39	0.19
TEu0.2	0.09	0.45	0.45	0.10	0.48	0.42
TEu0.5	0.20	0.40	0.40	0.25	0.46	0.29
TEu2	0.50	0.25	0.25	0.62	0.30	0.076
TEu3	0.60	0.20	0.20	0.772	0.20	0.028
TEu4.5	0.82	0.09	0.09	0.92	0.06	0.01
TCe0.2	0.45	0.45	0.09	0.47	0.45	0.07
TCe0.5	0.40	0.40	0.20	0.43	0.43	0.14
TCe2	0.25	0.25	0.50	0.41	0.38	0.20
TCe3	0.20	0.20	0.60	0.42	0.38	0.20
TCe4.5	0.09	0.09	0.82	0.46	0.24	0.30

### 9.3. Luminescent aluminoborosilicate glass with lead halide nanoparticles and cuprous ion

#### 9.3.1. Quantity of oxides used to prepare 30 g of each aluminoborosilicate glass

**Table 9.5.** Quantity of oxides used to prepare 30 g of the glasses synthesized in chapter 4.

Glasses	Composition for a 30g batch (g)												
	SiO <sub>2</sub>	B <sub>2</sub> O <sub>3</sub>	Al <sub>2</sub> O <sub>3</sub>	Li <sub>2</sub> O	Na <sub>2</sub> O	K <sub>2</sub> O	BaO	ZrO <sub>2</sub>	PbO	CuO	F	Cl	Br
<b>1</b>	16.28	4.80	2.73	0.69	0.90	0.42	1.98	0.57	1.29	0.009	0.03	0.15	0.15
<b>2</b>	16.29	4.80	2.73	0.69	0.90	0.42	1.98	0.57	1.29	-	0.03	0.15	0.15
<b>3</b>	16.46	4.85	2.76	0.70	0.91	0.42	2.00	0.58	1.30	0.009	-	-	-
<b>4</b>	16.53	4.89	2.87	0.70	0.92	0.43	2.02	-	1.31	-	0.03	0.15	0.15
<b>5</b>	16.93	5.01	2.94	0.72	0.94	0.44	2.07	0.6	-	-	0.03	0.16	0.16
<b>6</b>	17.27	5.12	3.01	0.73	0.96	0.45	2.11	-	-	-	0.03	0.16	0.16
<b>7</b>	16.78	4.95	2.81	0.71	0.93	0.43	2.04	-	1.33	-	-	-	-
<b>8</b>	17.52	5.20	2.96	0.75	0.98	0.45	2.14	-	-	-	-	-	-
<b>9 (base glass)</b>	18.91	5.57	3.17	0.80	1.04	0.49	-	-	-	-	-	-	-
<b>10</b>	18.01	5.31	3.02	0.76	0.99	0.46	-	-	1.43	-	-	-	-
<b>11</b>	17.79	5.25	2.98	0.75	0.98	0.46	-	-	1.41	-	0.03	0.16	0.16
<b>12</b>	18.91	5.57	3.17	0.80	1.04	0.49	-	-	-	0.01	-	-	-
<b>13</b>	18.01	5.31	3.02	0.76	0.99	0.46	-	-	1.43	0.01	-	-	-

**Table 9.6.** Quantity of oxides used to prepare 30 g of the glasses synthesized in chapter 4 with different halides

Glasses	Composition for a 30g batch (g)											
	SiO <sub>2</sub>	B <sub>2</sub> O <sub>3</sub>	Al <sub>2</sub> O <sub>3</sub>	Li <sub>2</sub> O	Na <sub>2</sub> O	K <sub>2</sub> O	BaO	PbO	NaF	NaCl	NaBr	NaI
<b>F</b>	16.56	4.91	2.79	0.70	0.68	0.43	2.02	1.32	0.33	-	-	-
<b>Cl</b>	16.56	4.91	2.79	0.70	0.68	0.43	2.02	1.32	-	0.46	-	-
<b>Br</b>	16.56	4.91	2.79	0.70	0.81	0.43	2.02	1.32	-	-	0.36	-
<b>I</b>	16.56	4.91	2.79	0.70	0.68	0.43	2.02	1.32	-	-	-	1.18

### 9.3.2. Raman spectra of aluminoborosilicate glass samples

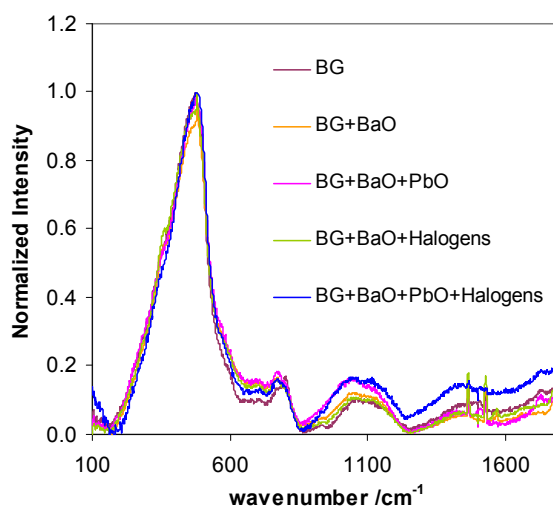


**Figure 9.10.** Normalized Raman spectra of the BG (base glass-purple line), BG+BaO (yellow line), BG+BaO+PbO (pink line), BG+BaO+Halogens (green line) and BG+BaO+PbO+Halogens.

### 9.3.3. $\mu$ - EDXRF analysis of the aluminoborosilicate glass doped with $\text{PbBr}_2$

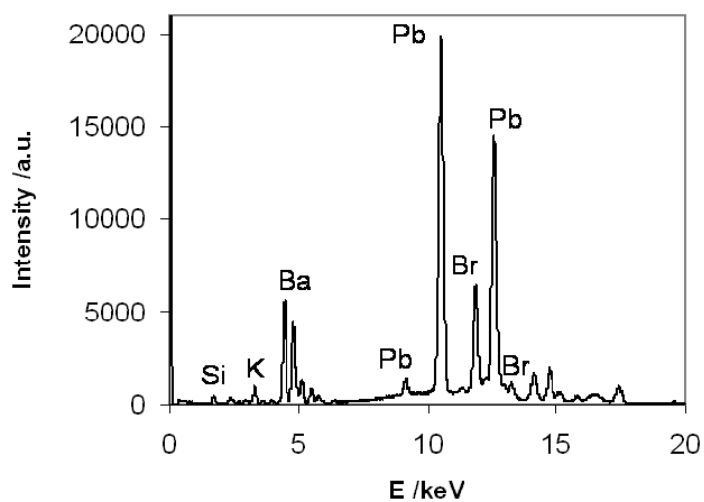


**Figure 9.11.**  $\mu$ -EDXRF analysis of the glass sample doped with  $\text{PbBr}_2$

#### 9.3.4. Emission spectra of $\text{PbBr}_2$ doped glass at different temperatures

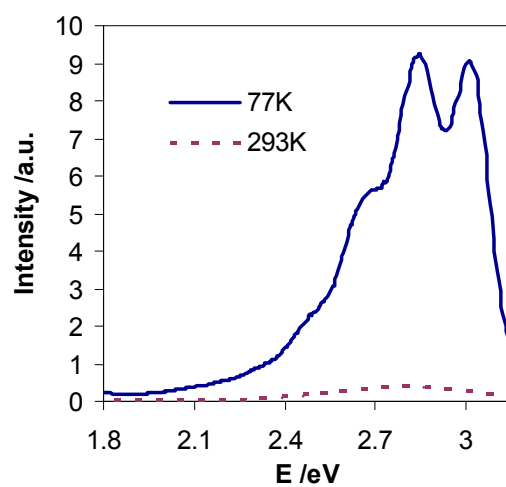


**Figure 9. 12.** Emission spectra of glass sample with  $\text{PbBr}_2$  nanoparticles at 77 K and at 293 K.

#### 9.4. Sol-gel glass materials with gold nanoparticles

##### 9.4.1 TEM images of the glass samples with gold nanoparticles

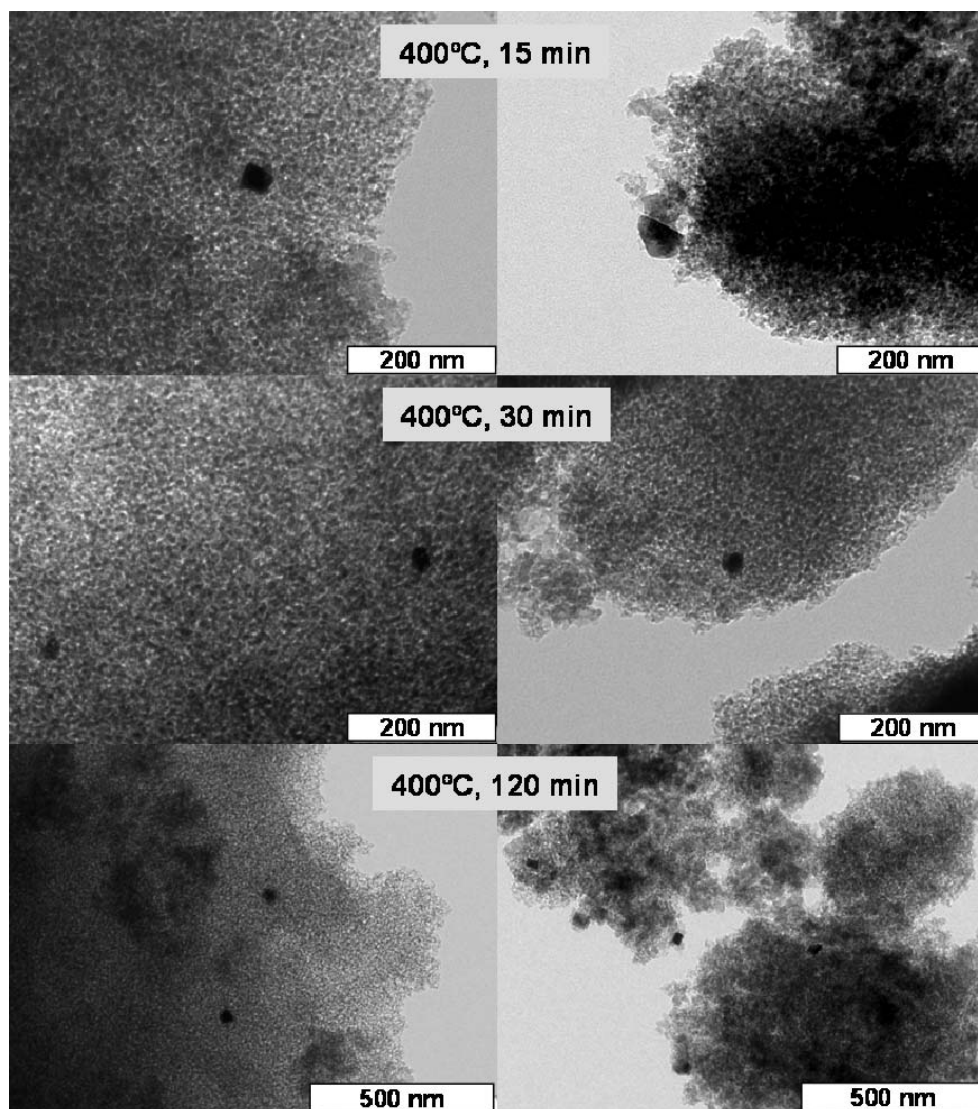


**Figure 9.13.** TEM image of the glass samples heat-treated at 400°C during different times: 15, 30 and 120 min.

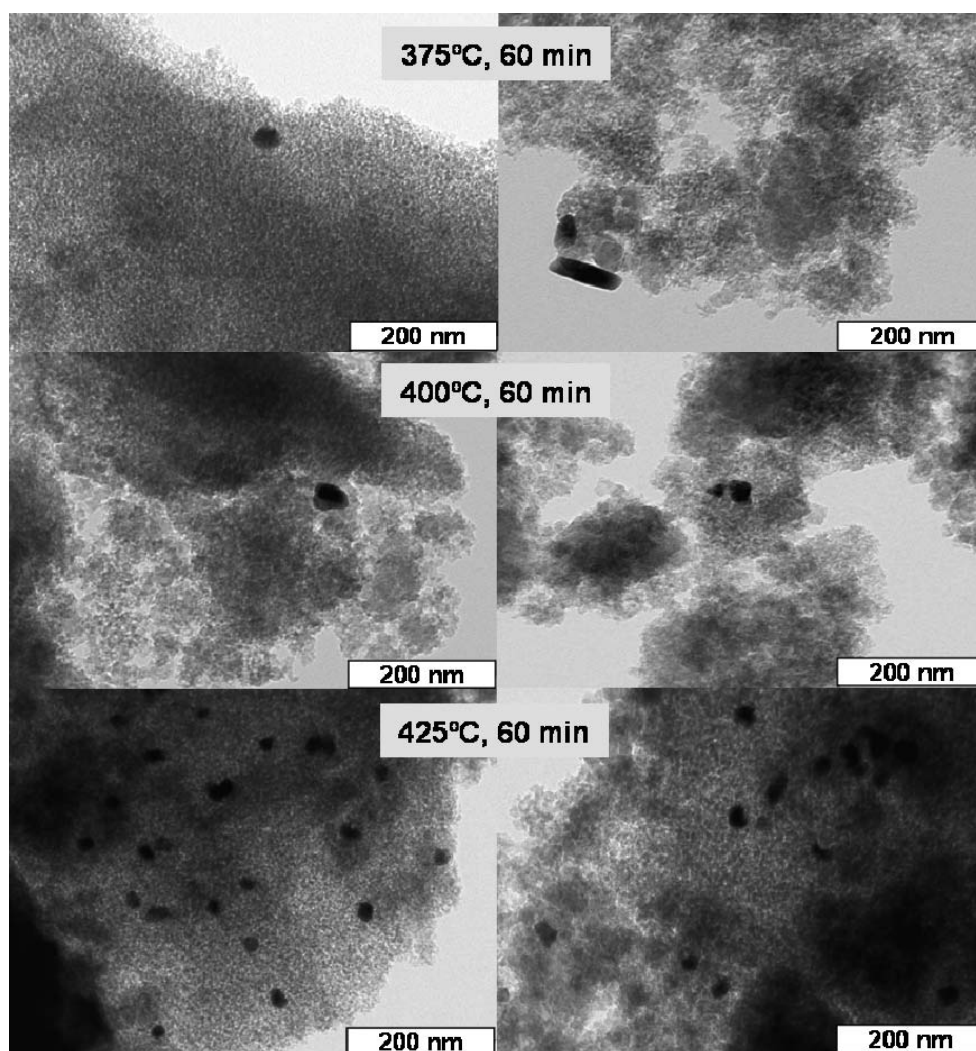


**Figure 9.14.** TEM image of the glass samples heat-treated at different temperatures: 375, 400 and 425°C during 60 min.

#### 9.4.2. FT-IR spectra of the glasses prepared with $\text{Eu}^{3+}$ and with the ionic liquid [bmim][ $\text{BF}_4$ ].

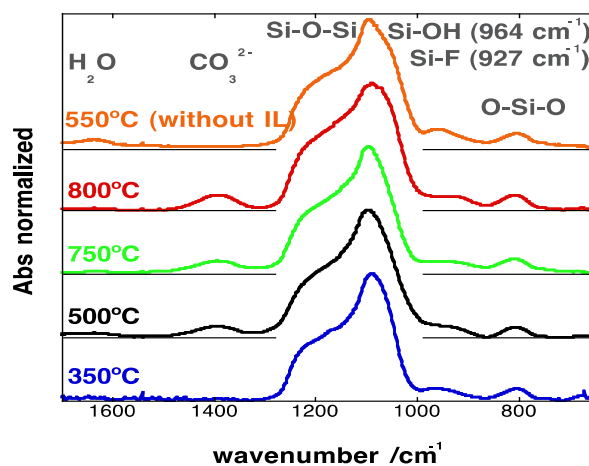


**Figure 9.15.** FT-IR spectra of the glasses prepared with  $\text{Eu}^{3+}$  and with the ionic liquid [bmim][ $\text{BF}_4$ ] treated at different temperatures: 350°C; 500°C; 750°C; 800°C; and without the ionic liquid treated at 550°C.

## 9.5. Impact of the produced materials in art

### 9.5.1. Photochromic glass – preliminary studies

A photochromic aluminoborosilicate glass was synthesized using a composition that was taken from the literature<sup>(3)</sup> A transparent uncoloured glass was obtained after being taken from the electric furnace at 1400°C. This glass was afterwards heat treated at 650°C, originating a yellow glass sample. Figure 9.16 illustrate that the glass sample A heat treated at 650°C is initially yellow but when exposed to daylight this glass becomes darker.

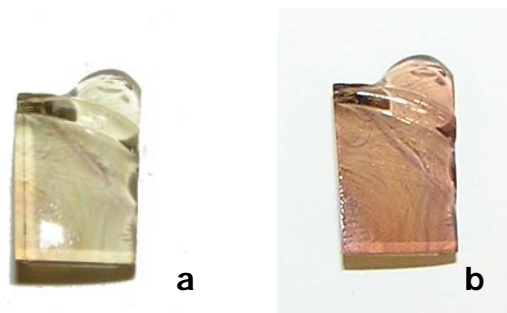


**Figure 9.16.** Glass sample before (a) and after (b) being exposed to day light.

The exposure of the glass sample to UV light gives rise to a broad absorption band in the visible wavelength range that is attributed to the formation of silver nanoparticles. The behaviour of this photochromic glass is illustrated in figure 9.17, where the increase of the absorption band at 520 nm using a medium pressure mercury lamp with a 366 nm band pass filter is observed. Using these conditions the darkening reaches its maximum of intensity after being irradiated 20 min.

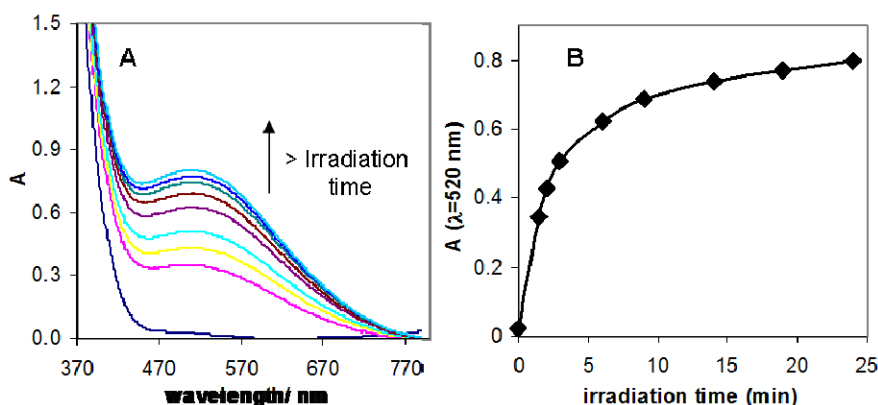


**Figure 9.17.** Optical absorption spectra (A) and absorbance at 520 nm after increasing the irradiation time, measured at different times.

(3) J. Navarro, El Vidrio, 3<sup>rd</sup> edition, Consejo Superior de Investigaciones Científicas, Sociedad Española de Cerámica y Vidrio, Madrid, 2003.



Photochromism applies to a phenomena characterized by a reversible change in colour. The absorption band formed after the glass sample irradiation decreases with time, which means that this reaction is reversible. The measurements were made after several minutes (figure 9.18)

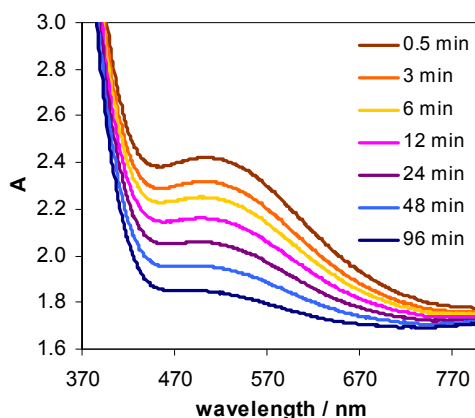


**Figure 9.18.** UV-Vis absorption spectra of the photocromic glass after being irradiated 5 min in a medium pressure mercury lamp using a 366 nm band pass filter.

Stability tests of the synthesized photocromic glass were also made. Figure 9.19 illustrates the reversible change in the absorption of the photocromic glass after a 5 min irradiation, using a 366 nm band pass filter, and after one hour without radiation. To prove the stability of the photocromic sample the procedure was repeated five times. The absorbance value at 520 nm maintains constant after the different irradiation cycles.

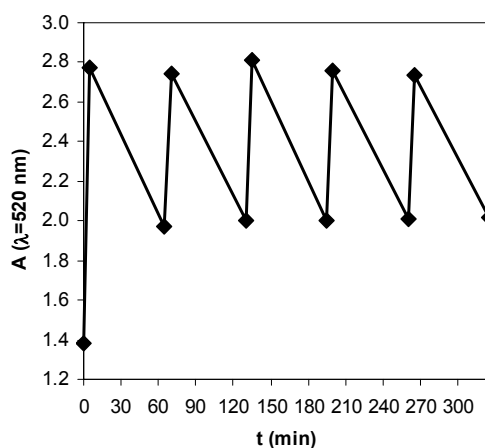


**Figure 9.19.** Absorbance at 520 nm, after irradiate glass A for 5 min and after waiting one hour. This procedure was repeated five times.

